DMSP SPECIAL SENSOR MICROWAVE/IMAGER CALIBRATION/VALIDATION

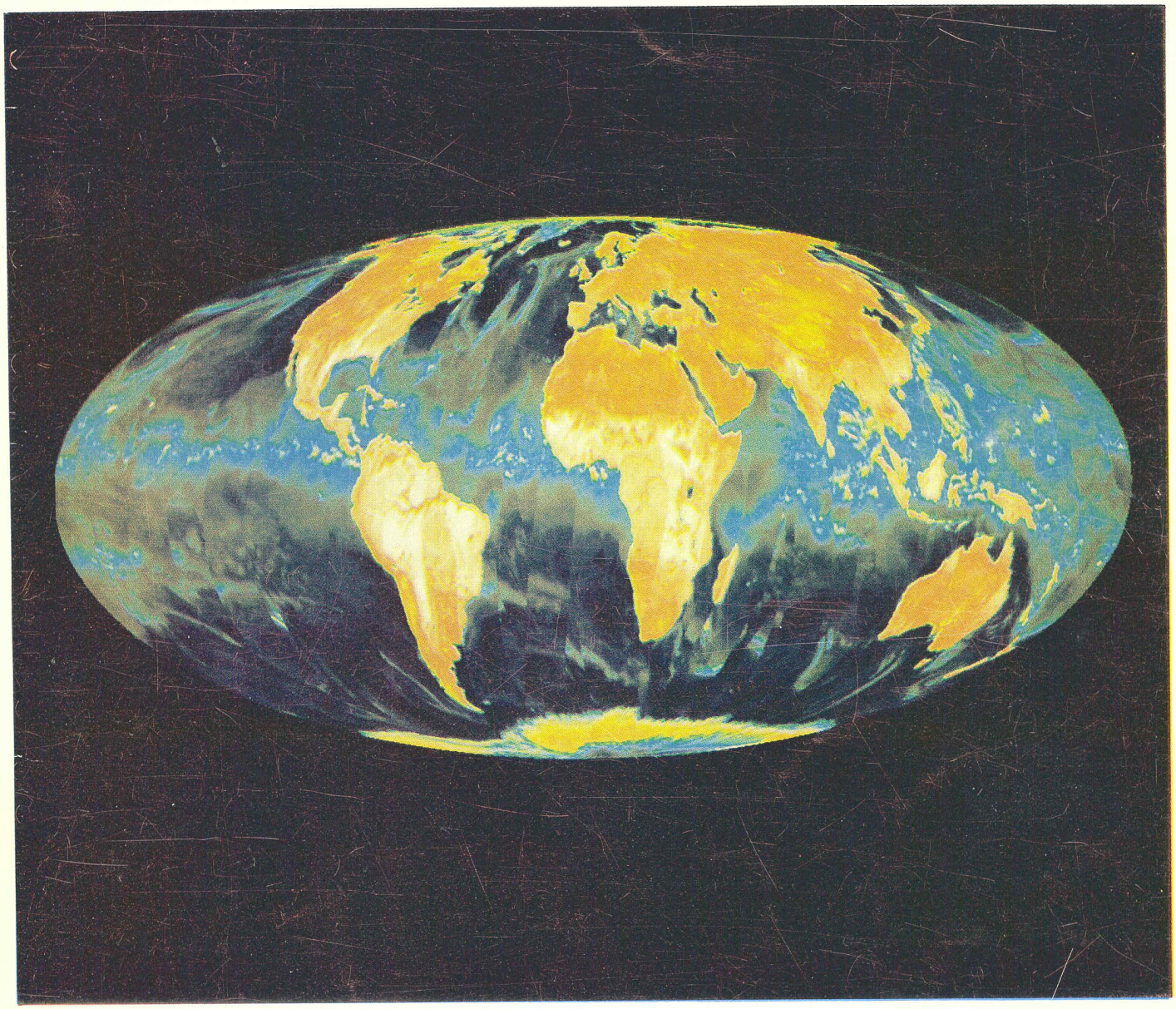

NAVAL
RESEARCH
LABORATORY
WASHINGTON, D.C.

FINAL REPORT VOLUME I

Cover Picture

The cover picture shows the brightness temperatures of the SSM/I 19 GHz horizontally polarized channel. The Mollweide equal-area projection is composed of SSM/I measurements from 62 consecutive revolutions of the DMSP satellite over a four day period in mid-September 1988. The brightness temperatures for this image range from 90 to 310 K. The lowest brightness temperatures are dark blue ranging up through shades of blue, green, yellow, and red to white. The natural radiation emitted by the earth is predominately in the infrared and microwave portions of the spectrum, but the microwave radiation penetrates the atmosphere better than the infrared to reveal details of surface and weather. The coolest parts of the globe are the polar oceans. The polar ice packs are warmer than the surrounding sea at 19 GHz. The warmest and brightest parts of the globe are low altitude land. Mountains, lakes, and rivers, such as the Amazon, are darker, cooler features on the continents. Clouds vary greatly in brightness, depending on the amount of water present. Rain and hail in thunderclouds are warmer than the surrounding clouds so that regions of precipitation are relatively light. Although the intertropical convergence zone is visible over the ocean, the view of land is relatively unobstructed where the clouds cross the continents. The SSM/I retrieves information on cloud concentration, precipitation, cloud water content, humidity and marine wind for meteorologists and naval operations. It detects, not only storms, but sea ice and delineates their boundaries for safe routing of ships, and measures land parameters for geological, agricultural, and military purposes.

DMSP SPECIAL SENSOR MICROWAVE/IMAGER

CALIBRATION/VALIDATION

DMSP SSM/I Cal/Val Team

Coordinated by

J. Hollinger
Space Sensing Branch
Naval Research Laboratory
Washington, DC 20375-5000

FINAL REPORT
VOLUME I

20 July 1989

CONTRIBUTORS

James P. Hollinger, Gene A. Poe and Louis A. Rose
Space Sensing Branch
Naval Research Laboratory
Washington D.C.

Robert H. Baldwin, Joseph W. Deaver, Dawn K. Conway,
Robert W. Conway, Mary Ann Craft, Nancy L. Leist,
Edward M. Overton, David J. Spangler, and Lloyd A. Walker
Bendix Field Engineering Corporation
Washington D.C.

James L. Peirce and Richard C. Savage
Hughes Aircraft Company
El Segundo, CA

John C. Alishouse and John C. Wilkerson
National Oceanic and Atmospheric Administration
National Environmental Satellite Data and Information Service
Washington, D.C.

Sheila Snyder, Jennifer Vongsathorn and Ralph Ferraro
S.M. Systems and Research Corporation
Landover, MD

Calvin T. Swift, Mark Goodberlet, Kuo-Hua Hsueh,
John Morris, Christopher Ruf and David Choi
University of Massachusetts
Amherst, MA

Frank Wentz
Remote Sensing Systems
Santa Rosa, CA

Marshall J. McFarland, Matthew Batchelor, Robert Miller
Jeffrey Miller, Richard Miller and Susan Steinberg
Departments of Agricultural Engineering, Meteorology,
and Electrical Engineering
Texas A&M University

Christopher M. U. Neale
Assistant Professor
Department of Agricultural and Irrigation Engineering
Utah State University

Rene O. Ramseier, Ken Asmus and Irene G. Rubinstein
Atmospheric Environment Service,
Centre for Research in Experimental Space Science, Microwave Group
York University
4700 Keele Street
North York, Ontario, Canada M3J 1P3

Cathryn Bjerkelund, Tom Hirose and Lyn D. Arsenault
Norland Science and Engineering, Ltd.
902-280 Albert Street
Ottawa, Ontario, Canada K1P 5G8

William S. Olson, Frank La Fontaine, William L. Smith,
Robert T. Merril, Barry A. Roth and Thomas H. Achtor
Cooperative Institute for Meteorological Satellite Studies
Space Science and Engineering Center
University of Wisconsin
Madison, Wisconsin

Gerald W. Felde
Department of the Air Force
Geophysics Laboratory
Hanscom Air Force Base, MA

TABLE OF CONTENTS

ACKNOWLEDGEMENT

The authors wish to thank CDR D. McConathy, now retired who played a large role in developing and supporting the procurement of the SSM/I instrument. A special acknowledgement is due CAPT F. Wooldridge, Space and Naval Warfare Systems Command, who initiated this calibration/validation effort and made it possible; CAPT T. Piwowar, Office of the Undersecretary of Defense, Joint Environmental Satellite Coordinating Group; LCDR L. Burgess, now retired, and CDR W. Elias, Navy Space Systems Activity, who continued the Navy effort; and Colonels S. McElroy, J. Curtis and J. Randmaa, Directors of the Defense Meteorological Satellite Program Office, and Capt T. Piatkowski, SSM/I Project Officer for their direction and strong support throughout the project. Special thanks are due Ms. M. Spangler who typed, proofread, and assembled this report.

List of Figures

List of Figures (Continued)

List of Figures (Continued)

List of Tables

1.0 EXECUTIVE SUMMARY

1.1 INTRODUCTION

The first Special Sensor Microwave/Imager (SSM/I) was launched 19 June 1987 aboard the Defense Meteorological Satellite Program (DMSP) Block 5D-2 Spacecraft F8. The SSM/I is a seven-channel, four-frequency, linearly-polarized, passive microwave radiometric system which measures atmospheric, ocean, and terrain microwave brightness temperatures at 19.3, 22.2, 37.0, and 85.5 GHz. It is built by Hughes Aircraft Company under the direction of the Air Force Space Division (USAF SD) and the Naval Space Systems Activity (NSSA) and represents a joint Air Force/Navy operational program to obtain synoptic maps of critical atmospheric, oceanographic, and selected land parameters on a global scale. This is the first of seven SSM/I's scheduled for launch over the next two decades.

The SSM/I data are processed by the Naval Oceanography Command and the Air Weather Service to obtain near real-time global maps of cloud water, rain rates, water vapor over ocean, marine wind speed, sea ice location, age and concentration, snow water content, and land surface type, moisture, and temperature. In addition, Air Force and Navy DMSP tactical sites will be capable of receiving the data directly to meet operational requirements. Table 1.1 presents a summary of the primary environmental parameters retrieved from the SSM/I along with the spatial resolution, parameter range, and measurement accuracy. The calibrated antenna temperature records (TDR), which are reversible to raw counts, the calibrated brightness temperature records (SDR), the retrieved environmental parameter records (EDR), sensor performance records (QDR), and files of the constants used to derive these records (SENCAL and PARMEX) are archived by the National Environmental Satellite, Data, and Information Service.

The Block 5D-2 F-8 spacecraft is in a circular sun-synchronous near-polar orbit at an altitude of approximately 833 km with an inclination of 98.8 degrees and an orbit period of 102.0 minutes. The orbit produces 14.1 full orbit revolutions per day and has an 0613 am local ascending node equatorial crossing. Figure 1.1 shows the SSM/I in the early morning orbit. The SSM/I swath width is 1400 km and results in a high ground track repeat coverage on successive days as shown in Figure 1.2. Small unmeasured circular sectors of 2.4 degrees occur at the North and South Poles. Figures 1.3 and 1.4 present typical SSM/I sub-satellite track and swath width coverage for successive orbits.

The Space Sensing Branch of the Naval Research Laboratory (NRL) was directed by USAF SD and NSSA to prepare and execute a plan to ensure that the SSM/I instrument and retrieval algorithms performed within specifications. With this objective NRL organized a team of sensor scientists from universities, industry, and government agencies and conducted the DMSP SSM/I calibration/validation effort. This document describes the results of that one-year effort.

Table 1.1

SSM/I Environmental Products

Parameter	Geometric Resolution (km)	Range of Values	Quantization Levels	Absolute Accuracy
Ocean Surface Wind Speed	25	3 to 25	1	$\pm$2 m/s
Ice				
o Area Covered	25	0 to 100	5	$\pm$12%
o Age	50	1st Year, Multiyear	1 yr,>2 yr	None
o Edge Location	25	N/A	N/A	$\pm$12.5 km
Precipitation Over Land Areas	25	0 to 25	0, 5, 10, 15, 20, $\geq$25	$\pm$5 mm/hr
Cloud Water	25	0 to 1	0.05	$\pm$0.1 kg/m^2
Integrated Water Vapor	25	0 to 80	0.10	$\pm$2.0 kg/m^2
Precipitation Over Water	25	0 to 25	0, 5, 10, 15, 20, $\geq$25	$\pm$5 mm/hr
Soil Moisture	50	0 - 60%	1	None
Land Surface Temperature	25	180 - 340K	1	None
Snow Water Content	25	0 - 50 cm	1	$\pm$3 cm
Surface Type	25	12 Types	N/A	N/A
Cloud Amount	25	0 - 100%	1	$\pm$20%

Figure 1.1 DMSP Block 5D-2 Satellite

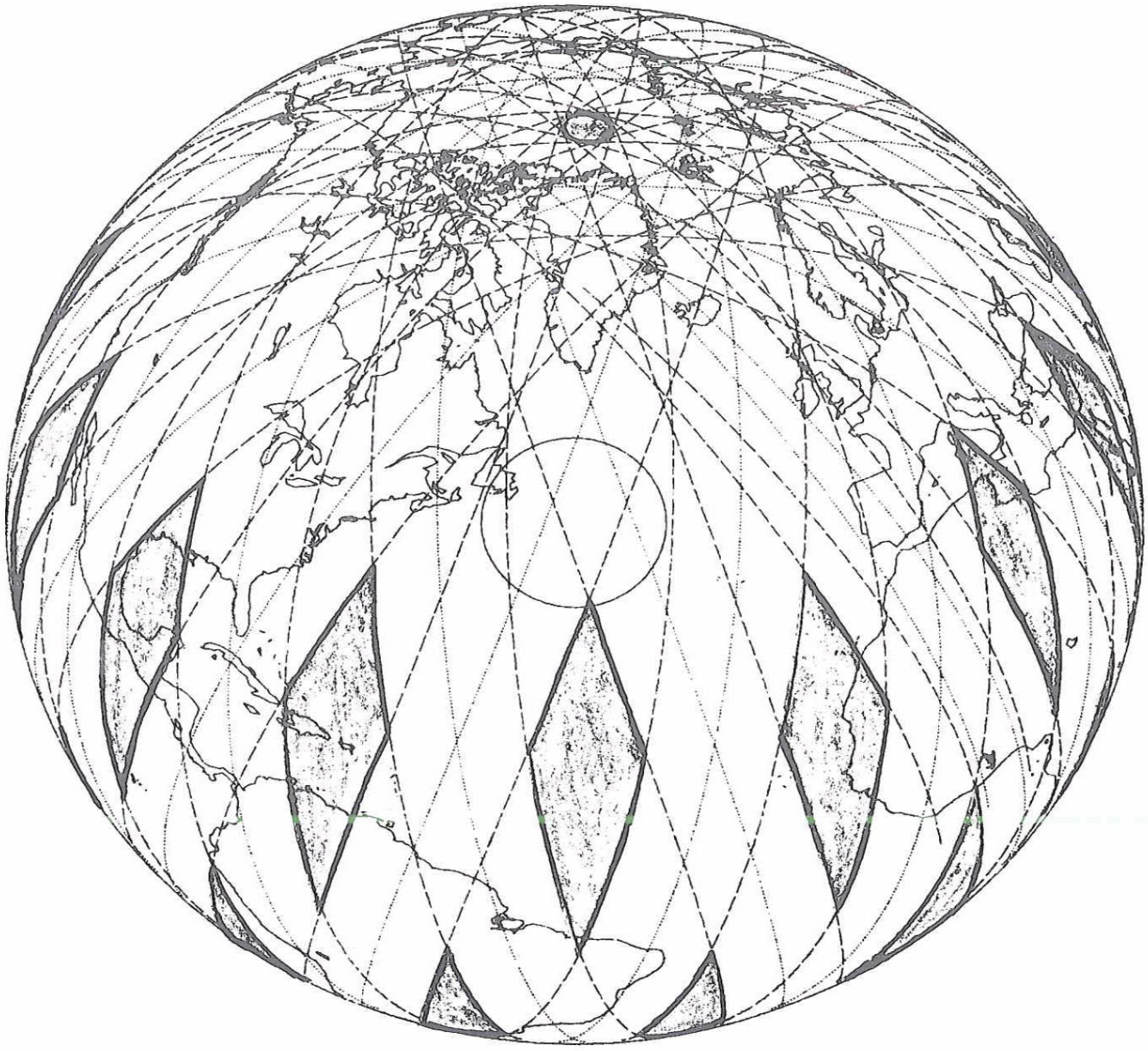

Figure 1.2 Coverage of SSM/I in 24 Hours

Figure 1.3 Equatorial View of Successive Orbits

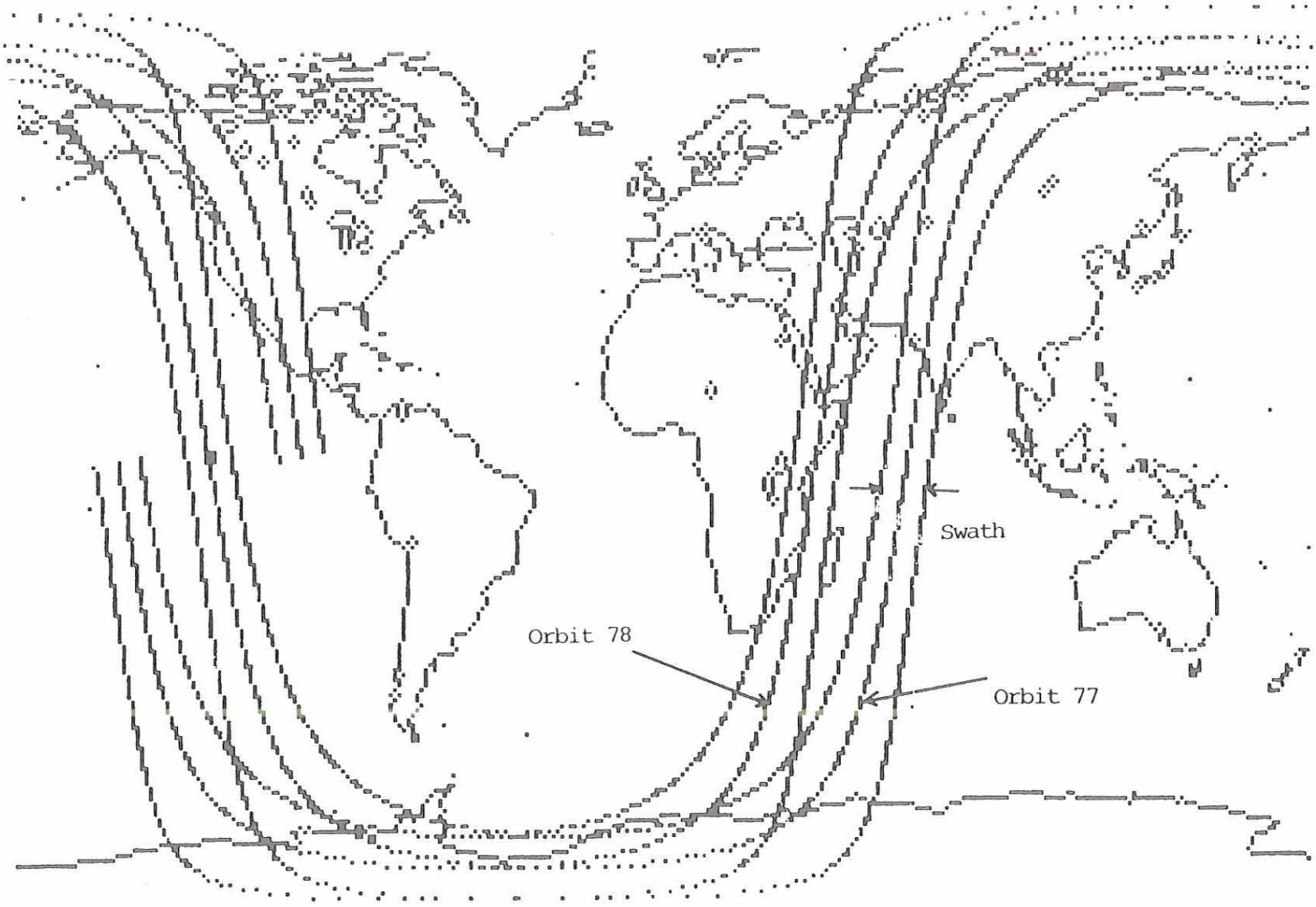

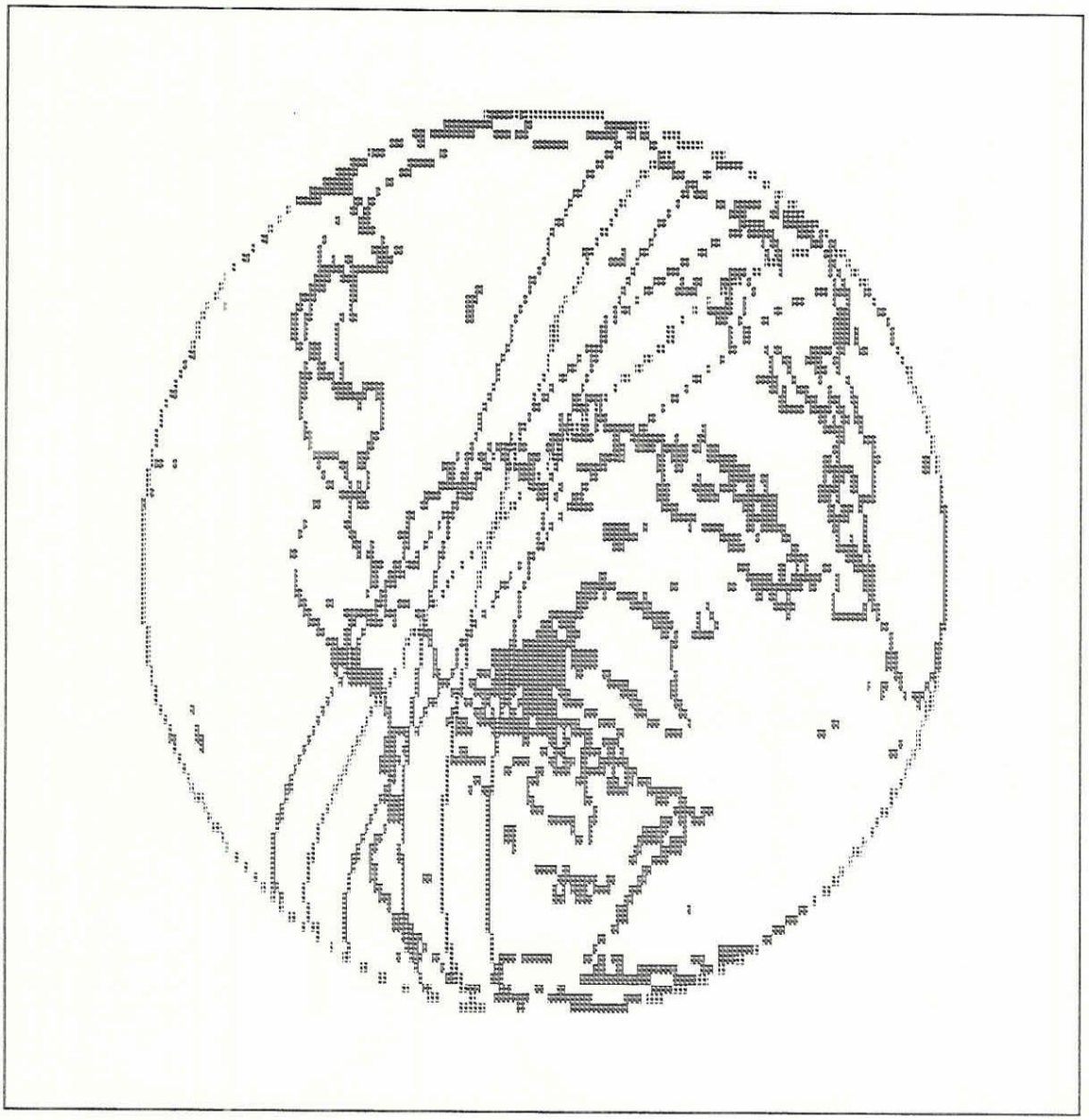

Figure 1.4 Polar View of Successive Orbits

The objective of this project is three fold. First, establish that the instrument is operating properly and making accurate, absolute brightness temperature measurements. This includes receiver stability; gain and noise; scan stability and sampling precision; pointing and geolocation; cross polarization and beam efficiency; and absolute calibration. Second, once the absolute calibration of the measured microwave brightness temperatures used by the retrieval algorithms is established, validate the accuracy of the retrieved environmental parameters. Finally, where retrieved products are found to be out of specification, make algorithm corrections, or, if necessary, generate entirely new algorithms to bring them within specification.

An executive summary of the DMSP SSM/I Cal/Val Project is given in Volume I, Section 1. Section 1.2 provides a brief description of the instrument performance and absolute calibration. Section 1.3 is a summary of the environmental parameter validation described in detail in Volume II. Section 1.4 contains recommendations to bring the instrument and environmental retrieval algorithms within specification and, in some cases, to extend and improve performance. This Section is complete. The following Sections of Volume I and Volume II amplify and provide in greater detail the information summarized in Section 1. The SSM/I instrument is described in Section 2. Section 3 contains details of the algorithms used to calibrate the output of the SSM/I in terms of antenna temperature and brightness temperature. Sections 4, 5, and 6 present the results of the instrument performance, absolute calibration, and pointing investigations. Sections 7 through 12 of Volume II present detailed descriptions of the validation of the environmental parameters.

1.2 INSTRUMENT PERFORMANCE

1.2.1 Stability

The SSM/I is the first satellite microwave radiometer to employ total-power receivers and achieve a factor of two improvement in sensitivity over "Dicke" switched type radiometers. Greater independence of gain variations is achieved with a "Dicke" radiometer but at the cost of reduced sensitivity. Thus, high interest was present during the SSM/I Cal/Val early orbit period when evaluating the on-orbit radiometer sensitivities and gain stabilities. Once the early orbit results demonstrated the success of the radiometer performance, the task remained to validate the absolute calibration accuracy and the radiometric sensitivities throughout the on-orbit extreme environmental conditions. For example, Figure 1.5 presents the sun angle defined by the angle between the vector normal to the spacecraft's orbit and the vector from the spacecraft to the sun and the percent of orbit not in earth shadow. The relatively large variation in the sun angle introduces a large variation of solar heating of the SSM/I and, consequently, possibly large temperature changes of the instrument electronics and Bearing and Power Transfer Assembly (BAPTA). Not only must the SSM/I survive these extreme conditions, it must also meet radiometric performances. Due to increased heating of the instrument in the winter of 1987, the SSM/I was turned off for a brief period from December 2, 1987 through January 12, 1988. This was done to avoid possible damage to the BAPTA when the temperature

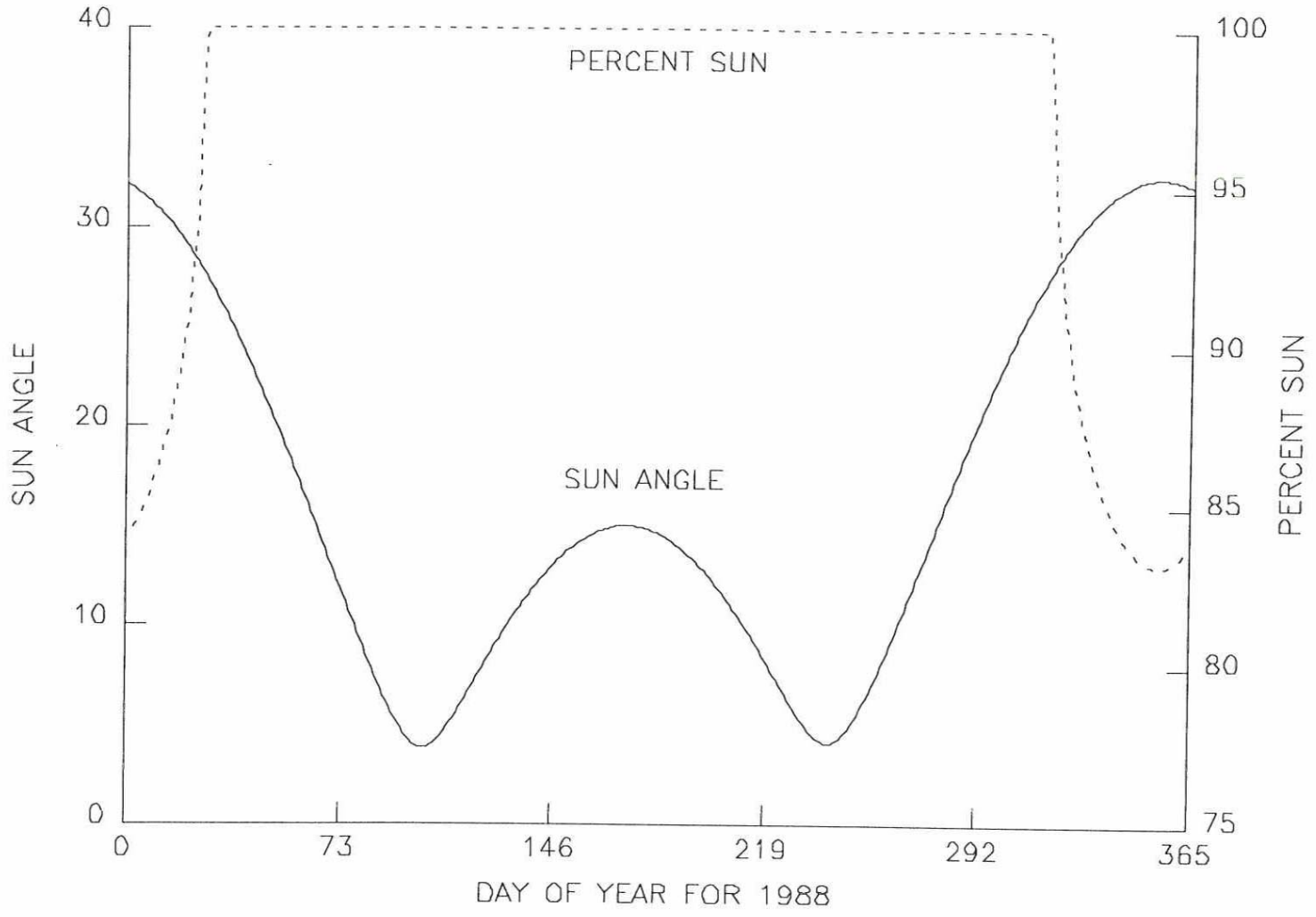

FIG. 1.5 VARIATION OF SUN ANGLE AND PERCENT SUN FOR F8

exceeded 41 degrees centigrade; the maximum temperature limit set by Hughes Aircraft Company. Except for the 85V channel, all channels returned to their performances prior to instrument turn off. The 85V channel developed sudden gain changes and a degradation of sensitivity. Although increased heating of the instrument occurred in the winter of 1988, the spacecraft solar arrays were repositioned to provide sufficient shading to avoid the necessity of shutting off the instrument. However, the 85V channel noise continued to increase and the channel became useless by the end of January 1989.

The Automatic Gain Control (AGC) is designed to insure long-term radiometer gain stability, i.e., on a seasonal basis. As the temperature of the receivers change, the power output is allowed to vary plus and minus 1 dB before a gain change is initiated. In this process each channel samples the hot load on every scan and commands a gain change up when the hot load is below 7/16th of the analog to digital converter range (4095) or commands a gain change stepped down if the hot load for that channel is above 3/4th of the ADC range (3072). The stepping can occur only once every 53 seconds on each channel. Note that if the gain goes up and down quickly and is in range at the end of the 53 seconds the gain will not be stepped.

Table 1.2 presents the gain level for each channel since launch. The long term gain stability is very good except for the 85V channel.

Table 1.2

RADIOMETER LONG-TERM GAIN STATE SUMMARY

CHANNEL Date		19V	19H	22V	37V	37H	85V	85H
1987	OCT	8	7	7	8	6	7	7
	NOV	7-8	6-7	6-7	8-9	8-9	7-8	7-8
1988	JAN	7	6	5-6	8	6	8-9	7-8
	FEB	7	6	5-6	8	6	8	7-8
	MARCH	7	6	6	8	6	8	7
	MAY	7	6	6	8	6	9-12	7
	JUNE	7	6	6	8	6	8-11	7
	JULY	7	6	6	8	6	8	7
	AUG	7	6	7	8	6	8-11	7
	SEPT	7	6	7	8	6	8-13	7
	OCT	7	6	7	8	6	8-14	7
	NOV	7	6	5-6	8	6	9-10	7-8
	DEC	7	6	5	8	6	10-15	8
1989	JAN	7	6	5	8	6	10	6-8
	FEB	7	6	5-6	8	6	9-10	8
	MAR	7	6	5-6	8	6	9	7

The 85V channel has shown both small (<.5 dB) and large (>2 dB) gain instabilities. The first of these large gain changes occurred on November 20, 1987. This occurrence lasted 50 seconds and was a large gain change with AGC stepping. Since then, the changes have occurred intermittently. Unfortunately, the 85V data during these times is of very limited use. Table 1.3 shows the percentage of gain stepping occurring during one orbit from May to early October 1988. Small gain changes started occurring in March 1988. These are evident as lines in the 85V Temperature Data Records (TDR).

TABLE 1.3

85V GAIN STEPPING AS A PERCENTAGE OF MONITORED ORBITS

1988

May	40%
June	8%
July	3%
August	22%
September	18%
October	25%

(Prior to May 1988 gain stepping rarely occurred)

Typical variations of the radiometer gain on a scan to scan basis are presented in Figure 1.6 for the 19 GHz channels. The data apply to REV 438 with parts of REV 437 and REV 439 included. Note the appearance of rapid fluctuations of the gain and a slowly varying oscillation over the orbit. The fluctuations arise from noise in the radiometer output calibration samples and may be reduced by averaging calibration data taken over several successive scans. For example, Figure 1.7 presents the relative improvement in the NEΔT as a function of the number of scans of calibration data averaged. The time interval between scans for channels 19, 22, and 37 GHz is 3.8 seconds and the time between scans for 85 GHz is 1.9 seconds. Note that there is appreciable reduction in the NEΔT when 10 scans are averaged at 19, 22, and 37 GHz and 20 scans are averaged at 85 GHz. The slowly varying component of the radiometer gain is due to orbital changes in the temperature of the SSM/I instrument. Figure 1.8 shows the orbital variation of the temperatures of the RF mixer and the forward radiator surface. Based on the data of Figure 1.8, the maximum shift in temperature of the RF mixer is approximately 0.6 K and introduces less than 0.025 dB change in the radiometer gain (peak to peak).

The SSM/I has been spinning at a rate of once per 1.8990 seconds with a ±0.0002 second variation since the initial turn on. This translates to an azimuthal angular position error of the antenna boresight of ±0.038 degrees. This, in turn, translate to approximately ±0.6 km pixel position error on the earth's surface. When the SSM/I was turned off, the SSM/I continued to spin.

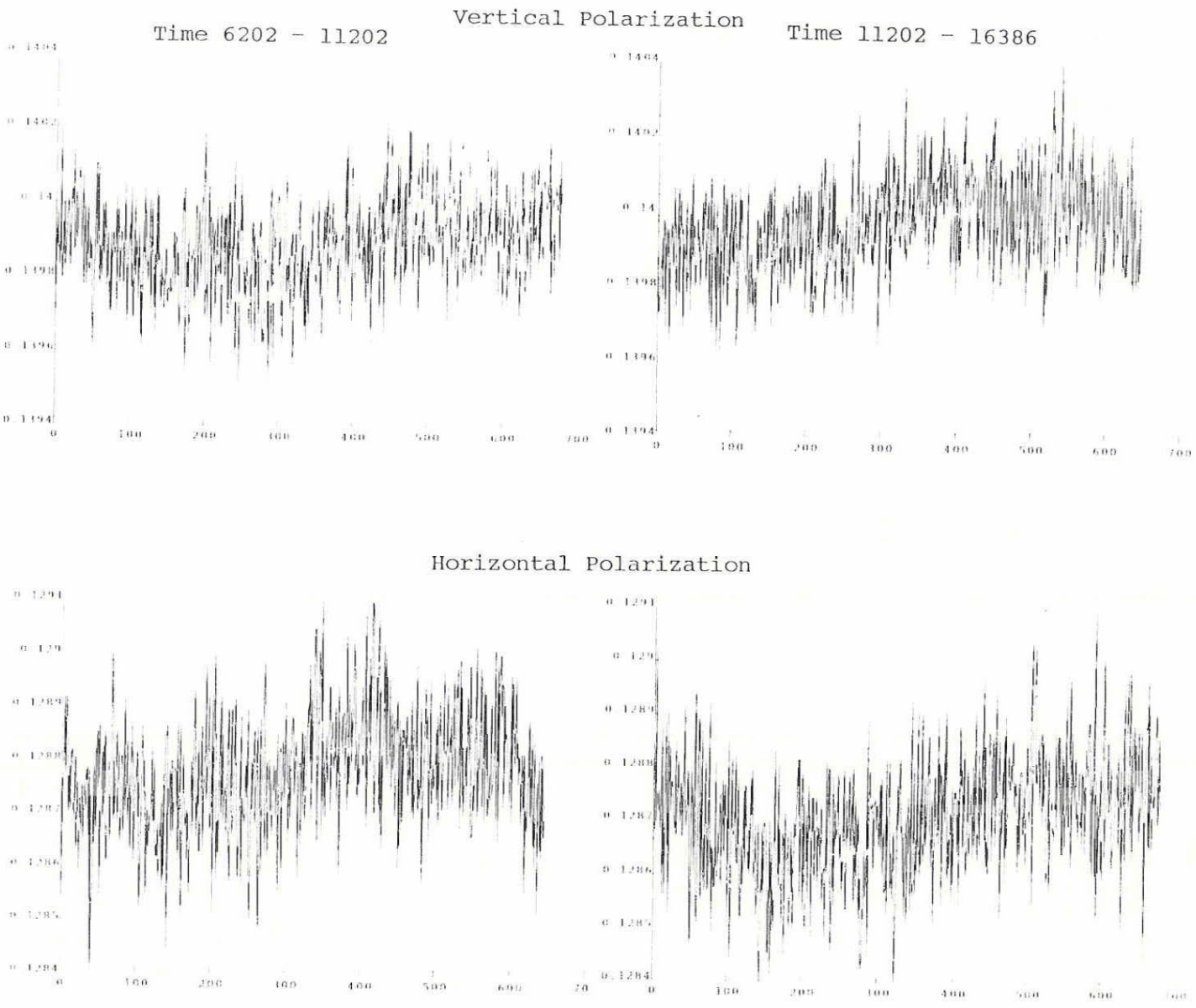

Figure 1.6 Variation of 19 GHz Radiometer Gain (K/count) REV 438

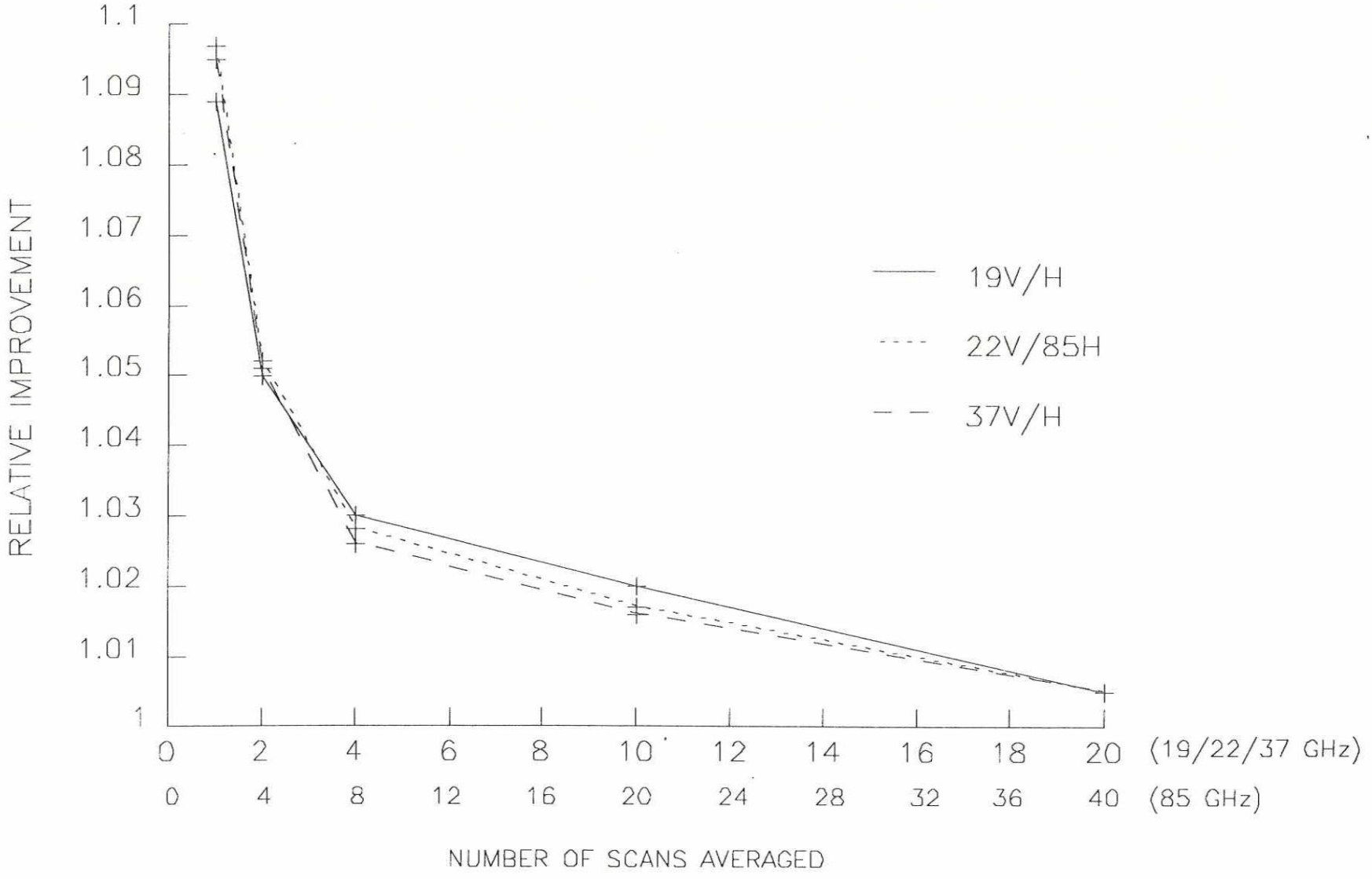

Figure 1.7 Reduction in the NEΔT due to Averaging Hot/Cold Calibration Samples

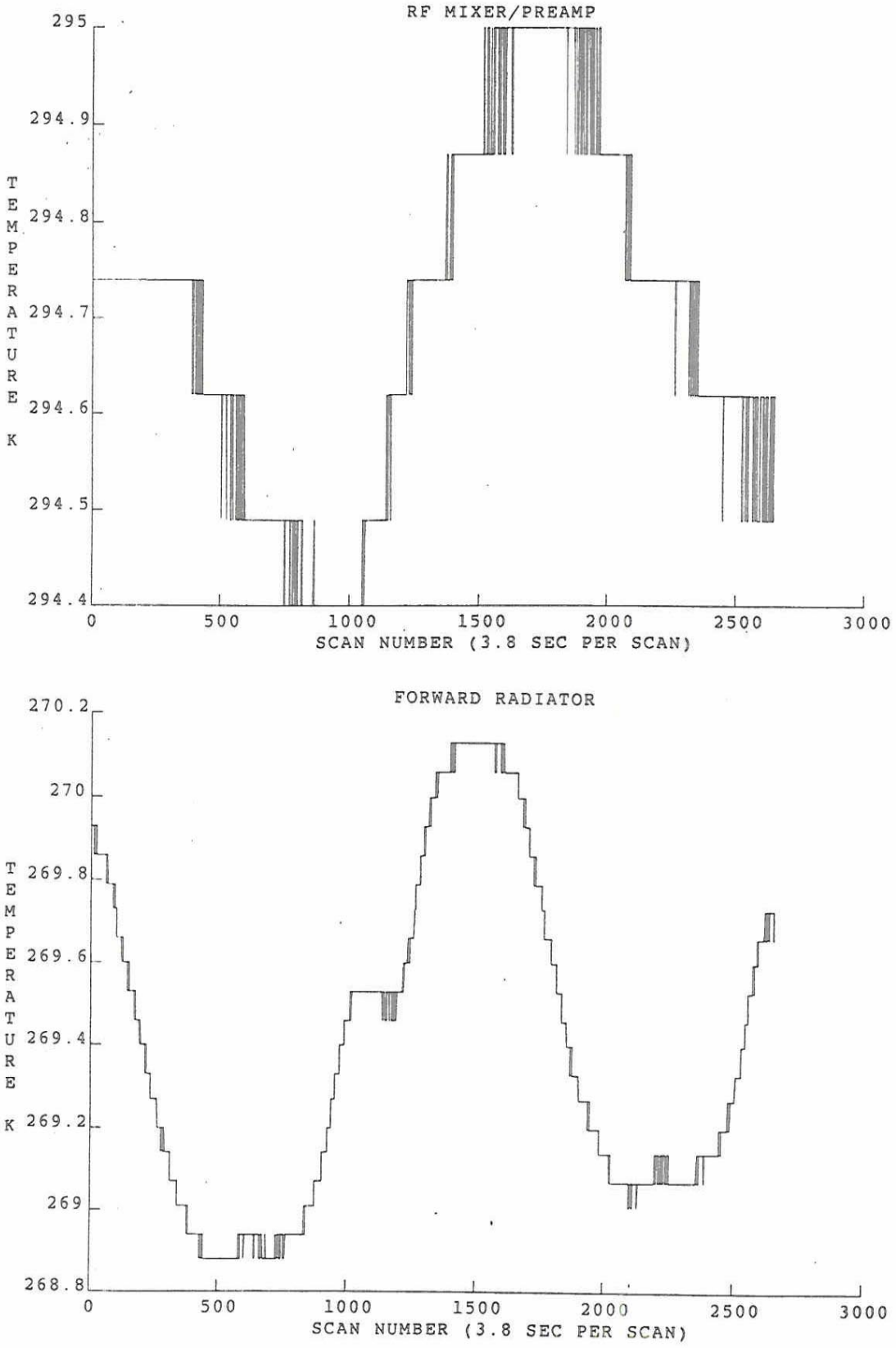

Figure 1.8 Variation of RF Mixer and Forward Radiator Temperatures (REV 438)

The long term calibration stability of the SSM/I was further verified by examining the repeatability of the absolute brightness temperatures (SDRs) for a number of diverse surface types. The regions included the Sargasso Sea, the Congo Basin, the Amazon Basin, the Gran Chaco, the Libyan Desert, the Great Sandy Desert, the Kalahari Desert, and the Gobi Desert. Histograms were generated for each of the regions and the mean and standard deviations noted. The means of the brightness temperatures differ by no more than 1-2 K for all channels, although the fine details of the histograms differ. This level of repeatability was typical of all regions examined and provides further evidence of the high calibration stability of the SSM/I.

1.2.2 Noise

The radiometer sensitivity or noise equivalent temperature differential NEΔT is the standard deviation of the radiometer output referenced to the energy of the waveform incident on the antenna aperture. For the SSM/I total-power radiometers are employed, hence the receiver gain fluctuation contributes directly to the NEΔT. Due to the frequent radiometric calibration of the SSM/I every 1.9 seconds and the development of amplifiers and detectors with low 1/f noise, the effect of receiver gain drift is extremely small over the calibration period. This enables a factor of 2 improvement of signal-to-noise for the total-power SSM/I system over a conventional "Dicke" switched radiometer system employed on previous radiometers.

Table 1.4 presents computations of the on-orbit radiometer NEΔT, while viewing the hot load target, for all seven channels covering the period starting when the SSM/I was turned on through March 1989. Except for channel 85V the sensitivities are extremely stable over the entire time period and show good agreement with the pre-launch results except for periods near January 1988 and 1989. The increase in NEΔT in this period is due to an increase in temperature of the instrument and is most pronounced at 85 GHz since these channels have the largest receiver noise temperatures. The channel sensitivities returned to values noted prior to instrument turnoff in December 1987 except for the 85V channel which continued to rise. The 85V channel NEΔT increased from approximately 0.8 K to 2.1 K and then in January 1989 reached 5 K just before total failure. Although the cause is not known conclusively, it is likely due to failure of the mixer portion of the receiver.

Using the cold reflector calibration radiometer output counts, computations of the NEΔT similar to those for the hot load target given in Table 1.4 were made. The NEΔTs were found to be quite stable over the time period of Table 1.4 and agree with the results to be expected when the scene brightness temperature is near 3 K; i.e., the cosmic background temperature seen by the cold reflector calibration target. The NEΔTs calculated using the cold reflector are considerably lower than those using the hot load target with the exception of the 85 GHz channels. This arises from the fact that for these channels the system noise temperatures are much larger than the other channels, and the scene temperature has a correspondingly smaller effect on the radiometer sensitivity. The NEΔT

calculated using the cold reflector target has a trend similar to Table 1.4 and also shows a dramatic increase of the 85V NEΔT after instrument turn-on in January 1988.

Table 1.4

ON-ORBIT RADIOMETER NEΔT (K)
(Hot Load Target)

	CHANNEL						
	19V	19H	22V	37V	37H	85V	85H
NEΔT Spec.(K)	0.8	0.8	0.8	0.6	0.6	1.1	1.1
Pre-Launch	.45	.42	.73	.37	.38	.69	.73
On-Orbit							
June 1987	.44	.38	.67	.33	.44	.78	.69
July 1987	.38	.34	.59	.32	.32	.75	.62
Aug. 1987	.37	.37	.58	.30	.33	.69	.59
Sept. 1987	.38	.35	.63	.29	.33	.73	.60
Oct. 1987	.45	.42	.69	.35	.44	.87	.70
Nov. 1987	.46	.42	.74	.40	.52	.91	.78
Jan. 1988	.5	.44	.74	.42	.58	1.12	.85
Feb. 1988	.43	.41	.72	.37	.42	1.32	.75
March 1988	.43	.41	.69	.33	.35	1.48	.73
April 1988	.42	.39	.70	.33	.37	1.70	.70
May 1988	.41	.40	.67	.32	.37	1.80	.70
June 1988	.42	.44	.68	.34	.38	1.80	.80
July 1988	.42	.41	.70	.31	.38	1.70	.71
Aug. 1988	.42	.40	.66	.32	.37	1.95	.70
Sept. 1988	.43	.39	.67	.36	.37	2.10	.71
Oct. 1988	.43	.41	.67	.33	.37	1.70	.72
Jan. 1989	.50	.45	.73	.44	.55	5.0	.86
Feb. 1989	.40	.40	.70	.35	.37	---	.88
Mar. 1989	.42	.35	.68	.33	.37	---	.83

1.2.3 Absolute Calibration

In general high gain antennas, like the SSM/I's, receive radiation primarily over a relatively narrow "main-beam" or solid angle. However some radiation is received in antenna side lobes in directions outside of the main-beam and from reflections from the spacecraft and direct spillover into the feed horn. This spurious radiation must be accounted for in order to obtain the mean radiance or brightness temperature from the scene averaged over the main-beam solid angle which is the quantity to be used in the environmental algorithms.

The evaluation of the absolute calibration of the SSM/I brightness temperatures is an extremely formidable task due to the difficulty in obtaining an accurate standard with which to compare the SSM/I. Two different methods are used. First the SSM/I brightness temperatures are compared with those derived from aircraft underflight measurements made during satellite overpass using the SSM/I Simulator radiometers mounted in the NRL RP-3A aircraft. The second method compares the SSM/I brightness temperatures with those calculated using theoretical models.

A total of 18 SSM/I Simulator underflights were made. Ten of these were over the ocean and are used for the brightness temperature calibration. The remaining flights were either in support of land and sea ice parameter validation or not useable due to problems with the aircraft, the SSM/I Simulator, or the SSM/I data. The underflights were in the form of a cross with 200 Km arms. They required approximately one and a half hours, centered on the satellite overpass time, to fly. In contrast the satellite passed over the test area in about a half minute. The surface resolution of the aircraft SSM/I Simulator radiometers is 1.5 Km compared to 13 to 70 Km, depending on frequency, for the SSM/I. The SSM/I integrates radiation over a much larger spatial region for a much shorter time than does the aircraft simulator; therefore any significant changes in the brightness distribution over the test region during the aircraft measurements will degrade the accuracy of the simulator calibration. The ideal flight conditions are clear skies with calm seas well away from land to provide a large homogeneous region with no antenna side-lobe effects and were not always obtained.

Except for the 85V channel, the SSM/I brightness temperatures are lower than the aircraft simulator. However only at 37 GHz do the SSM/I Simulator differences exceed 4 K. These measurements show the standard error of the determination of the SSM/I absolute calibration to be ±3 K and are consistent with little or no error in the SSM/I absolute brightness temperatures.

Three different regions were chosen for comparison of theoretically generated brightness temperatures with those measured by the SSM/I: (1) clear, calm ocean areas selected by having the coldest 85 GHz brightness temperatures observed over the ocean, (2) the Amazon rain forest, and (3) the Arabian desert. These regions were selected because they are homogeneous over large areas, relatively unchanging, and work has been done to develop models for them. The ocean areas are the most accurately modeled of the regions selected. The greatest uncertainty is the uniformity and degree to which the selected areas satisfy the assumption of calm, clear ocean, and the uncertainty in the physical temperature of the sea. The Amazon rain forest is expected to be a diffuse scatterer, unpolarized, and approximately a black body. Reasonably accurate model calculations are possible. Modeling of the Arabian desert is the least certain as there is very little data on the dielectric constant of sandy soils and the effects of scattering and roughness especially above 19 GHz are not well known. As expected, the ocean and Amazon rain forest modeled brightness temperatures show the best agreement with the SSM/I measurements. The Arabian desert results show poorest agreement for the 37 and 85.5 GHz channels where the effects of roughness and scattering are most

uncertain in the model. With the exception of the 37V, 85V, and 85H for the Arabian desert, all of the model comparisons are consistent with a standard error on the absolute calibration of the SSM/I of ±3 K. Again there is an apparent trend for the SSM/I brightness temperatures to be lower then the modeled values, especially for the higher frequency channels. However the uncertainty of modeling does not allow a definite determination to be made.

In summary, all of the SSM/I Simulator measurements and model calculations, with the exception of the 37 channel simulator measurements and the 37V and 85 GHz channel Arabian desert calculations, are in good agreement with the SSM/I data. The accuracy of the determination of the calibration of the SSM/I appears somewhat better at 19 and 22 GHz becoming less certain at 37 GHz and then 85 GHz. Although there is an apparent trend for the absolute calibration of the SSM/I to be low, especially at 37 GHz, both the aircraft simulator and model differences are consistent with little or no errors in the SSM/I absolute brightness temperatures. The present assessment of the standard error of the determination of the absolute calibration of the SSM/I is that it is ±3 K.

1.2.4 Geolocation

The current process of geolocating SSM/I pixels is illustrated in Figure 1.9. The spacecraft downlinks SSM/I data to receiving ground stations, which in turn forward the data to both Air Force Global Weather Center (AFGWC), Omaha, Nebraska and Fleet Numerical Oceanography Center (FNOC), Monterey, California. Since only the data processed at FNOC is archived, the SSM/I calibration/validation effort is focused primarily on the data processed at FNOC.

FNOC receives a set of orbital elements from the US Space Command (North American Defense Command (NORAD)) once a week and generates a ten-day prediction of the spacecraft ephemeris based on these orbital elements using the ephemeris computer program TRACE 66. The ephemeris prediction consists of a tabulation of the subsatellite geodetic latitude, longitude, and spacecraft altitude as a function of time in one-minute increments over the ten-day period. This predicted ephemeris is then input to the SSM/I pixel registration algorithm, developed by Hughes Aircraft Company (HAC), to geolocate the SSM/I data.

A number of assumptions and approximations enter into the HAC geolocation algorithm. The algorithm assumes that (1) the spacecraft nadir vector is always pointed in a direction normal to the geoid, (2) the surface of the earth is adequately modeled by an oblate spheroid, and (3) no corrections are necessary for possible spacecraft attitude variations or for possible misalignment of the SSM/I to the spacecraft. In addition, the algorithm takes into account (4) orbital variations of spacecraft altitude, (5) effects of earth rotation as it influences spacecraft heading, and (6) azimuthal and elevation angular offsets of the antenna boresight directions. The offsets (6) are defined within the SSM/I coordinate system and currently do not include possible misalignment of the SSM/I to the spacecraft.

SSM/I PIXEL GEOLOCATION PROCESS

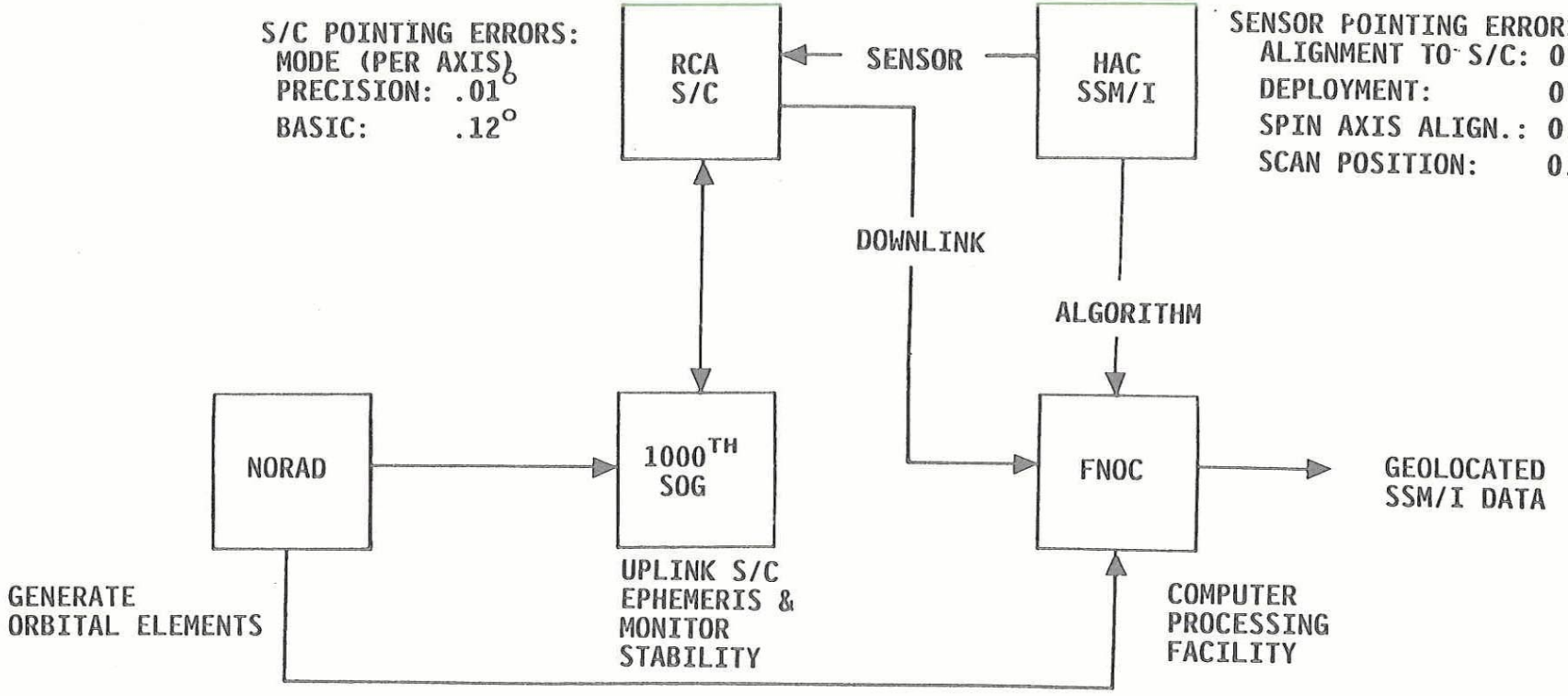

Figure 1.9 SSM/I Pixel Geolocation Process at FNOC

The reported spacecraft attitude and SSM/I pointing errors are presented in Figure 1.9. The maximum misalignment of the SSM/I to the spacecraft is reported to be not greater than 0.1 degrees while the SSM/I deployment errors are reported to be less than 0.03 degrees and the spin-axis misalignment is reported to be less than 0.01 degrees. The azimuthal scan position error is reported to be less than 0.03 degrees. Projecting these angular errors onto the earth's surface results in geolocation errors of the order 2 - 4 km, well below the 20 - 30 km errors observed in the SSM/I data.

The spacecraft receives its pointing and ephemeris information from the 1000th Satellite Operations Group (SOG), Space Command, Offutt Air Force Base, Nebraska. The 1000th SOG generates this data on a daily basis using daily orbital elements received from NORAD. The pointing and ephemeris data in 12- minute increments are up-linked to the spacecraft and continuously monitored to determine the attitude stability of the spacecraft. Table 1.5 presents typical spacecraft attitude information analyzed by the 1000th SOG for DMSP F8 for orbital revolution numbers 3106 - 3111 (January 26, 1988). These stabilities indicate that the spacecraft

TABLE 1.5

Variation of Spacecraft F8 Attitude (Degrees)
(January 26, 1988)

	Pitch		Roll		Yaw		Number of
REV	Max	Min	Max	Min	Max	Min	Samples
3106	---	-.035	.028	-.028	.063	-.021	5910
3107	.049	-.042	.021	-.028	.014	-.014	6081
3108	.042	-.042	.021	-.028	.007	-.021	5659
3109	.042	-.042	.021	-.028	.000	-.070	5806
3110	.049	-.042	.021	-.035	-.049	-.049	6112
3111	.049	-.049	.021	-.028	.035	-.021	6043

(Data Courtesy of CAPT Rust of the 1000th SOG, Offutt AFB)

is operating in its basic mode of attitude control which keeps the pitch, roll, and yaw variations within ±0.1 degrees per axis. The basic mode is a back-up mode of operation that occurs when the precision mode, which keeps the pitch, roll, and yaw variations within ±0.01 degrees per axis, is not maintained. Projecting the angular variations of Table 1.5 onto the earth's surface results in geolocation errors less than 2 km. It should be noted that spacecraft F8 celestial sensors had an unexpected problem with false star reflections off the SSM/I antenna, causing the spacecraft to operate in the basic mode. This glint problem was resolved in March 1988 by a software package implemented at the 1000th SOG.

In view of the reported sensor alignment accuracies and stabilities of the spacecraft F8, it is difficult to see how a 20 - 30 km geolocation error can occur in the SSM/I data. In an effort to ascertain the origin of these large errors, a list of candidate error sources were identified:

(1) Spacecraft orbital elements
(2) Predict spacecraft ephemeris
(3) Sensor pixel location algorithm
(4) Sensor deployment/spin axis misalignment
(5) Sensor alignment to spacecraft
(6) Spacecraft attitude

To these we must include errors in the geographical maps used to compare with the SSM/I data as well as errors due to interpolation and remapping of the SSM/I during image processing.

During the course of the Cal/Val effort, a relatively large number of SSM/I images were produced for detailed analysis. To insure the results derived from the images were not biased significantly, an attempt was made to include a wide range of possible influences. These included, for example, ascending and descending orbits, seasonal effects, latitudinal dependence, hemispheric variations, and along- and cross-track effects. It was also desired to evaluate the relative reduction of the geolocation errors in the images when the true spacecraft ephemeris was used. In addition, it was desired to determine whether a fixed set of angular coordinate corrections, such as pitch, roll, and yaw, would bring any residual geolocation errors to within half the spatial resolution of the 85 GHz channels, i.e., within 6 km, which is the system geolocation error budget for the SSM/I.

To illustrate the major results derived from the analysis of the images, Figure 1.10 presents a sequence of three 85H images. At the left the FNOC predict ephemeris is used during the image formation. In the middle the spacecraft ephemeris is used while at the right the spacecraft ephemeris is used along with pitch, roll, and yaw corrections for antenna boresight correction. The spacecraft ephemeris was extracted from OLS data tapes received from AFGWC and used with the NRL geolocation routine, described in Section 6, to geolocate the SSM/I data. Relatively large geolocation errors are evident when using the FNOC ephemeris. The Mediterranean coastlines of Morocco and Algeria show 20 - 30 km errors while similar errors are visible with the Islands Mallorca, Menorca, and Ibiza. The northern coastline of Spain and the French peninsula in the Bay of Biscay also reveal large geolocation errors. In all cases the image needs to be shifted backward along the spacecraft track to reduce these errors. The middle image shows a dramatic reduction in geolocation error when the spacecraft ephemeris is used, although a residual geolocation error of 10 - 12 km remains. Through a trial and error process pitch, roll, and yaw values were found which would remove the residual geolocation errors. It was found that if the values

Pitch = -0.1 (degrees)
Roll = -0.4
Yaw = -0.6

were employed the residual errors were reduced to less than 3 - 5 km. Furthermore, the same set of values were found to reduce geolocation errors to less than 3 - 5 km for the sets of SSM/I images produced once

SSM/I GEOLOCATION VALIDATION

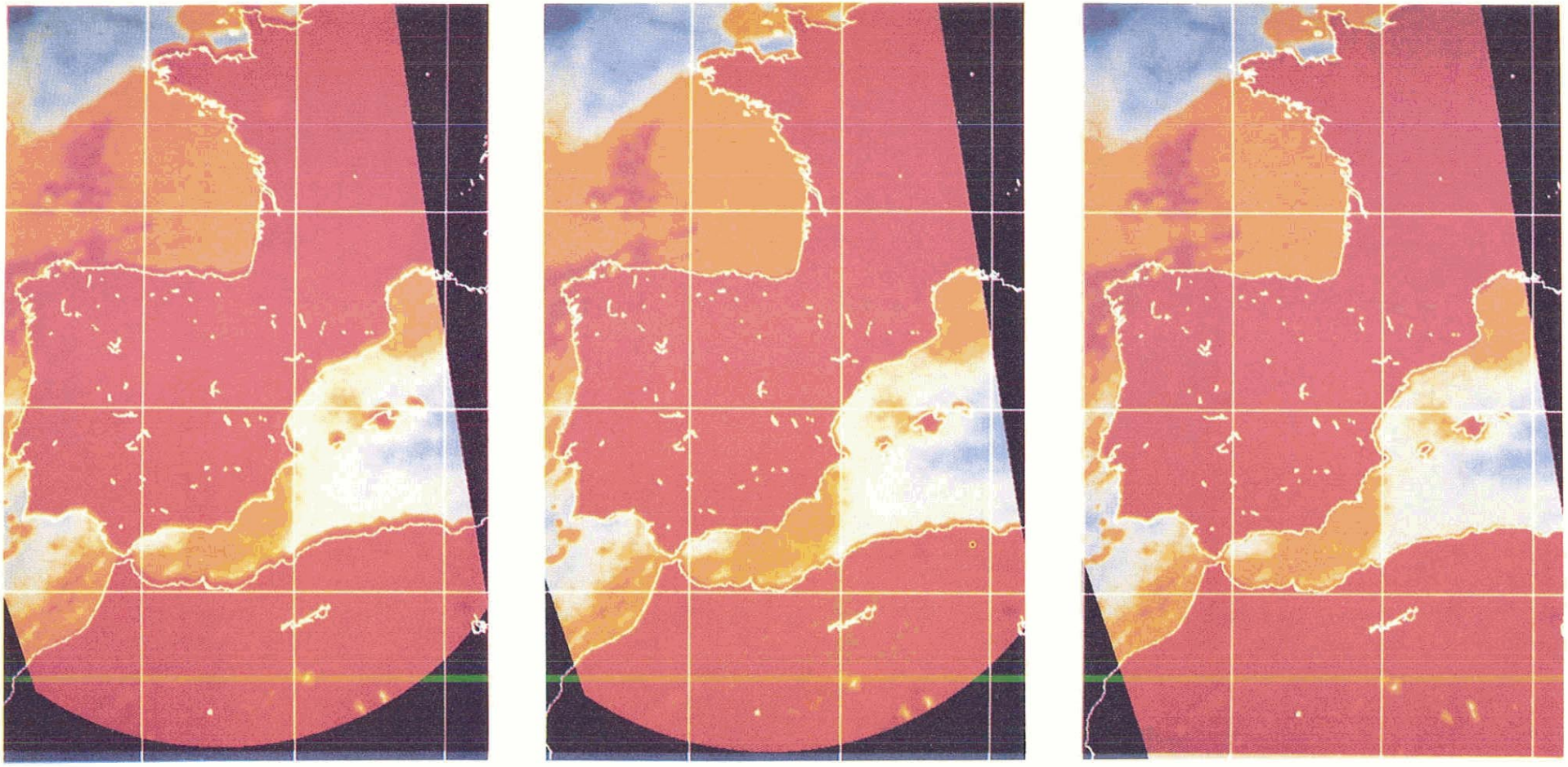

FNOC PREDICT EPHEMERIS 20-30 KM ERROR

SATELLITE EPHEMERIS 10-12 KM ERROR

SATELLITE EPHEMERIS + BORESIGHT CORRECTION < 5 KM ERROR

Figure 1.10 REV 5100 JUNE 15, 1988 85 H CHANNEL
(5°GRID)

the FNOC ephemeris errors were removed. The number of SSM/I images analyzed was limited to 12 due to the limited number of OLS spacecraft ephemeris data sets available and the extensive time required to regenerate the satellite ephemeris, and process and re-geolocate the image with the selected pitch/roll/yaw corrections.

Other results found in the geolocation Cal/Val effort include: The orbital elements generated by NORAD were a negligible contributor to the SSM/I geolocation error, typically less then 1 - 1.5 km. The spacecraft ephemeris generated at FNOC with TRACE 66 was compared with the spacecraft ephemeris generated by the 1000th SOG and with the ephemeris generated at NORAD and found to exhibit significant and variable differences. In some instances the FNOC ephemeris disagreed by as much as 15 km. Numerical approximations appearing in the geolocation algorithm developed by HAC were found to contribute up to 4 km geolocation error. In addition, the last pixel sampled on each scan had a large geolocation error, 15 - 20 km, for subsatellite latitudes outside ±60 degrees. The cause of this error was traced to an interpolation error in the computer module LOCINT in Subroutine SMISDP. Due to the magnitude of the pitch and roll corrections needed to remove the non-ephemeris geolocation errors, the pixel earth incidence angle was found to vary significantly, nearly 0.9 degrees, across the scan. For the relatively few cases analyzed, a fixed set of pitch, roll, and yaw corrections were found to reduce the OLS geolocation error below 3 - 5 km. These corrections were not the same as found for the SSM/I. Finally, it should be noted that the source(s) of the geolocation errors not due to ephemeris errors could not be determined conclusively. Although the error could be due to (a) sensor deployment or spin axis misalignment, (b) sensor misalignment with the spacecraft, or (c) spacecraft attitude errors, the results presented suggest that (c) is probably not the main contributor. In conclusion, approximately one half (~12 km) of the SSM/I geolocation error is due to the predict ephemeris used at FNOC and will be removed when the satellite ephemeris is adopted. The remaining error of ~12 km, while apparently constant and removable with a software implemented effective realignment of the SSM/I spin axis of about 0.5 degrees, has yet to be determined precisely.

1.3 ENVIRONMENTAL ALGORITHM PERFORMANCE

1.3.1 Water Vapor and Cloud Water

The Hughes algorithms for the retrieval of integrated water vapor and cloud liquid water are divided into eleven climate codes in each hemisphere. Each climate code represents a set of coefficients for a particular latitude zone and season. There are three distinct sets of coefficients for the retrieval of water vapor and nine for the retrieval of cloud water over the ocean. For the retrieval of cloud water over land, there are eleven distinct sets of coefficients.

Validating the Hughes algorithm required the acquisition of surface measurements from a variety of latitude zones and seasons. For the integrated water vapor validation, data were collected from small island radiosonde stations and the few remaining weather ships. Initially a list of about 50 potential stations was compiled with size and latitude being

the only considerations. However orbit and equatorial crossing time allow data from only 19 stations to meet our match-up criteria. The criteria are that the satellite observation and radiosonde must be coincident within 2 hours and 2 degrees of latitude and longitude. These radiosonde observations were collected from National Meteorological Center (NMC) files, integrated to obtain the total precipitable water vapor, and matched with the satellite data. The period of collection of data was from June 1987 to April 1988.

In evaluating the algorithms, the following criteria were considered: (1) the RMS difference between the surface measurement and the satellite retrieval of the parameter with allowance for measurement uncertainties, (2) the bias or difference between the mean surface measurement and the mean satellite retrieval, the bias being a measure of whether the algorithm is under or overestimating the derived quantity, and (3) whether there was a physically unrealistic gradient across the latitudinal boundary associated with the climate codes.

Data for the cloud liquid water determinations over the ocean were taken by NOAA/Wave Propagation Laboratory (WPL) personnel from San Nicolas Island as part of Project FIRE and by University of Massachusetts personnel from Kwajalein Island. Data over land were taken by NOAA/WPL from the four stations that make up the Colorado remote profiling network.

It was found that the Hughes algorithm for water vapor with its segmented structure did not meet the SSM/I specification of 0.2 g/cm^2 over the range 0-8 g/cm^2. In addition, unrealistic gradients were generated at the boundaries of the climate code zones. It was also found that the Hughes algorithm had a distinct tendency to underestimate the amount of water vapor in the polar regions (low values) and overestimate in the tropical regions (high values). Figure 1.11 shows the retrieved (Hughes) versus actual values (raob) of total precipitable water in g/cm^2 for the three sets of coefficients for the Hughes algorithm.

Attempts were made to improve the Hughes algorithm within the present D-matrix format. A global linear algorithm (i.e., there would be no latitude or seasonal segments and the brightness temperatures appear only to the first power in the algorithm) was considered. Unfortunately, due to the wide range of air temperatures and water vapor amounts, this algorithm also could not meet specifications. Next a non-linear global algorithm was devised. This algorithm uses brightness temperatures at 19V, 22V, 37V, and 22V squared. Figure 1.12 shows the retrieved values in gm/cm^2 versus actual values (raob) for the non-linear global algorithm. This algorithm, while showing some tendency to underestimate at the highest water vapor values, eliminates the gradents at the boundaries of the original segmented algorithm and represents a significant improvement in overall accuracy, 0.24 g/cm^2 rms error on a global scale. It is felt that as the data base increases in size and range the algorithm can be improved to retrieve water vapor to within specification globally. This improvement will be pursued as a follow on effort.

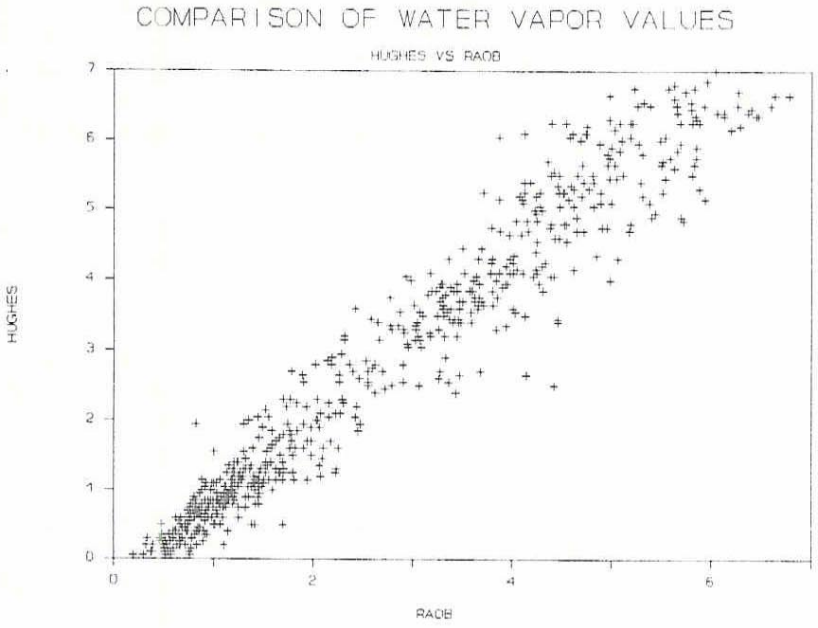

Figure 1.11

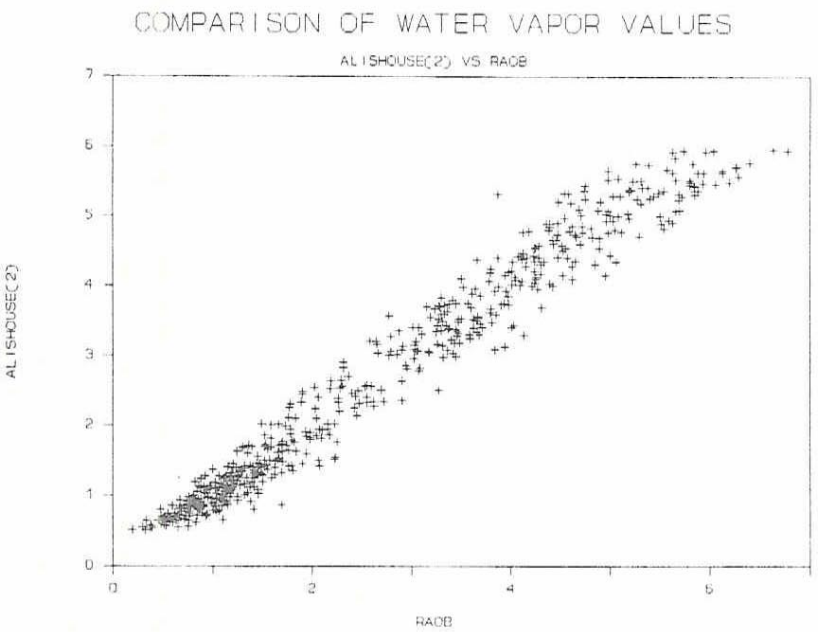

Figure 1.12

In evaluating the Hughes algorithms for cloud liquid water, it was found that more than 90% of the values retrieved by the coefficients used for our test areas produced indeterminate or out-of-limits values. This was sufficient evidence to conclude that some improvements could be made. By regressing matched brightness temperatures against cloud liquid water values derived from upward looking microwave radiometers, an algorithm for determining cloud liquid water over the ocean was derived. Although for a limited range of cloud water, Figure 1.13 shows retrieved values in gm/cm^2 versus observed values with an rms error of 0.004 g/cm^2. Our analysis of measurements over land showed little correlation between cloud liquid water content and SSM/I brightness temperatures. Our recommendation is that there be no retrieval of cloud liquid water over land, until further research has been done to demonstrate its feasibility.

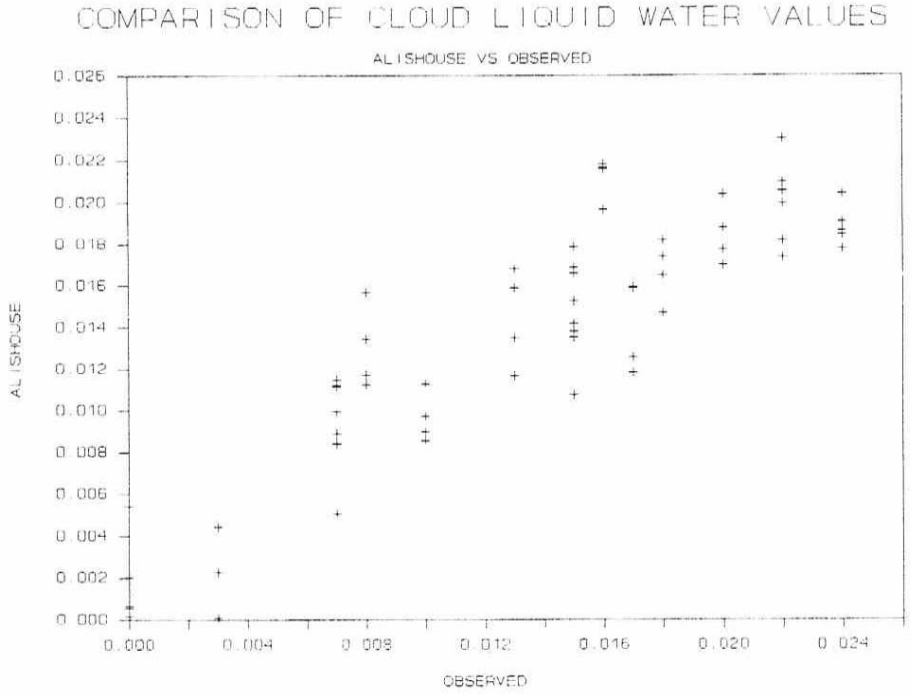

Figure 1.13

1.3.2 Wind Speed

The wind speed algorithm validation was performed using all SSM/I data recorded during the first year of operation. The validation consisted of two major thrusts: (1) assessment of the D-matrix algorithm based on direct comparisons of SSM/I wind speed observations with coincident surface wind speed measurements from ocean buoys; and (2)

qualitative analysis of monthly and seasonal global SSM/I wind fields for self consistency and reliability, with comparisons to climatology for realism. Other factors considered include: error budget modeling, improved algorithms, rain flag thresholds, zonal discontinuities, scan position bias, geolocation errors, and performance loss with one or more inoperative channels.

The results of comparing SSM/I retrievals with surface buoy measurements showed that the Hughes operational D-matrix algorithm did not meet the specification accuracy of ±2 m/s. All eleven versions of the algorithm (characterized by season and location) produced large biases and slope errors in scatter plots of SSM/I against buoy winds. The performance of Climate Code 5 (mid-latitude, summer) shown in Figure 1.14 was typical, with a bias of 5.7 m/s and a scaling factor of 0.85 instead of

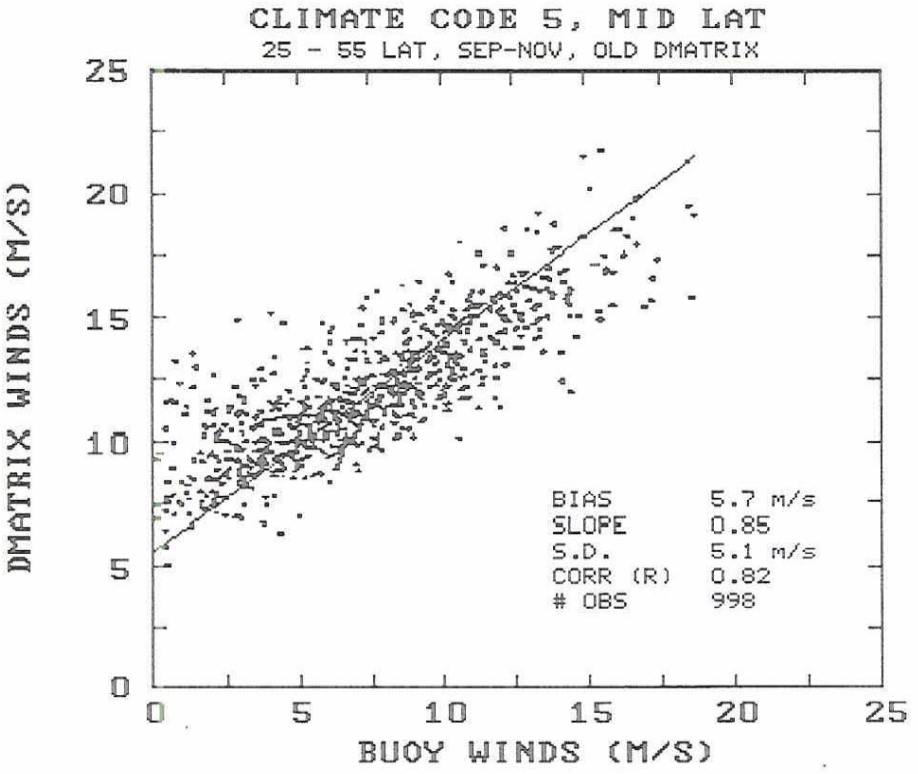

Figure 1.14 Performance of the Original D-Matrix Algorithm for Climate Code 5

unity. These errors were corrected by changing the coefficients of the D-matrix generated using standard linear regression of buoy wind speeds on coincident SSM/I brightness temperature measurements. New coefficients were derived for each of the eleven versions of the algorithm and tests of performance were carried out using data not included in the coefficient determination. Performance of the new Climate Code 5 coefficients is shown in Figure 1.15. Performance of all of the Climate Code operational

algorithms with new coefficients is within specification, although the D-matrix algorithm with revised coefficients still underestimates the high wind speeds and produces discontinuities at some of the climate code interfaces.

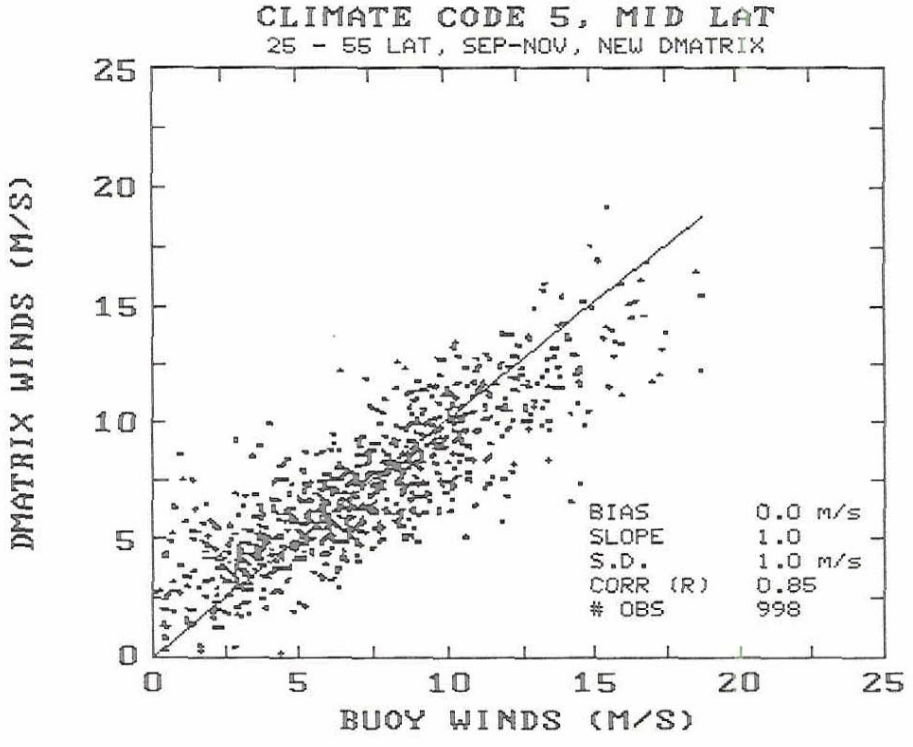

Figure 1.15. Performance of the Revised D-Matrix Algorithm for Climate Code 5

Having shown that the new D-matrix algorithm met the ±2 m/s accuracy specification, an alternate D-matrix algorithm with a single set of coefficients was developed. Using a weighted linear regression on randomly selected coincident SSM/I-buoy pairs from each of the climate codes, it was possible to produce a set of coefficients that were valid for all latitudes and seasons. The channel selection in the alternate algorithm differs slightly from the original in that $T_{B(19V)}$ is used instead of $T_{B(19H)}$. The performance of this all-purpose D-matrix algorithm, shown in Figure 1.16, not only meets the accuracy specification of ±2 m/s over the full range of wind speeds but removes the high wind speed bias that was associated with the original D-matrix retrievals. Further, the use of a single set of coefficients for all latitudes and seasons eliminates the zonal discontinuities produced by the original algorithm.

To address the issue of loss of one or more channels, sets of coefficients were derived for a 3-channel and a 4-channel algorithm. Retrieval accuracies for each possible combination of channels confirm

that operation, at reduced performance, would be possible should one of the SSM/I channels fail.

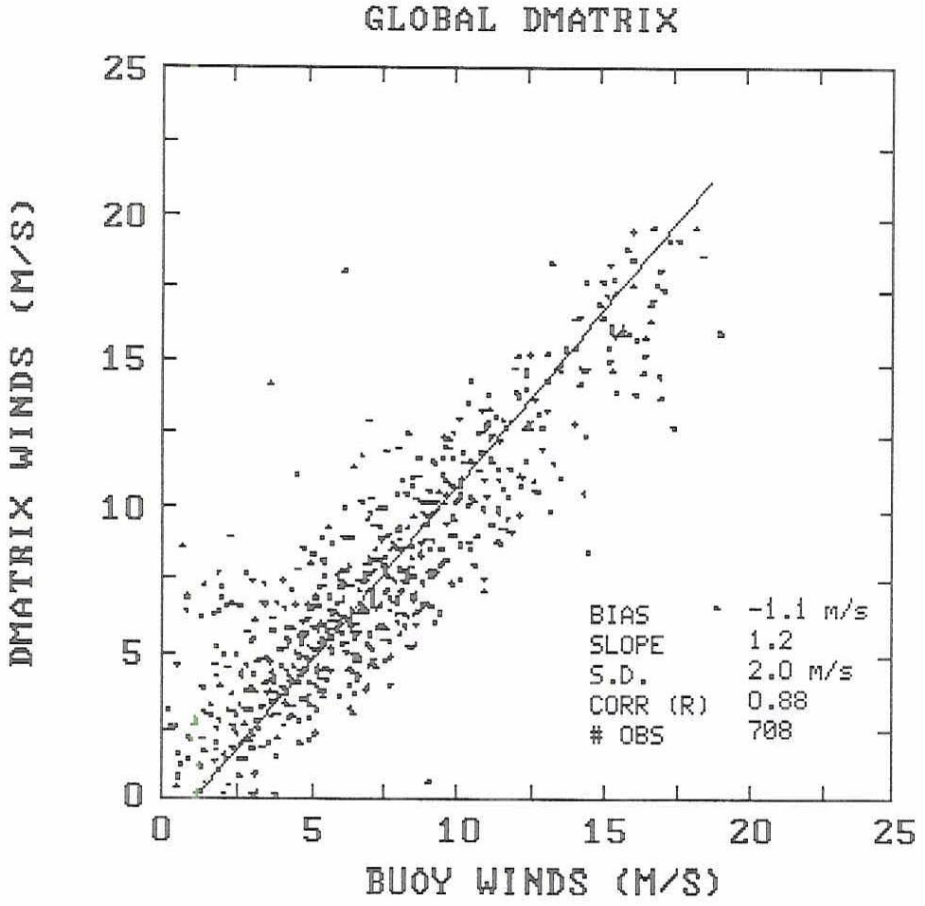

Figure 1.16. Performance of the Global D-Matrix Algorithm

There were no wind speed comparisons in excess of 25 m/s. This can be explained by the fact that winds above 25 m/s are most always associated with storm systems having high levels of precipitation and clouds. Since the D-matrix rapidly degrades in the presence of light rain, high wind retrievals in tropical storms, typhoons, and hurricanes can not be accurately observed. This inability stems from the fact that microwave radiation at 19, 22, and 37 GHz is highly attenuated by rain, effectively masking the roughness signature of the ocean generated by foam and waves which is the physical basis of the wind retrieval. The deterioration in retrieval accuracy in the presence of rain, prompted a re-evaluation of the rain-flag criteria. New, more restrictive, rain-flag thresholds were determined as a function of rain-flag parameters, (T_{B37V}-T_{B37H}) and T_{B19H}. New rain-flag cutoffs were determined by locating values of the rain-flag parameters for which the standard deviation and bias curves crossed predetermined accuracy levels. In this way, four rain-flag

categories were defined; one more than previously provided. By lowering the parameter thresholds for rain-flag 0 (the rain-free condition) to coincide with a zero bias and standard deviation of 2 m/s, it was possible to assure that all flag 0 retrievals would be within specifications. For rain-flags 1, 2, and 3, other cutoff values (with their associated accuracy limits) were used to represent conditions of increasing amounts of water vapor and precipitation. The retrieval accuracy standard deviations of rain-flags 1, 2, and 3 were found to be 2-5 m/s, 5-10 m/s and > 10 m/s, respectively.

1.3.3 Land Parameters

The Hughes land surface type classification logic in EXTLND resulted in numerous misclassifications. Since it is imperative that the surface type be correctly identified before the proper retrieval algorithm can be validated or applied operationally, it was essential first to develop an accurate surface identification scheme. Test areas were selected for dense vegetation, deserts and arid areas, and arable land. Atmospheric conditions of heavy rain and/or clouds containing large water droplets were identified. Surface conditions of snow covered, large extent of surface water, and flooded arable land were included in the test data sets. Rules were developed for the classification of the following land surface types: rain over vegetation, rain over soil, flooded soil, composite soil and water, composite vegetation and water, dense vegetation, desert, semi arid, dry arable soil, moist arable soil, agricultural crops and range, snow, composite snow and soil, and glacial. These rules are based on a statistical analysis of passive microwave signatures over the known land surfaces. Histograms of brightness temperatures, polarization differences, and other combinations of the SSM/I channels were used to determine appropriate discriminators and thresholds.

The original Hughes algorithm for retrieval of land surface temperature had three forms. Temperature over cloudy land (TLC) was not investigated due to an inability to discriminate non-precipitating clouds in the land surface classification module. Previous experience indicates that temperature over snow (STS) and cloud covered snow (TSC) is extremely difficult, if not impossible, to retrieve because a very small component of the microwave radiation received from a snow covered surface is emitted by the snow itself. The majority of the radiation comes from the underlying surface and passes through the nearly transparent snow layer. Therefore, it is recommended that snow surface temperature not be retrieved.

All land surface temperature algorithms performed better in the Central Plains of the United States than in the Western Desert test area. The dry soil and desert classifications were conspicuous in their deviation from the regression patterns of the other land surface types. The 85V channel exhibited the most variance of any channel. The implications are that either the ground truth has significant variance as a result of non-representative locations or that the physics of sandy soils differ from agricultural soils. The dielectric constant is higher for quartz sands (permittivity in the 3 to 4 range) than soils, so a physical basis exists for a differing microwave response. A very high

polarization difference is an indication of the unique response of deserts. Even though the RMSE, as a combination of variance in the ground truth and the retrieval algorithms, is only within 4 C, the implementation of the land surface temperature algorithms is recommended.

The snow depths and the microwave brightness temperatures are highly correlated. A visual correlation shows excellent agreement. However, when multiple linear regression was performed, the best R squared was in the vicinity of 0.20 with an RMSE of 11 cm. The snow depths in this case generally matched the observed depressions in the SSM/I channels, but the localized nature of the heavier amounts and the mislocation problem of the SSM/I pixels may be sources of variance. Although algorithms could be implemented, the current structure of the snow categories of EXTLND does not allow for the necessary flexibility in the selection of algorithms. More snow data are needed in order to develop a rule based logic system for the classification of snow into dry accumulating snow, dry snow with morphological changes, surface melting and refreezing, and stage of ripening. The nature of the underlying surface and the influence of vegetation should be included.

A soil moisture algorithm was developed to retrieve antecedent precipitation, which is consistent with literature on retrieved soil (or surface) moisture. The data base for the development of the soil moisture algorithm excluded rain, dense vegetation, desert and dry soil, and snow. For test areas in the Central Plains, the soil moisture algorithm performance was good. The R squared was 0.61 and the standard error was about 11 mm. The ground truth consisted of an antecedent precipitation index (API) based on daily rainfall from the climatological network. Surface estimates of temperature were not used to calculate an emissivity. A soil moisture algorithm is recommended for implementation.

The revised rules for EXTLND and the recommended algorithms for land surface temperature and land surface moisture are given in Section 1.4.4. Work is continuing to develop an algorithm to retrieve snow water equivalent, to incorporate land surface temperature into the surface moisture estimation retrievals, to develop a dynamic data base, and to replace the 85V GHz channel where it appears in all of the land classification and retrieval algorithms.

1.3.4 Sea Ice

The validation of the sea-ice parameters was carried out by the Atmospheric Environment Service (AES), Canada from June 1987 to September 1988, and involved the statistical analysis of SSM/I data with almost coincident radar imagery. The validation also included the operational demonstration of the AES/YORK algorithm for ice reconnaissance and forecasting, and was carried out at the AES Ice Branch in Ottawa and at the U.S. Navy/NOAA Joint Ice Center and Navy Polar Oceanographic Center in Washington, D.C.

The validation objective was to assess the accuracy of the Hughes and AES/YORK algorithm products using the best corroborative information available. The performance of the algorithms was assessed for total ice

concentration, ice fraction concentration, and ice edge location for season and ice regimes. One of the main requirements imposed on the algorithms was for them to be operationally useful under all weather conditions.

The validation procedure involved the geographical registration of the radar imagery with the algorithm derived environmental parameter maps provided at an equivalent scale to that of the radar imagery. The imagery was analyzed at each footprint for ice concentration and/or ice fraction, and along the contours used for ice edge location. Inaccuracy which could be introduced by interpreter bias in estimating ice concentration was reduced by the use of a sampling template. Errors because of orbit shift were minimized by implementing a constant 25 km backward shift along the track. However, this did not eliminate systematic errors such as the interpretation of open water or thin ice, rough first-year ice, or old ice. The higher resolution of the radar imagery (which can vary from 30 m to 400 m in azimuth as a function of range for the SLAR, and 18 m across all the range of the SAR) caused interpretation difficulties for convoluted ice edges when compared to the SSM/I grid spacing of 25 by 25 km, which results in a relatively smooth ice edge. Radar data were available only during weather conditions suitable for flying, which eliminated validation of SSM/I under severe storm conditions. Altogether 1.6 million sq km were validated for ice concentration, and more than 6000 km were validated for ice edge position.

Table 1.6 summarizes the validation results. The results indicate that the AES/YORK algorithm performed better than the Hughes algorithm for geographic area, season, and time class. The AES/YORK algorithm met the acceptance criteria for ice edge location more frequently than the Hughes algorithm. The results from the ice fraction validation were inconclusive because of the small sample size.

There were additional shortcomings concerning the Hughes algorithm which were not apparent in the statistical results. In particular storms, e.g., in the Gulf of Alaska, there were areas occasionally shown by the algorithm as ice covered where no ice was present. This situation also occurred in the Labrador Sea, as shown in Figure 1.17, where ice along the coast was extended by the algorithm into an apparent ice cover all the way to the Greenland coast. The problem could be eliminated by a suitable weather filter algorithm, as is incorporated in the AES/YORK algorithm, and is illustrated in Figure 1.18.

Another shortcoming was the extrapolated ice edge contour (0% ice concentration) as observed on the radar imagery which corresponded to a Hughes algorithm ice concentration between 25 and 50%, with an average of 35% ice concentration, depending on ice type. The 30% Hughes algorithm ice edge was observed to correspond to an average ice concentration of 56%. The AES/YORK algorithm at the 0% radar ice concentration contour corresponded to an ice concentration of between 0 and 25%, with an average ice concentration of 16%, depending on ice type. The 10% AES/YORK algorithm ice edge corresponded to an average ice concentration of 25%.

Table 1.6 Final Conclusion on the SSM/I and AES/York Algorithm Performance

Major Group	Ice concentration			Ice edge displacement		
	accuracy (%)	95% C.I	meets criteria	accuracy (km)	95% C.I.	meets criteria
SSM/I algorithm	+/-12%			+/-12.5 km		
Combined Area:						
Pooled, less than 3 h	-17.2	1.6	no	-10.3	2.3	marginal
Season:						
Ice formation	-19.5	1.4	no	- 9.8	2.8	marginal
Winter	-18.9	1.7	no	+ 4.2	9.0	no
Initial ice melt	- 6.6	1.9	yes	-12.6	3.9	no
Ice melt	-20.7	1.7	no	-11.8	5.0	no
Arctic:						
Pooled, less than 3 h	-13.6	1.7	no	-10.5	2.5	marginal
Ice Fraction:						
First-year	+ 6.5	5.4	marginal			
Old-ice	-10.8	5.4	no			
Gulf of St. Lawrence:						
Pooled, less than 3 h	-27.5	3.2	no	- 9.7	3.8	marginal
AES/YORK algorithm	+/-10%			+/-12.5 km		
Combined Area:						
Pooled, less than 3 h	- 6.6	1.4	yes	- 0.2	1.9	yes
Season:						
Ice formation	- 9.1	1.3	marginal	- 0.7	2.6	yes
Winter	- 6.9	1.4	yes	+21.1	9.6	no
Initial ice melt	- 5.1	2.7	yes	- 4.0	9.5	marginal
Ice melt	-11.5	1.7	no	- 4.3	3.6	yes
Arctic:						
Pooled, less than 3 h	- 6.2	1.7	yes	- 3.1	2.1	yes
Ice Fraction:						
First-year	- 7.3	4.7	marginal			
Old ice	+ 7.3	4.7	marginal			
Gulf of St. Lawrence:						
Pooled, less than 3 h	- 7.8	2.2	yes	+ 7.4	4.2	yes

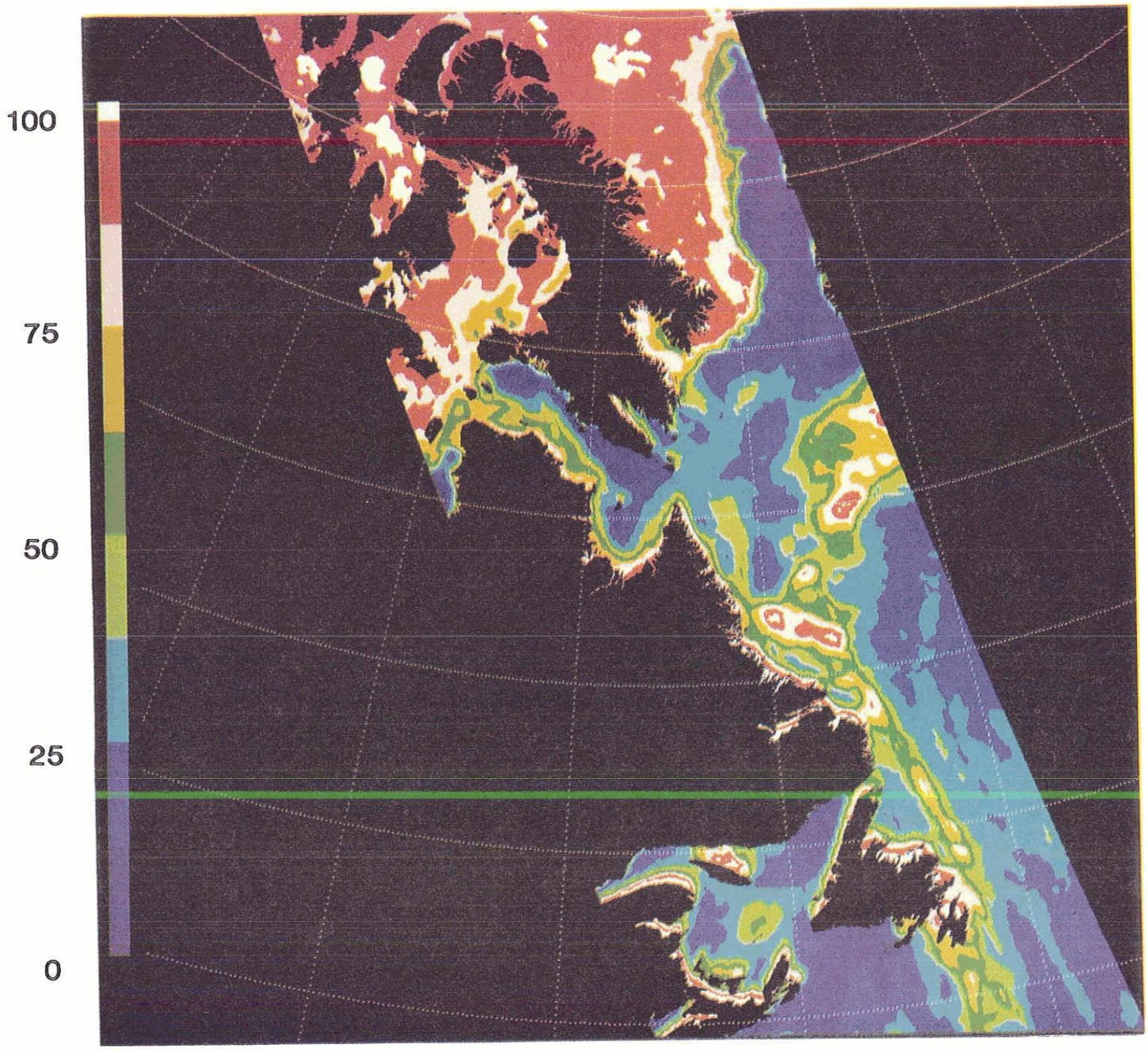

Figure 1.17. Hughes Algorithm Total Ice Concentration REV 2194

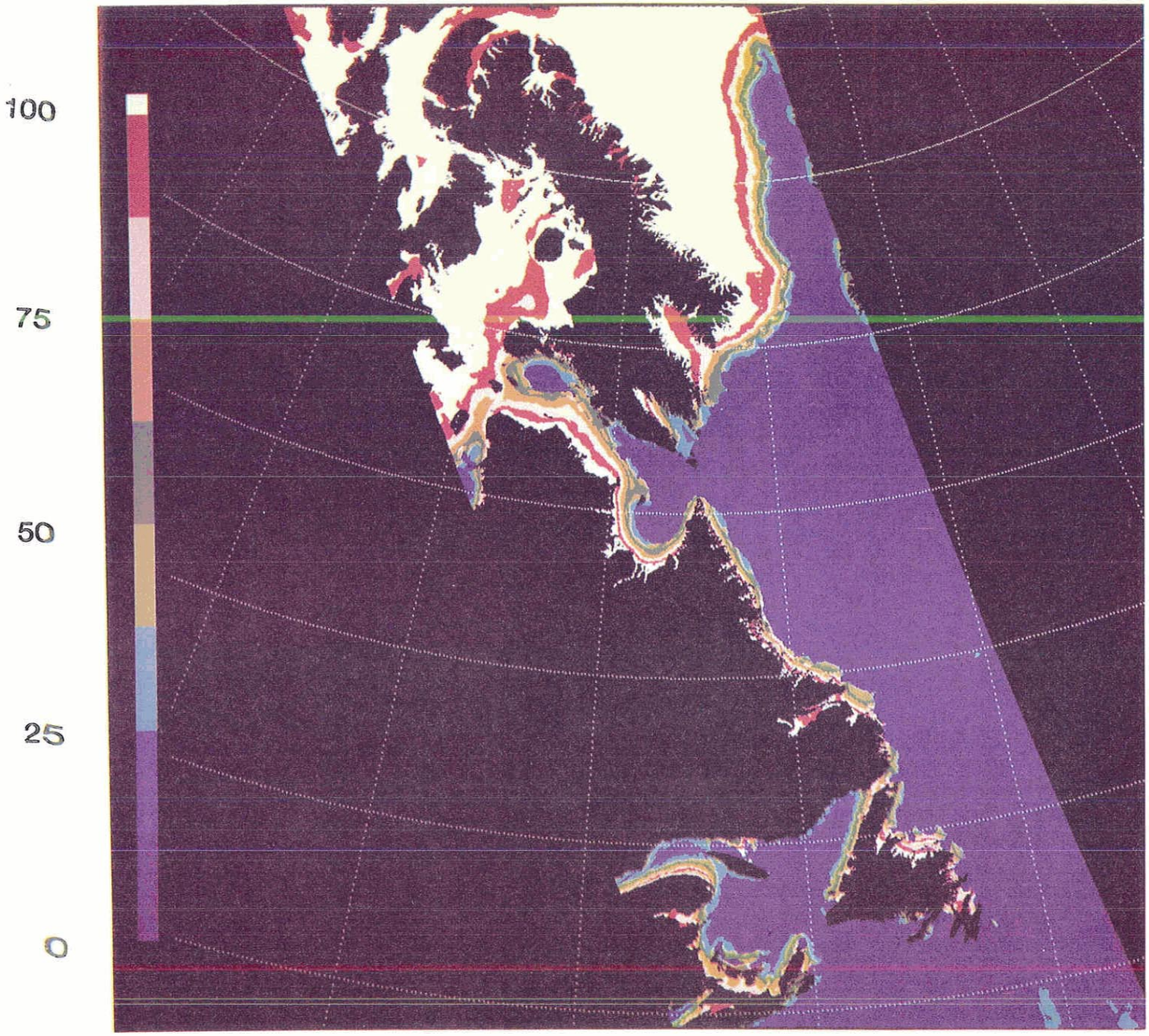

Figure 1.18. AES Algorithm Total Ice Concentration REV 2194

The Hughes algorithm was designed to flag the presence of old ice only when the old ice concentration reached about 35% or more of the total ice concentration. Because it only flags, but does not determine, the ice fraction concentration, this reduces its usefulness for operational purposes. The AES/YORK algorithm is designed to provide thin ice, first-year, and old ice fractions.

1.3.5 Precipitation

Evaluations of SSM/I data show that useful rainfall rate estimates can be achieved, particularly over ocean areas. However, the Hughes D-matrix retrieval algorithm applied at midlatitudes does not meet specified accuracies over land. A general trend was found: at low radar-derived rainfall rates the Hughes algorithm tends to over-estimate rainfall rates, while at high rainfall rates, it tends to under-estimate rain intensity. Regression analysis of collocated SSM/I brightness temperatures and radar-derived rainfall rates is utilized to create formulas for improved retrievals of rainfall rates over land and ocean. The retrieval formulas can be implemented within the framework of the SSM/I operational software. Over land and ocean surfaces, linear regression formulas or exponential regression formulas both show the potential for meeting the ±5 mm/hr DMSP specification. The exponential formulas produce estimates with less rain rate dependent bias.

Two approaches were taken in an attempt to compensate for the nonlinear relationship between brightness temperature and rainfall rate. First the residuals in the linear regression are weighted to emphasize errors at the higher rainfall rates. Weighting by an increasing function of rainfall rate helps to compensate for the skewed distribution of rainfall rates which is dominated by low rain rates. Second, the problems experienced with linear regression models can be partly overcome by utilizing nonlinear algorithms. The simplest nonlinear algorithm to implement operationally is one in which the rainfall rate is expressed as an exponential function of the SSM/I brightness temperatures. The two approaches lead to retrieval algorithms which yield rainfall estimates within a 5 mm/hr standard deviation of radar "ground truth" data, over both land and ocean backgrounds. The new retrieval algorithms are presented in Section 1.4.6.

Figure 1.19 shows the Hughes D-matrix and regression estimates of rainfall rate versus radar-derived rainfall rate at midlatitudes. The regressions are based upon collocated SSM/I brightness temperatures and radar-derived rainfall rates for which the D-matrix and radar rain rates were between 0 and 25 mm/hr during the summer and spring-fall seasons. D-matrix rain rate estimates over land are plotted in (a). Linear regression estimates over land and logarithmic regression estimates (c=4.0) over land are plotted in (b) and (c), respectively. D-Matrix rain rate estimates over ocean are plotted in (d), and linear regression estimates over ocean are plotted in (e). Solid lines define the ±5 mm/hr retrieval error limits.

Regression-based retrieval formulas are applied to SSM/I data from an overpass of Hurricane Florence at 0021 GMT on September 10, 1988.

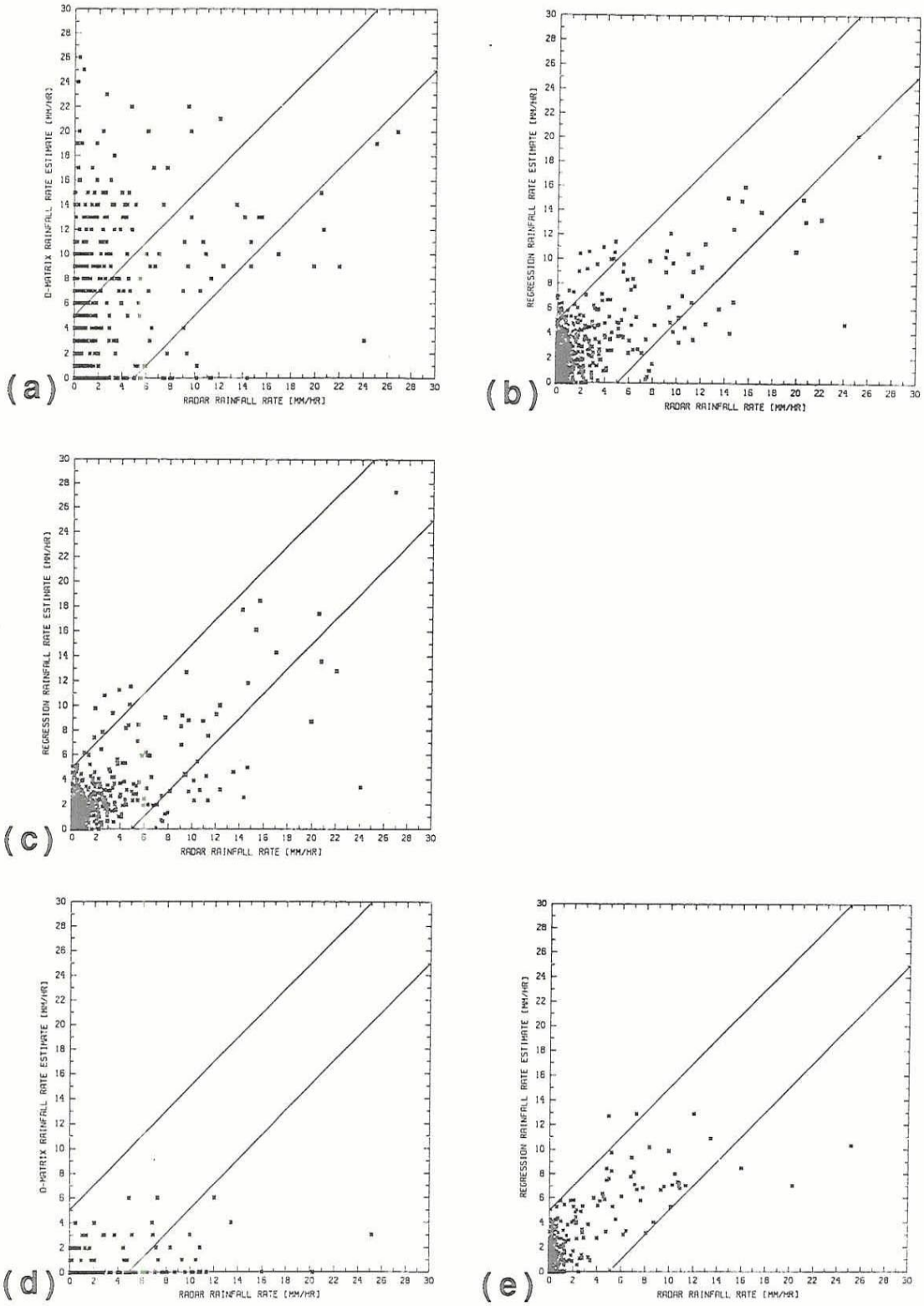

Figure 1-19. Hughes D-Matrix and the New Regression Estimates of Rainfall Rate versus Radar-Derived Rainfall Rate at Midlatitudes

SSM/I imagery in the 85.5H GHz and 37V GHz channels, which contribute to rain rate retrievals, is presented in Figures 1.20(a) and 1.20(b). Hydrometeor scattering leads to depressions in the 85.5 GHz brightness temperatures in regions of precipitation. At 37 GHz the scattering effect is less pronounced over land, and hydrometeor emission leads to an elevation in brightness temperatures relative to the low-emissivity ocean background.

The alternate algorithm retrieval of rainfall rates in Florence is presented in Figure 1.20(c). Retrievals within about 25 km of the coast are filtered because the radiometer measurements in the immediate vicinity of the coast contained significant contributions from both land and ocean backgrounds. The rain retrievals may be compared to the radar-derived rain rates obtained from the NWS WSR-57 station at Slidell, Louisiana in Figure 1.20(d).

Note that there is a good spatial correlation between SSM/I retrieved rainfall rates and radar-derived rates within the observing range of the radar. The retrieval algorithm tends to overestimate the rain rates (with respect to radar), because the proportion of graupel and ice particles to liquid precipitation is relatively high outside the eyewall in hurricanes [1]. The response of the 85.5 GHz channel data to an increase in the rain rate is greater in clouds which contain a greater proportion of ice. The response of the 37 GHz measurements to ice is similar, but less pronounced. Since the alternate retrieval algorithm is "tuned" to mean cloud conditions at midlatitudes, the increased response in the 85.5 and 37 GHz channels may lead to overestimates of rainfall rates in Florence.

Work is continuing to complete the validation of the SSM/I rain retrieval algorithms in the tropics during warm and cool seasons. New retrieval algorithms will be developed if necessary in an attempt to meet the ±5 mm/hr retrieval error specification. In addition, new versions of all of the algorithms which do not utilize the 85 GHz vertical channel are being developed, now that this channel has failed.

1.3.6 Cloud Amount

Hughes Aircraft Company developed two algorithms for estimating cloud amounts (percent cloud coverage) from SSM/I brightness temperatures. One is applicable over snow backgrounds; the other over land backgrounds. Hughes has not been tasked to develop a cloud amount estimation algorithm for ocean backgrounds. The algorithm development was based entirely on simulated data which indicated the main cloud signature over land and snow backgrounds was the loss of polarization at 85 GHz in the presence of cloud.

The Hughes cloud algorithms were evaluated for completeness and accuracy for four case study scenes selected to include different background and seasonal variations. "Truth" cloud amounts for each case study scene were derived from manual analyses of 3 nmi resolution visible and infrared imagery data obtained from the Operational Linescan System (OLS) sensor on the same DMSP spacecraft as the SSM/I. The Air Force

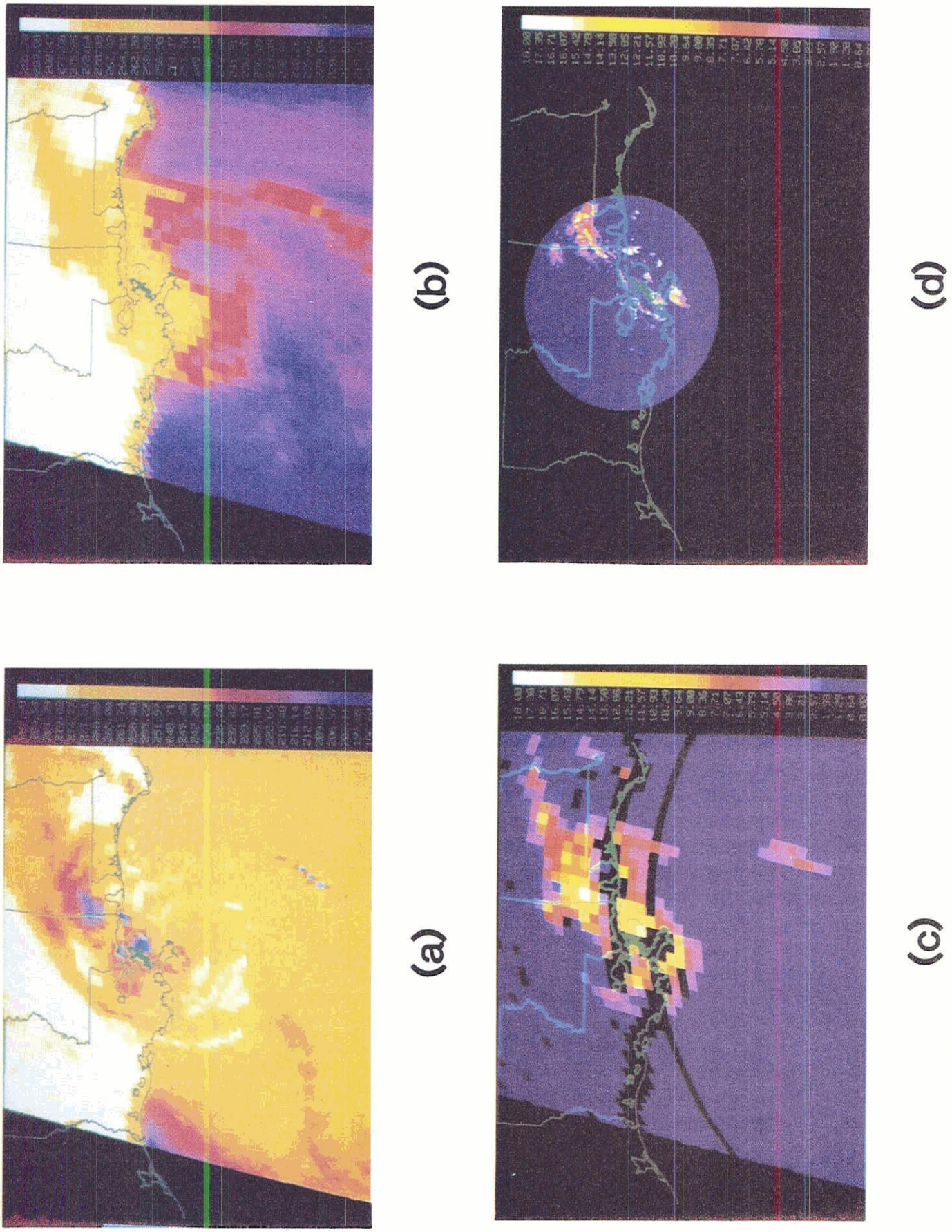

Figure 1.20

Interactive Meteorological System (AIMS) at the Geophysics Laboratory (GL) was used as the test bed for the validation study. AIMS interactive image processing and display functions were used extensively to aid the analyst in his manual interpretation of the OLS imagery. A threshold blanking technique was used to convert the manual analyses into synthetic digital images containing the cloud truth information. OLS "truth" cloud amounts were statistically compared to the corresponding SSM/I cloud amounts.

The results of these comparisons show that the SSM/I cloud amount algorithms for both backgrounds, land and snow, have no skill at estimating the correct cloud amounts. In other words, there is no discernable cloud signature from 85 GHz polarization values. Even if the SSM/I algorithms had shown some skill, their use would have been limited because of the large percentage of "out-of-limits" values they generate. The "out-of-limits" flag accounts for physically meaningless cloud amount values and is arbitrarily assigned to estimates less than -20% or greater than 120%. The actual numerical "out-of-limits" values were all negative which implies that many of the 85 GHz polarization values actually observed were significantly larger than those predicted by the simulations used in the algorithm development.

The failure of the algorithms is due to the use of a very limited set of cloud conditions, precipitation states, and atmospheric temperature, and humidity profiles for obtaining the simulated brightness temperatures that were used in the development of the algorithms. The full range of natural variability of the atmosphere and earth's surface was not accounted for. For example, only one cloud type was used with a liquid water content that is moderate to large for a non-precipitating cloud. Another contributing factor was error in the models of the atmospheric and surface conditions that were used.

1.4 RECOMMENDATIONS

1.4.1 Instrument

The excellent radiometric stability of the SSM/I makes it possible to average the antenna temperature calibration parameters for more than one scan as is presently done. As described in Section 3.2, five samples of the radiometer output voltages are taken when the feed horn is viewing the cold cosmic background and when viewing the hot reference load each scan. These voltages along with the measured temperature of the hot load and the known brightness temperature of the cosmic background are used to establish the absolute antenna temperatures. To reduce the effects of instrument noise, it is recommended that these voltages be averaged over 10 scans (50 samples with 3.8 sec/scan) for channels 19, 22, and 37 GHz and over 20 scans (100 samples with 1.9 sec/scan) for 85 GHz. This will reduce the instrument noise contribution to the antenna temperature calibration and improve the accuracy of the absolute brightness temperatures. As shown in Figure 1.7, the relative improvement in NEΔT approaches 10% when the averaging is performed.

As a result of the geolocation calibration, it is recommended that the current FNOC ephemeris generating program be replaced with the actual

spacecraft ephemeris which is down-linked with the OLS data. A remaining task is to verify that the pitch, roll, and yaw corrections found for the SSM/I data are constant, or, if variable, to determine their time dependance. The current values have been tested for only 12 selected orbits; a very limited set of conditions. To minimize the size and complexity of this effort it should await the implementation of the spacecraft ephemeris at FNOC to remove that source of error. A further comparison of OLS and SSM/I geolocation errors should be made. It is possible that upon further examination of OLS and SSM/I imagery, the source(s) of the non-ephemeris geolocation errors may be determined. Once the geolocation and pointing errors are eliminated, a routine to compute the earth incidence angle at each sample point should be implemented. This will allow brightness temperature corrections to be made and should result in an improvement in the absolute brightness temperatures. It will also reduce the errors in the retrieved environmental parameters. Finally, the extrapolation error associated with the last pixel sampled on each scan for latitudes outside ±60° should be corrected in the SSM/I geolocation algorithm.

It is recommended that further effort be directed toward an antenna pattern correction to improve the absolute brightness temperatures sampled near coastal boundaries due to antenna side lobe contaminations. The current algorithm does not consistently improve the brightness temperatures near coastal boundaries and by design does not introduce large errors. However, it is felt that further simulation and analysis may result in an algorithm which would allow retrievals of environmental parameters closer to coastal boundaries than now possible. Attention to algorithm complexity and associated computer processing requirements and amplification of instrument noise must be addressed in the algorithm development. In addition, it is recommended that the image reconstruction/restoration techniques be reviewed for their applicability to enhancing SSM/I imagery. In particular, the image enhancement of sea ice boundaries and large storm system structures should be addressed. The instrument recommendations are summarized in Table 1.7.

TABLE 1.7

INSTRUMENT RECOMMENDATIONS

- Substitute satellite ephemeris for predict ephemeris.
- Average hot and cold reference counts for 10 scans (50 samples) for channels 1 through 5 and 20 scans (100 samples) for channels 6 and 7. Preferably using an equal number of scans before and after the scan being calibrated.
- Correct software error which results in position error of last pixel of each scan above 60 degrees north/south latitude*.
- When available, implement software scan axis alignment correction to remove remaining geolocation error.
- Generate incidence angle for each pixel location.
- Use incidence angle to correct brightness temperature/environmental products.
- Study possible improvements in antenna pattern correction to increase brightness temperature accuracies near coastal and ice boundaries.
- Study further improvements in image reconstruction/restoration techniques.

**We believe software error lies in subroutine LOCINT, lines LOCINT 174 - LOCINT 182. (Vol II Program Maintenance Manual for a CDRL item 013A1) The computation within these lines should not be done for latitudes above 60 degrees North/South.*

1.4.2 Water Vapor and Cloud Water

There are two basic recommendations for the retrieval of water vapor (total precipitable water) and cloud liquid water over ocean. The first is the use of the new algorithms presented in Table 1.8 for the retrieval of these parameters and the institution of some quality control measures to insure the continued retrieval of reliable and accurate products from the SSM/I.

In the case of water vapor, our study has demonstrated the problems associated with the use of segmented algorithms. They lead to unnaturally large gradients at the boundaries of the segments. It has also shown that the original algorithms did not meet the accuracy requirements. A large body of data (more than any other published validation of total precipitable water) has been assembled. Both linear and non-linear algorithms have been examined and the non-linear algorithm given in Table 1.8 developed. Our recommendation is for the continued periodic collection of radiosonde observations as a quality control for the present algorithm and for its eventual refinement and improvement.

TABLE 1.8

INTEGRATED WATER VAPOR AND CLOUD WATER OVER OCEAN

COEFFICIENT	WATER VAPOR (OCEAN)	CLW (OCEAN)
C_0	0.235407 E3	-0.372284 E1
C_1	-0.129241	0.166909 E-1
C_2	------	-0.53605 E-2
C_3	-0.186322 E1	-0.49260 E-2
C_4	0.625270 E-2	-------
C_5	-0.377398	0.97800 E-2
C_6	-----	0.47938 E-2
C_7	-----	---------
C_8	------	-0.22900 E-2

$$\text{Water Vapor } (Kg/m^2) = C_0 + C_1 T_{B19V} + C_3 T_{B22V} + C_4 T_{B22V}^2 + C_5 T_{B37V}$$

$$\text{Cloud Water } (Kg/m^2) = C_0 + C_1 T_{B19V} + C_2 T_{B19H} + C_3 T_{B22V} + C_5 T_{B37V} + C_6 T_{B37H} + C_8 T_{B85H}.$$

The initial cloud liquid water algorithm(s) produced out-of-limits or indeterminate values for over 90% of the retrievals at our test sites indicating the necessity for improvements. Our investigation found little basis for the feasibility of retrievals over highly emissive surfaces such as land, ice, or snow. We were able to find a single algorithm that meets the accuracy requirements for cloud liquid water over the ocean. Our recommendations are for the implementation of our single algorithm for cloud water over the ocean given in Table 1.8 and to do no retrievals over land until a viable algorithm has been developed and demonstrated. It is also recommended that a simple quality control procedure be adopted for the cloud liquid water product. The procedure could be the examination of OLS or GOES images.

1.4.3 Wind Speed

It is recommended that the global D-matrix algorithm presented in Table 1.9 be used to retrieve ocean surface wind speeds. It is more restrictive in flagging rain and does not give biased wind speed estimates in the high and low wind speed ranges or generate zonal discontinuities. Further, it is recommended that wind speed Environmental Data Records be calculated to 1-decimal point accuracy (not rounded to the nearest m/s as is currently done) in order to eliminate conversion errors by users when going from m/s to miles/hour or knots.

TABLE 1.9

MARINE WIND SPEED

$$SW = 147.90 + 1.0969 \cdot T_{B19V} - 0.4555 \cdot T_{B22V} - 1.7600 \cdot T_{B37V} + 0.7860 \cdot T_{B37H}$$

RAIN FLAG	CRITERIA	ACCURACY
0	$T_{B37V} - T_{B37H} > 50$ $T_{B19H} < 165$	< 2 m/s
1	$T_{B37V} - T_{B37H} < 50$ $T_{B19H} > 165$	2 - 5 m/s
2	$T_{B37V} - T_{B37H} < 37$	5 - 10 m/s
3	$T_{B37V} - T_{B37H} < 30$	> 10 m/s

It is recommended that wind speeds be calculated in the presence of large storm systems. Although retrievals contaminated by dense clouds and rain may be out of specification, they help to outline areas of high winds. Approximately 85% of the time, algorithm retrievals are in areas of no rain (rain-flag 0). These retrievals meet the 2 m/s accuracy specification. The remaining 15% of the time, retrievals are in areas of high water vapor or rain, flagged 1, 2, or 3, with reduced accuracies ranging from ±2 m/s to > ±10 m/s.

Although the D-matrix wind speed retrievals meet design specifications under rain-free conditions, it has been suggested that an iterative-type algorithm might improve retrieval accuracy. This is true. Limited investigation of an iterative algorithm has shown that somewhat lower standard deviations (SD) also result because the iterative technique partially corrects for attenuation due to rain. Use of such an algorithm would probably lower the SD to 1.5 m/s for winds in the range of 3-25 m/s. However this approach is not recommended at this time because the wind speed retrieval errors are brought within specification by the computationally simpler global D-matrix algorithm. It will be investigated as a follow on effort.

1.4.4 Land Parameters

It is recommended that the decision logic of EXTLND be revised to include the rules and thresholds for the classification of dense vegetation, agricultural crops and range, dry arable soil, moist arable soil, semi-arid, desert, rain over vegetation, rain over soil, flooded soil, composite vegetation and water, composite soil and water, snow, composite snow and soil, and glacial. The revised rules and brightness temperature thresholds are given in Table 1.10. The environmental data products to be retrieved following EXTLND surface classification are given in Table 1.11.

TABLE 1.10

LAND SURFACE TYPE CLASSIFICATION RULES AND CORRESPONDING BRIGHTNESS TEMPERATURE COMBINATION THRESHOLD VALUES

LAND SURFACE TYPE CLASSIFICATION RULES	BRIGHTNESS TEMPERATURE COMBINATION THRESHOLD VALUES							
	[a] (K)	[b] (K)	[c] (K)	[d] (K)	[e] (K)	[f] (K)	[g] (K)	[h] (K)
Standing Water or Flooded Conditions	>4							
Dense Vegetation (Jungle)	≤4	≤1.9		≥0	<4.5		>262	
Agricultural/ Rangeland Vegetation	≤4	>1.9 ≤4		≥0	<4.5		>262	
Arable Soil (Dry)	≤4	>4 ≤9.8	≥-6.5	<0 ≥-5	<4.2		>257	
Soil (Moist Surface)	≤4	>4 <19	≥-6.5	≥0 <4	<4.2		>257	
Semi-Arid Surface	≤0.9	>9.8 <19	≤[d]	<0	<6	>7	>257	
Desert	≤0.8	≥19			>-1		>257	
Precipitation Over Vegetation	≤4	≤4		<0			>262	
Precipitation Over Soil	≤4	>4	<-3	<-5	<-4		>257	
Composite Vegetation and Water	≤4	<6.4		≥0	≥4.5			
Composite Soil and Water/Wet Soil Surface	≤4	>6.4		>-2	≥4.2			
Snow	≤4	>4	<-6.5				≤257	≥5

[a] 22V - 19V [b] [(19V+37V)/2] - [(19H+37H)/2] [c] 37V - 19V

[d] 85V - 37V [e] 85H - 37H [f] 37V - 37H

[g] 19V [h] 19V - 19H

TABLE 1.11

EDR EXECUTION FROM EXTLND CATEGORIES

CATEGORY	EDRS TO RETRIEVE
Precipitation over soil	Precipitation over land
Precipitation over vegetation	Precipitation over land
Lakes, standing water	none
Snow	Snow water content (under development)
Glacier, frozen surface	none
Dense and less dense vegetation	Land surface temperature, vegetation (STV)
Soils with moisture	Land surface temperature, moist soils (STL1)
	Surface moisture (SM)
Agricultural and range	Land surface temperature, arable land (STL2)
Dry soil, semiarid, desert	Land surface temperature, dry soils (STD)

When the pixel geolocation errors are removed, it is recommended that a dynamic database be created for the storage of surface type classification information relative to previous passes over a location. Such a database would serve as a surface type memory and could be accessed by the EXTLND software in situations requiring temporal information for more precise classifications. This is the case of additional snow rules for melting and refrozen snow for example, which would benefit from the history of prior conditions. SMISYRFTYP, the fixed geographical feature database being presently used does not contain enough detail regarding lakes and other water bodies. Thus if a dynamic database were used, locations containing a small lake for example would be continuously flagged for a composite soil and water condition and essentially become a fixed feature within the dynamic database. Retrievals of surface moisture would be enhanced as in some cases, it is impossible to discern between a footprint that is contaminated by the presence of a lake or river and that which contains water from a large rainstorm. A rule could be developed that would use the history of classifications over a particular spot to differentiate between these cases.

Retrieval algorithms should be implemented for dense vegetation, vegetation and crops (STV), arable soils (STL), and dry soil and desert (STD). Retrieval algorithms should be deferred for cloudy land (TLC), snow (STS), cloudy snow (TSC), and glacial (STG). Follow-on research should include OLS digital thermal infrared into the analysis. While this will be of use only in clear, relatively dry atmospheric conditions, the algorithms for surface temperatures over snow, desert, and forest vegetation could be further calibrated and the variance inherent in the ground truth could be identified. The recommended algorithms to retrieve land surface temperature in degrees Kelvin are contained in Table 1.12.

TABLE 1.12

LAND SURFACE TEMPERATURE ALGORITHMS

	C_0	$C_{1(19H)}$	$C_{2(22V)}$	$C_{3(37V)}$	$C_{4(85V)}$
STV - vegetation	24.94	-1.2784	0.8800	0.5933	0.7299
STL1 - moist soils	23.16	-0.1873	0.5221	-0.6271	1.232
STL2 - ag and range	6.97	-0.6266	0.2716	-0.1297	1.482
STD - dry soils	72.68	-0.4598	0.5984	0.8828	-0.2623

SURFACE MOISTURE ALGORITHM

Surface moisture is expressed as an antecedent precipitation index (API), which includes both soil moisture and surface water in place of percentage as originally specified. The units are millimeters.

	C_0	$C_{1(19V)}$	$C_{2(19H)}$	$C_{3(22V)}$	$C_{4(85V)}$
SM(API)	-291.7	0.190	-2.63	1.28	2.16

The API is preferred over soil moisture in percent because the same infiltration from rainfall would produce differing soil moisture (%) for soils of varying infiltration and percolation characteristics, which include texture, structure, soil depth, vegetative cover, and cultural practices. All of these have successfully been combined into API models that have been operationally used to convert rainfall into an antecedent moisture for runoff estimation models. An API may be translated into an additional soil moisture (% by volume) by dividing the API by the depth of the soil layer (mm). Division by the soil bulk density would produce the soil moisture in percent by weight.

Follow-on research should categorize the nature of the snow and the underlying surface before algorithms are implemented to avoid an automatic retrieval of parameters that are not physically consistent with the actual conditions. The snow edge classification embedded in EXTLND has sufficient accuracy for inclusion in the software.

The surface moisture retrieval algorithms developed consist of two main components: (1) classification rules which identify the presence of moisture at the soil surface and (2) retrieval algorithms based on the antecedent precipitation index (API) as a measure of the amount of water at the soil surface layer as well as water stored in depression storage. Due to the importance of accurately classifying the surface type prior to using the developed retrieval algorithm, it is recommended that a dynamic database scheme be incorporated into the EXTLND classification software in order to improve the sensing of moisture at the surface for any region in the world over time. This will require proper surface location of the SSM/I footprints.

It is recommended that the soil moisture retrieval algorithm given in Table 1.12 be implemented for the land surface classifications that include moisture in or on the soil surface.

1.4.5 Sea Ice

It is recommended that a tailored or reduced version of the AES/YORK algorithm be implemented for operational use. This tailoring is necessary for two major reasons. First, the AES/YORK was constructed to retrieve not only the basic SSM/I parameter of sea ice concentration and identify first-year and multi-year ice types but also additional parameters such as the fractions of first-year, multi-year, and thin ice within the SSM/I footprint as well as ocean surface wind speed and vertical columns of water vapor and liquid cloud water. Second, the computer resources required to implement the complete AES/YORK algorithm are significantly greater than the proposed tailored version. The error in the retrieved sea ice concentration using the tailored AES/YORK algorithm is essentially that associated with the complete algorithm and as discussed earlier is typically less than 10-12%.

Figure 1.21 presents a top-level flow chart of the proposed tailored version of the AES/YORK sea ice algorithm. Specific equations and decision tests employed in the algorithm are presented in Table 1.13. The initial test identified in the flow chart, Test 1, checks for the reasonableness of the 19V, 19H, 37V, and 37H SDRs and polarization differences 19V-19H, 37V-37H. If any of the inequalities in Test 1 of Table 1.13 are true, no sea ice concentration or ice type identification is retrieved. If none of these inequalities are true, the SDRs are reasonable for open ocean or sea ice and total sea ice concentration, TOTICE, is computed either for winter/fall conditions or summer/spring conditions. Equation A in Table 1.13 is used to compute TOTICE and employs only the 19V and 37V SDRs. Depending on the value of TOTICE and several subsequent threshold tests, new values of TOTICE may be computed. As shown in Figure 1.21, a threshold TC is selected depending on the condition of winter/fall or summer/spring. TC is essentially an atmospheric offset threshold used later. The next step in the algorithm is to compute a discriminate D which is an estimate of the total ice concentration independent of Equation A and is expressed by Equation C in Table 1.13. Test 2 which follows the computation of D is a consistency

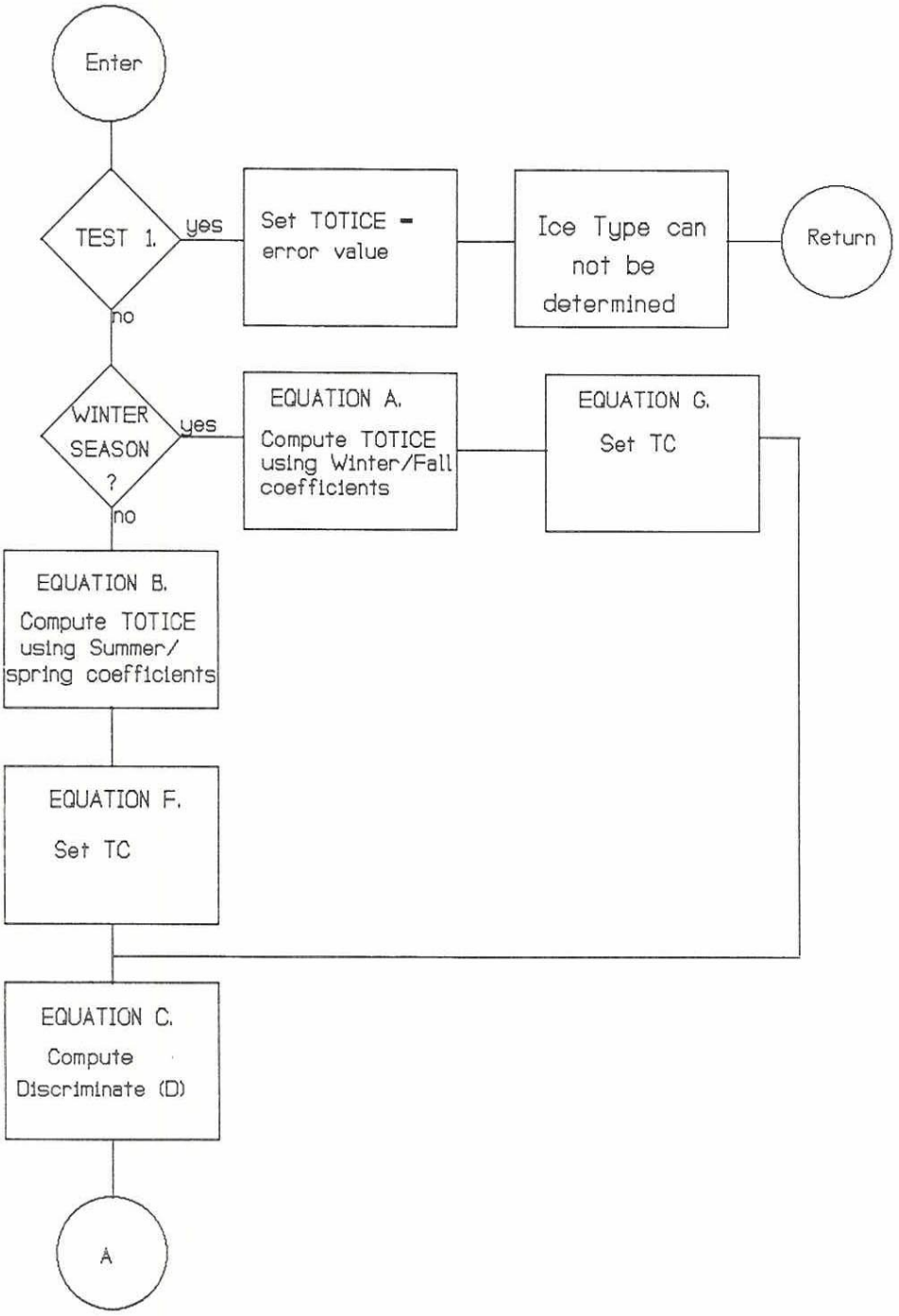

Figure 1-21. Flow Chart of Recommended Ice Concentration Algorithm

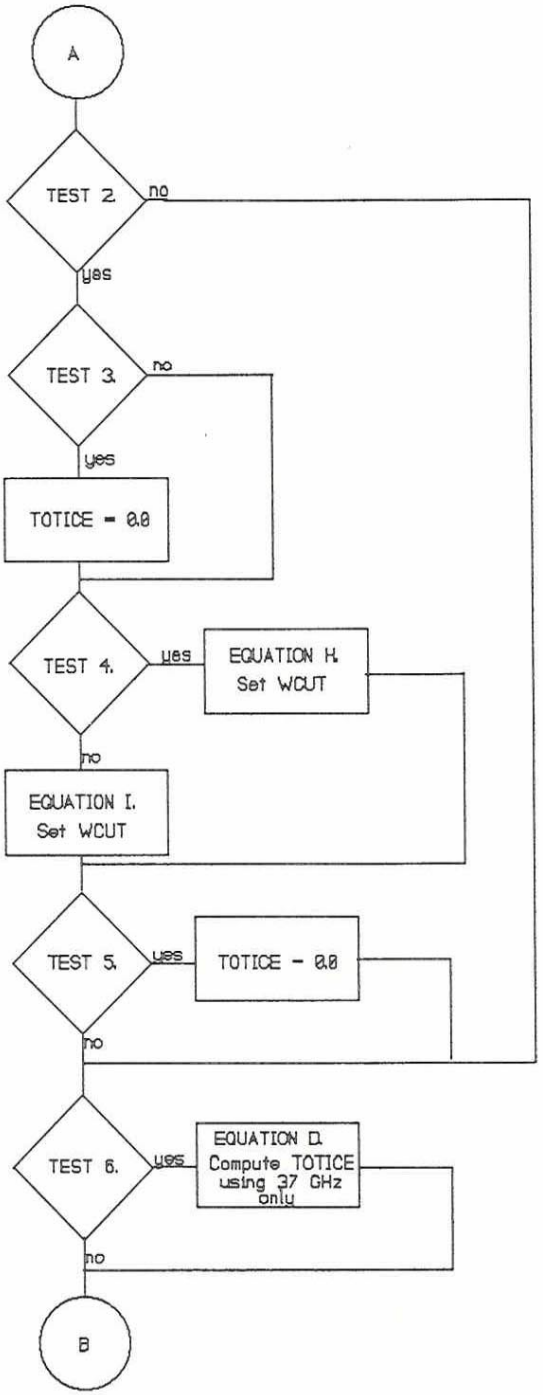

Figure 1-21. Continued

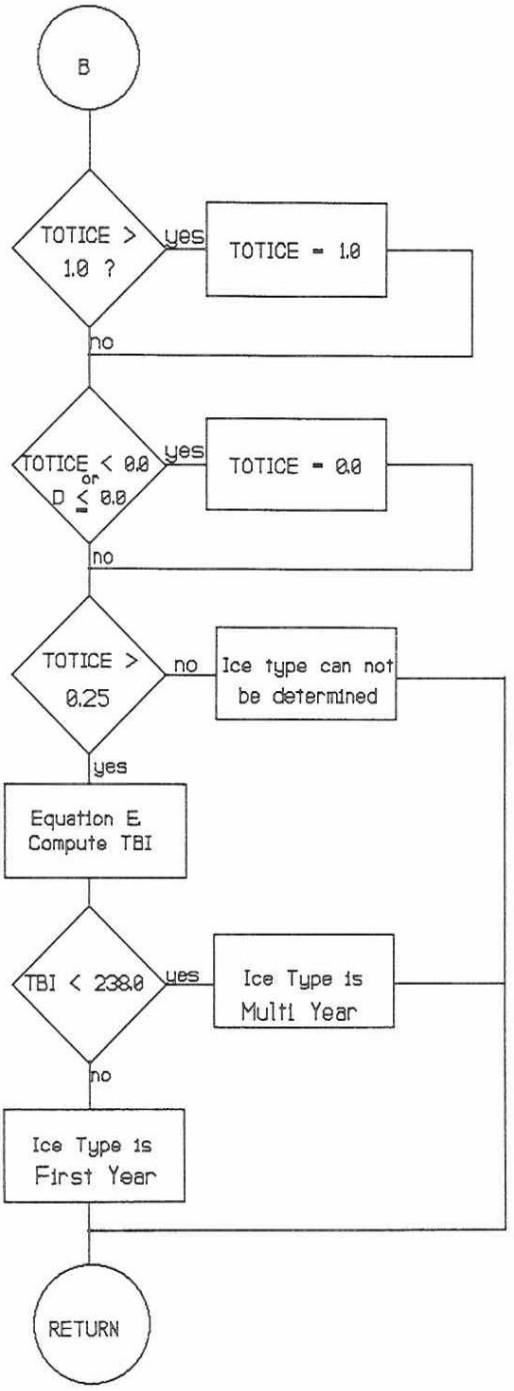

Figure 1-21. Continued

TABLE 1.13

EQUATIONS AND TESTS USED IN RECOMMENDED SEA ICE ALGORITHM

EQUATIONS

A. $TOTICE = CWF(1) * T_{B37V} + CWF(2) * T_{B19V} + CWF(3)$

B. $TOTICE = CSS(1) * T_{B37V} + CSS(2) * T_{B19V} + CSS(3)$

C. $D = 1.0 - 0.0513 * (T_{B37V} - T_{B19V})$

D. $TOTICE = (T_{B37V} + 0.5 * T_{B37H} - 265.0) * 0.01$

E. $TBI = [T_{B19V} - TC - (1.0 - TOTICE) * 180]/TOTICE$

F. $TC = 14.0$

G. $TC = 6.8$

H. $WCUT = 6.0$

I. $WCUT = 8.5$

WINTER/FALL COEFFICIENTS

$CWF(1) = -0.013656219$
$CWF(2) = 0.024412842$
$CWF(3) = -1.677645$

SUMMER/SPRING COEFFICIENTS

$CSS(1) = -0.015231617$
$CSS(2) = 0.025911011$
$CSS(3) = -1.656920$

TESTS

1.
$$\begin{aligned} T_{B19V} &\leq 151.0 \quad OR \\ T_{B19H} &\leq 92.0 \quad OR \\ T_{B37V} &\leq 171.0 \quad OR \\ T_{B37H} &\leq 125.0 \quad OR \\ (T_{B19V} - T_{B19H}) &\geq 80.0 \quad OR \\ (T_{B37V} - T_{B37H}) &\geq 80.0 \quad OR \\ T_{B19H} &> T_{B19V} \quad OR \\ T_{B37H} &> T_{B37V} \end{aligned}$$

2. $TOTICE \leq 0.7$ AND $D \leq 0.7$

3. $D \leq 0.3$ AND $[T_{B37V} * 1.5 - T_{B19V}] > 120.0$

4. $T_{B37V} \leq 215.0$

5. $D \leq 0.15$ OR $[T_{B37H} - 2 * T_{B37V} + 270.0] \geq WCUT$

6. $TOTICE \leq 0.5$ AND $D > 0.15$

check between TOTICE and D. If TOTICE and D are both less than or equal to 0.7, additional testing is necessary to determine the influence of clouds and/or ocean roughness. These tests are identified as tests, 3, 4, and 5 in the flow diagram. If TOTICE is greater than 0.7 or in the event the output of these tests results in TOTICE being less than or equal to 0.5 and D greater than 0.15 (test 6), then the effects of cloud and ocean roughness are unimportant and the algorithm recomputes TOTICE using only the 37V and 37H channels with Equation D of Table 1.13. This is done to take advantage of the higher resolution of the 37 GHz data and provides greater accuracy in determining the sea ice edge. (The highest resolution 85 GHz channels are currently not employed in sea ice concentration retrievals. Under clear skies and calm ocean surface, the 85 GHz data offers the potential for determining sea ice edge to ±6 km.) In the event clouds or ocean roughness is important, the previous value of TOTICE is used. Test 6 is followed by out-of-bounds checking of TOTICE and if TOTICE is less than 0.25 no ice type identification is made. If TOTICE is greater than or equal to 0.25, the ice type identifier TBI is computed with Equation E. If TBI is less than 238, the fraction of ice is predominately multi-year ice. Otherwise the fraction is predominately first-year.

AES plans to continue the validation of the AES/YORK algorithm for another year to fine tune the algorithm using the best combination of observations available (from AIMR, SAR, infrared, etc.) and will make available these results and any improvements developed. The airborne imaging microwave radiometer (AIMR), operating at 37 and 90 GHz with dual polarization, will be the primary sensor used in this extended validation and to test possible improvements in the sea ice parameters with the introduction of higher frequency channels. Detailed analysis of major experimental data from (a) the NRL P-3 Gulf of St. Lawrence experiment (January 1988), (b) the BEPERS experiment in the Gulf of Bothnia (March 1988), (c) LIMEX experiment in the Labrador Sea (March 1989), (d) the Polarstern experiment (April-July 1989) in the Arctic Ocean and East Greenland Sea, and (e) the Polarstern experiment in the Weddell Sea (August-October 1989), should provide a more global evaluation of the ice algorithm.

1.4.6 Precipitation

The following is the recommended midlatitude rain retrieval algorithm, including screening logic to test for the presence of rain.

Screening Logic:

If $T_{B85V} - T_{B85H} < -2$ K or
$T_{B37V} - T_{B37H} < -2$ K or
$T_{B19V} - T_{B19H} < -2$ K, then flag as indeterminate

Else if SSM/I measurement is over land, then

If $T_{B22V} - T_{B19V} \leq 4$ K and
$(T_{B19V} + T_{B37V})/2 - (T_{B19H} + T_{B37H})/2 \leq 4$ K and
$T_{B85V} - T_{B37V} < 0$ K and
$T_{B19V} > 262$ K

or

$T_{B22V} - T_{B19V} \leq 4$ K and
$(T_{B19V} + T_{B37V})/2 - (T_{B19H} + T_{B37H})/2 > 4$ K and
$T_{B37V} - T_{B19V} < -3$ K and
$T_{B85V} - T_{B37V} < -5$ K and
$T_{B85H} - T_{B37H} < -4$ K and
$T_{B19V} > 257$ K, then compute rain rate over land,

Else rain rate = 0 mm/hr.

Else if SSM/I measurement is over ocean, then

If $-11.7939 - .02727\ T_{B37V} + .09920\ T_{B37H} > 0$ K, then
Compute rain rate over ocean,

Else rain rate = 0 mm/hr.

Else SSM/I measurement is coastal; flag as indeterminate.

Algorithms:

If a rainfall rate over land is to be computed, then use

$$R = \exp(1.32526 - .08150\ T_{B37V} + .01638\ T_{B37H} + .03561\ T_{B22V} + .05079\ T_{B19V} - .01875\ T_{B19H}) - 8.0 \text{ mm/hr} .$$

If a rainfall rate over ocean is to be computed, then use

$$R = \exp(-.36025 - .0091856\ T_{B85V} - .00555\ T_{B22V} + .02696\ T_{B19V}) - 4.0 \text{ mm/hr}.$$

Alternatively, if the 85.5 GHz vertical channel is unusable, then over ocean apply

$$R = \exp(-.42383 - .0082985\ T_{B85H} + .01496\ T_{B19V} + .00583\ T_{B19H}) - 4.0 \text{ mm/hr} .$$

If any of these formulae yield a rainfall rate less than zero, then set the rain rate equal to 0 mm/hr.

1.4.7 Cloud Amount

It is concluded that the present Hughes SSM/I cloud amount algorithms over land and snow backgrounds do not work. However, well developed convective clouds, which contain a thick layer of ice particles,

have a strong cold signature at 85 GHz over land and snow backgrounds, as well as all other backgrounds, including ocean. Further if the land surface type can be reliably identified and the surface brightness temperature determined, a cloud amount algorithm is feasible. Evidence to date indicates that this is possible. Over oceanic backgrounds, all cloud types, except for cirrus and strong convective cells, have a warm signature at 37 and 85 GHz. A newly developed SSM/I cloud amount algorithm for oceanic backgrounds [2] requires validation. Thus there is potential for developing a cloud amount algorithm.

False color composite multispectral imagery constructed from OLS and SSM/I data can be used to readily distinguish several cloud types. An example of such an image is shown in Figure 1.22. This image contains cloud information over the Southern African land mass; as well as, a bit of ocean south of the land, for January 14, 1988. It was generated on an AIMS image processing workstation at GL by having the OLS visible channel, IR channel, and SSM/I horizontally polarized 85 GHz channel drive the red, green, and blue color guns, respectively. The relative signal strength of the individual channels determine the color seen in the composite image. In the African image over land backgrounds; clear areas are black; strong convective cells are white and cyan; thick cirrus clouds are yellow; thin cirrus clouds are green; and low altitude water clouds are red. While over ocean backgrounds; clear areas are blue; thick cirrus and middle altitude water clouds are yellow; thin cirrus clouds are cyan; and low altitude water clouds are red and magenta.

SSM/I data could be used to improve the AFGWC's (Air Force Global Weather Central) operational automated cloud analysis. The cloud analysis, known as the RTNEPH (Real-Time Nephanalysis) produces global estimates of cloud cover, altitude, and type. Its main source of data is the infrared and visible digital imagery from the DMSP OLS sensor. Knowledge of the location of snow and ice backgrounds, as well as, accurate estimation of expected surface IR temperature for clear conditions are important for the RTNEPH analysis. The SSM/I is good at snow and ice detection because of the strong microwave signatures of these surfaces. Use of this timely and accurate information in the RTNEPH cloud analysis would improve it. Savage et al. [3] have found that the expected surface IR brightness temperature for clear conditions over vegetated land backgrounds can be predicted from SSM/I brightness temperatures. They believe predictions also can be made over desert backgrounds. Their technique is potentially more accurate than the current technique of estimating the expected surface IR temperature from surface reports of air temperature, and thus incorporation of their technique into the RTNEPH could potentially improve it.

It is recommended that new cloud amount algorithms coupled with the land surface type identification described in Section 1.3.3 along with a new cloud amount algorithm over ocean be developed and tested.

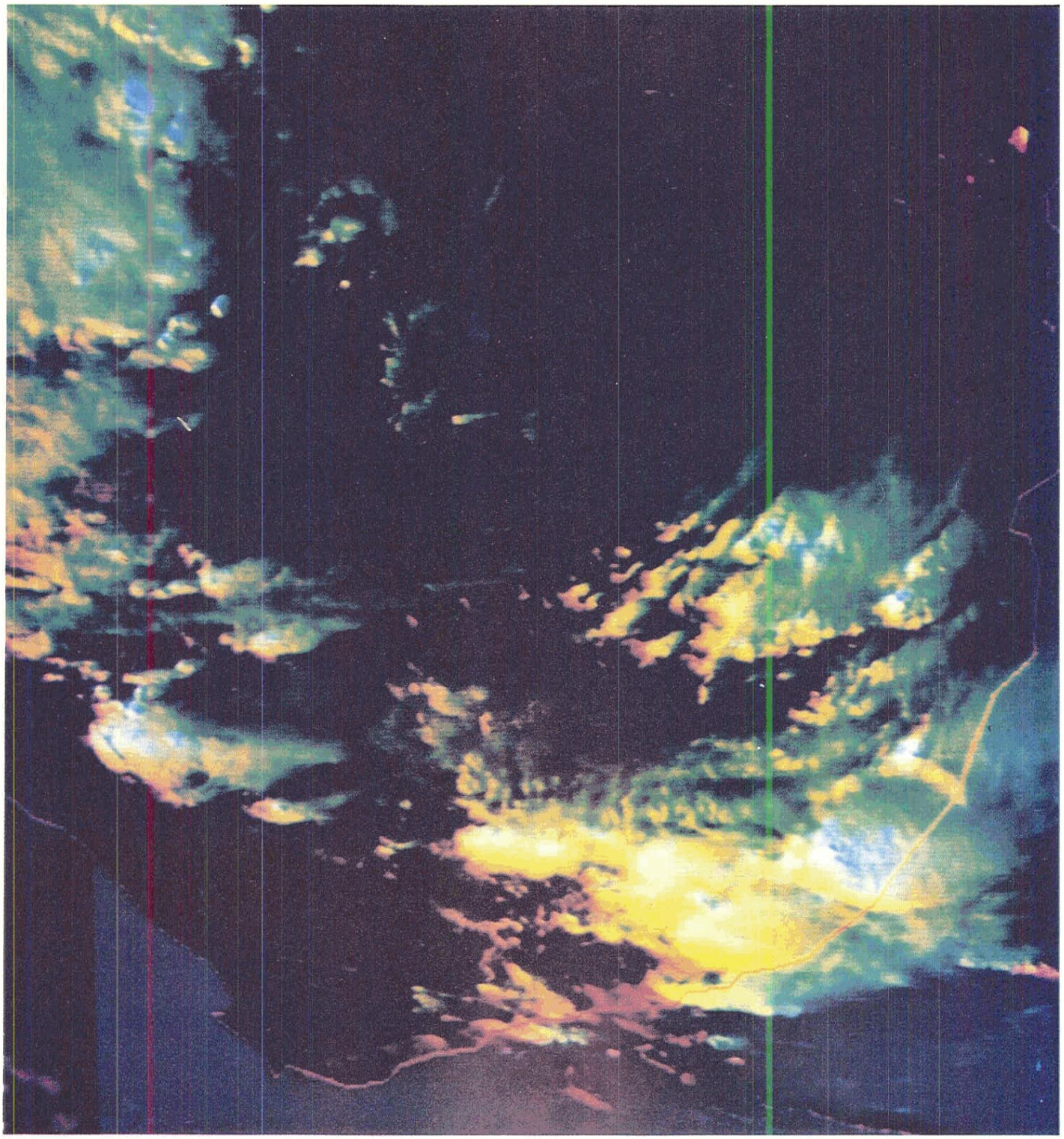

Figure 1.22

1.5 REFERENCES

[1] Willoughby, H. E., D. P. Jorgensen, R. A. Black, and S. L. Rosenthal, 1985: Project STORMFURY: A scientific chronicle 1962 - 1983. *Bull. Amer. Meteor. Soc., 66* 505-514.

[2] Rubinstein, I. G. (York University - Canada), 1988: Personal communication.

[3] Savage, R.C., J. F. Heinrichs, and A. J. Koscielny, 1989: Cloud Identification Using IR and Microwave Imagery. Preprint, Fifth International Conference on Interactive Information and Processing Systems for Meteorology, Oceanography, and Hydrology, AMS, Boston, MA.

2.0 INSTRUMENT DESCRIPTION

2.1 OVERVIEW

The SSM/I is a seven-channel, four-frequency, linearly-polarized, passive microwave radiometric system. A more detailed description of the SSM/I and the Hughes environmental parameter retrieval algorithms, than given here, is available in the SSM/I User's Guide [1]. The instrument consists of an offset parabolic reflector of dimensions 24 x 26 inches, fed by a corrugated, broad-band, seven-port horn antenna. The reflector and feed are mounted on a drum which contains the radiometers, digital data subsystem, mechanical scanning subsystem, and power subsystem. Figure 2.1 presents an overview of the major subsystems. The reflector-feed-drum assembly is rotated about the axis of the drum by a coaxially mounted bearing and power transfer assembly (BAPTA). All data, commands, timing and telemetry signals, and power pass through the BAPTA on slip ring connectors to the rotating assembly.

A small mirror and a hot reference absorber are mounted on the BAPTA and do not rotate with the drum assembly. They are positioned off axis such that they pass between the feed horn and the parabolic reflector, occulting the feed once each scan. The mirror reflects cold sky radiation into the feed thus serving, along with the hot reference absorber, as calibration references for the SSM/I. This scheme provides an overall absolute calibration which includes the feed horn. Corrections for spillover and antenna pattern effects from the parabolic reflector are incorporated in the data processing algorithms.

The SSM/I rotates continuously about an axis parallel to the local spacecraft vertical at 31.6 rpm and measures the upwelling scene brightness temperatures over an angular sector of 102.4° about the sub-satellite track. The scan direction is from the left to the right when looking in the aft direction of the spacecraft with the active scene measurements lying $\pm 51.2^{\circ}$ about the aft direction. This results in a swath width of 1400 km. The spin rate provides a period of 1.9 seconds during which the spacecraft sub-satellite point travels 12.5 km. Each scan 128 discrete uniformly spaced radiometric samples are taken at the two 85.5 GHz channels and, on alternate scans, 64 discrete samples are taken at the remaining five lower frequency channels.

A total-power radiometer configuration is employed in the SSM/I. A functional block diagram of a typical radiometer is shown in Figure 2.2. The signal from the output of the feedhorn is down-converted by a balanced mixer, amplified by IF amplifiers, and converted to a video voltage with a square-law detector. The bandpass filter is used to define the receiver passband and to improve out-of-band rejection. The detected video signal is then amplified and offset to remove part of the component of receiver output due to receiver noise. The output of the video amplifier is integrated by an integrate and dump filter for 3.89 msec at 85.5 GHz and 7.95 msec for the remaining channels and delivered to the data processing system. The time between radiometer output samples is 4.22 msec at 85.5 GHz and is the same time required for the antenna beam to scan 12.5 km in

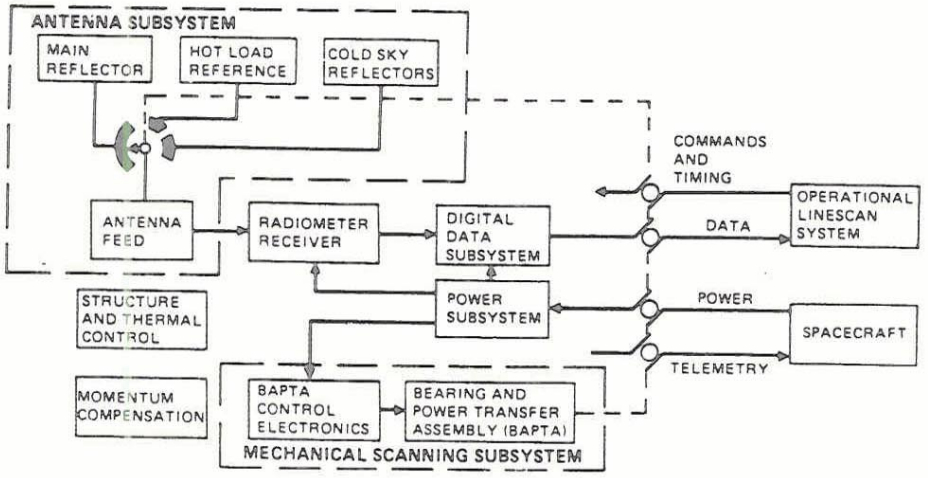

Figure 2.1 Sensor Overview

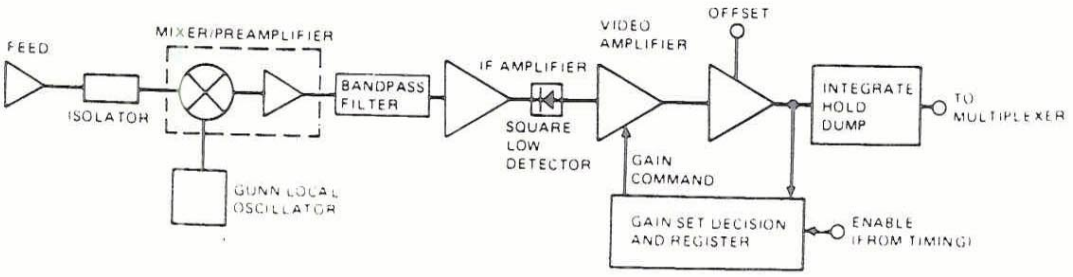

Figure 2.2 Radiometer Block Diagram

the cross-track direction. The time between samples at the remaining frequencies is 8.44 msec.

The data processor multiplexes the seven radiometer output signals with an analog multiplexer and samples and holds the signals before being digitized into 12-bit words. In addition, twelve channels are multiplexed with the radiometer data. These channels contain three hot target temperature measurements, two temperature sensor measurements within the radiometer, reference voltage, and reference return data. A microprocessor supervises instrument timing, control, and data buffering with the DMSP Operational Line Scanner (OLS) instrument which records all SSM/I data. The average data rate of the SSM/I including zeros required to match the OLS interface is 3276 bps.

The SSM/I instrument is shown in the stowed position in Figure 2.3 and deployed in Figure 2.4. The feedhorn antenna may be seen in Figure 2.3 and the calibration reflector in Figure 2.4. The hot calibration target is hidden by the thermal blanket in both figures. Photographs of the feedhorn, calibration reflector, and hot target are presented in Figures 2.5 through 2.7. The SSM/I sensor weighs 107 lbs. A high speed momentum wheel weighing 16 lbs is mounted inside the spacecraft. The SSM/I system consumes 45 watts.

2.2 SCAN GEOMETRY

Figure 2.8 presents the instantaneous field of view (IFOV) of the SSM/I for the channel frequencies during the scan region of the scene sector. The ellipses denote projections of the antenna 3 dB beamwidths onto the earth's surface. The SSM/I spins about an axis parallel to the local spacecraft vertical unit vector, the X direction in Figure 2.8, at a rate of 31.6 rpm as the sub-satellite track moves along the -Y direction at 6.58 km/sec. This results in a separation between successive scans of 12.5 km along the in-track direction which is nearly equal to the resolution of the 85 GHz beams. On each scan 128 uniformly spaced samples of the 85.5 GHz scene data are taken over a 102.4 degree scan region. The sampling interval is 4.22 msec and equals the time for the beam to travel 12.5 km in the cross track direction. Radiometer data at the remaining frequencies are sampled every other scan with 64 uniformly spaced samples having an 8.44 msec interval. Scan A denotes scans in which all channels are sampled while Scan B denotes scans in which only 85.5 GHz data are taken. The start and stop times of the integrate and dump filters at 19.35, 22.235, and 37.0 GHz are selected to maximize the radiometer integration time and achieve concentric beams for all sampled data. Figure 2.9 presents the beam sizes and sampling grid for a region near the ground track of the sub-satellite point and near the edge of the swath. The effect of the radiometer integration times is to increase the effective along scan beam diameter and make the beams at 37 and 85 GHz nearly circular. Note the greater overlapping of beams near the edge of the swath.

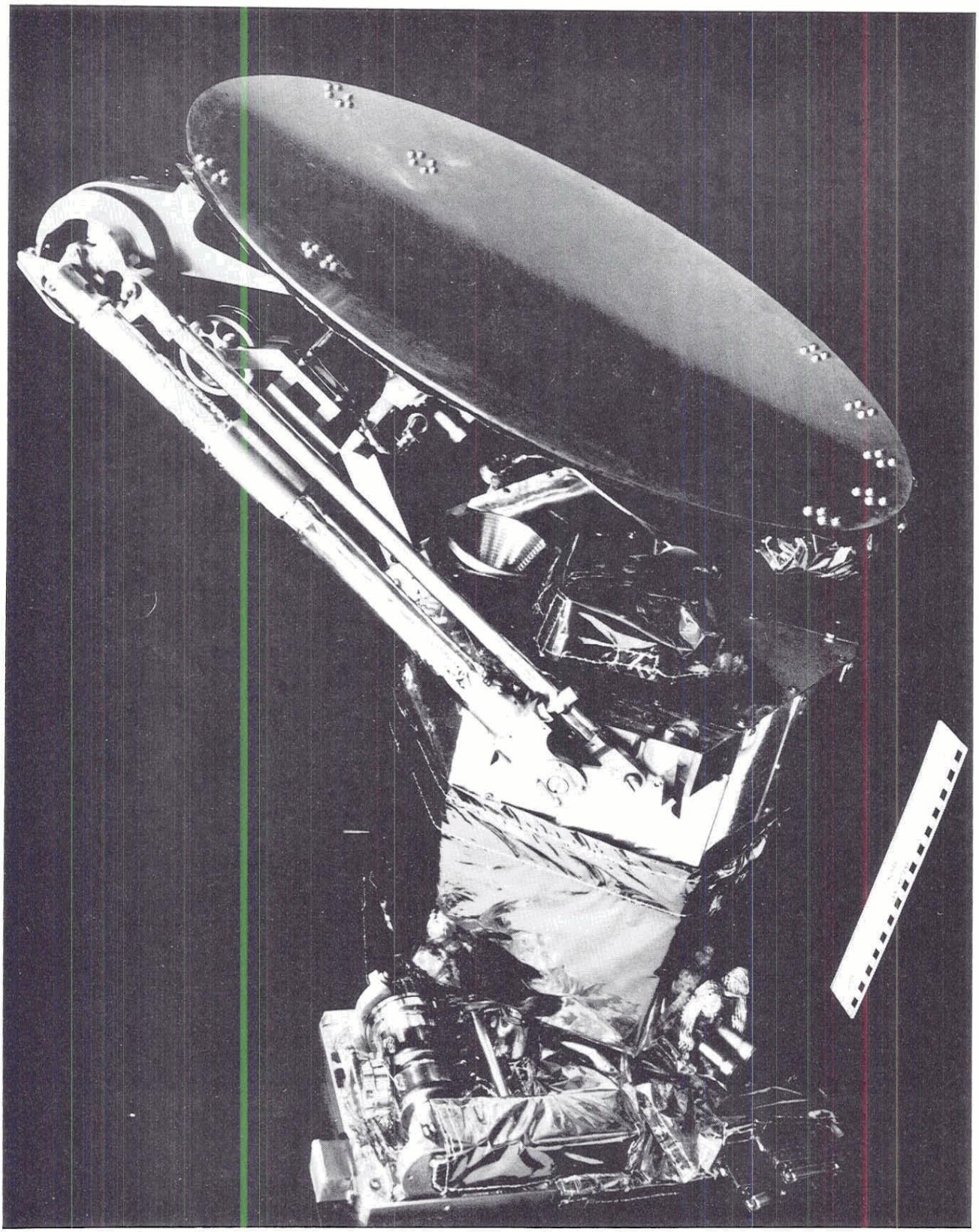

Figure 2.3 SSM/I in Stowed Position

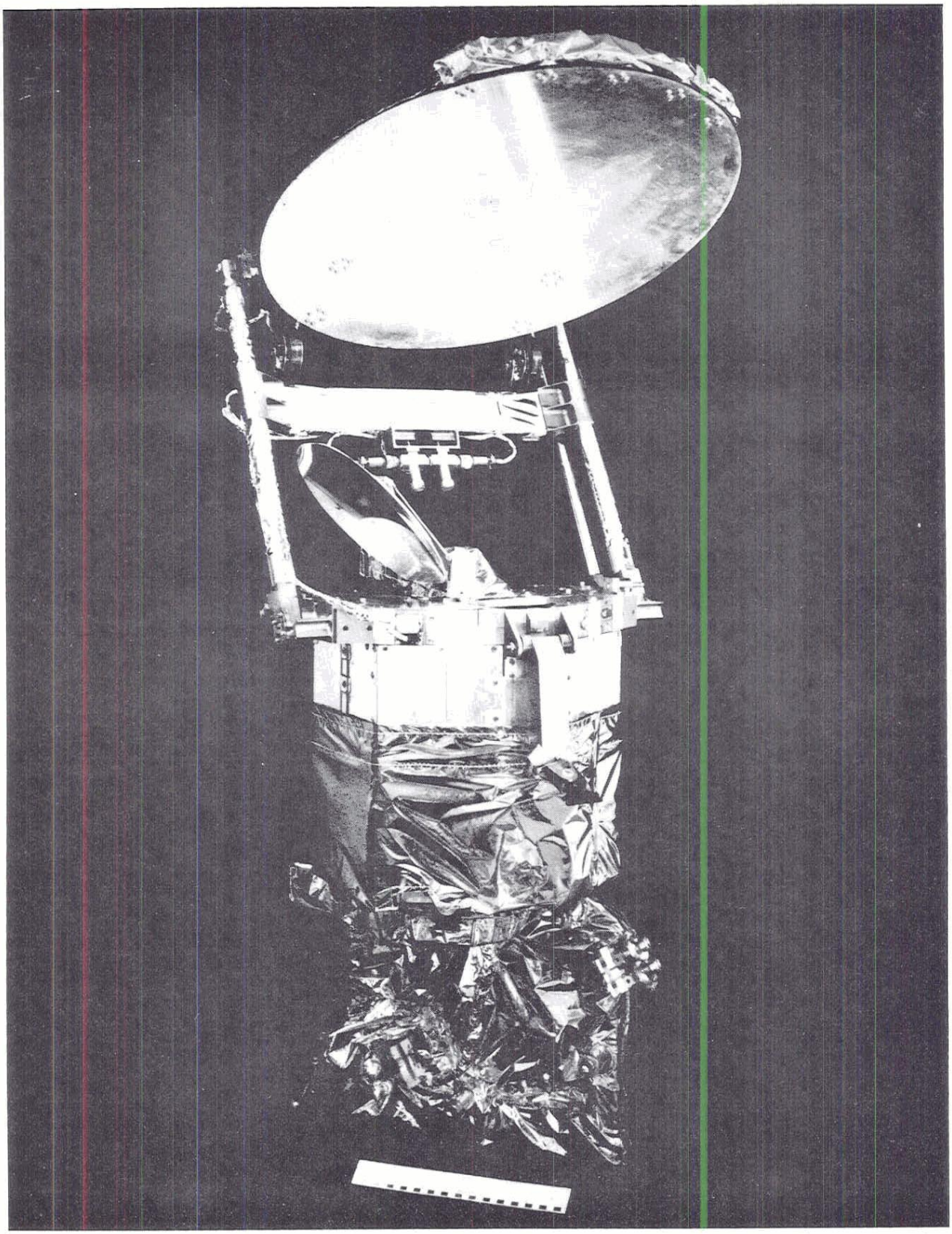

Figure 2.4 SSM/I in Deployed Position

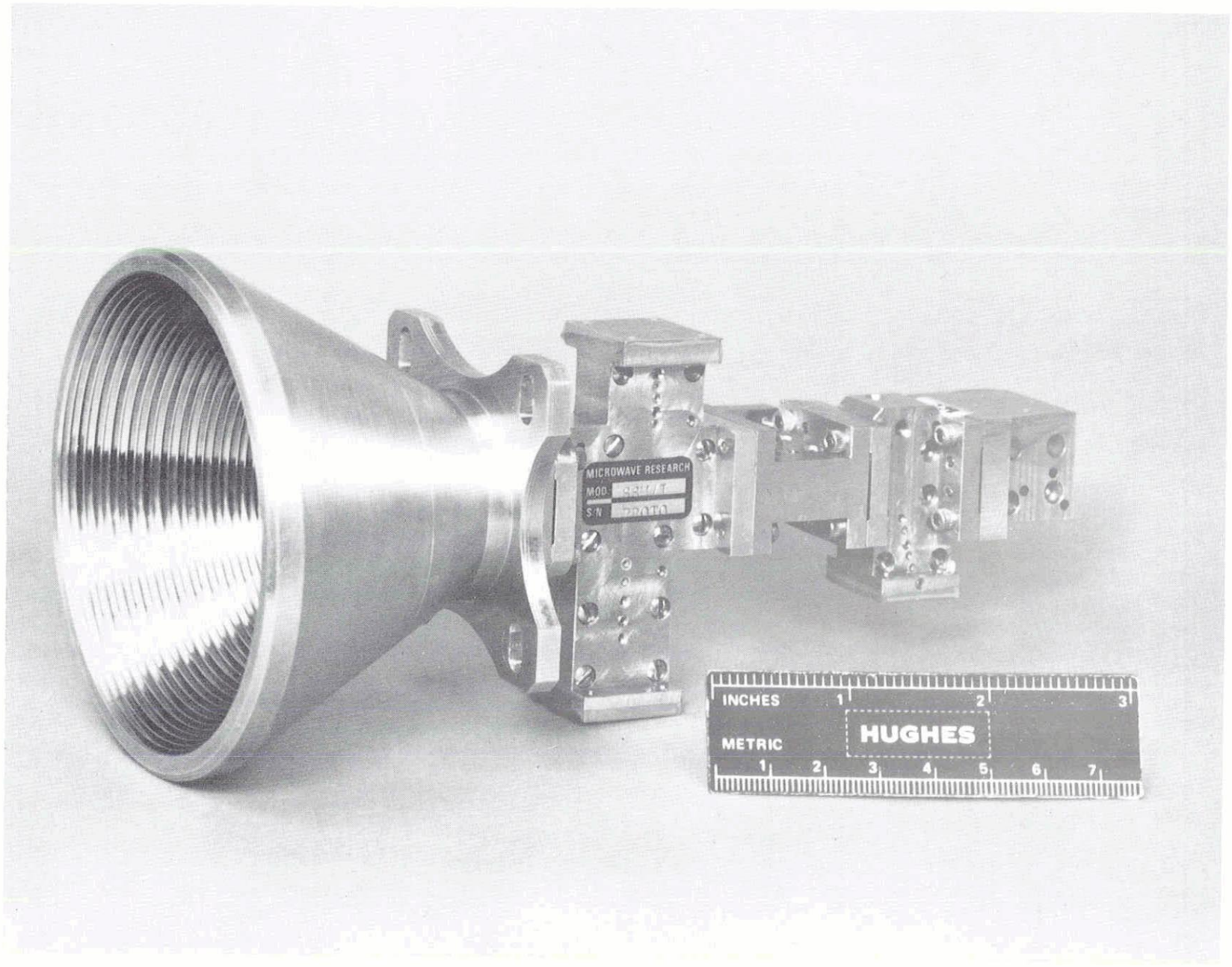

Figure 2.5 SSM/I Feedhorn

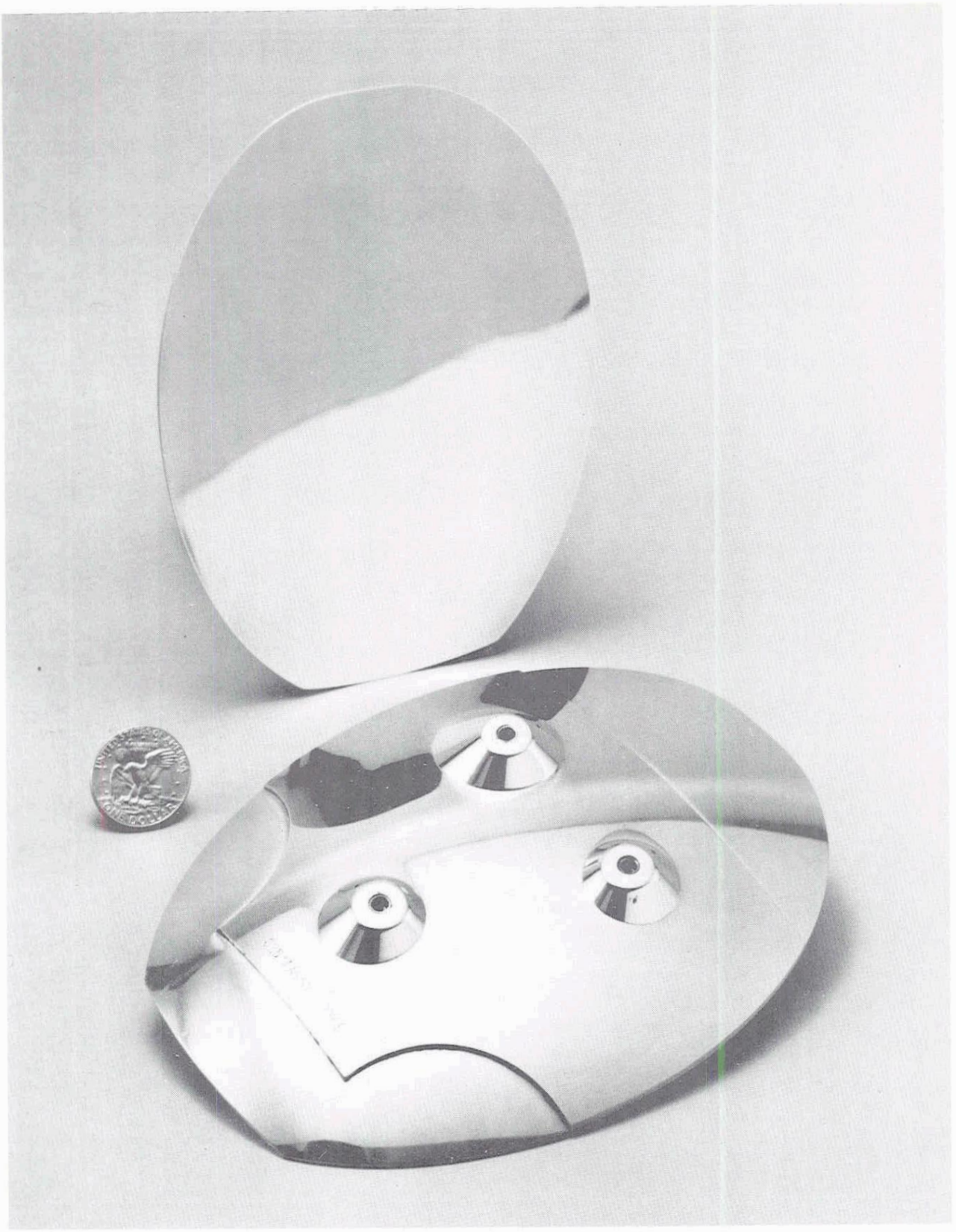

Figure 2.6 SSM/I Cold Sky Calibration Reflector

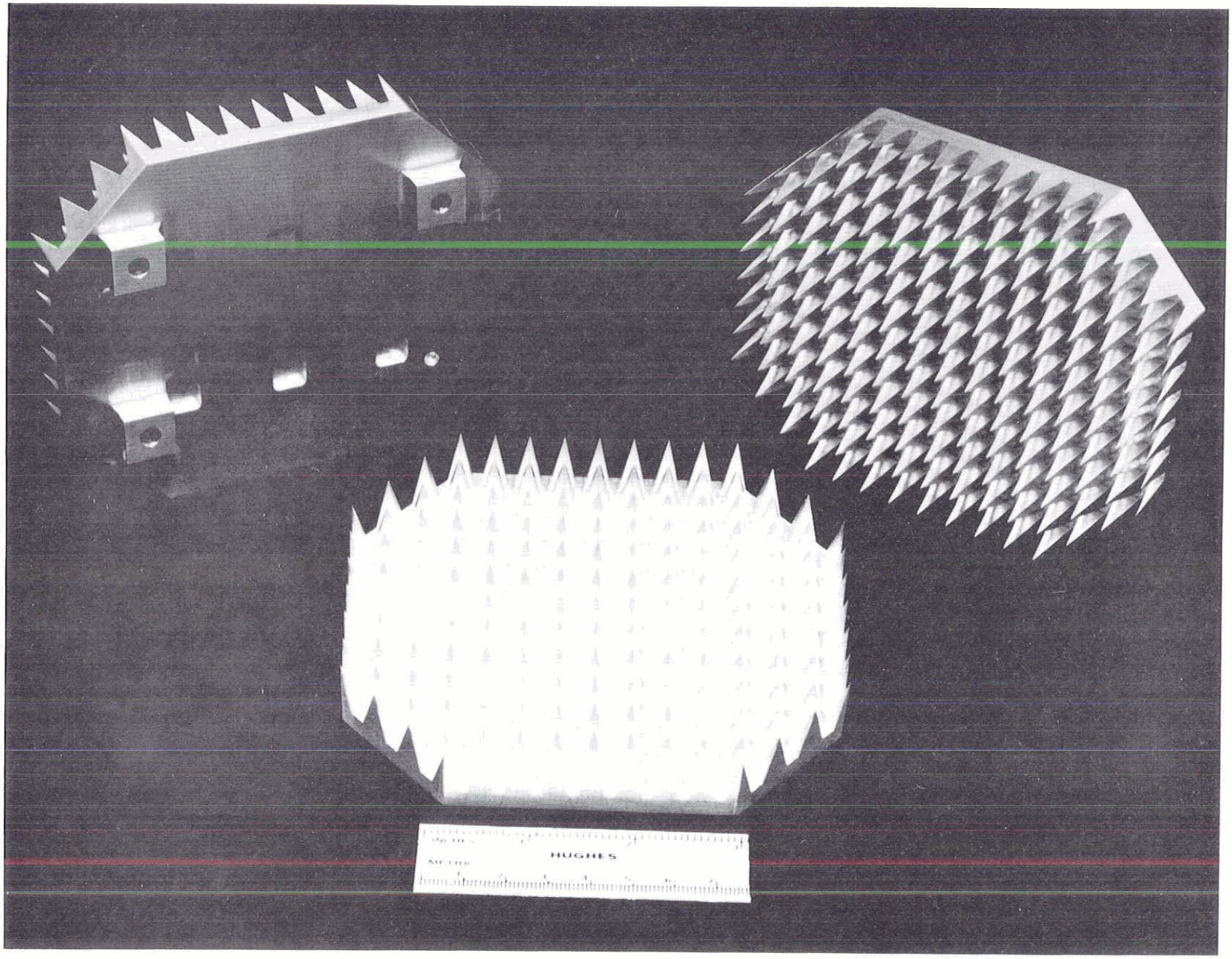

Figure 2.7 SSM/I Hot Load Calibration Target

SCAN A	
SCENE STATIONS/SCAN	128
PIXELS/SCAN	576
SCAN B	
SCENE STATIONS/SCAN	128
PIXELS/SCAN	256
SCENE STATION/ORBIT	404,224
PIXELS/ORBIT	1,313,728

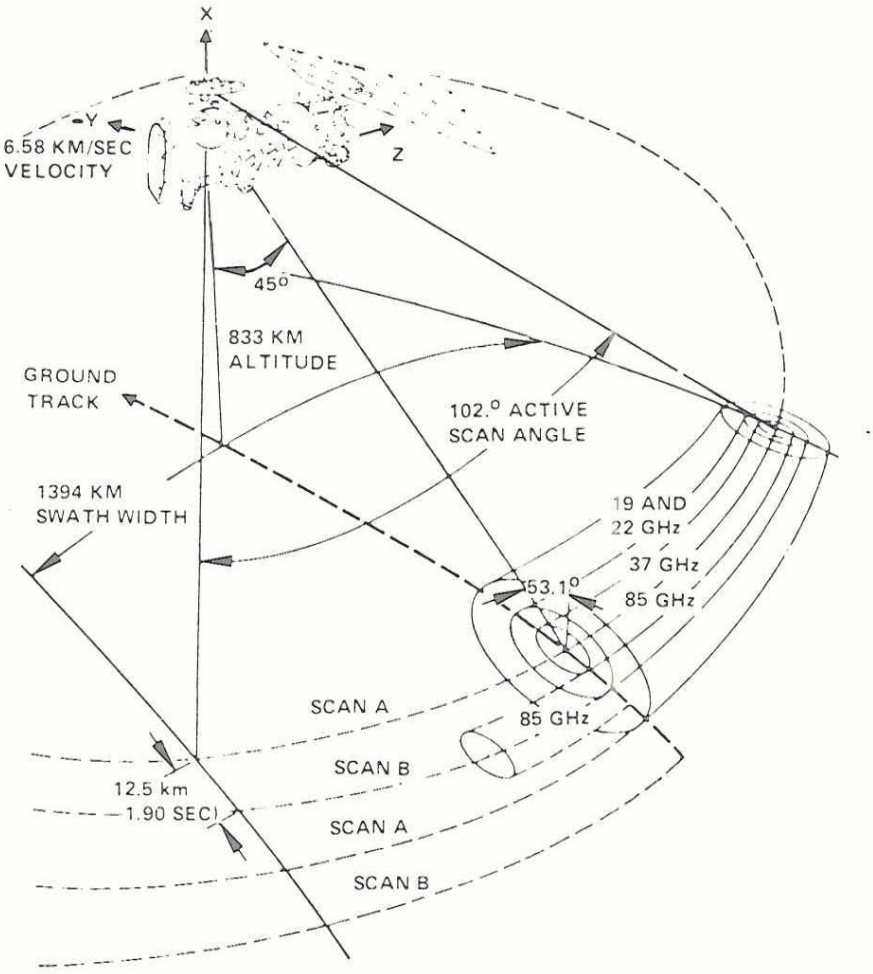

Figure 2.8 SSM/I Scan Geometry

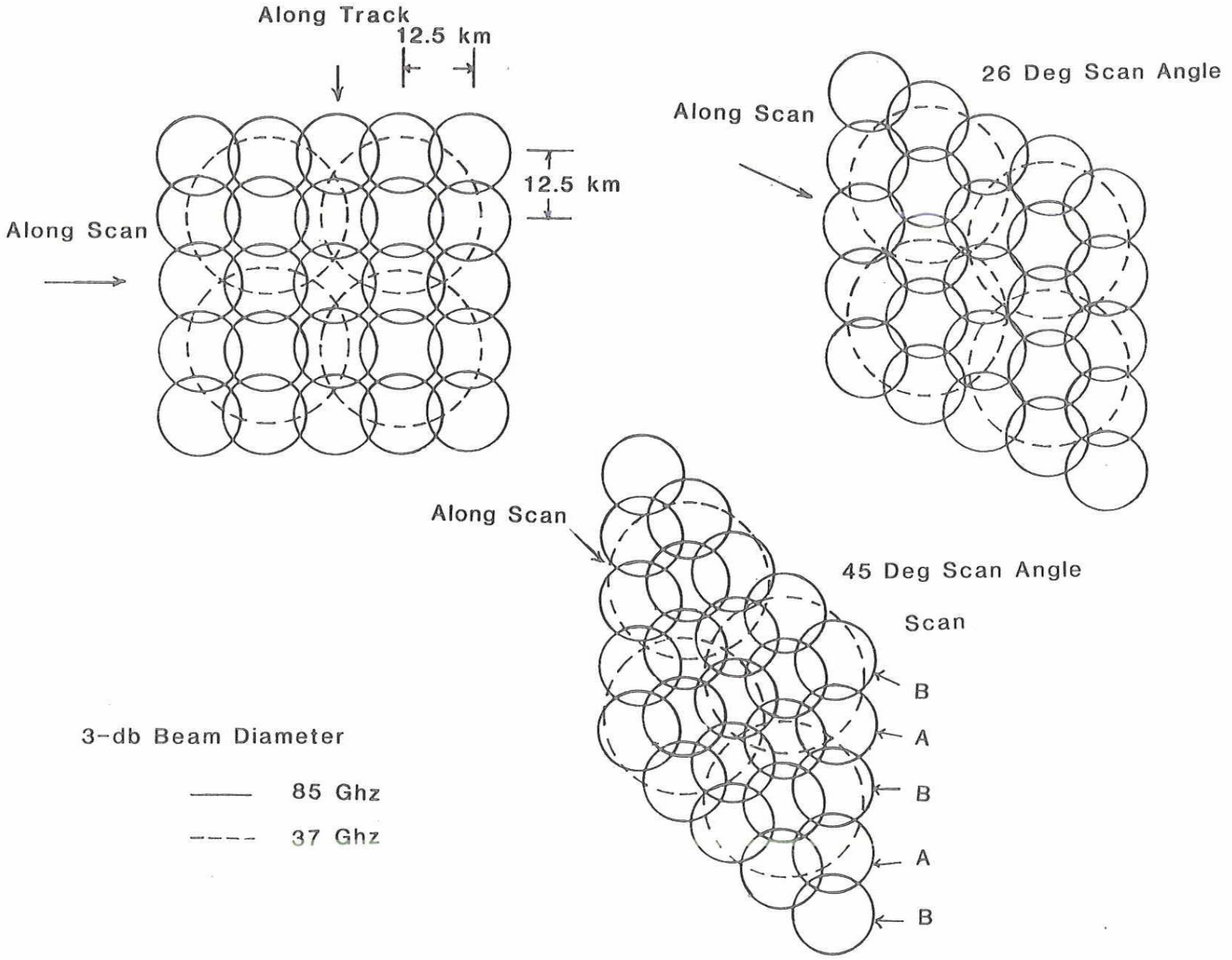

Figure 2.9 Spatial Sampling

2.3 ANTENNA BEAM CHARACTERISTICS

Table 2.1 presents measurements of the IFOV 3-dB beamwidths of the secondary radiation patterns as a function of channel frequency and polarization for SSM/I. The data apply to Sensor S/N 002 and are based on antenna pattern measurements which have been averaged over the RF passbands. Similar beamwidths apply to other sensor serial numbers. Since the radiometer integrate-and-dump filter integrates the instantaneous radiometer output over 3.89 msec at 85.5 GHz and 7.95 msec at the remaining channels, an effective field of view (EFOV) may be defined for each sampled radiometer brightness temperature which takes the integration time into account. (As noted earlier, the time between samples is 4.22 msec for 85 GHz and 8.44 msec for 19/22/37 GHz channels which includes both the integration time and time to sample and dump the data.) The EFOV is significantly larger than the IFOV in the cross-track direction (or, H-plane direction) and essentially the same in the along-track direction. Table 2.1 presents the EFOV 3-dB beamwidths next to the IFOV beamwidths. Also shown are the along-track and cross-track dimensions of the EFOV beamwidths when projected onto the earth's surface.

Table 2.1

SSM/I Antenna Beamwidths
(S/N 002)

Channel Frequency (GHz)	Pol. V/H	IF Pass-Band (MHz)	Beamwidth (Deg) E-Plane IFOV	H-Plane IFOV	H-Plane EFOV	EFOV on Earth Surface (km) Along-Track	Cross-Track
19.35	V	10-250	1.86	1.87	1.93	69	43
19.35	H	10-250	1.88	1.87	1.93	69	43
22.235	V	10-250	1.60	1.65	1.83	60	40
37.0	V	100-1000	1.00	1.10	1.27	37	28
37.0	H	100-1000	1.00	1.10	1.31	37	29
85.5	V	100-1500	0.41	0.43	0.60	15	13
85.5	H	100-1500	0.42	0.45	0.60	15	13

Another important antenna performance parameter is the main beam efficiency and is defined as the percentage of energy received within the main beam of the far-field radiation pattern in the desired polarization within the prescribed bandwidth to the total energy received. The far-field antenna pattern is the combination of the radiation patterns of the feedhorn antenna and the parabolic reflector antenna. Table 2.2 presents antenna beam efficiencies as a function of channel frequency and polarization for instrument S/N 002. The data are based on antenna range measurements of both the feedhorn patterns and the radiation patterns from the reflector. The antenna sidelobe column denotes the percentage energy

lying outside 2.5 times the 3-dB beamwidth of the far-field pattern when normalized to the sum of the co- and cross-polarization energies. The cross-polarization column is the percentage of cross-polarized energy appearing at the output of the feedhorn and includes contributions from both the reflector and feedhorn. The feedhorn spillover factor refers to the loss of the energy in the far-field pattern not intercepted by the reflector. Thus the feedhorn spillover loss is a multiplicative factor in the computation of beam efficiency. Slightly different values of sidelobe and cross-polarization energies occur for the other sensor serial numbers with beam efficiencies all greater than 90%. The beam efficiencies in the table may be improved with an antenna pattern correction algorithm and is discussed in Section 3.1.

Table 2.2

SSM/I Beam Efficiencies
(S/N 002)

Channel Frequency (GHz)	Pol. V/H	Antenna Sidelobe (%)	Cross-Polarization (%)	Feedhorn Spillover Factor	Beam Efficiency (%)
19.35	V	0.8	0.35	0.969	96.1
19.35	H	0.4	0.30	0.969	96.5
22.235	V	2.0	0.65	0.974	95.5
37.0	V	7.3	1.80	0.986	91.4
37.0	H	4.7	1.20	0.986	94.0
85.5	V	5.7	0.60	0.988	93.2
85.5	H	7.8	1.40	0.988	91.1

Although not shown in Table 2.2, the loss in beam efficiency due to small scale surface roughness of the reflector surface is very small at all frequencies. The rms surface roughness is less than 1.0 mils, and translates to a loss of 0.8% at 85.5 GHz and less than 0.15% at the remaining frequencies.

2.4 REFERENCES

[1] Hollinger, J.P., R.C. Lo, G.A. Poe, R. Savage, and J. Peirce, SSM/I User's Guide, Naval Research Laboratory, Washington, DC 20375-5000, 14 September 1987.

3.0 RADIOMETRIC CALIBRATION DESCRIPTION

3.1 INTRODUCTION

The absolute brightness temperature of the scene (T_B) incident upon the antenna is received and spatially filtered by the antenna to produce an effective input signal or antenna temperature (T_A) at the input of the feedhorn antenna. Section 3.2 presents the overall radiometer calibration algorithm used to convert the measured output of the A/D converter into absolutely calibrated antenna temperatures which are contained in the temperature data record (TDR) file. To obtain an estimate of T_B from T_A it is necessary to apply an antenna pattern correction (APC) to correct for spurious energy received in the antenna side lobes, cross-polarization coupling and feedhorn spillover loss. The estimates of the main-beam brightness temperature derived from T_A using the APC are contained in the sensor data record (SDR) file. The APC algorithm is discussed in Section 3.3.

3.2 ANTENNA TEMPERATURE CALIBRATION

The antenna temperature of the SSM/I is calibrated each scan from the input to the feedhorn through the output of the A/D converter. This is accomplished by passing the feedhorn beneath two fixed calibration reference targets: a hot-load black-body radiator at a nominal temperature of 250K and a small calibration reflector which reflects the cold cosmic background radiation of 3K into the feedhorn field-of-view. The calibration error of the hot load was determined pre-launch by comparison with a variable precision calibration reference target over a range of 100K to 375K during thermal vacuum calibration. These tests show the error of the in-orbit hot load to be $\leq$0.05K rms with no systematic calibration error detectable.

The radiometric temperature of the cosmic background is consistent with a blackbody radiator at 3.0°K. The SSM/I calibration reflector is designed to reflect the cold cosmic background into the feedhorn and minimize the possible reception of extraneous energy from the spacecraft, the earth, and other undesired sources of radiation. An analysis of the calibration reflector antenna patterns when the SSM/I is in the calibration position reveals that the reception of earth and spacecraft radiation is extremely small; less than a few tenths of a degree. Figure 3.1 shows the broadest calibration antenna patterns which occur at 19.35 GHz. Note that essentially all of the antenna pattern energy lies within ~28° of boresight, except for the feedhorn spillover energy. The spillover energy views the cosmic background since the SSM/I is located on top of the spacecraft and since the calibration reflector completely occults the primary reflector during the calibration measurements. Thus it is believed that the SSM/I calibration reflector provides a clear view of the cosmic background to the feedhorn and hence provides a highly accurate blackbody calibration reference at 3.0°K.

At measurement temperatures equal to the hot load and cosmic background calibration references, the calibration uncertainty is simply

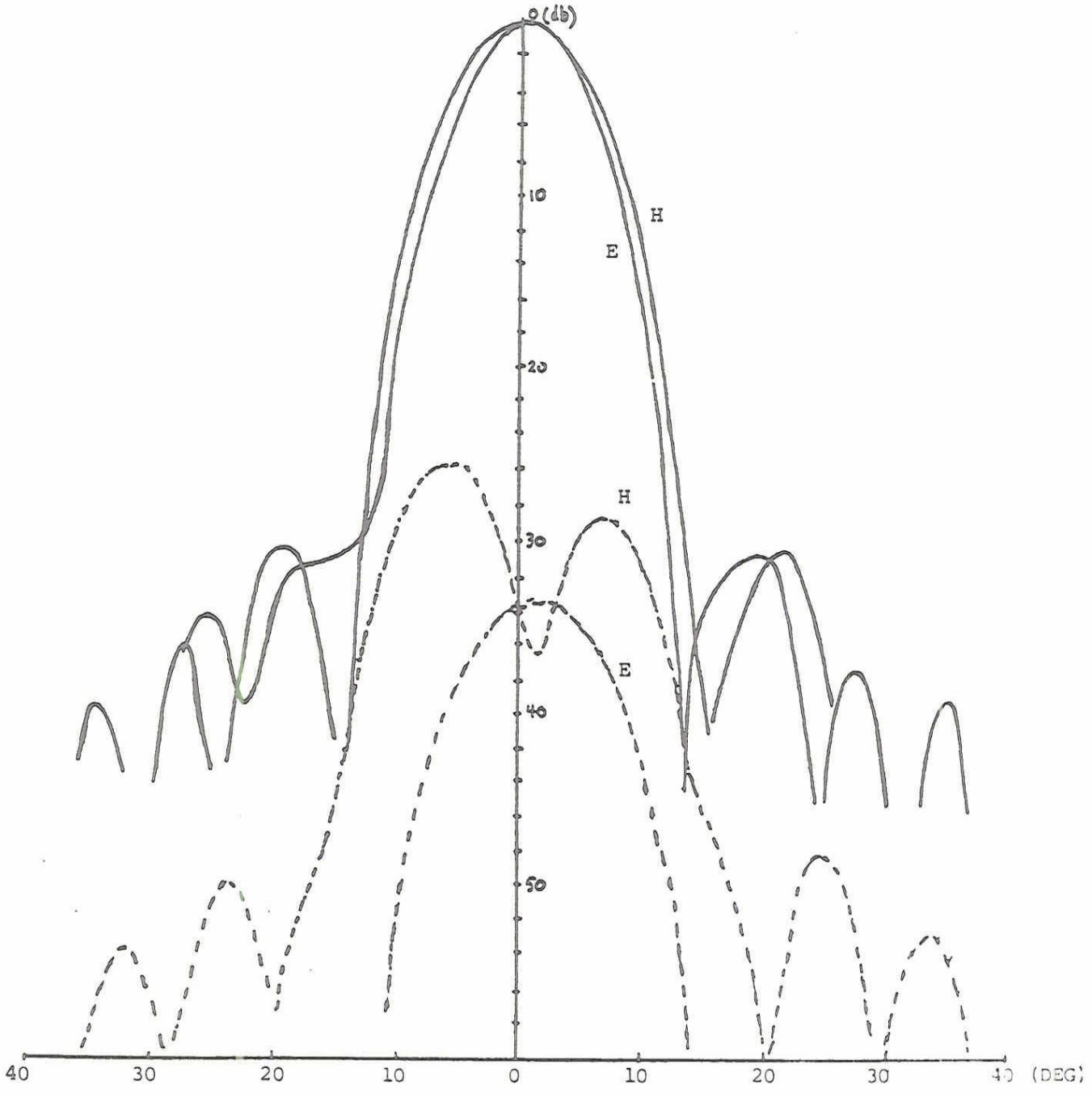

Figure 3.1 Antenna Patterns of E and H Plane of Cold Calibration Reflector at 19.35 GHz Vertical Polarization (—— Co, ---- Cross Pol)

the accuracy of the reference. At intermediate temperatures, radiometer nonlinearity and calibration reference temperature errors contribute to the total uncertainty with the errors weighted according to the temperature difference between the input and the calibration references. These errors are included in the total system calibration accuracy results obtained during the thermal vacuum calibration tests. A linear function is used to model the radiometer transfer function which relate the digitized output voltage to the temperature incident at the feedhorn. Based on thermal/vacuum calibration measurements, this model results in a maximum radiometer error less than ±1K. (Reference [1], pages 35-37). Letting V_H and V_C denote the A/D output voltages associated with viewing the hot-load and cosmic background brightness temperatures, then the brightness temperature of the scene incident at the feedhorn T_A is expressed in terms of the measured output voltage V_S at time t by

$$T_A = \hat{T}_C + (\hat{T}_H - \hat{T}_C) \frac{\bar{V}_S - \hat{V}_C}{\hat{V}_H - \hat{V}_C}$$

where

$\hat{V}_H$ = estimate of the radiometer calibration voltage of the hot-load at time t which is based on the set of measured hot-load calibration voltages

$\hat{V}_C$ = estimate of the radiometer calibration voltage of the cosmic background at time t which is based on the set of measured cosmic-background calibration voltages.

$\hat{T}_H$ = estimate of the effective brightness temperature of the hot-load at time t from the set of measured temperatures of the hot-load.

$\hat{T}_C$ = estimate of the effective brightness temperature seen by the feedhorn when viewing the calibration reflector.

The bar on V_S denote the time average over the radiometer integration time. Figure 3.2 presents a time series of calibration and scene voltages that occur each scan.

Five samples of V_{Hi} and V_{Cj} (i = 1,...5) are taken each scan and averaged to reduce the sensor noise in the estimates V_H and V_C

$$\hat{V}_H = \frac{1}{5}\sum_{i=1}^{5} V_{Hi}$$

$$\hat{V}_C = \frac{1}{5}\sum_{i=1}^{5} V_{Ci}$$

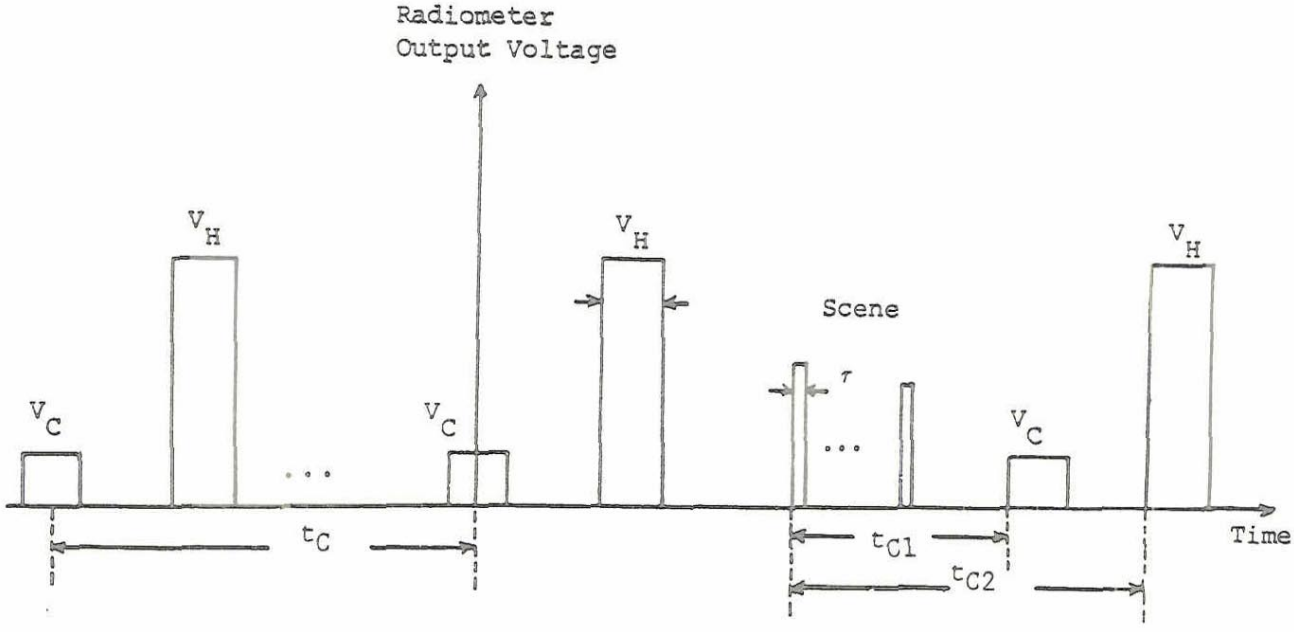

τ = Radiometer integration times:

3.89 msec at 85 GHz

7.95 msec at 19/22/37 GHz

t_C = Calibration period 1.9 sec

V_C = Calibration voltage of cosmic background

V_H = Calibration voltage of hot load

t_{C1} = Time from start of scene voltages to cold calibration

0.925 sec (175 Deg rotation)

t_{C2} = Time from start of scene voltages to hot calibration

1.376 sec (260 Deg rotation)

$\hat{T}_C$ = Effective radiometric temperature of cold calibration target

$\hat{T}_H$ = Effective radiometric temperature of hot calibration target

Figure 3.2 Sequence of Calibration and Scene Measurements

Three high resolution temperature sensors are used to estimate the average surface temperature of the hot-load

$$\overline{T}_H = \frac{\sum_{i=1}^{3} x_i T_{Hi}}{\sum_{i=1}^{3} x_i}$$

where x_i is either 1 or 0 depending on whether the temperature sensor is functioning properly or not. This temperature is used for all frequencies and polarizations.

To account for radiative coupling between the hot-load and the top plate of the rotating drum assembly which faces the hot-load when not being viewed during calibration, a correction is applied to the average hot-load temperature T_H

$$\hat{T}_H = \overline{T}_H + \alpha\left(T_P - \overline{T}_H\right)$$

where

$\hat{T}_H$ = effective hot-load temperature
α = empirical correction determined from thermal-vacuum calibration
T_P = temperature of the plate facing the hot-load.

Based on calibration data taken during thermal-vacuum testing α = 0.01. A temperature sensor measures T_P.

The effective radiometric temperature of the cosmic background seen by the feedhorn when viewing the calibration reflector may be expressed as

$$\hat{T}_C(\hat{k}) = \oint_{4\pi} d\Omega' G\left(\hat{k}, \hat{k}'\right) T_{inc}\left(\hat{k}'\right)$$

where G is the far-field antenna power pattern which weights the angular distribution of the brightness temperature T_{inc} incident in direction k' on the antenna (reflection and feedhorn) when the antenna is pointed in direction k. As noted earlier by appropriate design of the calibration reflector and selection of calibration regions, $T_{inc} \simeq T_{cosmic}$ where T_{cosmic} is the radiometric temperature of the cosmic background which is consistent with a blackbody radiator at 3.0°K. Analysis of the antenna pattern, G, shows that the effects of energy received from the spacecraft and earth are extremely small, less than 0.1 - 0.2K. Thus, T_c may be determined solely on the basis of the radiometer temperature of the cosmic background:

Frequency (GHz)	T_c (K)
19.35 - 22.235	2.7
37.0	2.8
85.5	3.2

The values presented include a correction to the Rayleigh-Jeans approximation which becomes important for very cold radiators at mm-wave frequencies.

The calibration parameters T_H, V_H, V_C are up-dated each scan to compute the scene brightness temperatures T_A before the next calibration occurs. Since, as shown in Section 4, the radiometers exhibit extremely good stability over a number of calibration data sets, it is possible to average T_H, V_H, and V_C over many scans to reduce the effects of sensor noise. This is not done at present but is discussed in Section 4 and a recommendation is made to increase the number of scans in the average for this sensor and those launched in the future.

3.3 ANTENNA PATTERN CORRECTION

3.3.1 Background

The antenna temperature T_A (i.e. the TDR of Section 3.2) may be expressed in terms of an integral of the scene brightness temperature distribution T_S incident on the antenna reflector and the effective co- and cross-polarized far-field antenna power patterns. For channel center frequency, ν_o, polarization, p, and with the antenna pointed in direction k, T_A may be written as

$$T_A(p,\hat{k}) = \int_{Earth} d\Omega' \left[G_{pv}(\hat{k},\hat{k}') T_S(v,\hat{k}') + G_{ph}(\hat{k},\hat{k}') T_S(h,\hat{k}') \right] + (1-\eta_p) T_{cosmic}$$

where $G_{pq}(\hat{k},\hat{k}')$ is the effective far-field antenna power pattern which weights the angular distribution of the brightness temperature incident in direction k′ in polarization q when the antenna is pointed in direction k and measuring polarization p.

The term effective identifies the fact that the effects of the radiometer integrate and dump low pass filter are included in G_{pq}. As noted earlier the filter widens the beam in the along scan direction and leaves the beam essentially unaltered in the along track direction.

The vertical or horizontal polarizations as measured on an antenna range are not the same as the local vertical and horizontal polarizations on the earth's surface over the antenna field of view. For narrow antenna beams such as the SSM/I, they may be considered to be the same to an excellent approximation.

The feedhorn spillover factor η_p is defined by the fraction of energy received from the reflector in polarization p to the total energy received by the feedhorn. For clarity the dependence of G_{pq}, T_s, η_p, and T_A on the channel center frequency is not shown but it should be understood that G_{pq} and η_p are averaged over the receiver passband.

Figure 3.3 presents the geometry of the integration variables: the angular integration $d\Omega'$ is taken over the earth field of view and T_{cosmic} is the brightness temperature of the cosmic background. When p = q, G_{pp} is the defined as the co-polarized patterns (i.e., G_{vv}, G_{hh}) and, when $p \neq q$, G_{pq} is defined as the cross-polarization patterns (i.e., G_{vh}, G_{hv}). In practice, G_{pq} and η_p are determined from antenna pattern measurements over 4π steradians on an antenna range. η_p is essentially the integrated feedhorn pattern over the solid angle subtended by the reflector.

Proper normalization requires for p = v or h polarizations:

$$\int_{Earth} d\Omega' \left[G_{pv}\left(\hat{k}, \hat{k}'\right) + G_{ph}\left(\hat{k}, \hat{k}'\right) \right] = \eta_p$$

The above expression for T_A assumes that the time variation of the scene brightness temperature over the integration time T_s is negligible and is a valid approximation for the SSM/I.

In principle, the accuracy of the scene brightness temperatures incident on the reflector T_s may be improved by making antenna pattern corrections (APC). These corrections are intended to remove the effects of:

(a) Feedhorn spillover loss η_p
(b) Cross-polarization coupling G_{pq} $(p \neq q)$
(c) Sidelobes contributions of G_{pp}.

For convenience corrections (a) and (b) are denoted as Level 1 and correction (c) as Level 2. Level 1 corrections are applied first to T_A and can be inverted, if desired, to obtain the original temperatures T_A. In general, Level 2 corrections cannot be inverted and usually require significantly more data processing than Level 1.

In addition, the benefits of Level 2 corrections are considerably more difficult to evaluate since, as will be discussed below, they depend on the spatial variations of T_s over the sidelobe regions of G_{pp}. Each of the corrections are discussed separately below. For clarity the corrections are presented for the vertical polarization p = v. Similar results apply for p = h.

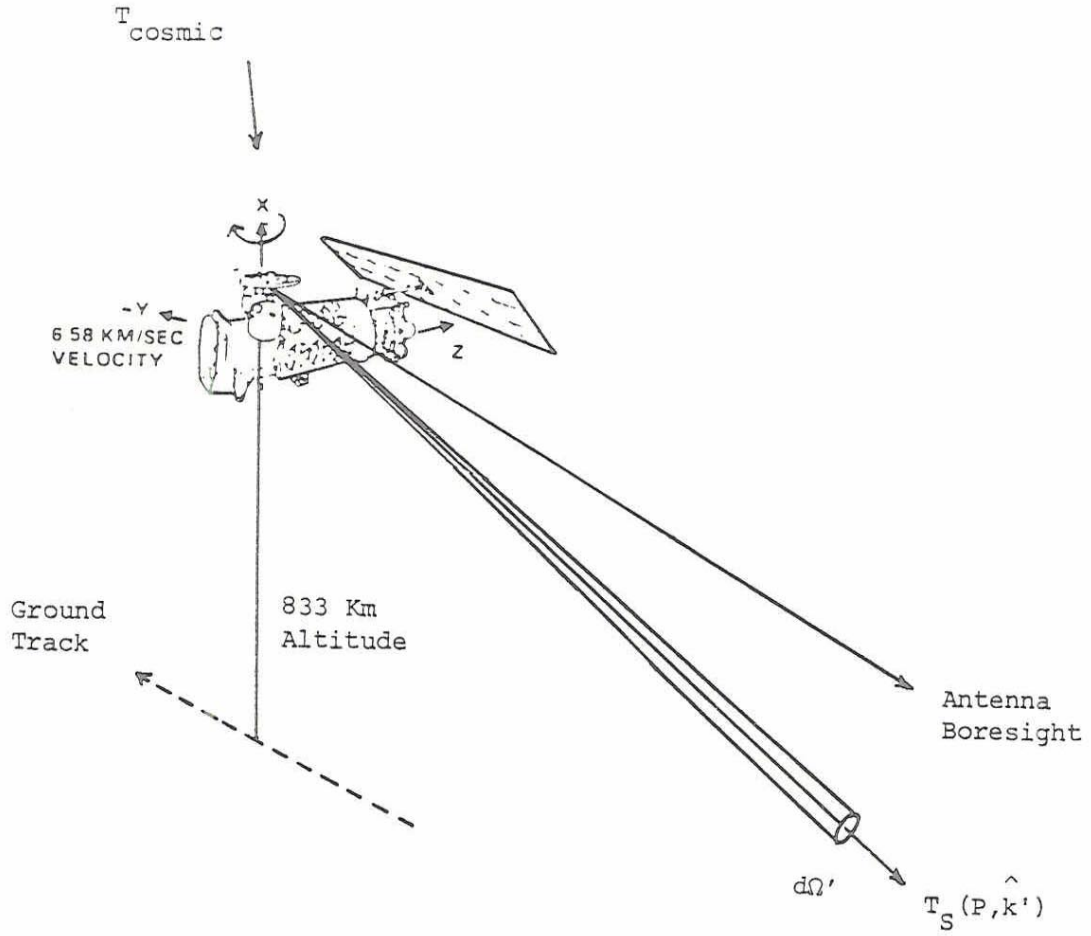

$$T_A(p,\hat{k}) = \int_{Earth} d\Omega' \left[G_{pv}(\hat{k},\hat{k}') T_S(v,\hat{k}') + G_{ph}(\hat{k},\hat{k}') T_S(h,\hat{k}') \right] + (1-\eta_p) T_{cosmic}$$

where

η_p = Feedhorn spillover factor

G_{pq} = Far-field antenna pattern

T_S = Scene brightness temperature incident on antenna

v,h = Vertical or horizontal polarizations

Figure 3.3 Geometry for Antenna Temperature Definition

3.3.2 Level 1 Corrections

Based on the antenna pattern measurements and the expression for T_A, the correction for feedhorn spillover loss and cross-polarization coupling is written as

$$\hat{T}_S(v,\hat{k}) = \frac{1}{\eta_v(1-b_v)}\left[\hat{T}_A(v,\hat{k}) - b_v\hat{T}_A(h,\hat{k})\right]$$

where $\hat{T}_A(v,\hat{k})$ and $\hat{T}_A(h,\hat{k})$ are the antenna temperatures (i.e. TDRs) for the vertical and horizontal polarizations for antenna boresight direction k. The justification for this algorithm is based on the fact that the spillover factor η_p is essentially the same for the v- and h-polarization at each frequency and that the cross polarization coupling occurs primarily within the mainbeam of G_{pp}. Note that the term b_v includes contributions from all sources. Also note that the form of the correction uses the fact that η_v is close to unity for all channels and hence the cosmic background contribution may be neglected.

Since the horizontally polarized brightness temperature is not measured for the 22.235 GHz channel, it is estimated using the horizontally polarized temperature at 19.35 GHz:

$$\hat{T}_A(22.235,\ h,\hat{k}) = 96.6 + 0.653\ \hat{T}_A\ (19.35,\ h,\hat{k})$$

This relationship is derived by correlating simulated radiometer data at the two channels for a wide range of environmental conditions over land, sea, and ice surfaces.

The antenna pattern portion of b_v is a measure of the integrated cross polarized coupling for the v-polarization and is selected on the basis of eliminating the cross-polarization coupling when the vertical and horizontal scene temperatures are uniform but not necessarily equal over the antenna field-of-view.

$$b_V = \frac{\int_{Earth} d\Omega' G_{vh}}{\int_{Earth} d\Omega' G_{hh}}$$

Based on antenna range measurements and computations to account for the action of the radiometer integrate and dump low pass filter Table 3.1 presents η_p and b_p for the SSM/I instrument S/N 002 currently in orbit on the DMSP F-8 satellite.

The accuracy of the algorithm to remove cross polarization coupling depends on the spatial variability of the incident cross-polarized scene brightness temperature. For a temperature distribution essentially uniform over the main beam, the correction is extremely accurate. The

accuracy degrades slightly in the event significant cross-polarized variations occur within the main beam.

Table 3.1 Coefficients for Feedhorn Spillover and Cross Polarization Coupling Corrections (S/N 002)

Center Frequency (GHz)	Polarization p = v/h	η_p	b_p
19.35	v	0.969	0.00473
	h	0.969	0.00415
22.235	v	0.974	0.01070
37.0	v	0.986	0.02170
	h	0.986	0.02612
85.5	v	0.988	0.01383
	h	0.988	0.01947

The accuracy of the algorithm to remove the feedhorn spillover loss depends on the accuracy of the spillover loss factor η_p which is currently obtained by integrating the feedhorn antenna pattern over the solid angle subtended by the reflector. Accurate knowledge of η_p is important since a 1% error in η_p can result in a 2°K error in the estimate of T_s.

3.3.3 Level 2 Correction

The task of attempting to improve the spatial resolution of G_{pp}, i.e., correcting for the imperfect spatial filtering of the antenna, or, more generally of inverting the integral relation between measured T_A and the up-welling scene temperature T_s contains mathematical features common to a large number of remote sensing problems. In particular the problem may be shown to be mathematically equivalent to the problem of inverting microwave or infrared measurements to obtain atmospheric temperature profiles in remote sounding data [2]. A great deal of literature published on the latter subject has shown that it is not desirable to attempt to obtain fine details in the sounding because of amplification of noise in the sensor data. This arises from the numerical instability of the Fredholm integral equation of the first kind which must be solved and the attendant amplification of errors that occurs in the inversion process.

In view of this situation, it is desirable to restrict the Level 2 algorithm for the SSM/I which minimizes the antenna sidelobe energy contributions outside the main beam and, if possible, not significantly alter the antenna pattern within the mainbeam. To this end, the Level 2 algorithm considered herein estimates the average scene brightness temperature over the main beam weighted by the antenna gain. Other

estimates, such as the true spatial average over the main beam, could be used but the discontinuity at the edge of the main beam introduces significant amplification of sensor noise.

The current Level 2 algorithm is expressed as a linear combination of antenna temperature measurements T_A in the immediate vicinity of the measured antenna temperature to be corrected. Other approaches for Level 2 corrections have been investigated [3]-[6] but require extensive data processing, which is not available for the SSM/I, to achieve only modest improvements in T_A. The restriction of antenna temperature samples to a small region surrounding the temperature to be corrected is not severe since, as shown by the antenna pattern measurements, essentially all of the sidelobe energies lies within the region defined by the set of 5 x 5 neighboring samples of brightness temperature surrounding the temperature to be corrected.

To reduce energy contributions in the sidelobes, antenna temperature samples are selected which lie outside the main beam. Furthermore, since the spatial samples of brightness temperature overlap at the 3-dB points (except at 19.35 and 22.235 GHz), the samples in the algorithm are separated by approximately one sample to avoid significant overlapping of the main beams of the measurement samples.

The current SSM/I Level 2 APC software module permits a maximum of four antenna temperature samples to be employed in a 5 x 5 matrix of neighboring samples and the selection may be changed in five angular sections across the scan as shown in Figure 3.4. Following the rationale discussed above, Figure 3.5 shows a reasonable selection of antenna temperature samples which may be used in the Level 2 APC as shaded for several positions across the scan for the 85 GHz channels. The circles indicate 3 dB contours. A similar geometry applies to the 37 GHz channels.

Due to the extremely high beam efficiencies achieved for the 19.35 and 22.235 GHz antenna patterns, little change occurs in the antenna temperature when performing Level 2 corrections at these frequencies. In view of this fact Level 2 corrections are not performed for these channels. The improvement in main beam efficiency is incorporated into the Level 1 correction which uses only the co- and cross-polarized central measurement samples.

To determine the relative merit of the Level 2 APC for 37 and 85 GHz channels the APC is written as

$$\hat{T}_S(v,\hat{k}) = a_o\left[\hat{T}_A(v,\hat{k}) - \sum_{n=1}^{4} a_n \hat{T}_A(v,\hat{k}_n)\right]$$

where $\hat{k}_n$ define the antenna bore-sight directions for the shaded beams in Figure 3.5.

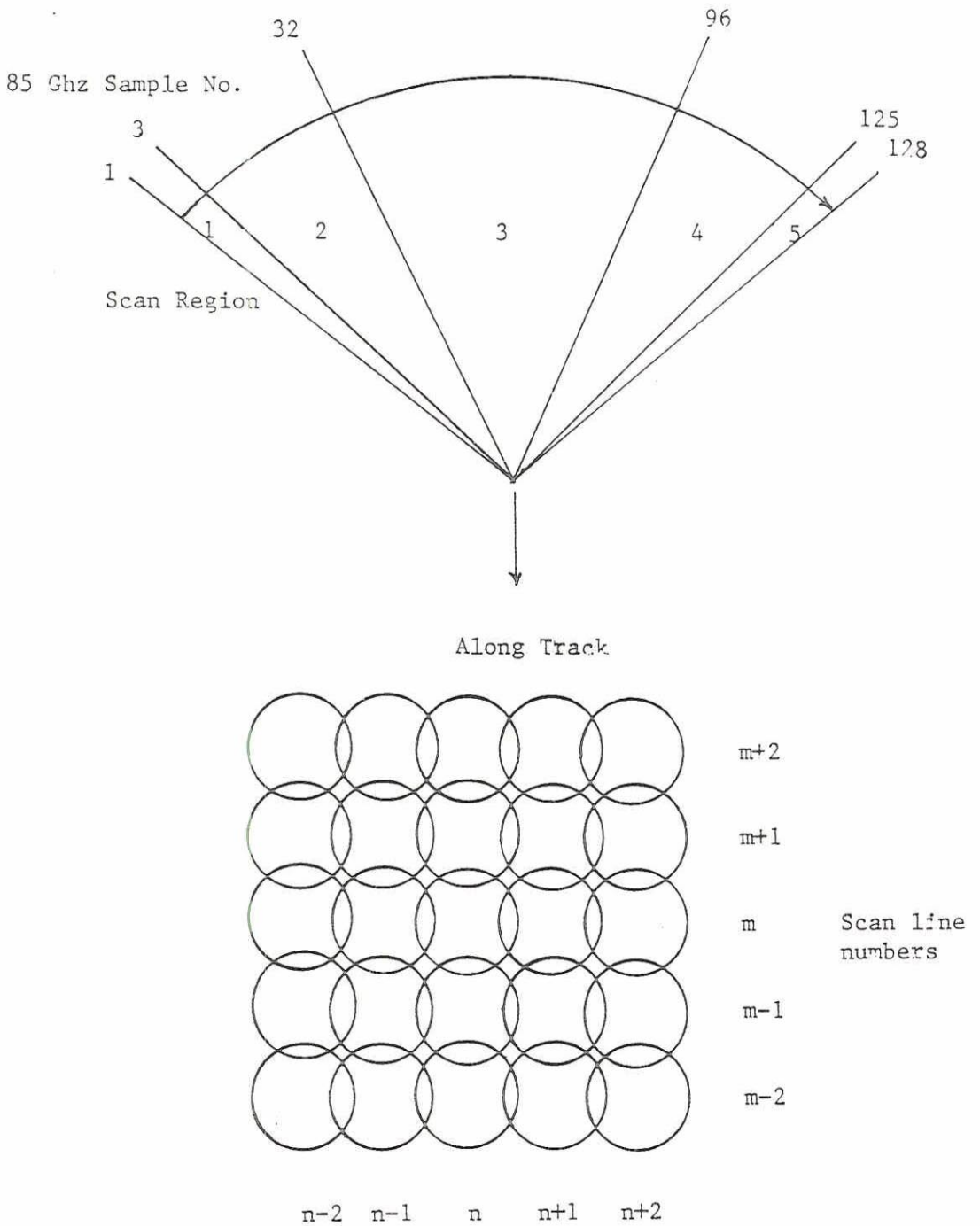

FIGURE 3.4 SCAN REGIONS TO VARY A_N AND SELECTION OF SAMPLES IN LEVEL 2 APC

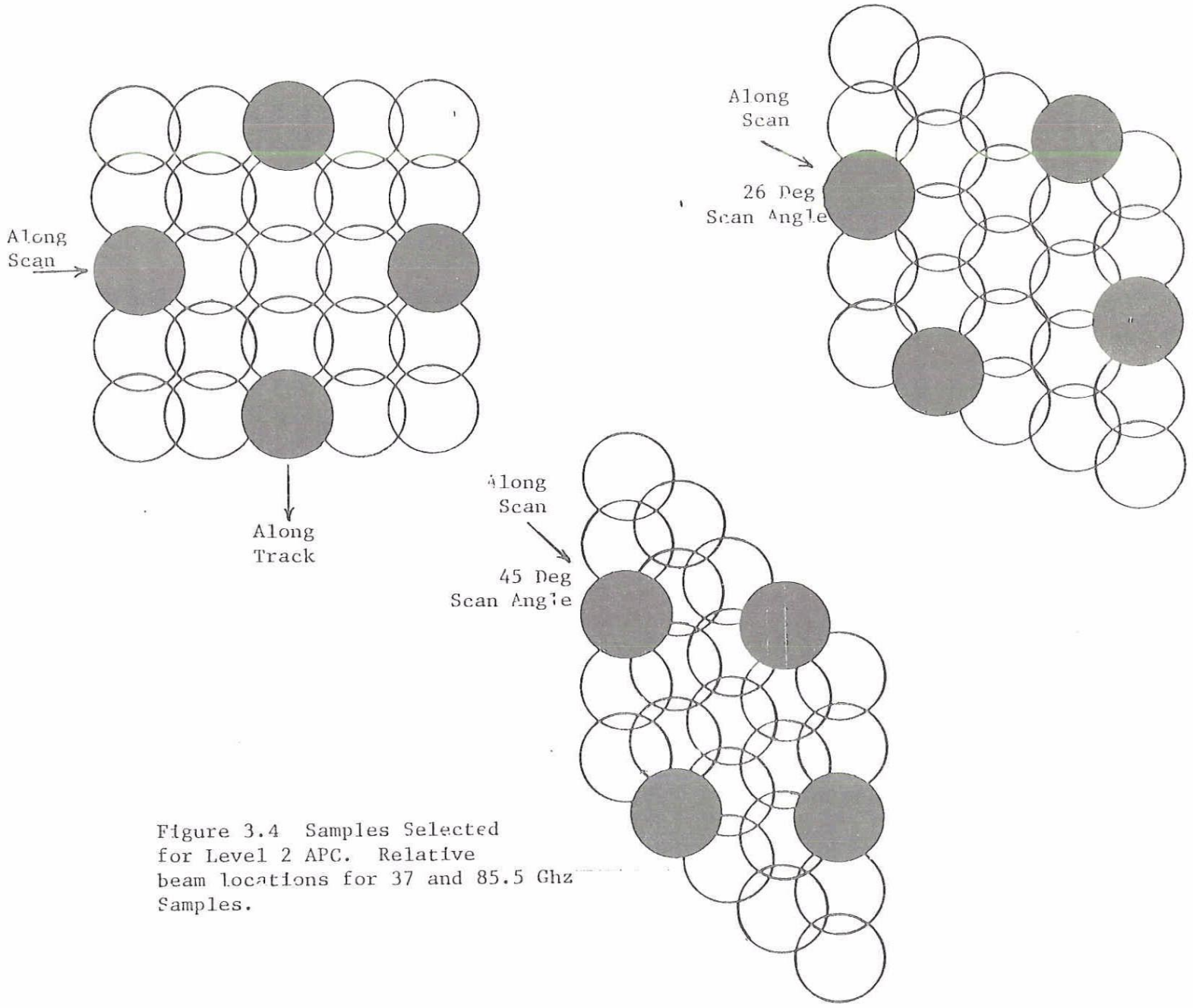

Figure 3.4 Samples Selected for Level 2 APC. Relative beam locations for 37 and 85.5 Ghz Samples.

FIGURE 3.5 SAMPLES SELECTED FOR LEVEL 2 APC (RELATIVE BEAM POSITIONS FOR 37 AND 85 GHZ SAMPLES)

The selection of the weighting coefficients a_n depends on the spatial distribution of energy lying outside the mainbeam. Qualitatively, a_n is a measure of the sidelobe energy lying within the angular region defined by the mainbeam of the samples selected in Figure 3.4. More precisely, the set a_n may be determined by solving the system of equations which requires the minimization of the integral

$$\int_{MB} d\Omega' \left[\frac{G_{vv}(\hat{k}, \hat{k}')}{c} - \sum_{n=1}^{4} a_n G_{vv}(\hat{k}_n, \hat{k}') \right]^2$$

where

MB = angular region defined by the main beam.

As noted earlier the main beam is defined by 2.5 times the 3 db beamwidth.

The coefficient a_o is determined by noting that proper normalization requires

$$a_o = \frac{1}{1 - \sum_{n=1}^{4} a_n}$$

Table 3.2 presents computations of coefficients $\{a_n\}$ which minimize the above integral over E_c for the set of shaded pixels shown in Figure 3.5. Results are shown for both polarization at 37 and 85 GHz. The scan regions are identified in Figure 3.4.

To test the effectiveness of the current Level 2 correction algorithm a simulated brightness temperature map was generated at 37 and 85 GHz using a scaled NOAA AVHRR IR image over the eastern coast of the United States. The SSM/I antenna patterns were convolved with the IR image in a scan geometry identical to the SSM/I. Although the simulated 37 and 85 GHz images cannot be expected to contain real responses to environmental conditions, they do provide a means to test the effectiveness of the current Level 2 APC. In particular the sharp contrast of the IR land-water boundary allows a stringent test of the Level 2 correction. Further description of the simulated images and general discussion of the APC problem for the SSM/I are available upon request.

The effectiveness of the current Level 2 APC may be viewed by comparing the resultant APC corrected image with a simulated image in which the antenna pattern used to convolve with the IR image has all sidelobe energy removed. If the current Level 2 APC did its job perfectly, the corrected image would be identical to the image generated with antenna patterns having no sidelobe energy. Two errors may be defined:

Table 3.2
Coefficients for Level 2 APC (See Figure 3.4 for Scan Regions)

Scan Region 5: $125 < n \leq 128$

Freq. (GHz)	Pol	a_0	a_1	a_2	a_3	a_4
Scan Line		m	m	m+2	m	m-2
Sample No.		n	n+2	n+1	n-2	n-1
37	V	1.0327	--	--	0.0083	0.0234
	H	1.0300	--	--	0.0146	0.0144
85.5	V	1.0216	--	--	0.0085	0.0126
	H	1.0395	--	--	0.0163	0.0217

Scan Region 4: $96 < n \leq 125$

Scan Line		m	m	m+2	m	m-2
Sample No.		n	n+2	n+1	n-2	n-1
		a_0	a_1	a_2	a_3	a_4
37	V	1.0723	0.0129	0.0228	0.0083	0.0234
	H	1.0623	0.0164	0.0132	0.0146	0.0144
85.5	V	1.0444	0.0080	0.0134	0.0085	0.0126
	H	1.0819	0.0276	0.0101	0.0163	0.0217

Scan Region 3: $32 \leq n \leq 96$

Scan Line		m	m	m+2	m	m-2
Sample No.		n	n+2	n	n-2	n
		a_0	a_1	a_2	a_3	a_5
37	V					
	H					
85.5	V	Same coefficients as Scan Region 2				
	H					

Scan Region 2: $3 \leq n < 32$

Scan Line		m	m	m+2	m	m-2
Sample No.		n	n+2	n-1	n-2	n+1
		a_0	a_1	a_2	a_3	a_4
37	V					
	H					
85.5	V	Same coefficients as Scan Region 2				
	H					

Scan Region 1: $1 \leq n < 3$

Scan Line		m	m	m+2	m	m-2
Sample No.		n	n+2	n-1	n-2	n+1
		a_0	a_1	a_2	a_3	a_4
37	V	1.0377	0.0129	--	--	0.0234
	H	1.0318	0.0164	--	--	0.0144
85.5	V	1.0210	0.0080	--	--	0.0126
	H	1.0519	0.0276	--	--	0.0217

(1) T_B (APC corrected image) - T_B (image with no sidelobe energy)

(2) T_B (uncorrected image) - T_B (image with no sidelobe energy)

Error (1) defines the difference between the brightness temperature resulting from an application of the current Level 2 APC and the brightness temperature associated with a "perfect" antenna pattern having no sidelobe energy outside the mainbeam. Error (2) defines the difference between the original brightness temperature without any APC and the brightness temperature having the "perfect" pattern.

A comparison of errors (1) and (2) provide a measure of the effectiveness of the Level 2 APC. Figures 3.6 and 3.7 present histograms of errors (1) and (2) for Port 5 (37 GHz V-pol) and Port 7 (85 GHz V-pol). The solid line corresponds to error (1) and the dashed line to error (2). The upper histograms in the figures apply to the open ocean where the radiometric variation in the simulated images occur over distances that are large in comparison with the antenna beamwidth. The bottom histograms apply to the transition region associated with land/water boundaries.

The results presented in both figures show in the majority of cases the Level 2 APC offers an improvement in the absolute brightness temperature of the simulated image. However at the same time numerous occasions appear in which the APC actually degrades the radiometric image. This interesting result is apparent in both the transition regions and in the open ocean and suggests that caution must be exercised in applying the current Level 2 APC to SSM/I data. Since the APC coefficients are extremely small, the corrections introduced by the current APC are reasonably small (< 1/2 K). At coastal boundaries however the magnitude of the correction can reach 6 K and unfortunately does not always represent an improvement in the brightness temperature. Clearly further effort is needed to select a suitable Level 2 APC to improve the accuracy of the SSM/I data near coastal boundaries.

3.3.4 Antenna Pattern Matching

A third level antenna pattern correction may be envisioned which would attempt to match the higher resolution beams, e.g., at 85 GHz, to the lower resolution beams, e.g., at 19.35, 22.235, or 37 GHz. This level would be applied to the scene brightness temperatures estimated from the Level 1 and Level 2 APC algorithms presented above. This correction may be viewed in terms of a spatial filter which smoothes the higher resolution sampled brightness temperatures to a level commensurate with the lower resolution data.

One of the simplest filters is to numerically average the set of brightness temperatures whose boresights lie within the coarser 3-dB beam cell. This estimate of the average brightness temperature at 85 GHz over a beam cell that is comparable to the 37 GHz beam may be improved upon using the theory developed by Stogryn [3]. In short this approach permits the determination of a set of coefficients $\{c_n\}$ which are optimum in the sense that

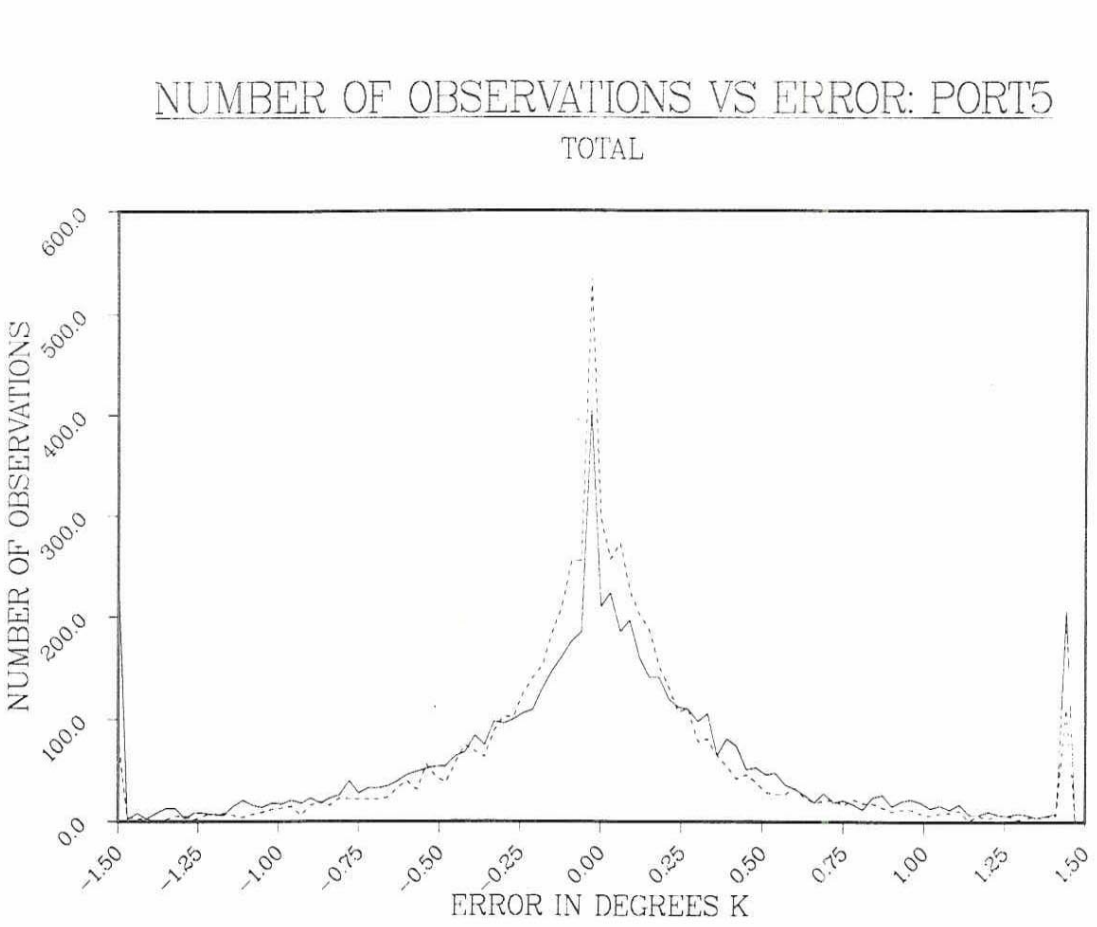

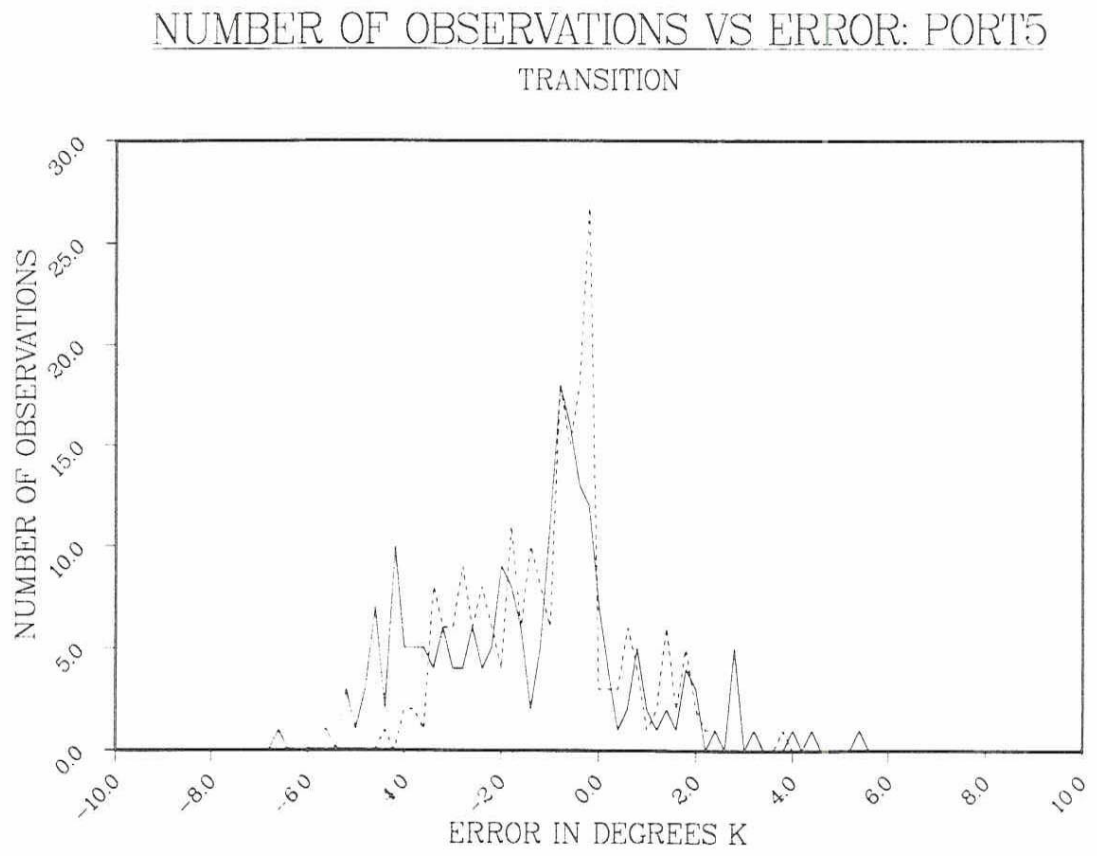

Figure 3.6. Histogram of Level 2 APC Errors at 37 GHz (--- Current APC, --- No APC)

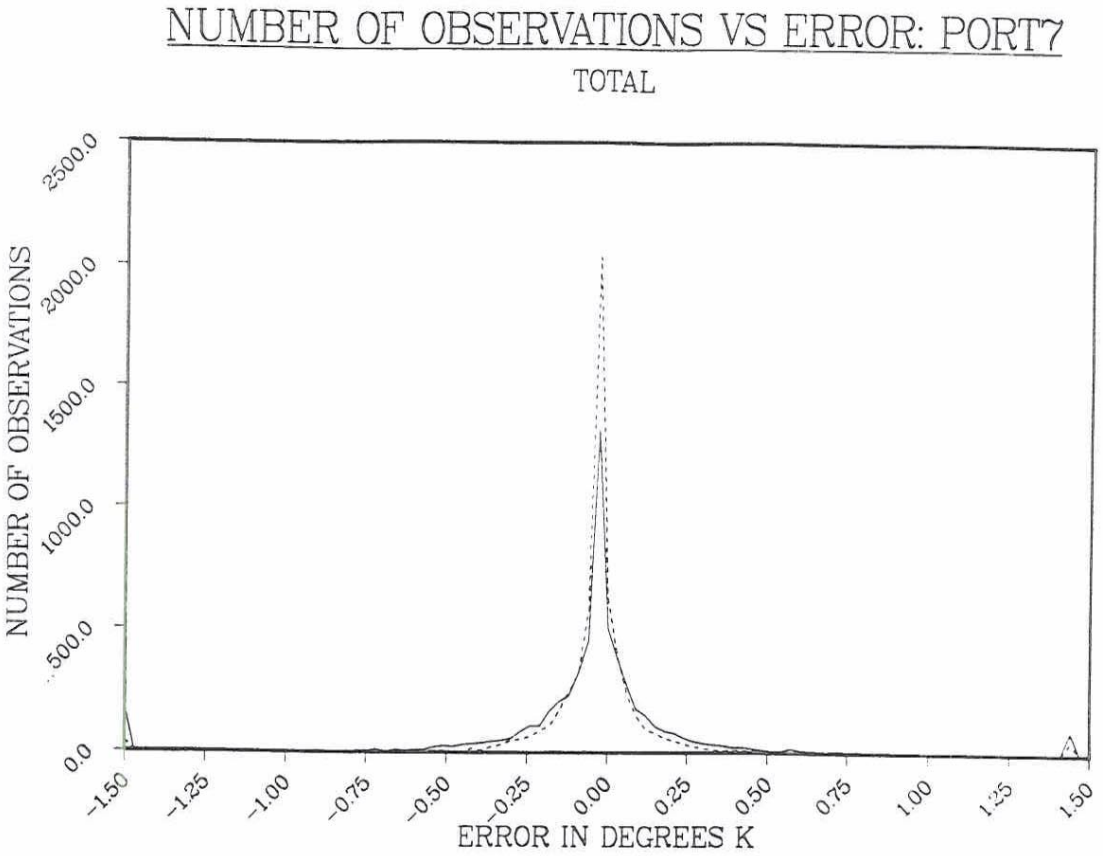

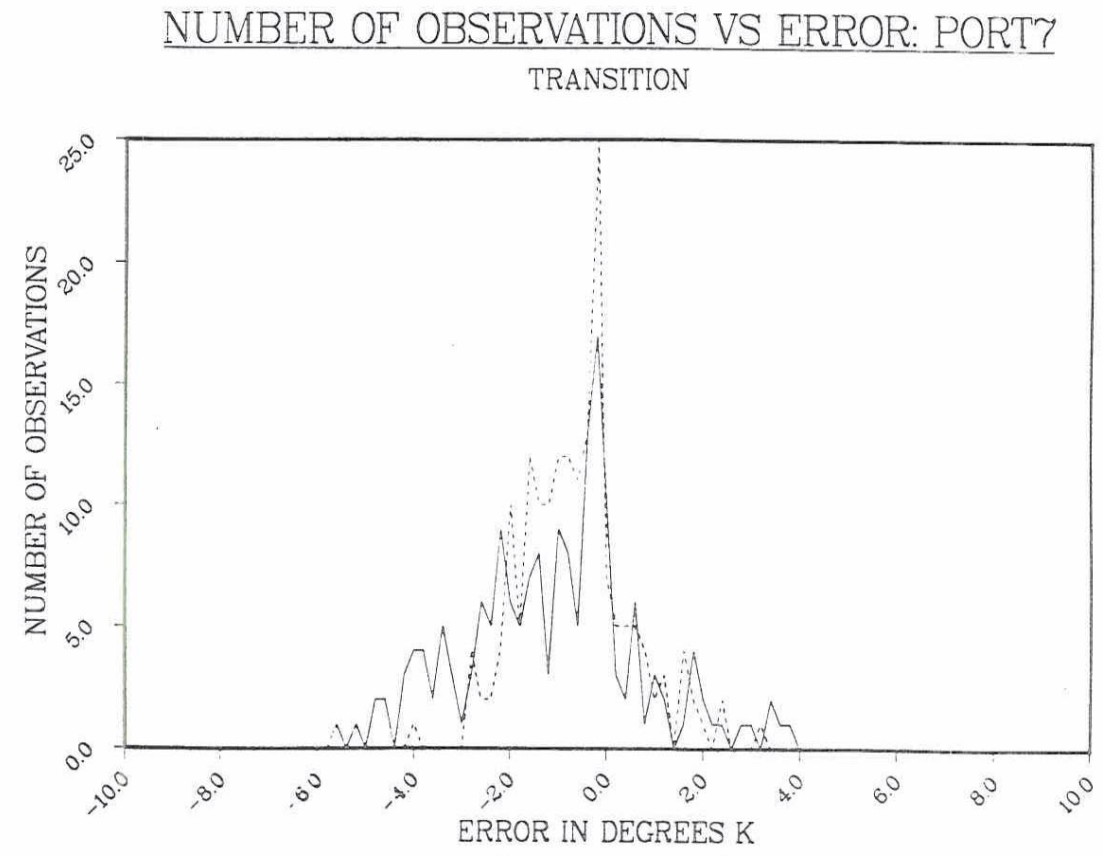

Figure 3.7. Histogram of Level 2 APC Errors at 85 GHz (——Current APC, --- No APC)

$$\int_{Earth} d\Omega' \left[G_{pp}(\nu_1, \hat{k}, \hat{k}') - \sum_{n=1}^{N} c_n G_{pp}(\nu_2, \hat{k}_n, \hat{k}') \right]^2$$

is minimized. The higher resolution antenna patterns at frequency ν_2 have boresights defined by vectors $\hat{k}_n$, n=1, ..., N. The lower resolution antenna pattern at frequency ν_1, has boresight at $\hat{k}$. Once the set $\{\hat{k}_n\}$ is selected, it is straightforward to solve for the set of coefficients $\{c_n\}$ which minimizes the above integral. A constraint is need to insure proper normalization of results

$$\sum_{n=1}^{N} c_n = 1$$

To demonstrate the efficacy of this approach to data smoothing, computations were made to determine the set of coefficients of a 3 x 3 matrix of 37 GHz pixels surrounding a 19 GHz pixel. Figure 3.8 presents the 19 GHz antenna pattern along with the resultant smoothed 37 GHz pattern defined by the sum

$$\sum_{n=1}^{N} c_n G_{pp}(\nu_2, \hat{k}_n, \hat{k}')$$

Computations were made for a scan region near the SSM/I ground-track and the results are presented in terms of distance on the surface of the earth. Note that the smoothed 37 GHz patterns are in remarkably good agreement with the 19 GHz patterns with the exception of the region where the antenna pattern is 30 db below the maximum gain. Similar results were obtained for the intercardinal pattern cuts in this example. The values of the coefficients $\{c_n\}$ varies somewhat across the SSM/I scan, but, in all cases studied using at least a 3 x 3 array, the resultant smoothed patterns are similar to those of Figure 3.8.

Similar computations were made to smooth the 85 GHz data to the resolution of the 37 GHz data. In this case a 5 x 5 array of 85 GHz pixels surrounding a 37 GHz pixel near the ground track was used. Figure 3.9 presents the 37 GHz antenna pattern and the resultant smoothed 85 GHz pattern. Again, good agreement occurs in the H-Plane cut (i.e. in the along scan direction) but appreciable disagreement occurs in the E-Plane cut (i.e., in the along track direction) when the pattern power lies 7 dB below the peak. Since the other patterns (i.e. the intercardinal cuts) gave results which closely resembled the results of the H-Plane cut, the disagreement in the single E-Plane cut is not expected to introduce an appreciable effect in the smoothed brightness temperature data. As in the case of matching the 37 GHz data to the 19 GHz data, the values of the

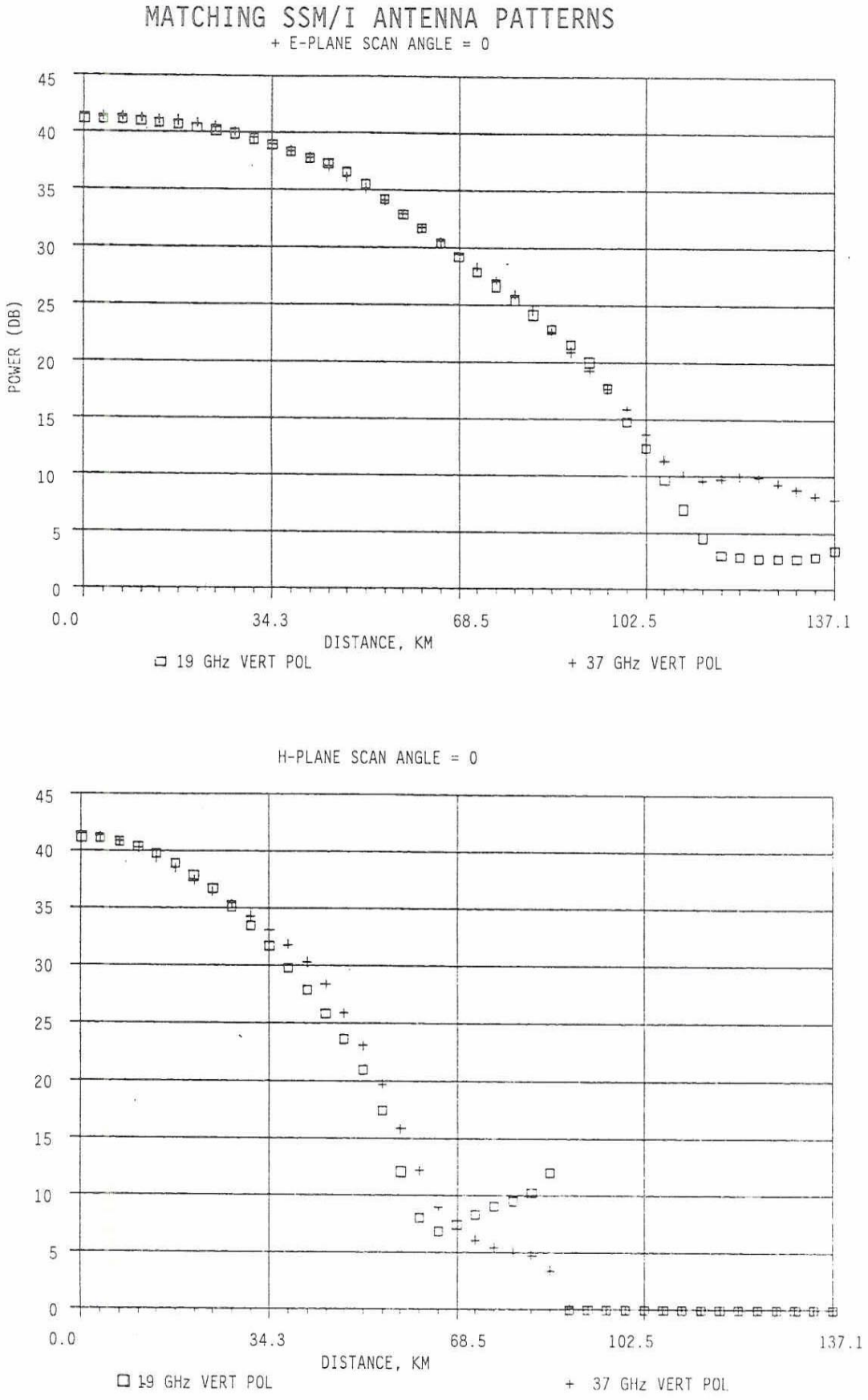

FIGURE 3.8 SMOOTHED 37 GHz ANTENNA PATTERN AND 19 GHz PATTERN

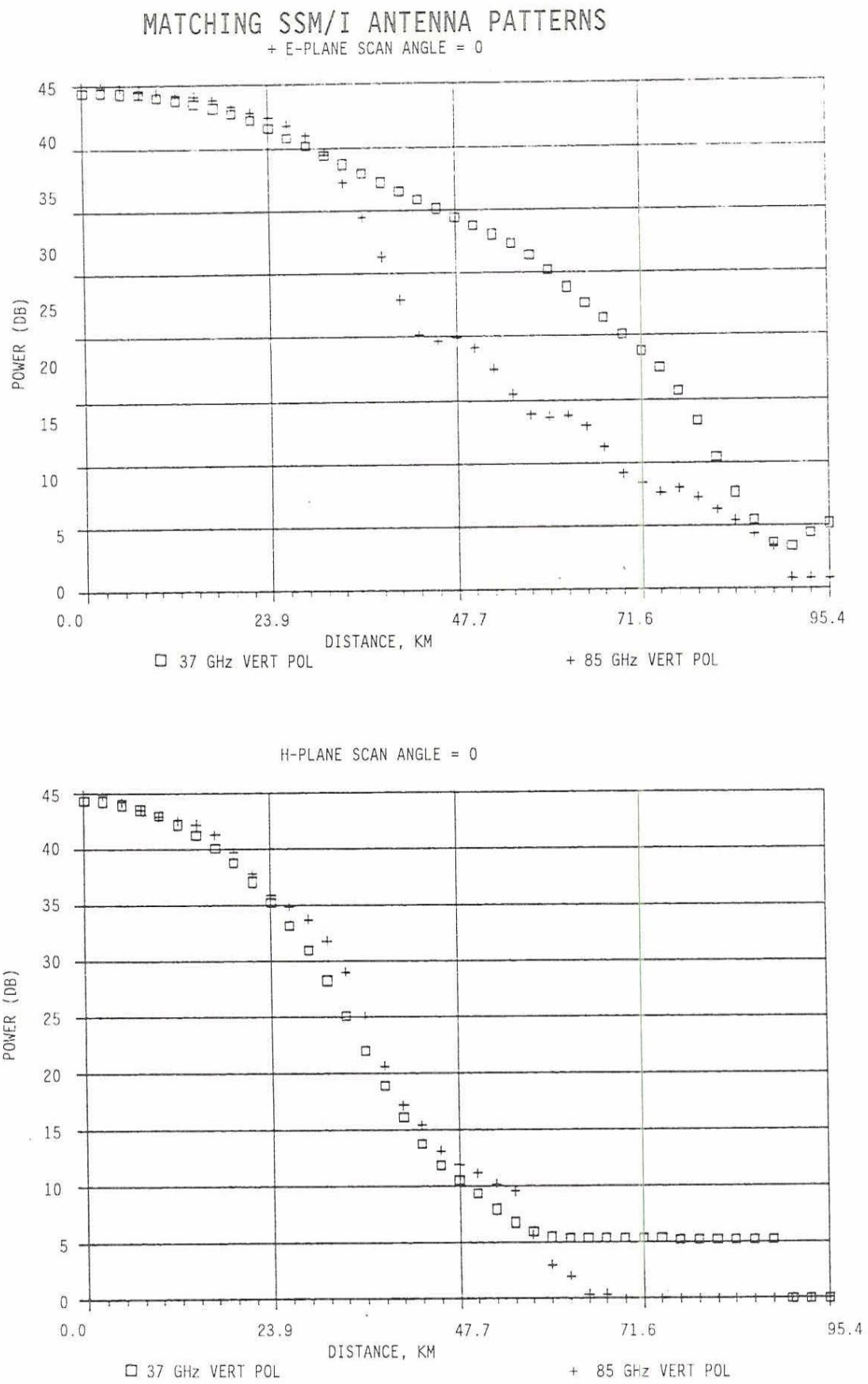

FIGURE 3.9 SMOOTHED 85 GHz ANTENNA PATTERN AND 37 GHz PATTERN

coefficients of a 5 x 5 array of 85 GHz data vary across the SSM/I scan. The resulting smoothed patterns display good agreement with 37 GHz pattern in all regions across the SSM/I swath.

Antenna pattern matching is not currently being exercised in the estimate of SSM/I scene brightness temperatures. This process may be performed with a modification to the current SSM/I SDR software module. The benefits of matching higher resolution SSM/I data to the lower resolution data need to be examined further before a recommendation can be made.

It should be noted that a reduction of sensor noise occurs in the process of smoothing the data. For the examples discussed above the rms noise in the smoothed 37 GHz data (3 x 3 array) is reduced by a factor of 0.45 and the noise in the smoothed 85 GHz data (5 x 5 array) is reduced by 0.25.

It should also be noted that the technique of selecting the set of coefficients $\{c_n\}$ to match an antenna pattern at frequency ν_1 is sufficiently general to cover the problem of data interpolation. For example, if frequency ν_1 is set to ν_2 (i.e., the high and low resolution patterns are the same), then the coefficients determined in the above antenna matching problem provides a means of interpolating the temperature at k from the set of temperatures at $\{k_n\}$, n=1, ..., N. Figures 3.10 - 3.12 present computations at 19, 37, and 85 GHz of the desired pattern at a prescribed k (which is the actual pattern centered at a point not sampled) and an "interpolated" pattern associated with the interpolated data point which is based on samples at $\{k_n\}$. The scan region for interpolation is taken to lie near the satellite ground track and the point of interpolation k is selected as a worst case situation, i.e., midway between successive scans and midway between samples. A 4 x 4 array of samples surrounding point k is selected for the interpolation.

The results appear very good at 19 GHz and not so good at 37 and 85 GHz. This situation arises from the fact that the 19 GHz data are spatially sampled near the Nyquist rate (i.e., approximately two samples per 3 dB beam diameter) while the 37 and 85 GHz are under sampled. To sample the 85 GHz at the Nyquist rate would require the SSM/I to spin at approximately twice the current rate and to sample at four times the present the sampling rate. (This option was not possible during the design of the SSM/I due to the data rate limitations imposed by the spacecraft data acquisition system.) In any event, the above technique of selecting coefficients is an attractive procedure to obtain accurate interpolated 19 GHz data and, if smoothed to match the lower resolution, interpolated 37 and 85 GHz data as well.

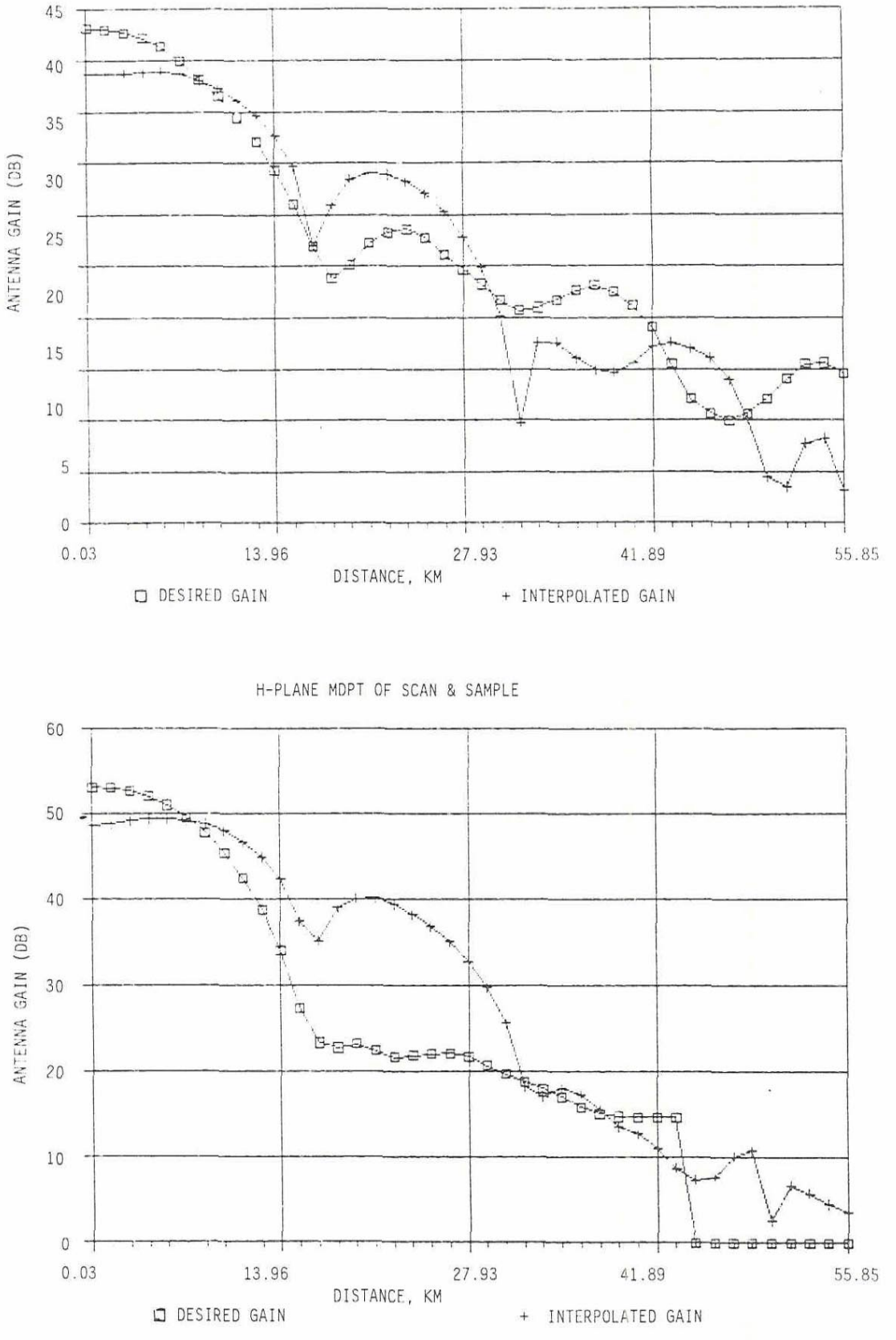

FIGURE 3.10. INTERPOLATED PATTERNS OF 85 GHz DATA (MIDPOINT BETWEEN SCANS AND SAMPLES)

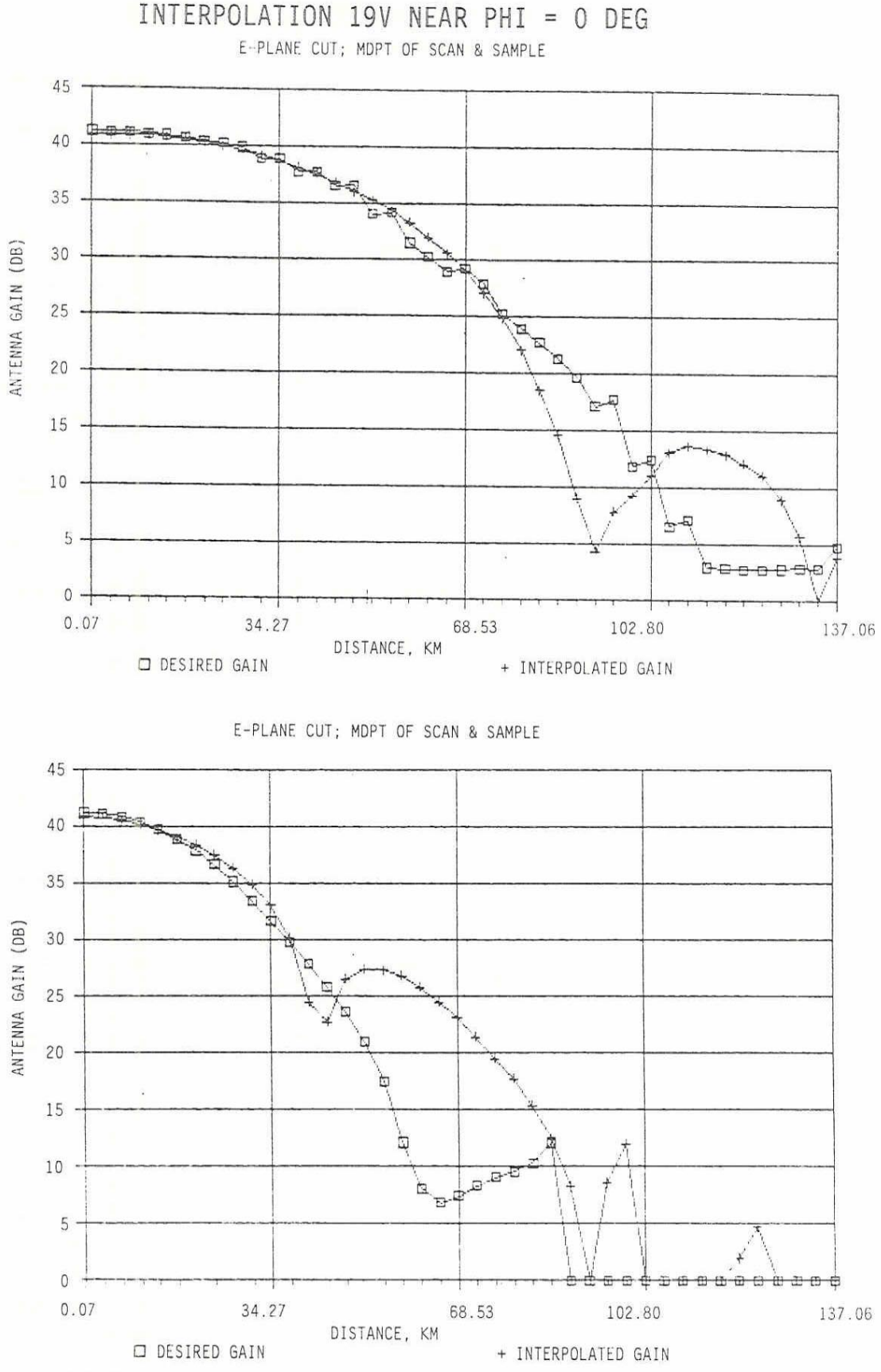

FIGURE 3.11. INTERPOLATED PATTERNS OF 19 GHz DATA (MIDPOINT BETWEEN SCANS AND SAMPLES)

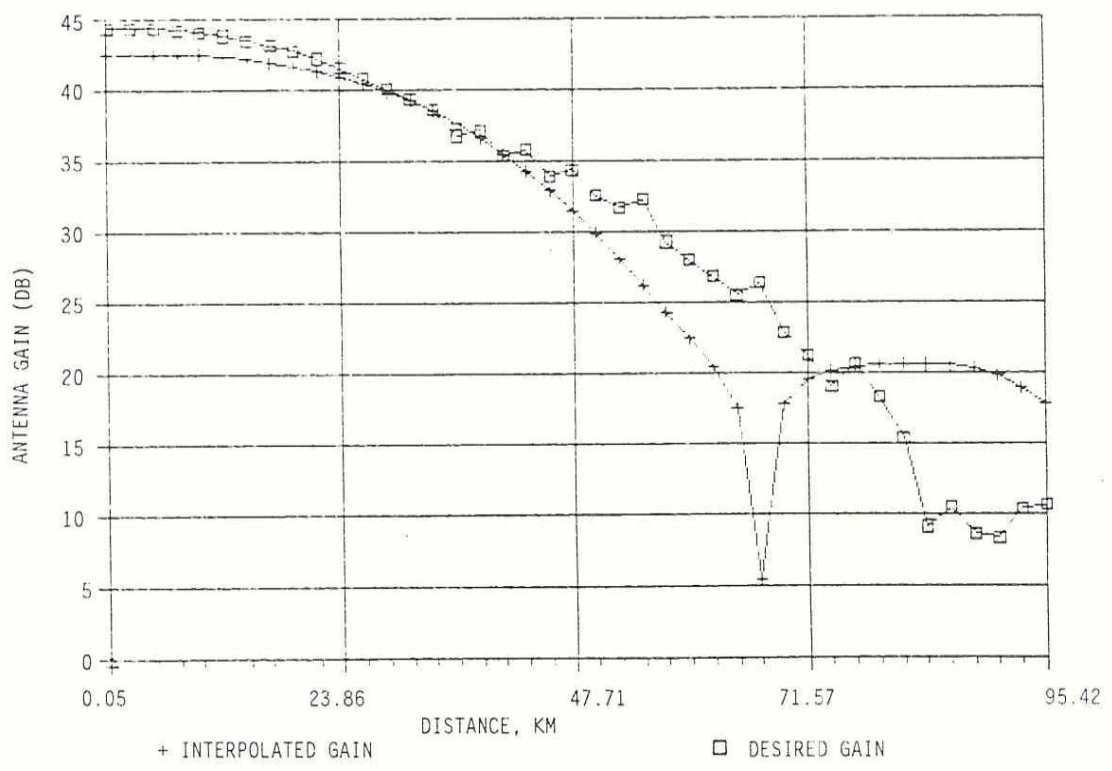

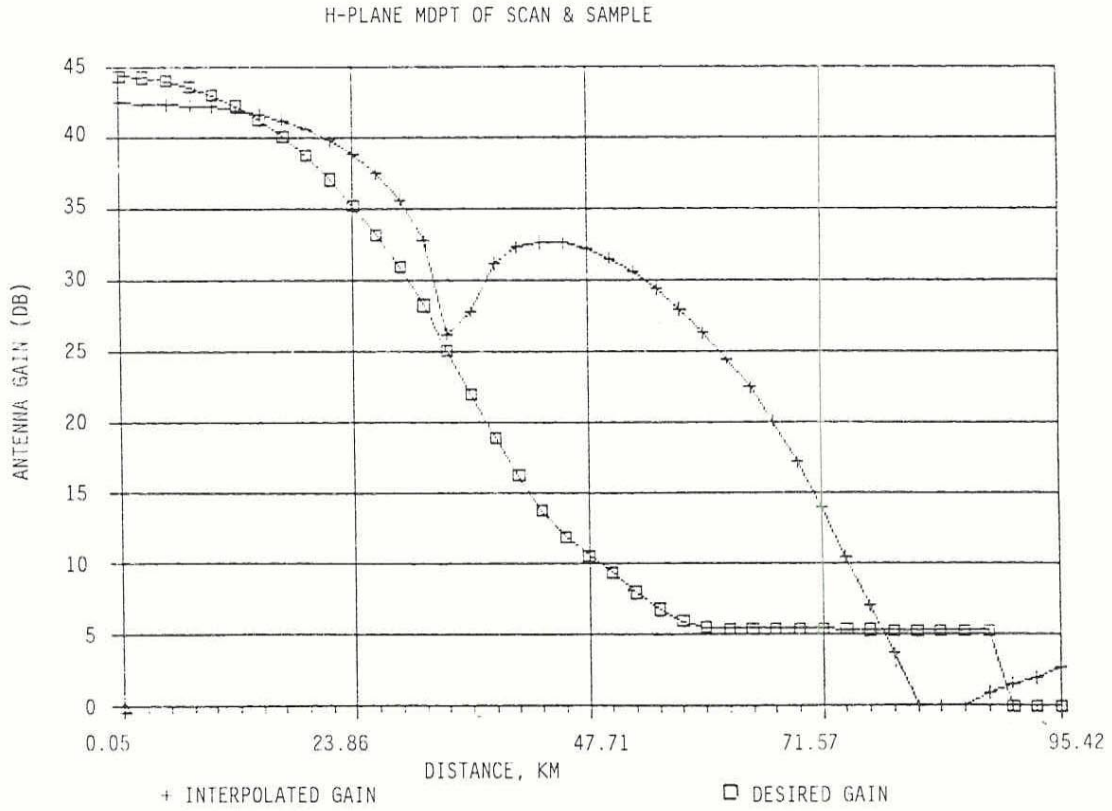

FIGURE 3.12. INTERPOLATED PATTERNS OF 37 GHz DATA (MIDPOINT BETWEEN SCANS AND SAMPLES)

3.4 REFERENCES

1. Hollinger, J. P., R. C. Lo, G. A. Poe, R. Savage, and J. Peirce, SSM/I User's Guide, Naval Research Laboratory, Washington, D.C. 20375, 14 September 1987.

2. Stogryn, A., " Estimate of Brightness Temperature from Scanning Radiometer Data," IEEE AP, Vol. AP-26, No. 5, Sept 1978.

3. NIMBUS 5, 6, 7 User's Guide, Goddard Space Flight Center, NASA LANDSAT/NIMBUS PROJECT, 1972, 1975, 1978.

4. Njoku, E. G., "Antenna Pattern Correction Procedures for the Scanning Multichannel Microwave Radiometer (SMMR)," Boundary-Layer Met., Vol. 18, pp. 79-98, 1980.

5. Milman, A. S., "Antenna Pattern Correction for the NIMBUS-7 SMMR," IEEE Trans. Geoscience and Remote Sensing, Vol. GE-24, No. 2, Mar. 1986.

6. Njoku, E. G., J. M. Stacey, and F. T. Barath, "The SEASAT Scanning Multichannel Microwave Radiometer SMMR): Instrument Description and Performance," IEEE J. Oceanic Eng., Vol OE-5, pp. 100-115, 1980.

4.0 INSTRUMENT PERFORMANCE

4.1 INTRODUCTION

The radiometric performance of the SSM/I is measured primarily in terms of the channel radiometer sensitivities, the radiometer gain stabilities and the absolute calibration accuracy, which is presented in detail in Section 5.0. Additional performance parameters include the stability of the instrument spin rate which influences the scan uniformity and the accuracy of the antenna boresight positions and the antenna beam efficiency which determines the fraction of energy received within the main beam region surrounding each pixel.

The SSM/I is the first satellite microwave radiometer to employ total-power receivers and achieve a factor of two improvement in sensitivity over "Dicke"-type radiometers. Greater independence of gain variations is achieved with a Dicke radiometer but at the cost of reduced sensitivity. Thus, high interest was present during the SSM/I Cal/Val early orbit period when evaluating the on-orbit radiometer sensitivities and gain stabilities. Once the early orbit results demonstrated the success of the radiometer performance the task remained to validate the absolute calibration accuracy and the radiometric sensitivities throughout the on-orbit extreme environmental conditions. For example, Figure 4.1 presents the sun angle defined by the angle between the vector normal to the spacecraft's orbit and the vector from the spacecraft to the sun and the percentage of the orbits not in the earth shadow. The relatively large variation in the sun angle introduces a large variation of solar heating on the SSM/I and consequently large temperature changes of the instrument electronics and Bearing and Power Transfer Assembly (BAPTA). Not only must the SSM/I survive these extreme conditions, it must also meet radiometric performance requirements. Due to increased heating of the instrument in the winter of 1987 the SSM/I was turned off for a brief period from December 2, 1987 through January 12, 1988. This was done to avoid possible damage to the BAPTA when the temperature exceeded 41 degrees centigrade, the maximum temperature limit set by Hughes Aircraft Company. Except for the 85V channel, all channels returned to their performance levels prior to instrument turn off. Problems with the 85V channel continued to develop; sudden gain changes and a degradation of the sensitivity. Although increased heating of the instrument has occurred in the winter of 1988, the spacecraft solar arrays have been repositioned to provide sufficient shading to avoid the SSM/I from reaching temperatures which require it to be turned off.

The following sections present the SSM/I radiometer sensitivities, radiometer gain stabilities and spin rate stability since launch. In addition the calibration target stability, instrument temperature history and analysis of antenna beam efficiencies are presented along with a number of conclusions.

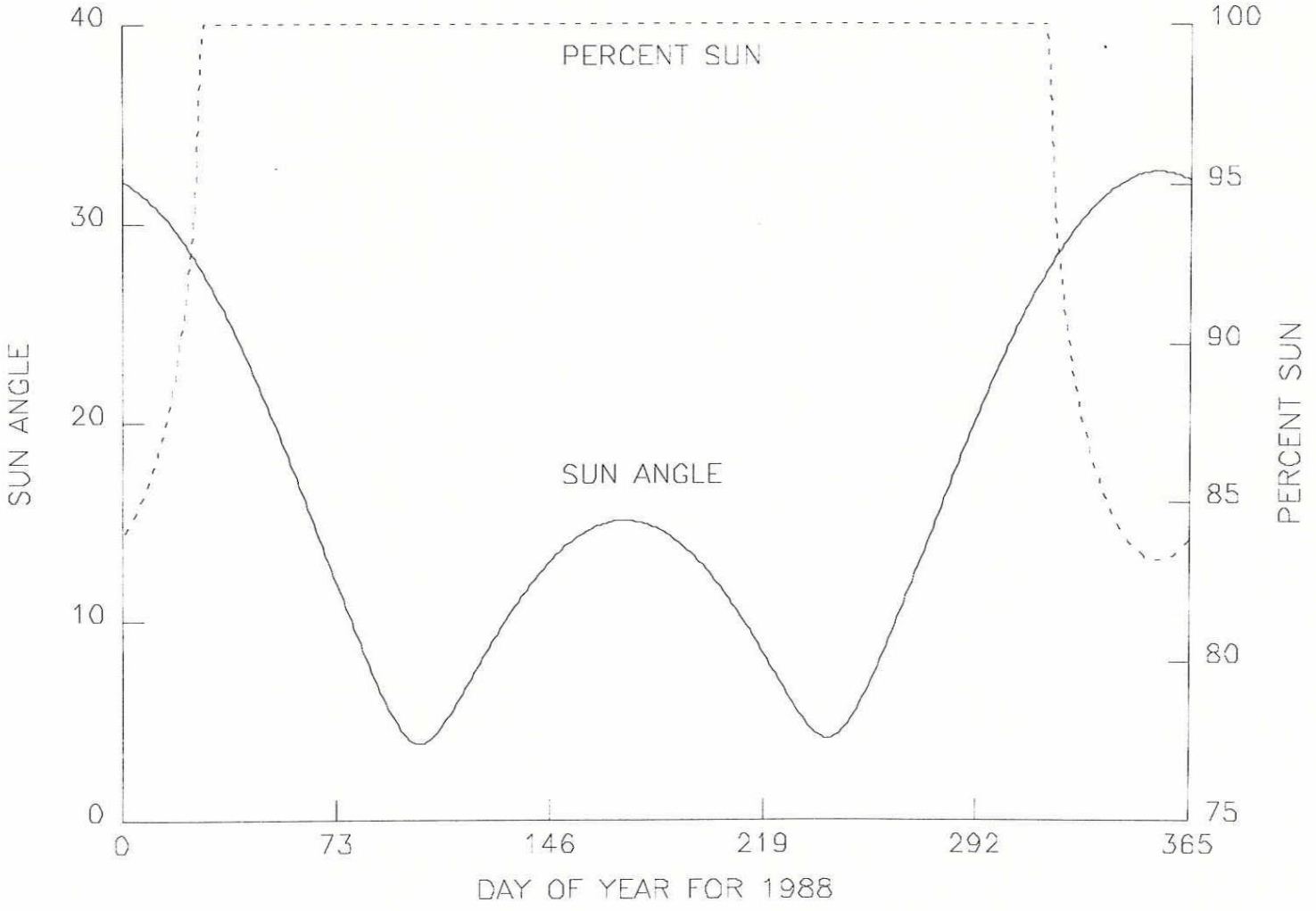

FIG. 4.1 VARIATION OF SUN ANGLE AND PERCENT SUN FOR F8

4.2 RADIOMETER SENSITIVITY

The radiometer sensitivity or noise equivalent temperature differential NEΔT is the standard deviation of the radiometer output referenced to the energy of the waveform incident on the antenna aperture. For the SSM/I total-power radiometers are employed and the sensitivity of each channel may be written as

$$\Delta T = T_{SYS} \sqrt{(1/B_C\tau) + (\Delta G/G)^2}$$

$$T_{SYS} = T_S + T_R$$

where

T_{SYS} = System noise temperature
T_R = Receiver noise temperature
T_S = Scene brightness temperature
B_C = Convolutional pre-detection bandwidth
τ = Radiometer integration time
$\Delta G/G$ = rms radiometer gain fluctuation and drift.

Although the receiver gain fluctuation contributes directly to the NEΔT, due to the frequent radiometric calibration of the SSM/I every 1.9 seconds and the development of amplifiers and detectors with low 1/f noise, the effect of receiver gain drift is extremely small over the calibration period. This enables a factor of 2 improvement of signal-to-noise for the total-power SSM/I system over a conventional "Dicke" switched radiometer system. Further discussion of gain fluctuations and drift is presented in Section 4.3.

Table 4.1 presents computations of the on-orbit radiometer NEΔT for all seven channels covering the period starting when the SSM/I was turned on through March 1989. The computations are based on first computing the variance of the radiometer output counts on each scan when the SSM/I antenna is viewing the hot load calibration target and then averaging the variance over the entire revolution. The variance in counts is referred to a variance in antenna temperature at the input of the SSM/I antenna (feedhorn) using the average gain of the radiometer (K/count) computed over the revolution. Except for channel 85V the sensitivities are extremely stable over the entire time period and show good agreement with the pre-launch results except for the November-January 1988 and 1989 periods. The increase in NEΔT in this period is due to an increase in the temperature of the instrument and is most pronounced at 85 GHz since these channels have the largest receiver noise temperatures. The channel sensitivities return to values noted prior to December 1987 except for the 85V channel which continued to rise. The 85V channel NEΔT increased from approximately 0.8 K to 2.1 K and then in January 1989 reached 5 K just before total failure. Although the cause is not known conclusively, it is likely due to the mixer portion of the receiver. Figure 4.2 presents the variation of the 85V NEΔT as a function of time where the shaded area is the variation in the NEΔT on a particular day. (The variation is a result of the averaging process used by FNOC to gather the statistics.) Also shown in the figure is the variation of the 85V mixer temperature.

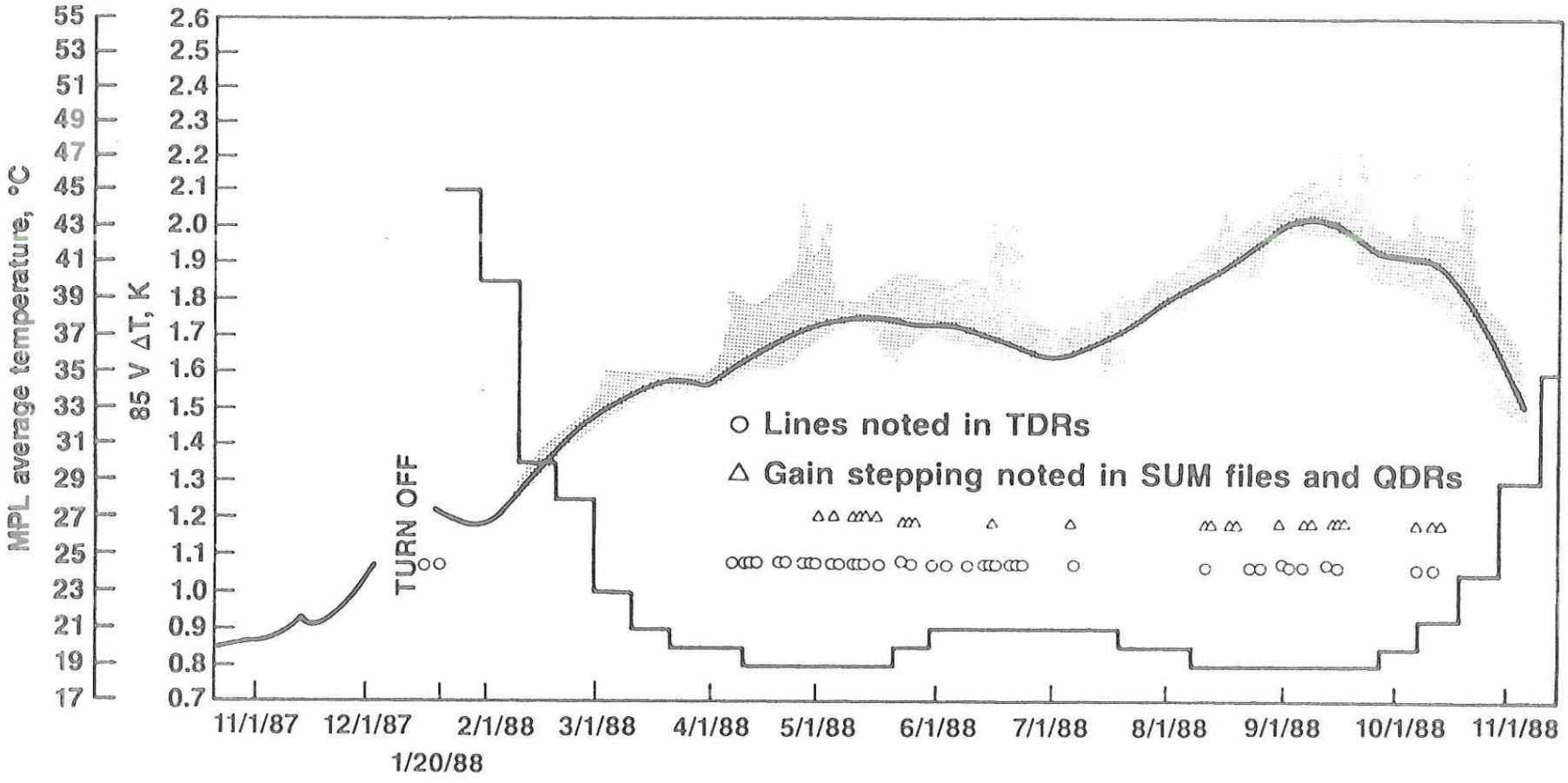

Figure 4.2 Variation of Receiver Temperature (MPL) and NEΔT of 85 V Channel

As noted above, the NEΔT is strongly correlated with the instrument temperature.

Using the cold reflector calibration radiometer output counts, computations similar to those for the hot load target were made on the radiometer sensitivities. The sensitivities were found to be quite stable over the period covered by Table 4.1 and agree with results one would expect when the scene brightness temperature is near 3 K, i.e., the cosmic background temperature seen by the cold reflector calibration target. The NEΔTs are considerably lower than those of Table 4.1 with the exception of the 85 GHz channels. For these channels the system noise temperature is much larger than the other channels and the scene temperature has a correspondingly smaller effect on the radiometer sensitivity. The sensitivities computed for the cold reflector target show the same trend as the data in Table 4.1 and exhibit the same dramatic increase of the 85V sensitivity after instrument turn on in January 1988.

Table 4.1

ON-ORBIT RADIOMETER SENSITIVITIES (K)
(Hot Load Target)

	CHANNEL						
	19V	19H	22V	37V	37H	85V	85H
Delta T Spec. (K)	0.8	0.8	0.8	0.6	0.6	1.1	1.1
Pre-Launch	.45	.42	.73	.37	.38	.69	.73
On-Orbit							
June 1987	.44	.38	.67	.33	.44	.78	.69
July 1987	.38	.34	.59	.32	.32	.75	.62
Aug. 1987	.37	.37	.58	.30	.33	.69	.59
Sept. 1987	.38	.35	.63	.29	.33	.73	.60
Oct. 1987	.45	.42	.69	.35	.44	.87	.70
Nov. 1987	.46	.42	.74	.40	.52	.91	.78
Jan. 1988	.5	.44	.74	.42	.58	1.12	.85
Feb. 1988	.43	.41	.72	.37	.42	1.32	.75
March 1988	.43	.41	.69	.33	.35	1.48	.73
April 1988	.42	.39	.70	.33	.37	1.70	.70
May 1988	.41	.40	.67	.32	.37	1.80	.70
June 1988	.42	.44	.68	.34	.38	1.80	.80
July 1988	.42	.41	.70	.31	.38	1.70	.71
Aug. 1988	.42	.40	.66	.32	.37	1.95	.70
Sept. 1988	.43	.39	.67	.36	.37	2.10	.71
Oct. 1988	.43	.41	.67	.33	.37	1.70	.72
Jan. 1989	.50	.45	.73	.44	.55	5.0	.86
Feb. 1989	.40	.40	.70	.35	.37	--	.88
Mar. 1989	.42	.35	.68	.33	.37	--	.83

4.3 GAIN STABILITY

The Automatic Gain Control (AGC) is designed to insure long-term radiometer gain stability, i.e., on a seasonal basis. As the temperature of the receivers change the power output is allowed to vary plus and minus 1 dB before a gain change is initiated. In this process each channel samples the hot load on every scan and commands a gain change up when the hot load is below 7/16th of the analog to digital converter range (4095) or commands a gain change stepped down if the hot load for that channel is above 3/4th of the ADC range (3072). The stepping can occur only once every 53 seconds on each channel. Note that if the gain goes up and down quickly and is within the above noted range at the end of the 53 second interval the gain will not be stepped.

Table 4.2 presents the gain level for each channel since launch. The long term gain stability is very good except for the 85V channel.

Table 4.2

RADIOMETER LONG-TERM GAIN STATE SUMMARY

CHANNEL		19V	19H	22V	37V	37H	85V	85H
Date								
1987	OCT	8	7	7	8	6	7	7
	NOV	7-8	6-7	6-7	8-9	8-9	7-8	7-8
1988	JAN	7	6	5-6	8	6	8-9	7-8
	FEB	7	6	5-6	8	6	8	7-8
	MARCH	7	6	6	8	6	8	7
	MAY	7	6	6	8	6	9-12	7
	JUNE	7	6	6	8	6	8-11	7
	JULY	7	6	6	8	6	8	7
	AUG	7	6	7	8	6	8-11	7
	SEPT	7	6	7	8	6	8-13	7
	OCT	7	6	7	8	6	8-14	7
	NOV	7	6	5-6	8	6	9-10	7-8
	DEC	7	6	5	8	6	10-15	8
1989	JAN	7	6	5	8	6	10	6-8
	FEB	7	6	5-6	8	6	9-10	8
	MAR	7	6	6	8	6	9	7

The 85V channel has shown both small (<.5 dB) and large (>2 dB) gain instabilities. The first of these large gain changes occurred on November 20, 1987. This occurrence lasted 50 seconds and was a large gain change with AGC stepping. Since then, the changes have occurred intermittently. Unfortunately, the 85V data during these times is of very limited use. Table 4.3 shows the percentage of gain stepping occurring during one orbit from May to early October 1988. Small gain changes started occurring in March 1988. These are evident as lines in the 85V Temperature Data Records (TDR).

TABLE 4.3

85V GAIN STEPPING AS A PERCENTAGE OF MONITORED ORBITS

1988

May	40%
June	8%
July	3%
August	22%
September	18%
October	25%

(Prior to May 1988 gain stepping rarely occurred)

Typical variations of the radiometer gain on a scan to scan basis are presented in Figures 4.3 through 4.6. The data apply to REV 438 with parts of REV 437 and REV 439 included. For convenience of presentation, the gains for all SSM/I channels are shown every 20th scan, where each scan period is 1.9 seconds. Note the appearance of rapid fluctuations of the gain and a slowly varying oscillation over the orbit. The fluctuations arise from noise in the radiometer output calibration samples and may be reduced by averaging calibration data taken over several successive scans which is discussed in more detail below. The slowly varying component of the radiometer gain is due to orbital changes in the temperature of the SSM/I instrument. Figure 4.7 shows the orbital variation of the temperatures of the RF mixer and the forward radiator surface. Based on the data of Figure 4.7 the maximum shift in temperature of the RF mixer is approximately 0.6 K and introduces less than 0.025 dB change in the radiometer gain (peak to peak). This change is considerably less than the gain change needed to activate the AGC circuit.

The errors arising from the rapidly varying portion of the radiometer gain may be reduced, as noted above, by averaging the calibration data taken on several adjacent scans. Figures 4.8 and 4.9 show the effects of averaging N scans of calibration data for the 22V and 85V channels as a function of scan number. The curves represent the difference between the scene brightness temperatures (SDRs) as determined by averaging N number of scans of calibration data and SDRs as determined by averaging all scans of calibration data. The slowly varying orbital drift in the figures is taken into account by the frequent calibration and does not contribute to the calibration errors. The fluctuations about the drift are due to both calibration and pixel or scene noise. Only the calibration noise component is reduced by averaging the calibration data but the reduction shown in Figures 4.8 and 4.9 include reduction of both calibration and scene noise. Figure 1.7 presents a summary of the reduction in calibration noise error when averaging the number of scans indicated. Based on these results, it appears that averaging 10 scans of calibration data (i.e., 50 samples) for channels 1-5 and 20 scans (i.e., 100 samples) for channels 6 and 7 will improve the calibration accuracy significantly. The drift of the radiometer gain is negligible over this

time period (approximately 38 seconds) of calibration data. Further averaging produces only a modest improvement in calibration accuracy at the expense of appreciable computation in the averaging process.

4.4 CALIBRATION TARGET STABILITY

Five samples of the 85 GHz radiometer output counts are taken each 1.9 second scan when viewing the hot and cold load calibration targets. Five samples are taken every other scan at the remaining channels. The computation of the variances of these counts over the period of a revolution and for numerous revolutions were used to estimate the SSM/I radiometer sensitivities presented above. These results indicate that the spread in these calibration samples were within the expected radiometric sensitivities. To confirm that the five calibration samples taken on each scan exhibited no systematic differences, the individual samples were plotted separately for an entire revolution. Figures 4.10 through 4.12 present the individual hot load calibration samples for the 19V channel for REV 438.

An examination of these figures reveals that the samples show no appreciable systematic differences. This result is in agreement with the calibration results obtained during ground thermal/vacuum testing. The rapid fluctuations are due to instrument noise and the slowly varying component is due to orbital temperature change of the instrument as noted earlier for the radiometer gain. Similar results were obtained for the remaining channels.

Figures 4.13 through 4.15 present plots of the 19V samples of the cold reflector calibration target during REV 438. These figures show the same slowly varying and fluctuating behavior over the orbit and also demonstrate that the five cold load samples exhibit negligible systematic differences. The latter is an important result since the radiometric performance of the cold reflector was not tested as a calibration reflector prior to launch. This does not mean that the samples are free from undesired contamination of spacecraft or earth emissions which is the subject of absolute calibration of the SSM/I, but it does mean that the five samples taken on each scan agree extremely well (i.e., to within the NEΔT). Similar results were obtained for the remaining channels.

Finally, Figures 4.16 and 4.17 show the variation of the hot load temperatures taken by the three temperature sensors over a complete orbit, REV 438, and the spread between these sensors for the satellite revolutions 109 through 735. These data indicate that the three sensor probes do not have significant calibration differences and that the relative rms measurement error between the sensors is less than 0.09 K.

4.5 SPIN RATE STABILITY

The SSM/I has been spinning at a rate of once per 1.8990 seconds with a ±.0002 second variation since the initial turn on. This translates to an azimuthal angular position error of the antenna boresight of ±0.038

degrees. This, in turn, translates to ~±0.6 km pixel position error on the earth's surface. When the SSM/I was turned off for the hot period, the SSM/I continued to spin. No ground or spacecraft RF interference has been noticed on the data examined by Hughes.

4.6 INSTRUMENT TEMPERATURE STABILITY

Plots of the average temperatures of the Bearing and Power Transfer Assembly (BAPTA) and BAPTA Control Electronics (BCE) are presented in Figure 4.18 for Julian Days beyond 80 for 1988 with a portion of 1989. Figure 4.19 presents the average temperatures of the thermal radiator and power supply unit and 4.20 presents the average temperatures of the mixer preamplifier section of the electronics (MPL) and the hot load calibration target.

The behavior in the vicinity of Julian Day 360 in the figures correlates well with the maximum angle of the sun with respect to the spacecraft shown in Figure 4.1 which is greatest at the winter solstice, December 21. To avoid overheating, the SSM/I was turned off from December 2, 1987 to January 18, 1988. An adjustment of the solar panels to increase sun shading on the SSM/I in December 1988 avoided overheating and the SSM/I remained on. Future SSM/I's will have a modified thermal control subsystem to avoid this problem.

4.7 SDR REPEATABILITY

The long term calibration stability of the SSM/I was further verified by examining the repeatability of the absolute brightness temperatures or sensor data record temperatures for a number of diverse surface types. The regions included the Sargasso Sea, the Congo Basin, the Amazon Basin, the Libyan Desert, and the Kalahari Desert. In each region, the SSM/I data for five ascending and five descending orbit revolutions were collected for a period of over one month. Histograms were generated for each of the regions and the mean and standard deviations noted. No attempt was made to exclude clouds or any perturbing storm systems, although no storms were encountered. Figures 4.21 - 4.23 present histogram results for two revolutions 407 (July 18, 1987) and 640 (August 4, 1987) for the Sargasso Sea. The means of the brightness temperatures differ by ~ 1 K for all channels, although the fine details of the histograms differ. This level of repeatability of the means was also typical of all land surfaces when examining individually the ascending or descending passes of data. (The mean of the descending passes were typically a couple of degrees higher than the ascending passes which is believed due to an increase in surface temperature) This level of repeatability gives further evidence of the high calibration stability of the SSM/I.

4.8 ANTENNA BEAM CHARACTERISTICS

The antenna 3 dB beamwidths and beam efficiencies computed from SSM/I antenna range pattern measurements are presented in Tables 2.1 and 2.2. A partial verification of these beam characteristics may be made by

examining the response of the brightness or SDR temperatures to land/water boundaries. Such a response would resemble a step response of the antenna pattern in the cross-track direction for a coastal region lying perpendicular to the scan direction or a step response in the along-track direction for a coastal region lying parallel to the scan direction. The partial derivatives of these responses should approximate the antenna pattern in the direction of interest. These computations were done for the 19, 37, and 85 GHz vertically and horizontally polarized channels and by fitting the SDR responses with cubic spline functions for SDR data taken on the western coast of the United States and the southern coast of Africa and Australia. Figures 4.24 and 4.25 present the derivatives in the cross-track and along-track directions as a function of cross-track or along-track distances for the 37 and 85 GHz channels. The results exhibit the expected antenna beam characteristic in the vicinity of the maximum gain (normalized to unity) and agree quite well with the 3dB beamwidths presented in Table 2.1 for both cross-track, and along-track directions. The smaller oscillations appearing in the figures are not antenna sidelobes but are due to variations of the scene brightness temperatures outside the coastal boundary. Similar results were obtained for the 19 and 22 GHz channels. The locations of the maximum gains were within 1 - 2 km for all channels for a given coastal boundary, indicating that the antenna beams share a common center.

4.9 CONCLUSIONS

In view of the results presented, it is clear that the on-orbit SSM/I channel radiometric sensitivities and receiver gain stabilities meet or exceed prelaunch performance specifications, except for the 85 GHz vertically polarized channel which never recovered the level of performance it had prior to when the instrument was turned off in December 1987. The instrument spin rate has been extremely stable since launch with a maximum variation of ±0.0002 seconds and translate to less than 0.6 km error in the pixel location. The calibration hot load target exhibited excellent short term stability which in conjunction with the receiver gain stability suggest that the calibration data taken on several adjacent scans may be averaged to improve the accuracy of the brightness temperatures. The calibration accuracy was observed to be very repeatable, providing stable brightness temperatures for a diverse set of surface types including a number of jungle basins, deserts, and the Sargasso Sea for over a month. The antenna beam characteristics were examined by analyzing the step response of the SSM/I to a coastal boundaries. The derived antenna patterns are consistent with published beamwidths computed on the basis of antenna pattern measurements. Plots of receiver electronics, power supply, hot load calibration target,and the Bearing and Power Transfer Assembly (BAPTA) correlate well with the sun angle to the spacecraft. Although the SSM/I experienced increased heating during the winter of 1987 and was turned off primarily to avoid damaging the BAPTA, the spacecraft solar arrays were adjusted to provide sufficient shade for the SSM/I to avoid shutting the instrument off. Future SSM/Is will have a modified thermal control subsystem to avoid this problem.

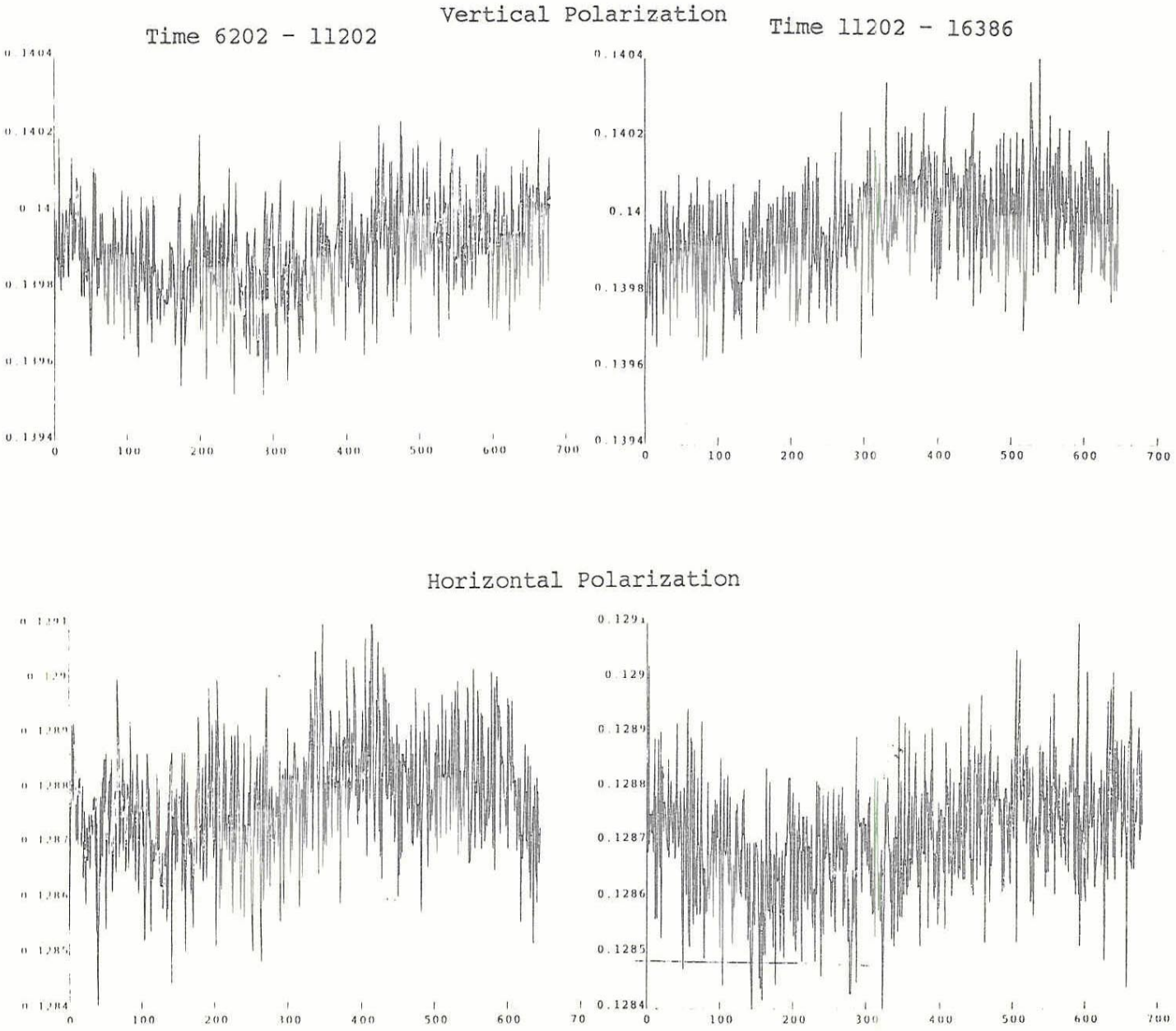

Figure 4.3 Variation of 19 Ghz Radiometer Gain (K/Count) for Rev 438.

Time 6202 - 11202

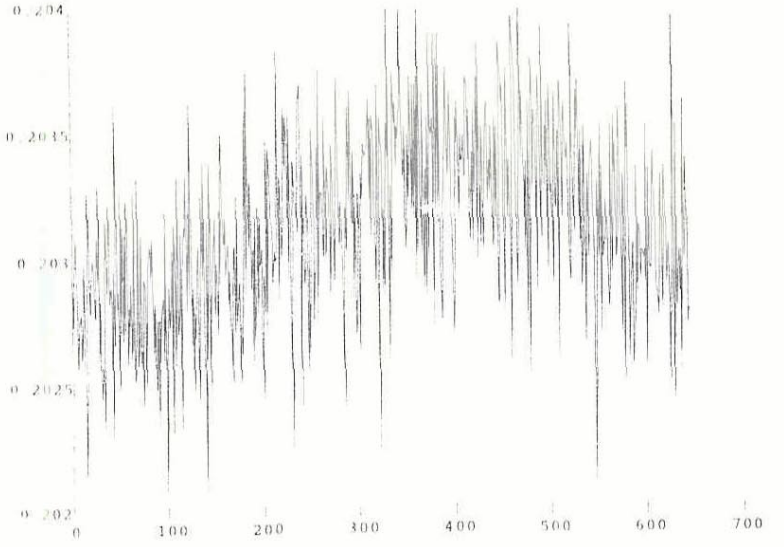

Time 11202 - 16386

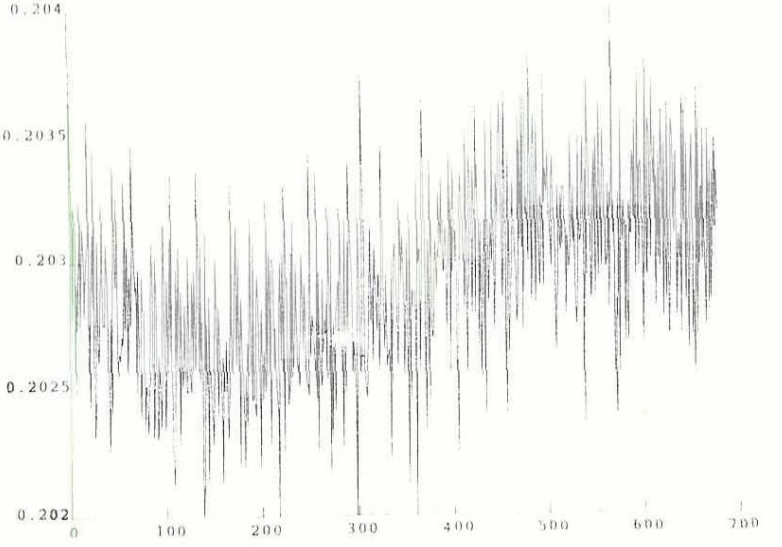

Scan Number(Every other scan with 3.8 sec/scan)

Figure 4.4 Variation of 22 GHz Radiometer Gain (K/Count) for REV 438

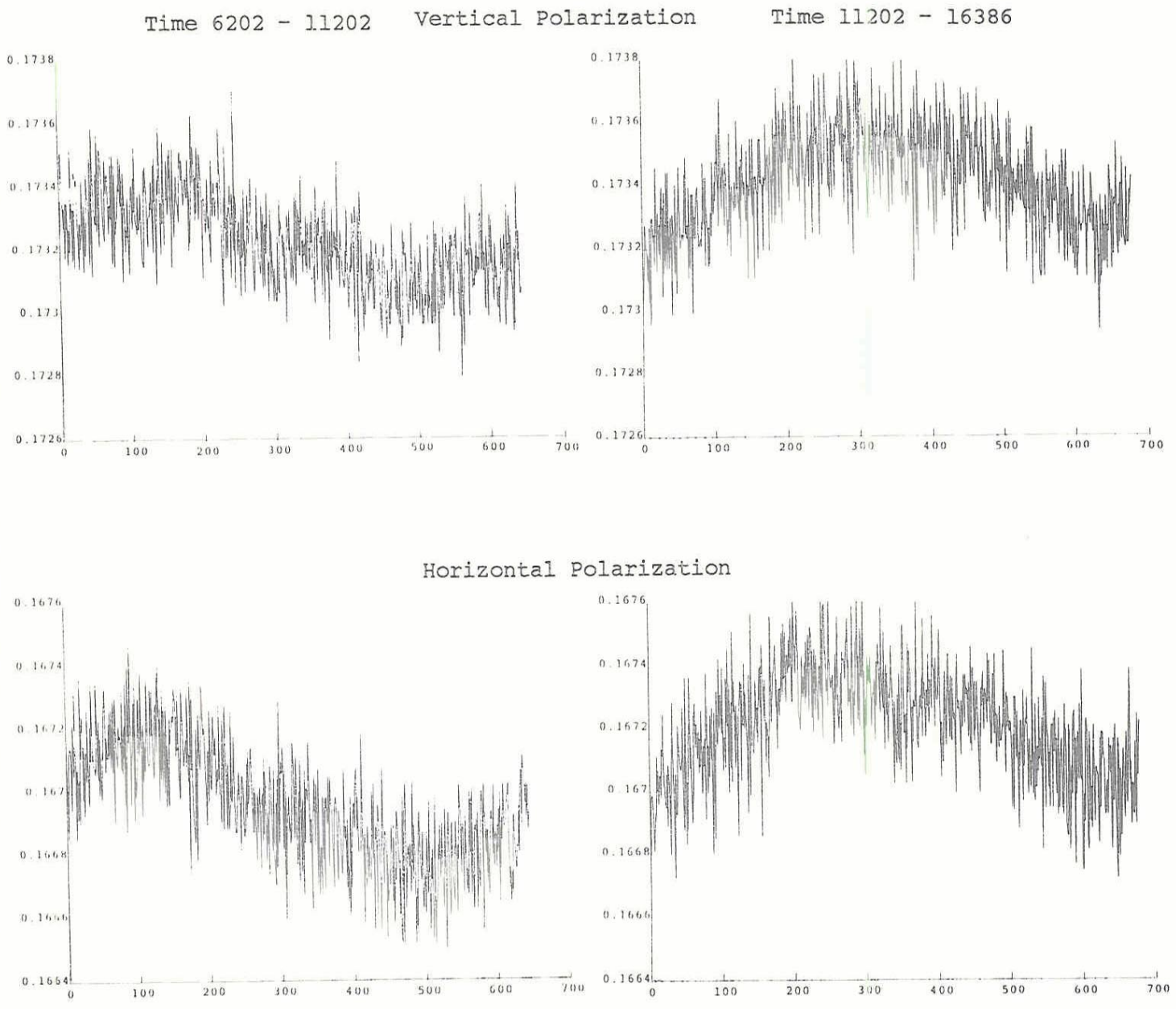

Figure 4.5 Variation of 37 Ghz Radiometer Gain (K/Count) for Rev 438.

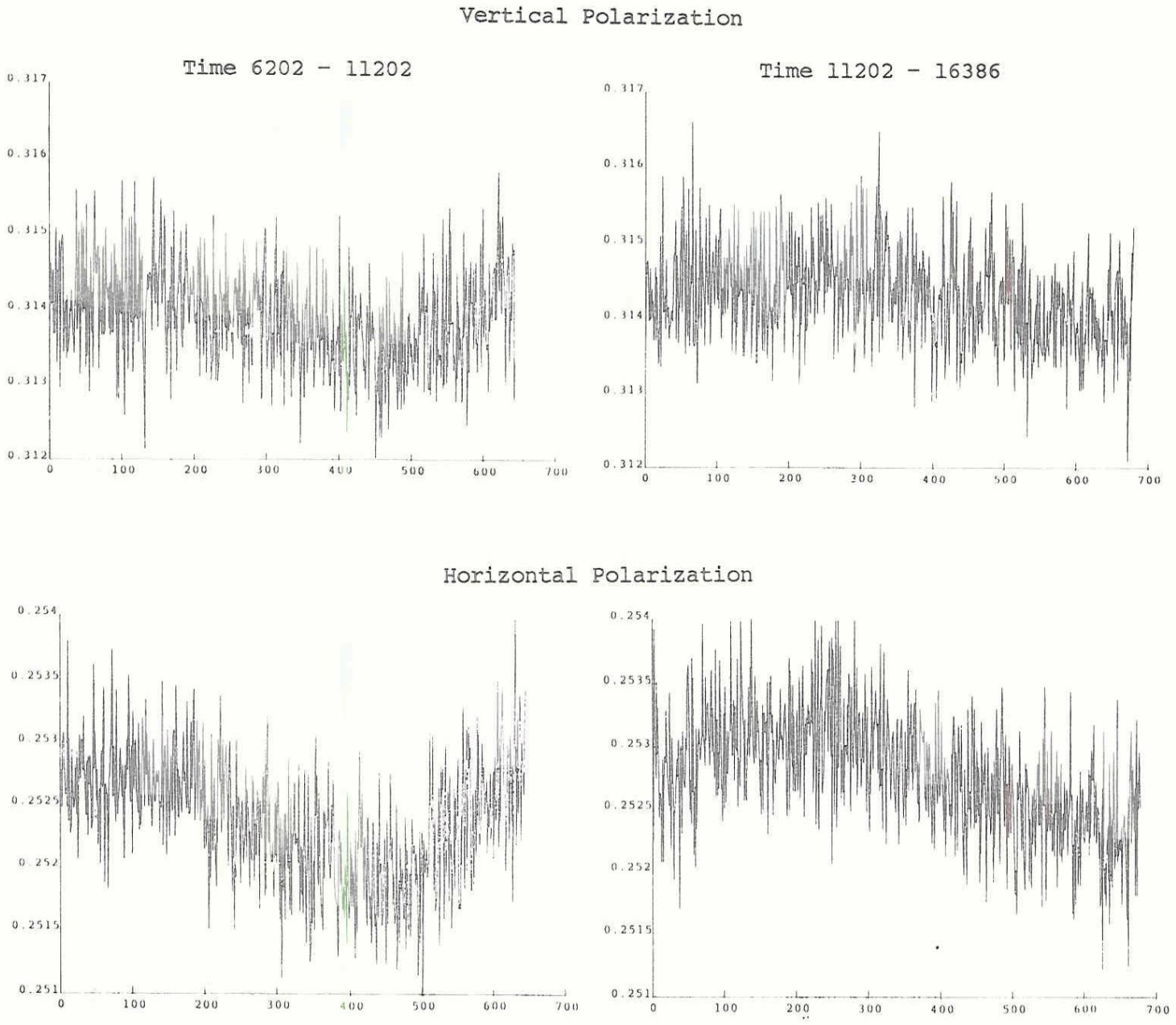

Figure 4.6 Variation of 85 Ghz Radiometer Gain (K/Count) for Rev 438.

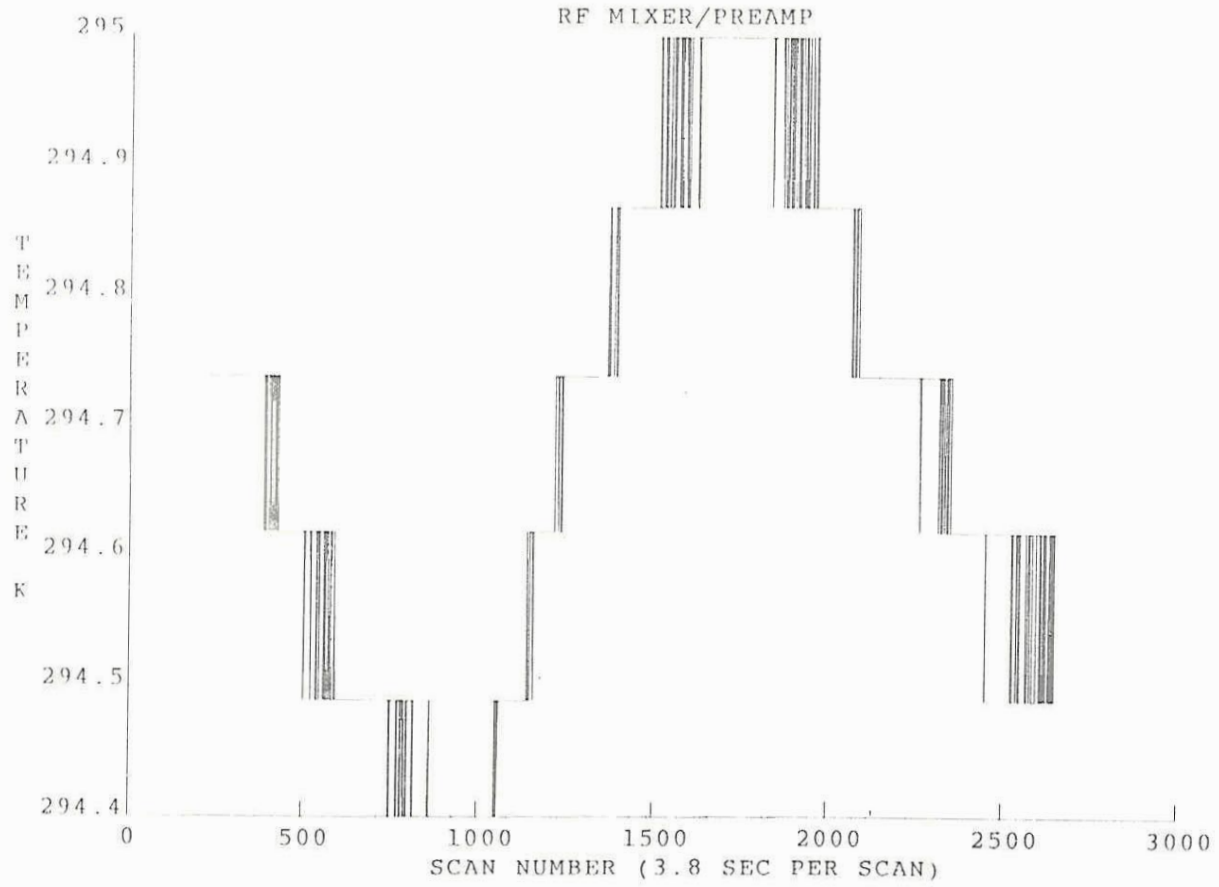

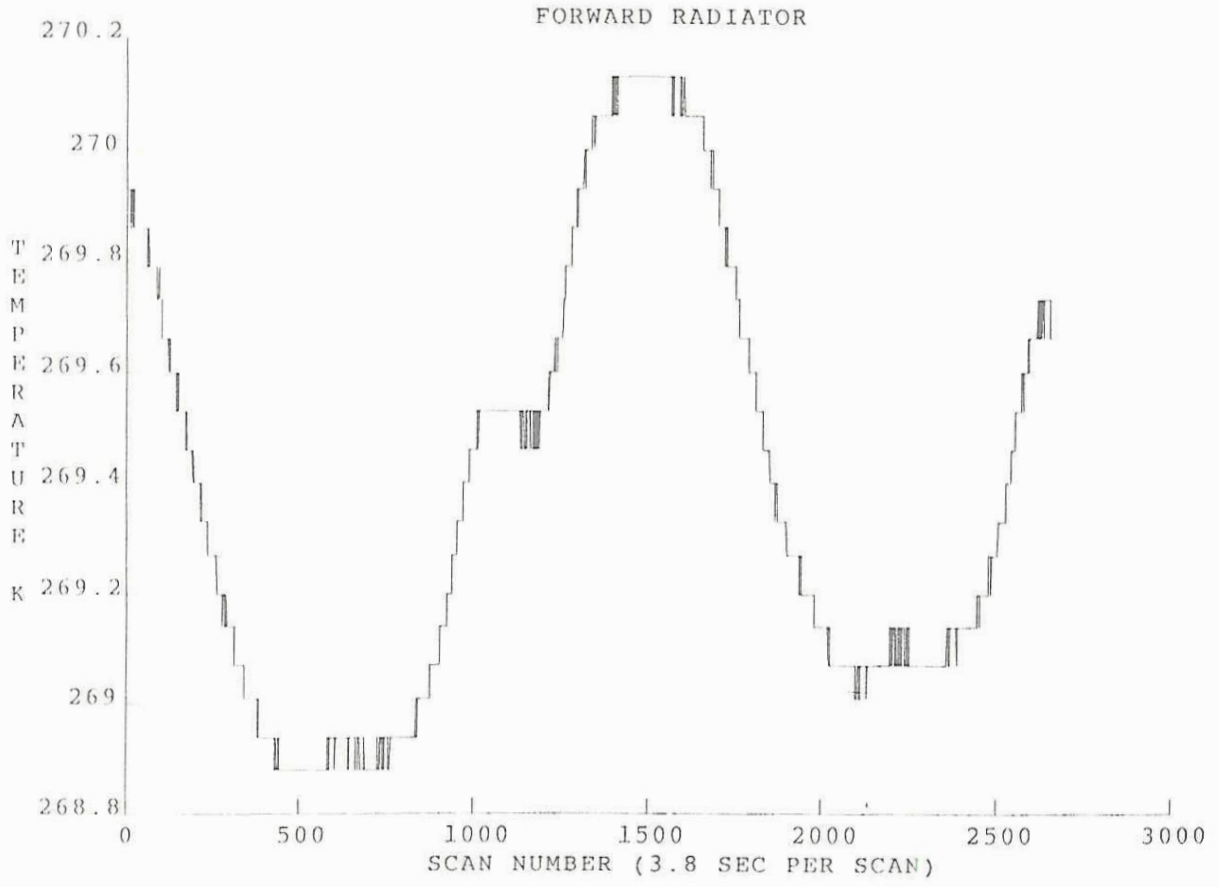

FIGURE 4.7 VARIATION OF RF MIXER AND FORWARD RADIATOR TEMPERATURES (REV 438)

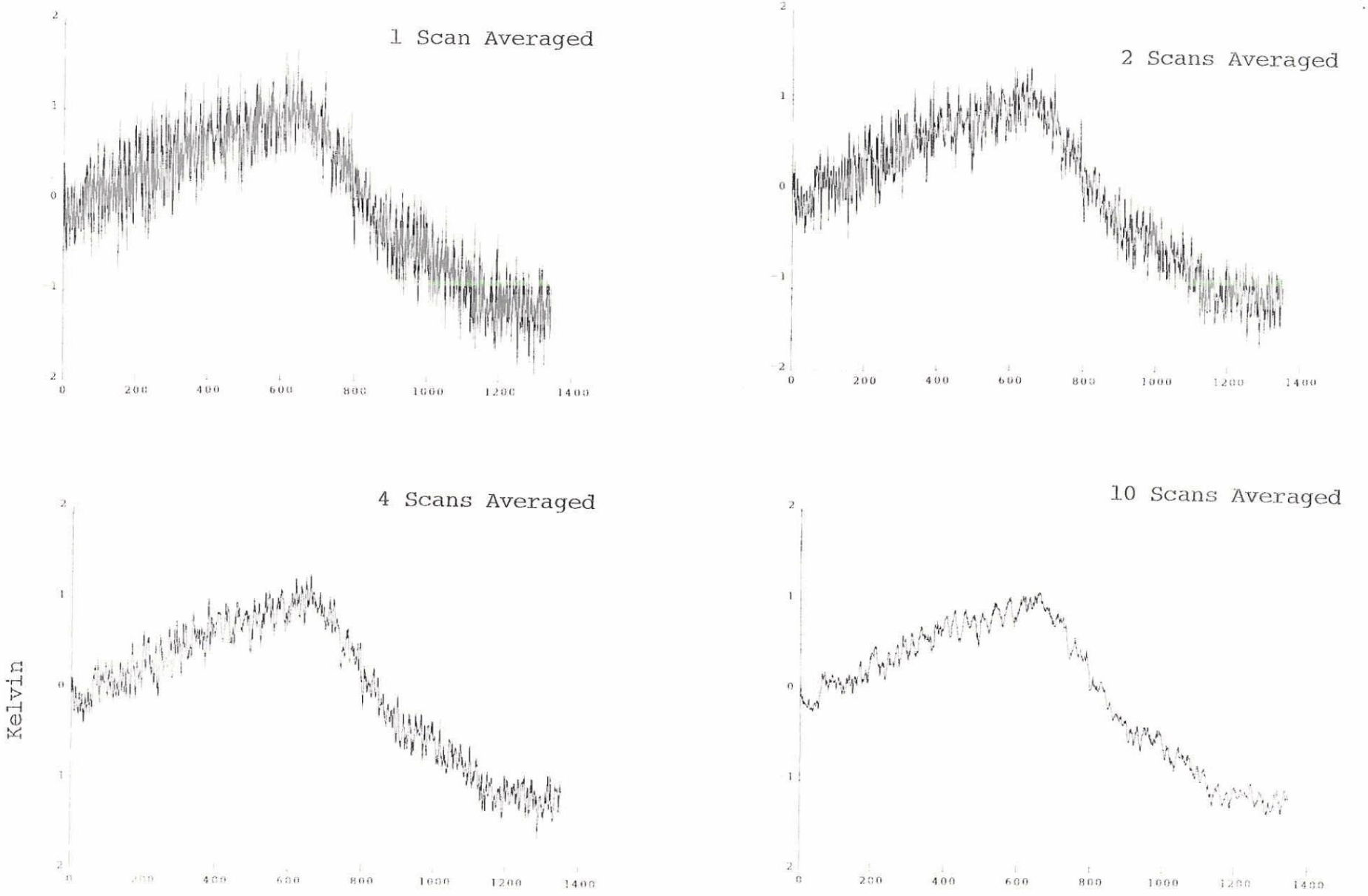

Figure 4.8 Reduction in Calibration Error for 22V Channel
Obtained by Averaging Calibration Data

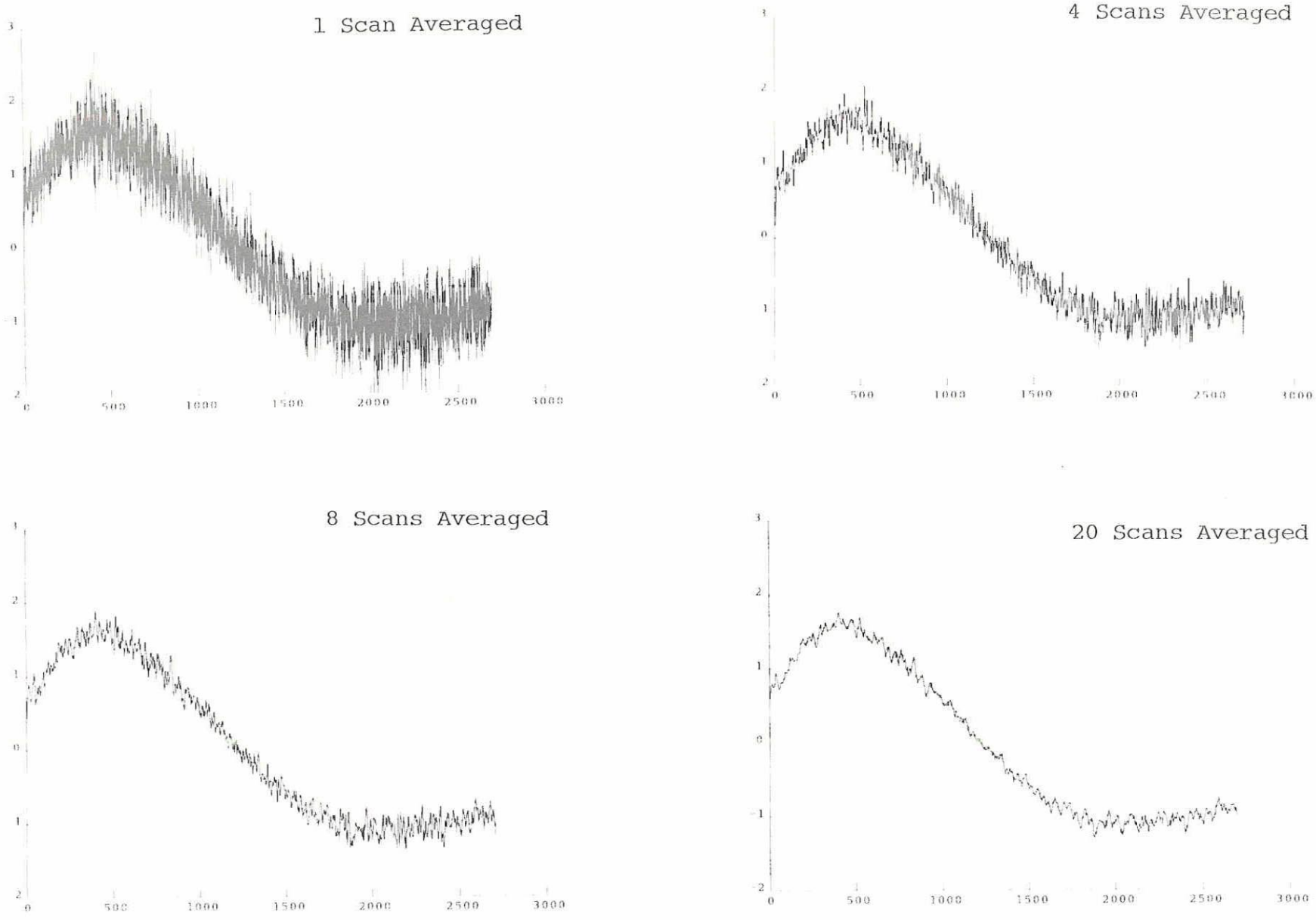

Figure 4.9 Reduction in Calibration Error for 85H Channel
Obtained by Averaging Calibration Data

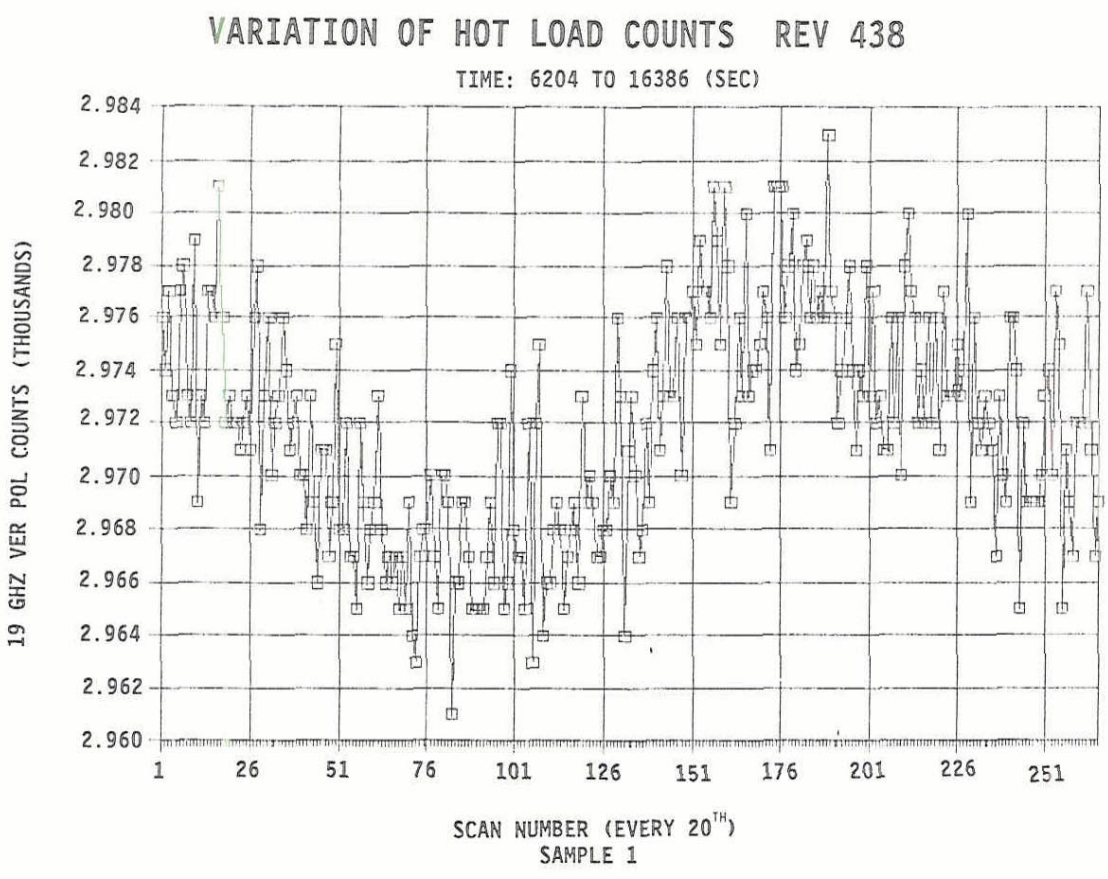

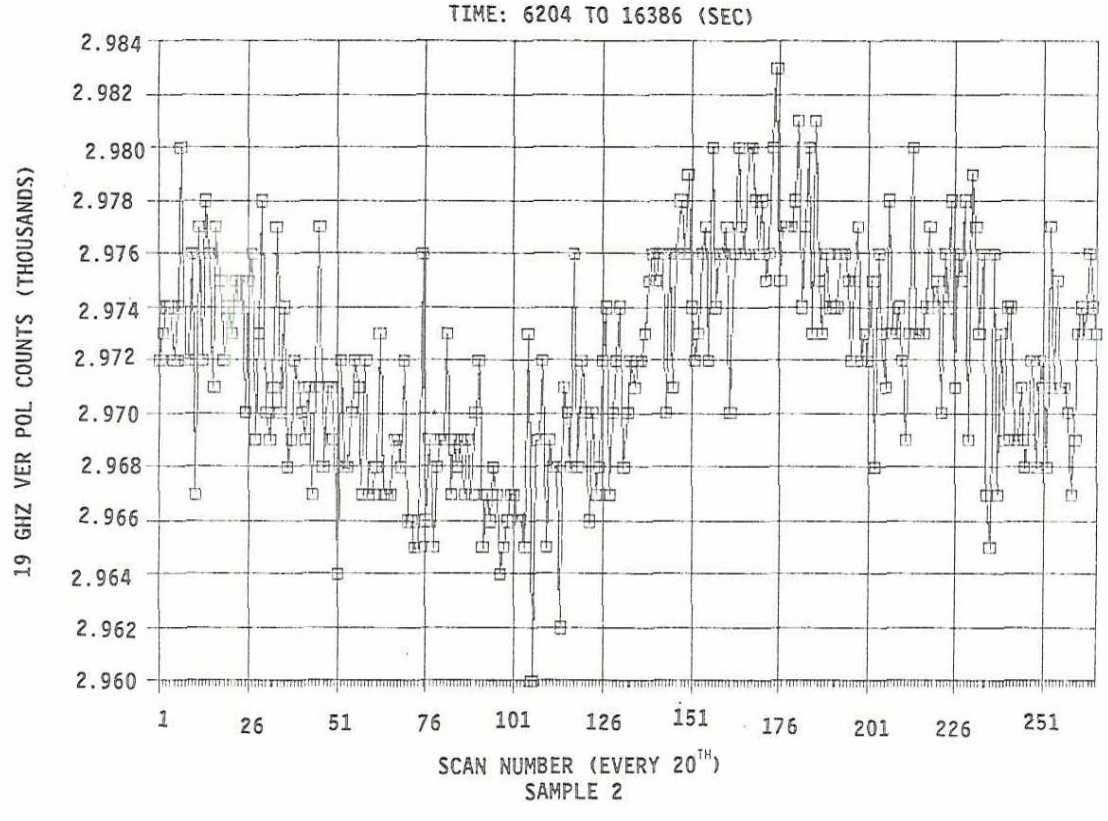

FIGURE 4.10 VARIATION OF 19 GHz VERTICAL POLARIZATION
HOT LOAD SAMPLES 1 AND 2 (REV 438)

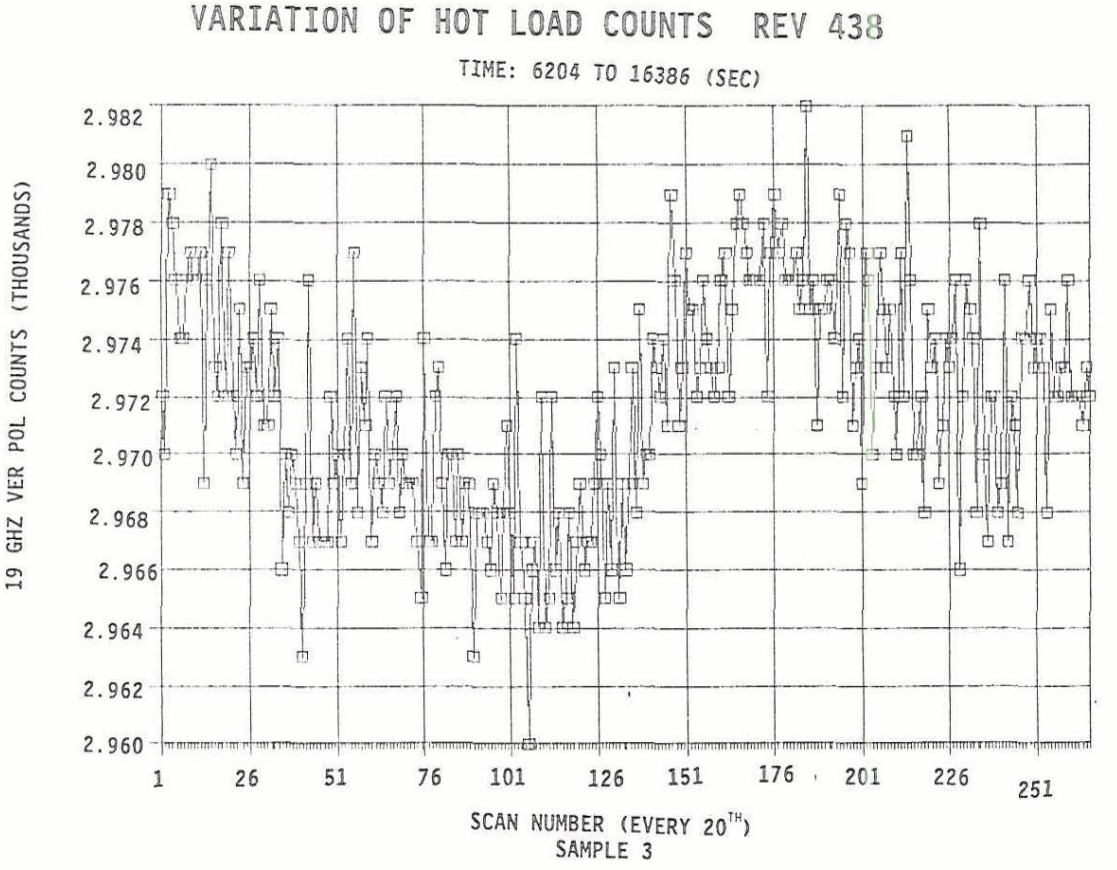

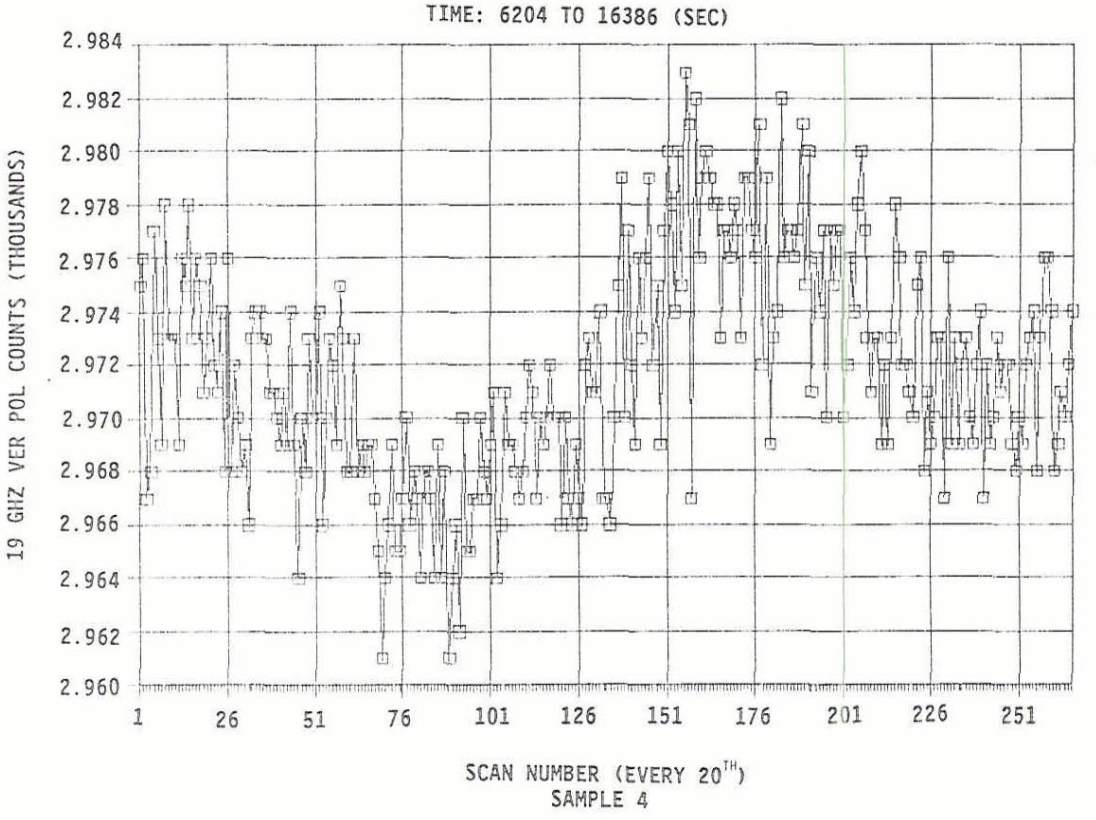

FIGURE 4.11 VARIATION OF 19 GHz VERTICAL POLARIZATION HOT LOAD SAMPLES 3 AND 4 (REV 438)

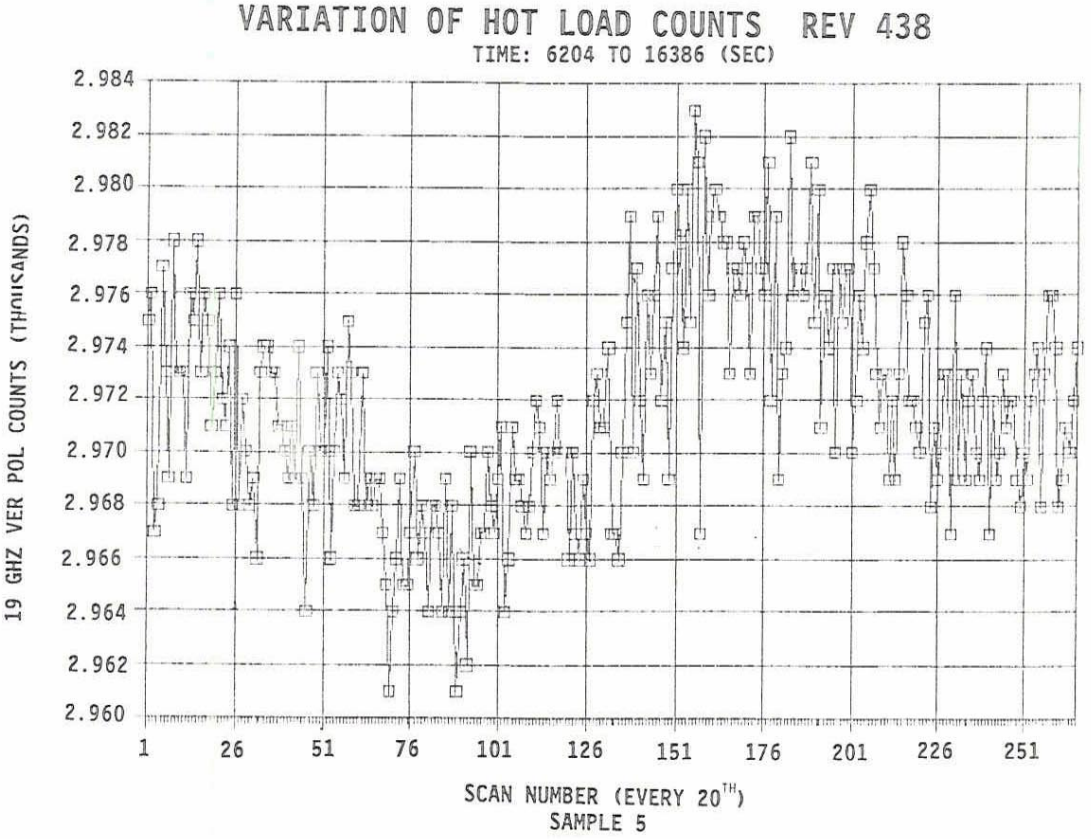

FIGURE 4.12 VARIATION OF 19 GHz VERTICAL POLARIZATION HOT LOAD SAMPLE 5 (REV 438)

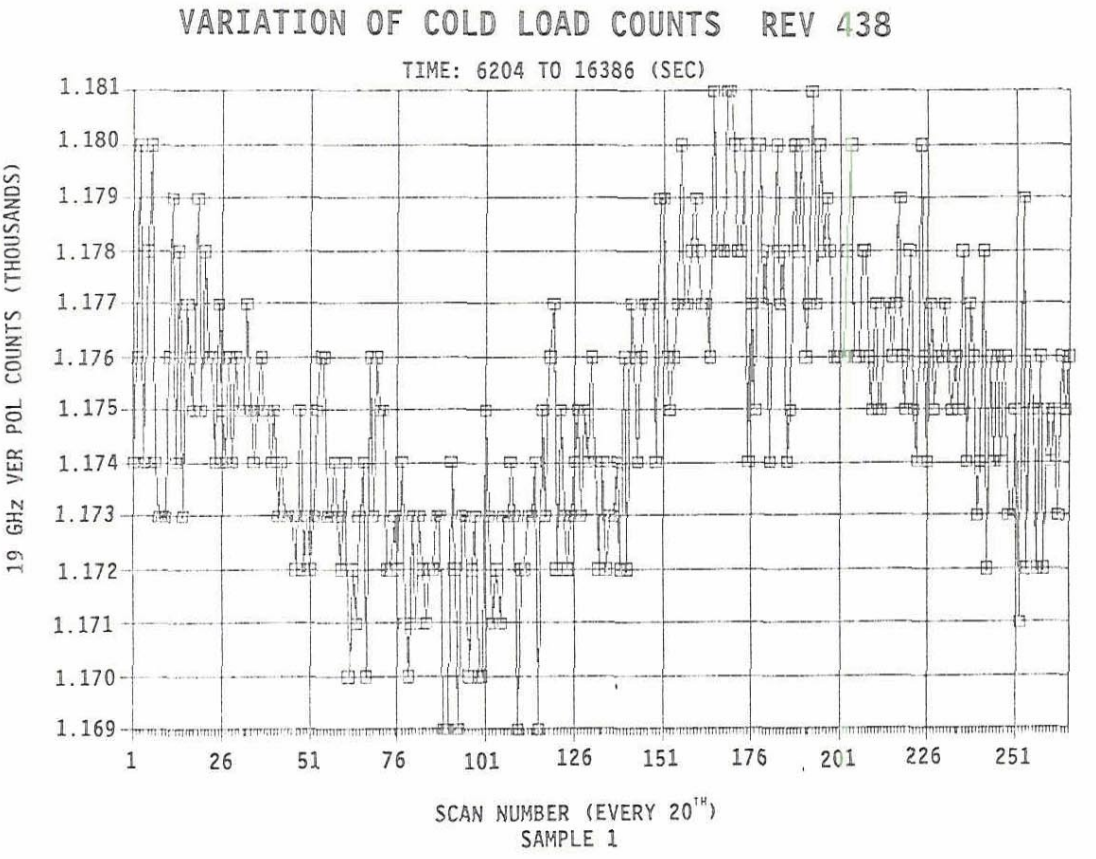

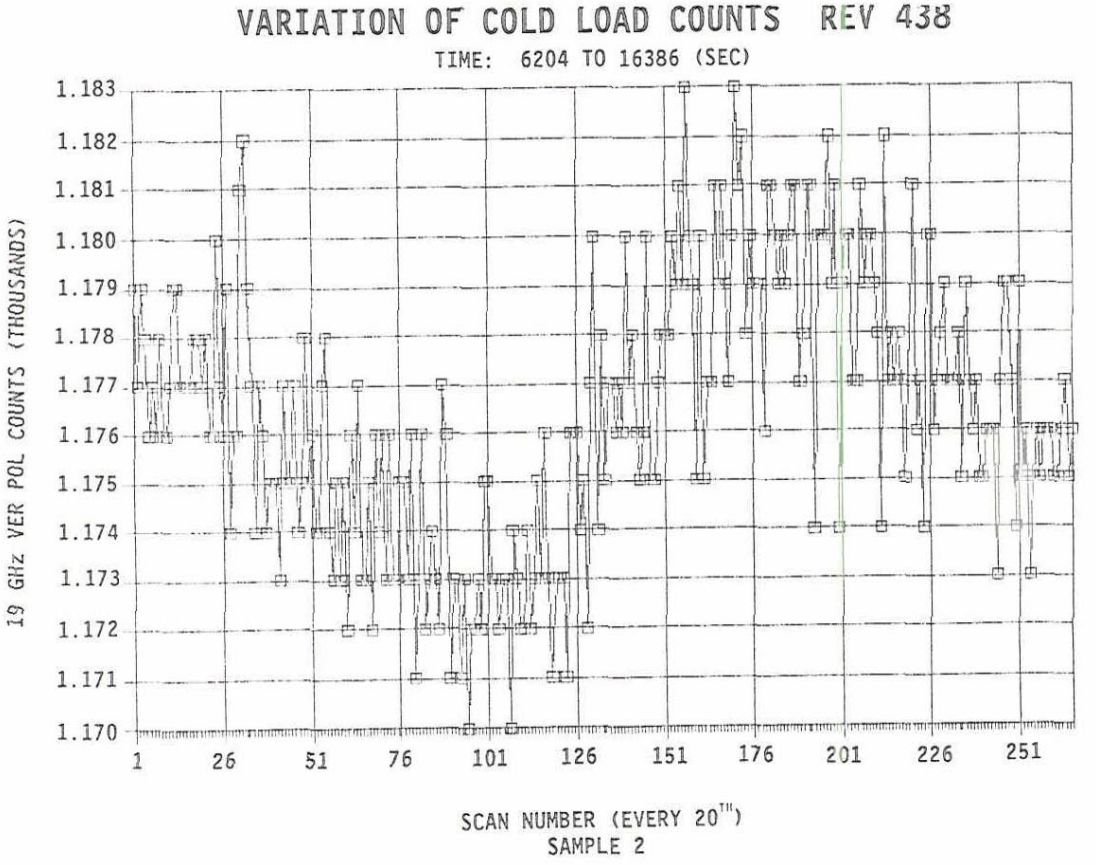

Figure 4.13 Variation of 19 GHz Vertical Polarization Cold Load Samples 1 and 2 (REV 438)

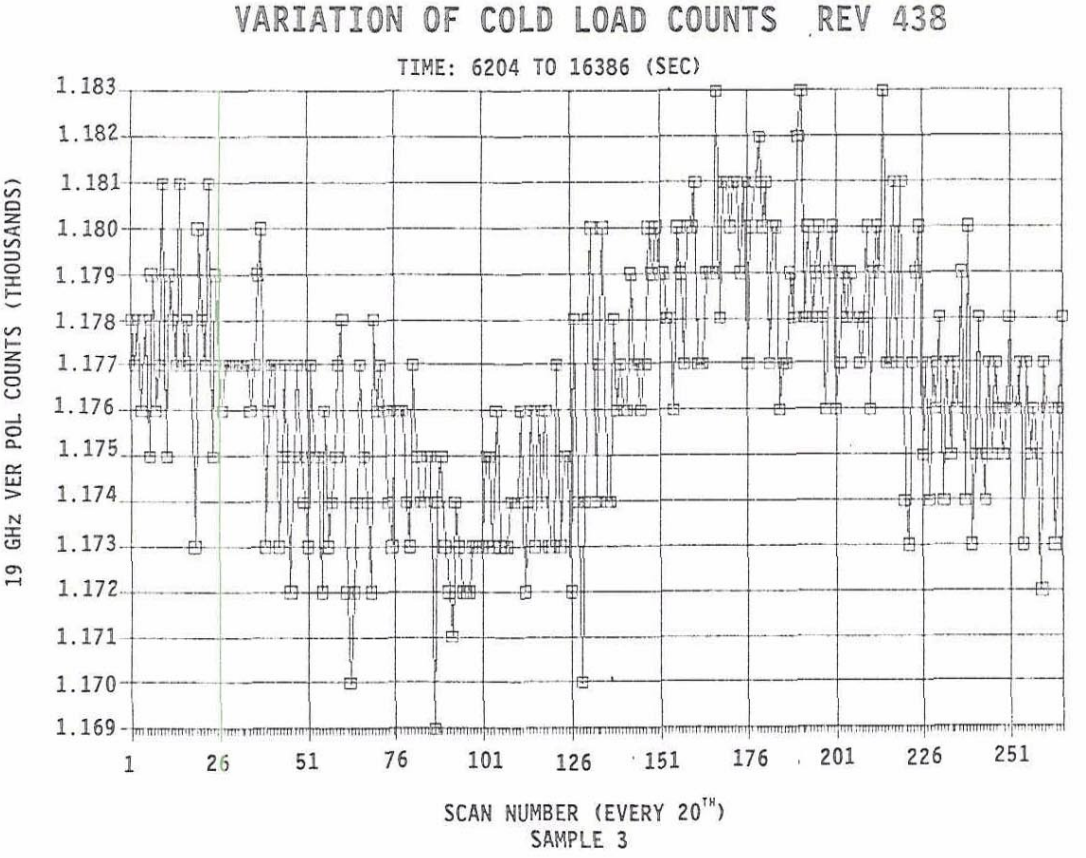

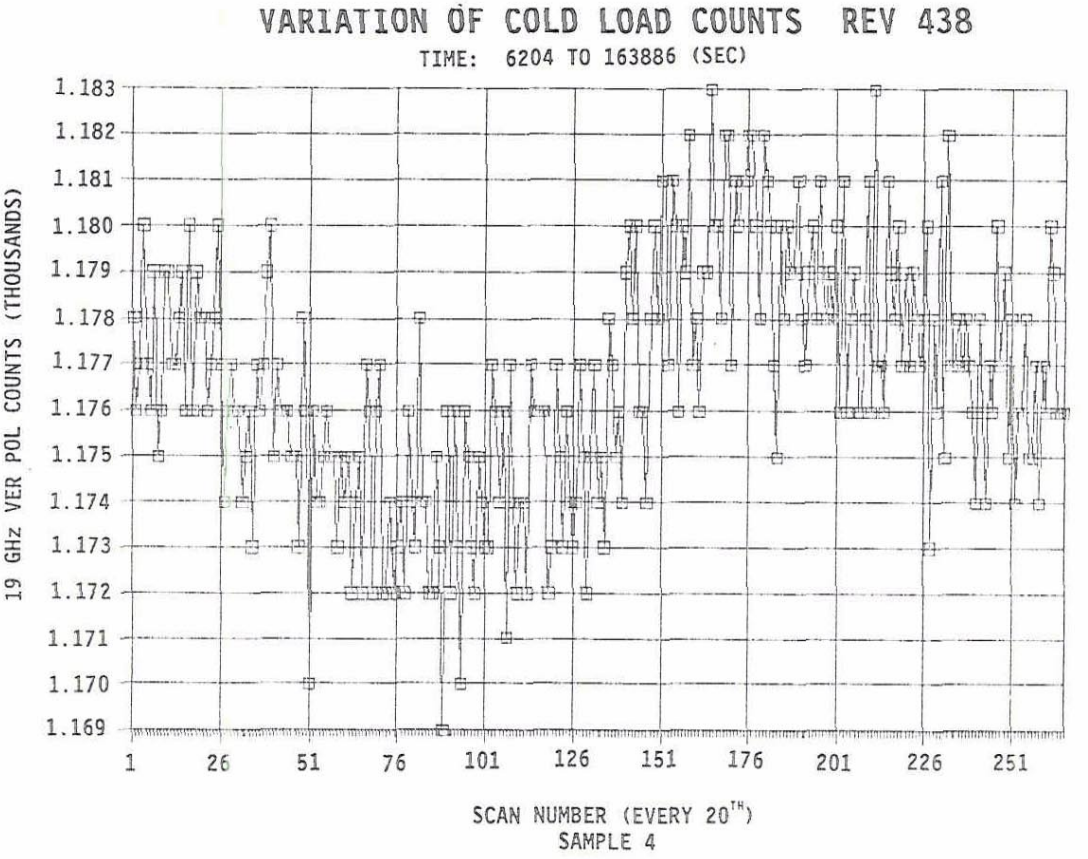

FIGURE 4.14 VARIATION OF 19 GHz VERTICAL POLARIZATION COLD LOAD SAMPLES 3 AND 4 (REV 438)

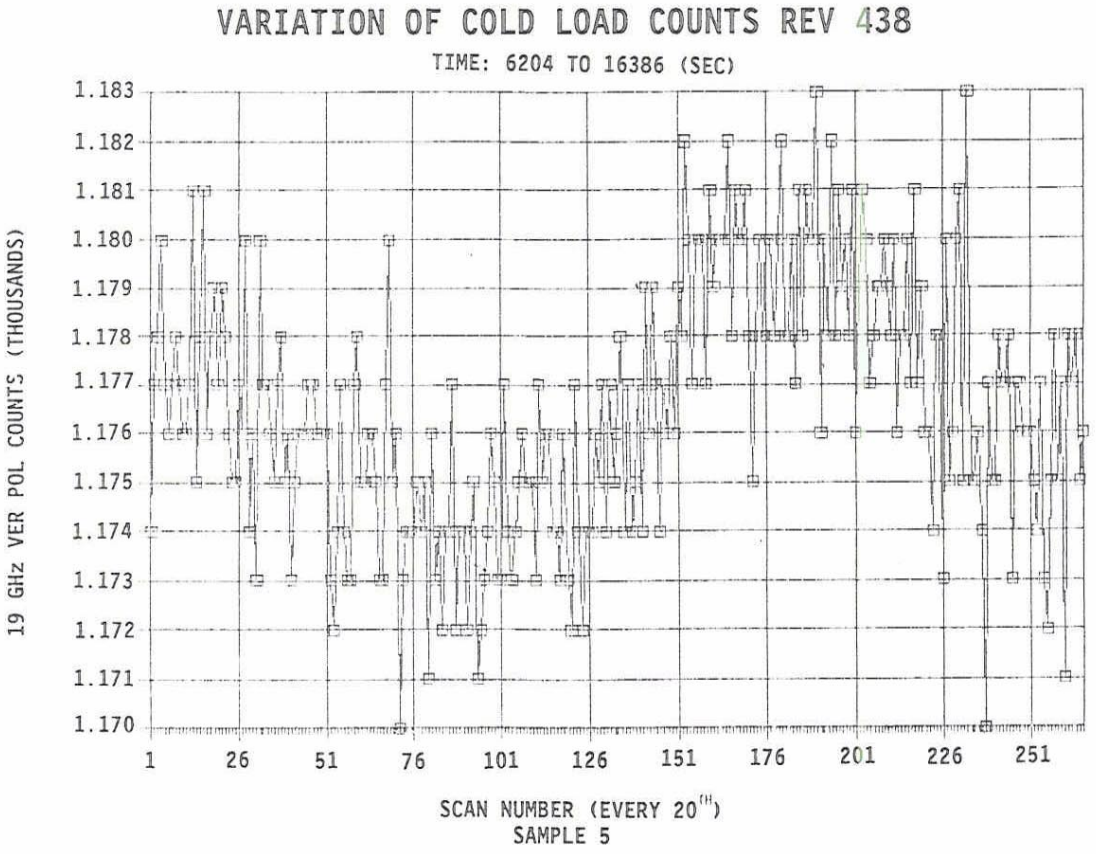

FIGURE 4.15 VARIATION OF 19 GHz VERTICAL POLARIZATION COLD LOAD SAMPLE 5 (REV 438)

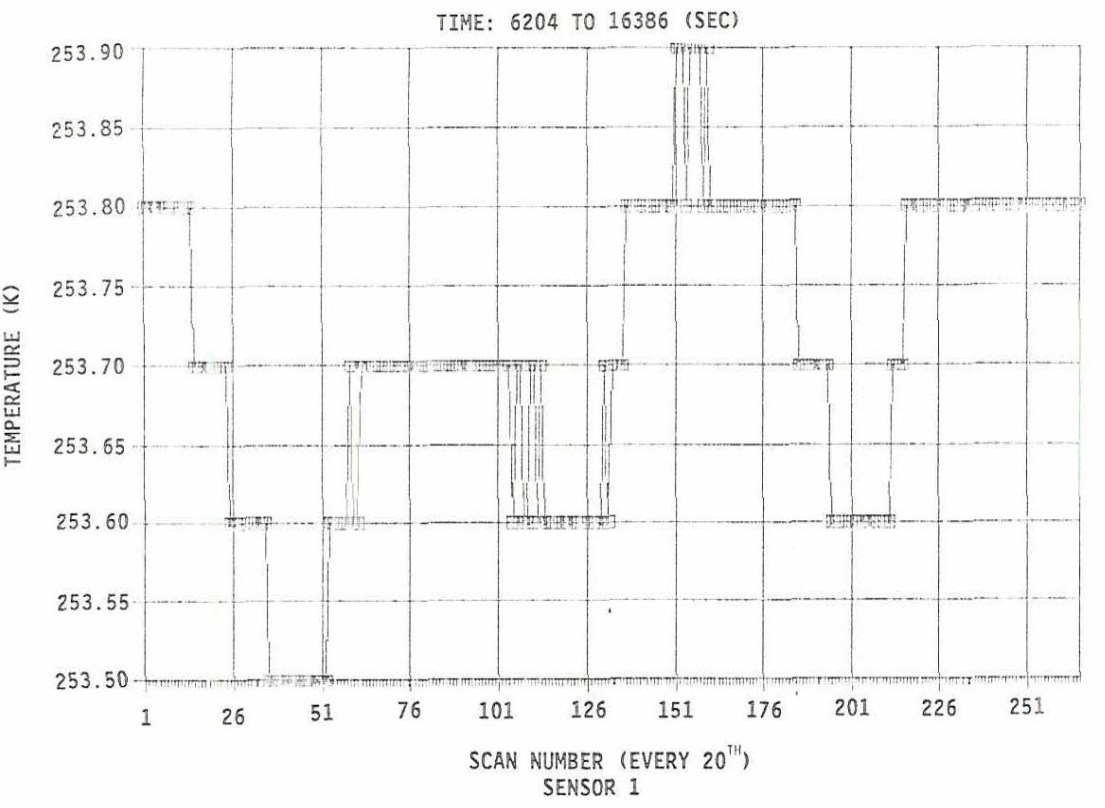

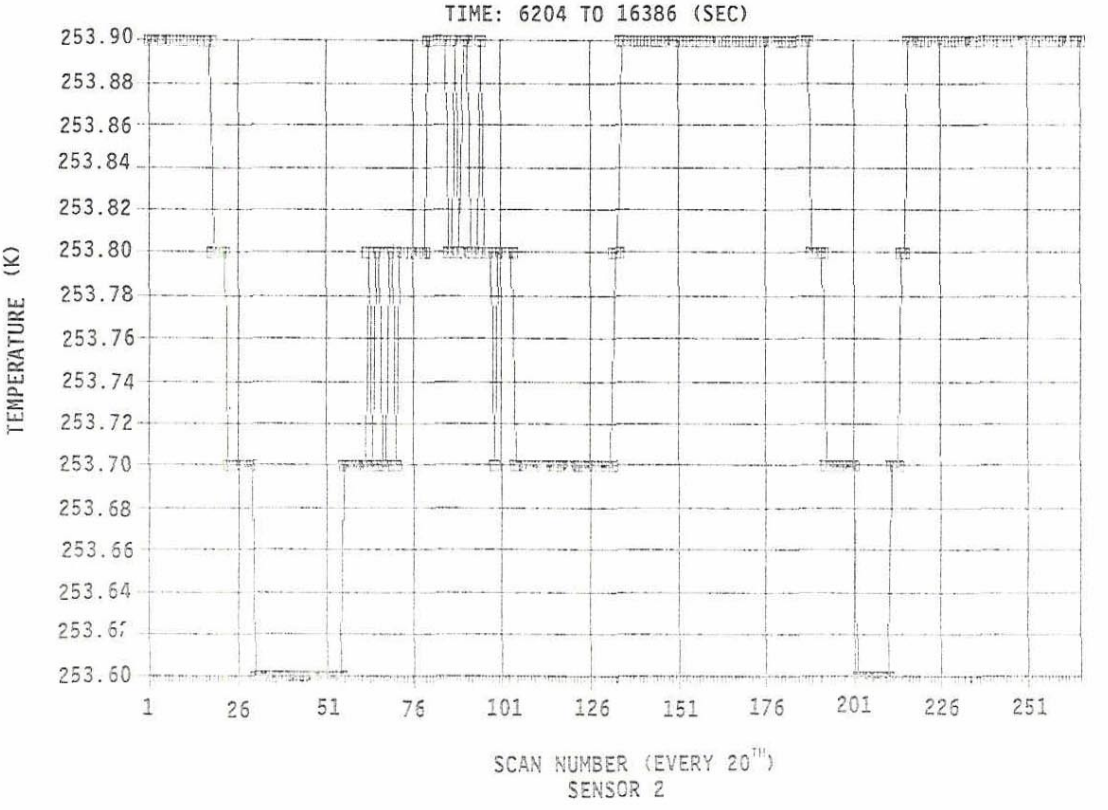

FIGURE 4.16 VARIATION OF HOT LOAD TEMPERATURE SENSORS 1 AND 2 (REV 438)

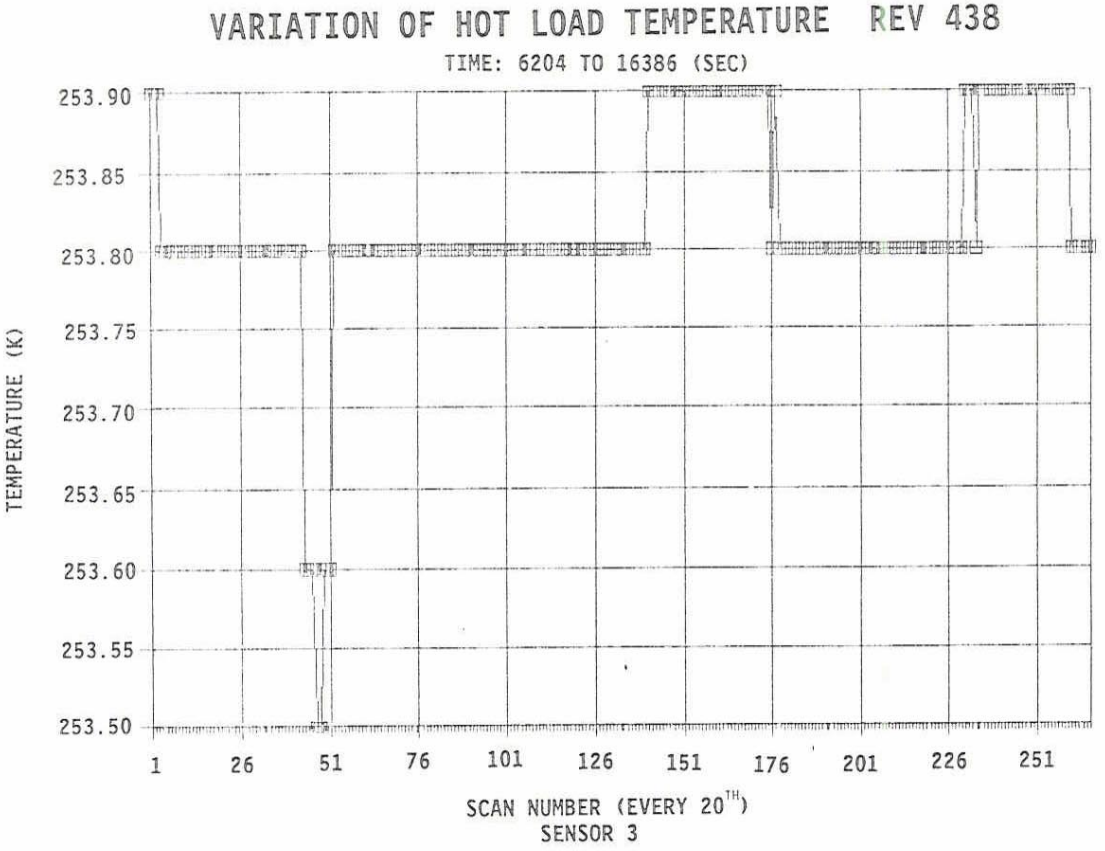

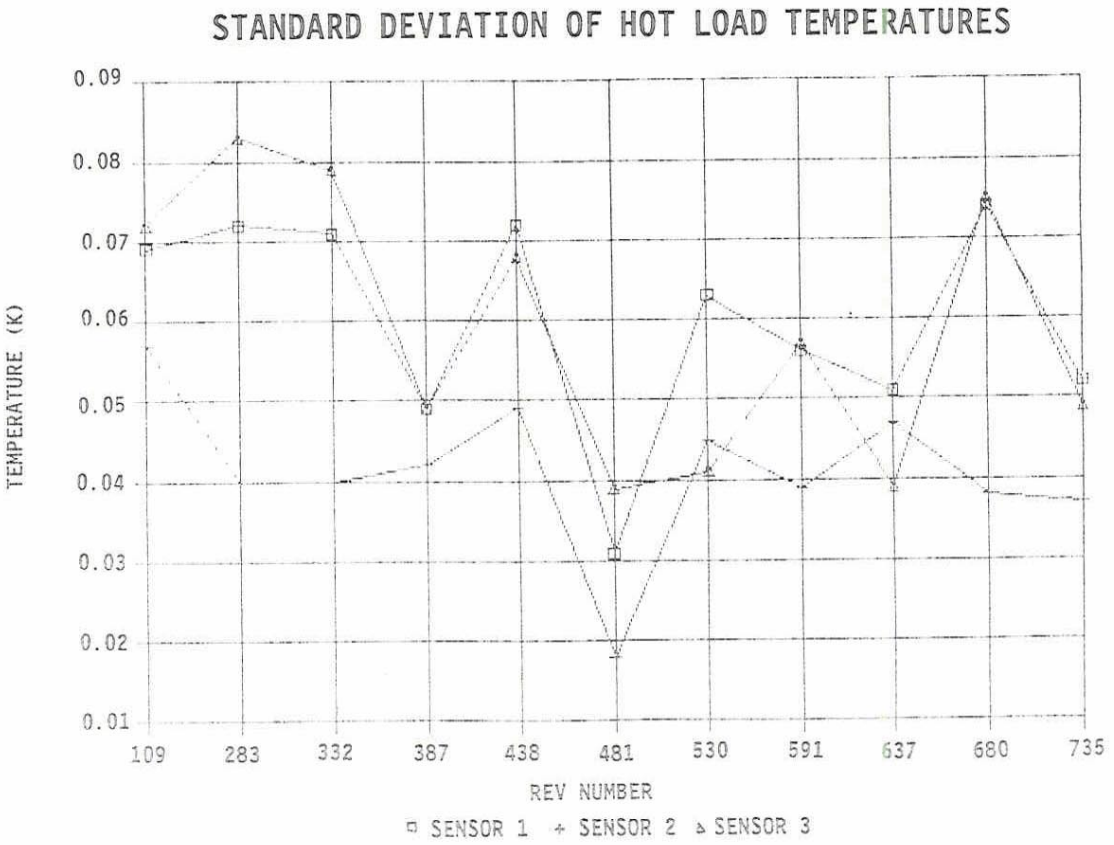

FIGURE 4.17 STANDARD DEVIATION OF HOT LOAD TEMPERATURES

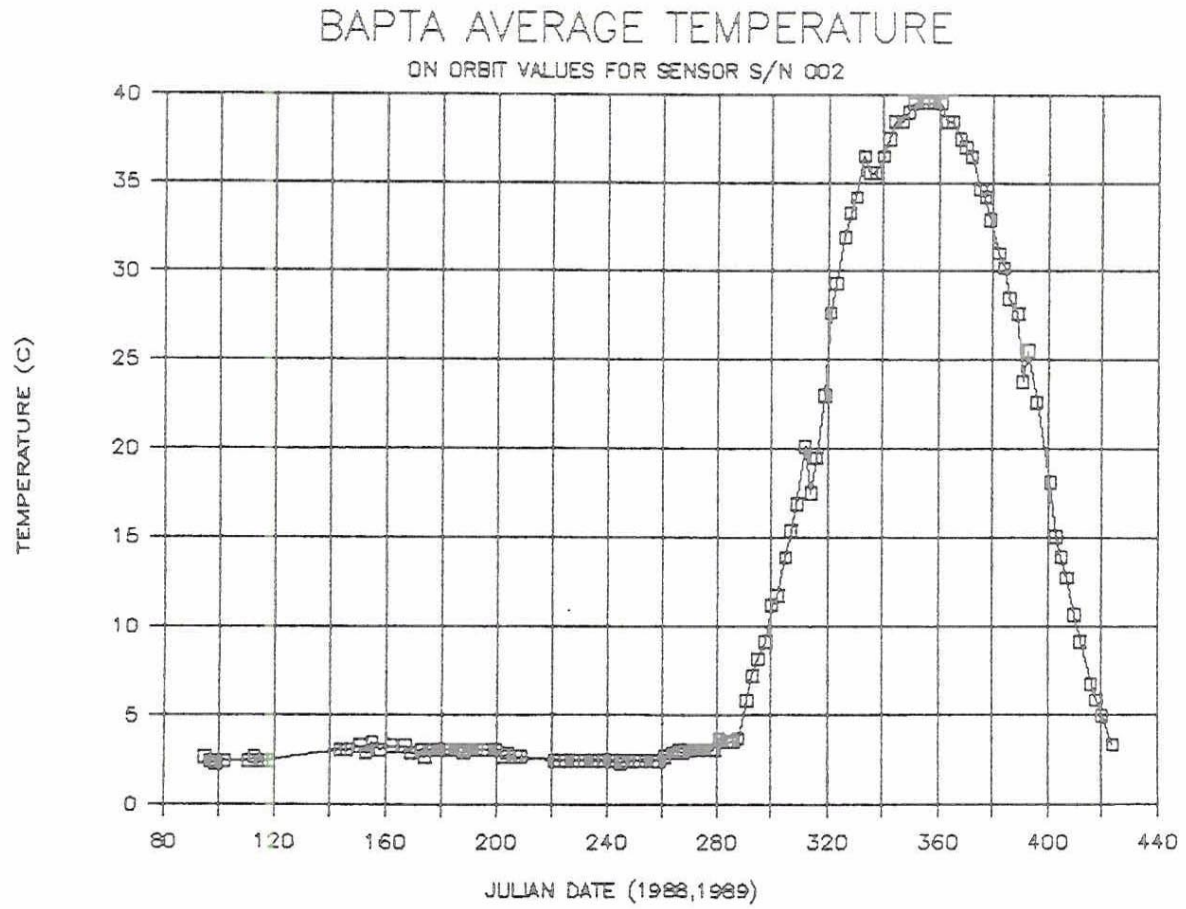

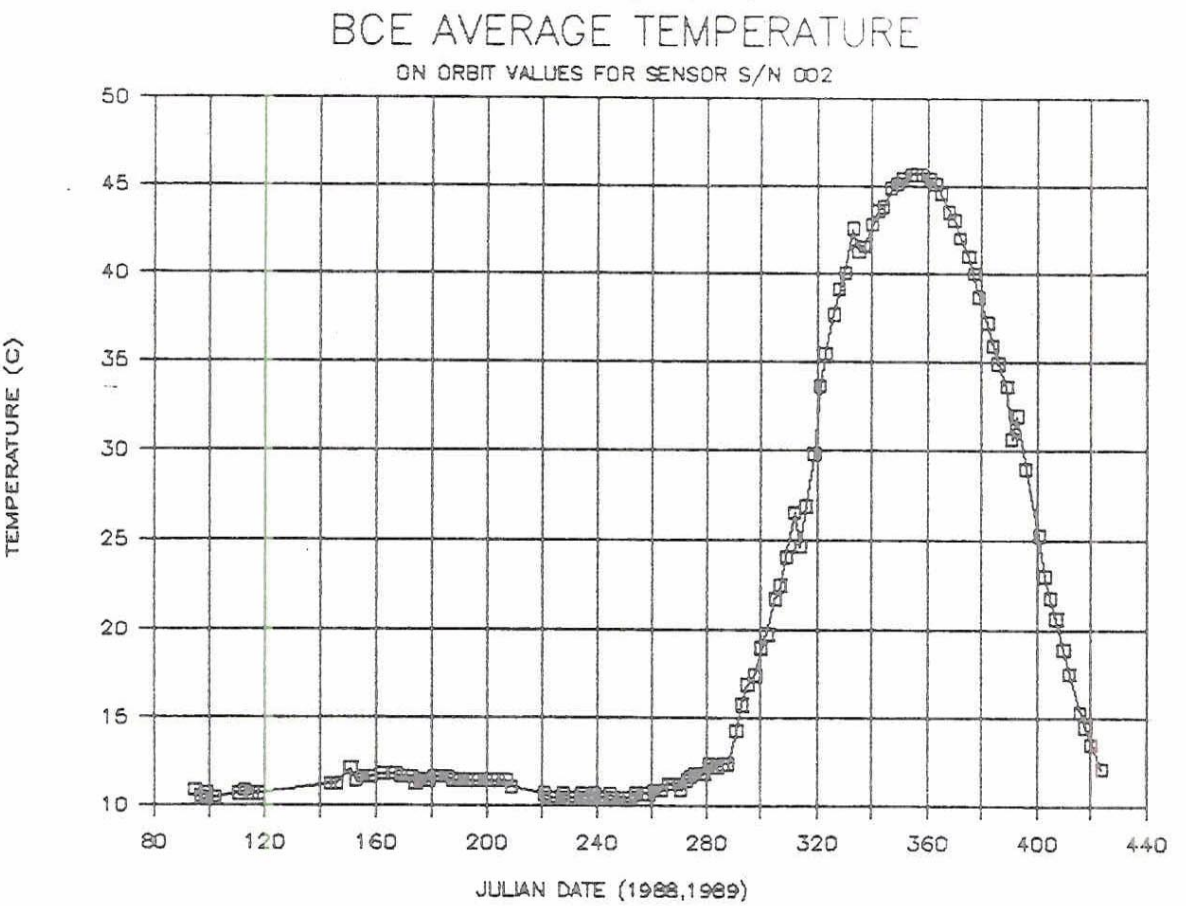

FIGURE 4.18 LONG TERM VARIATION OF BAPTA AND BAPTA CONTROL ELECTRONICS BCE TEMPERATURES.

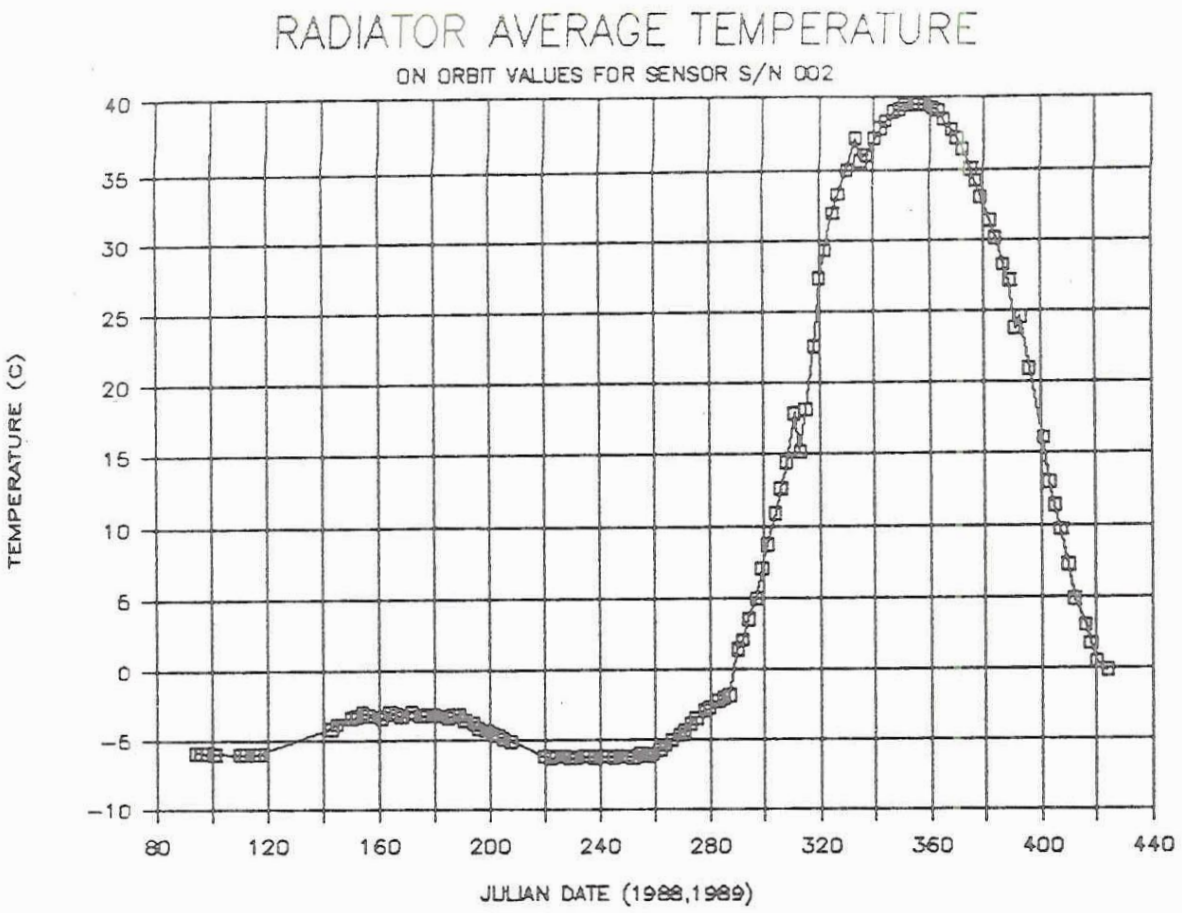

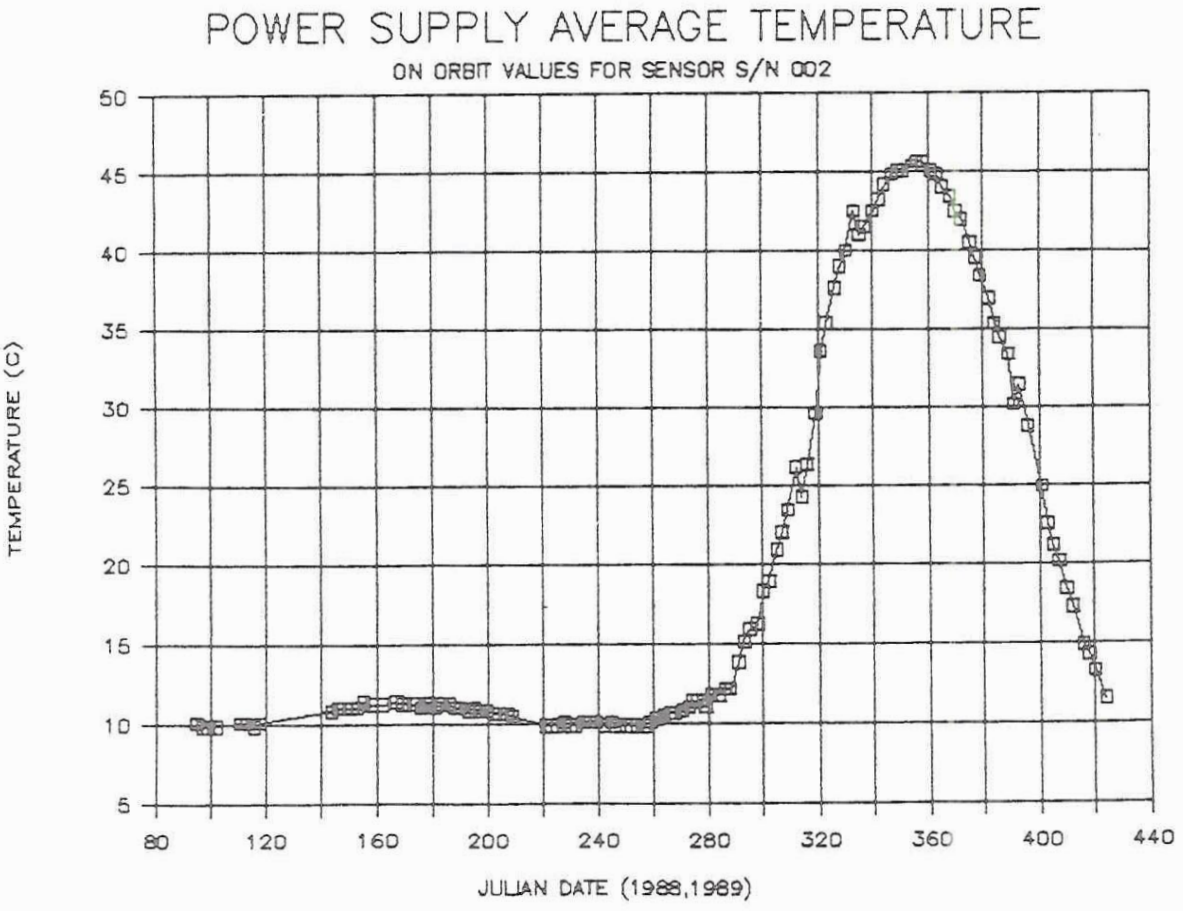

FIGURE 4.19 LONG TERM VARIATION OF RADIATOR AND POWER SUPPLY TEMPERATURES.

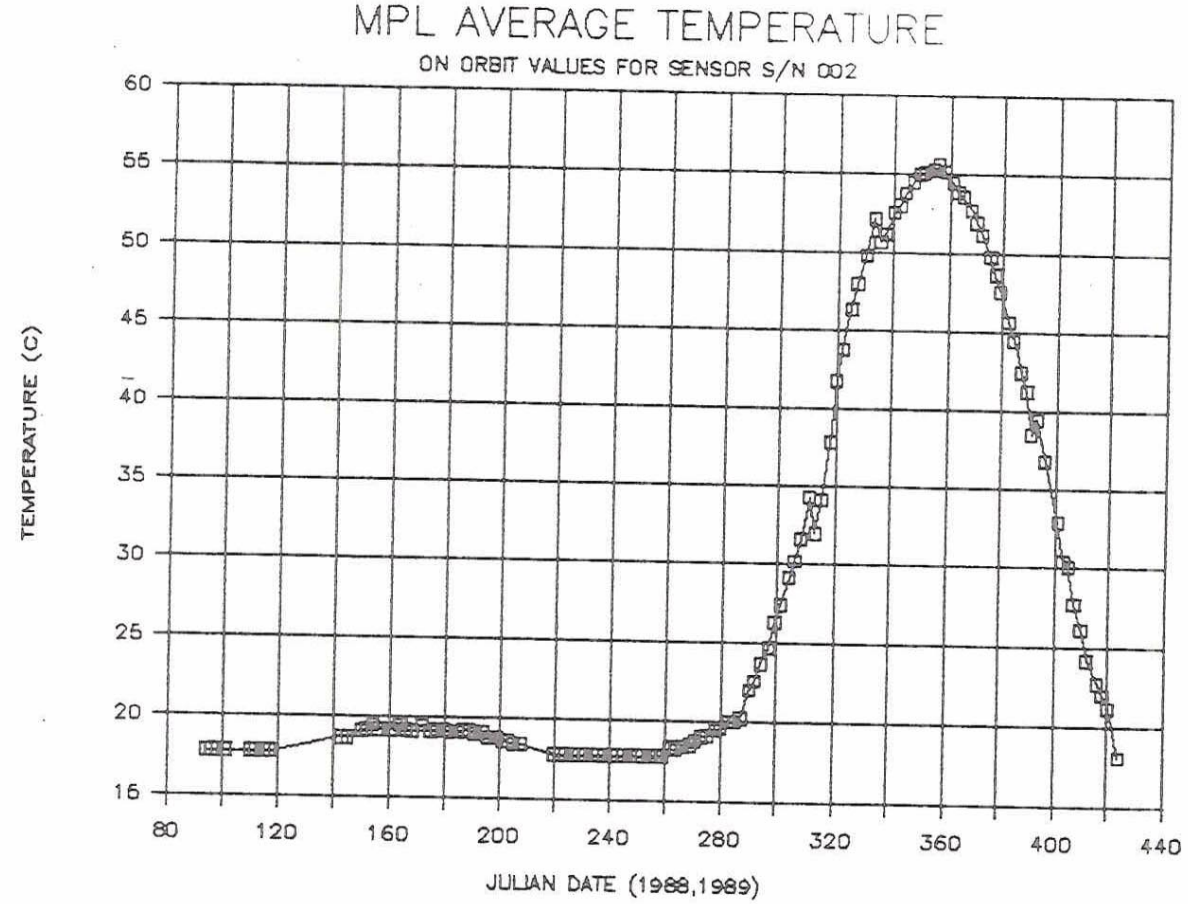

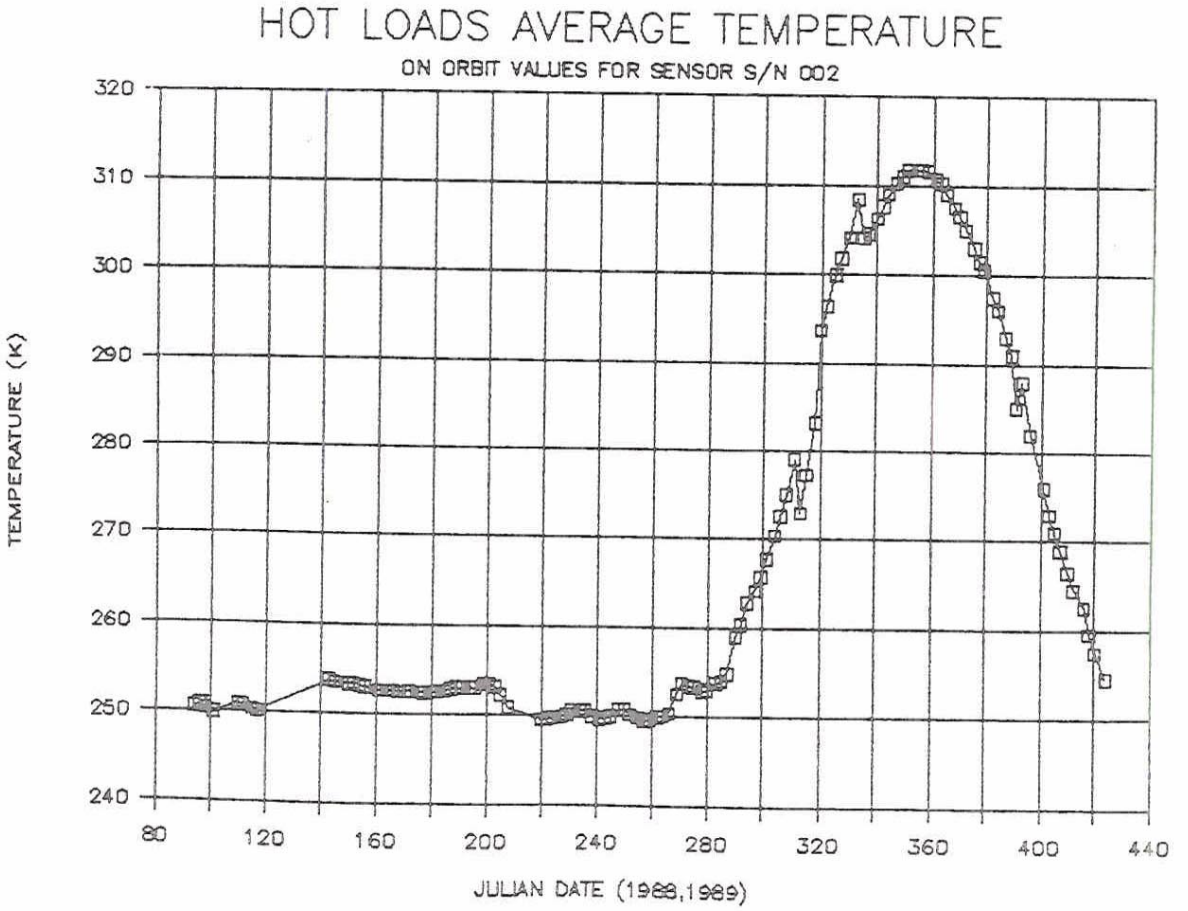

FIGURE 4.20 LONG TERM VARIATION OF MIXER/PREAMP ELECTRONICS (MPL) AND HOT LOAD CALIBRATION TEMPERATURES.

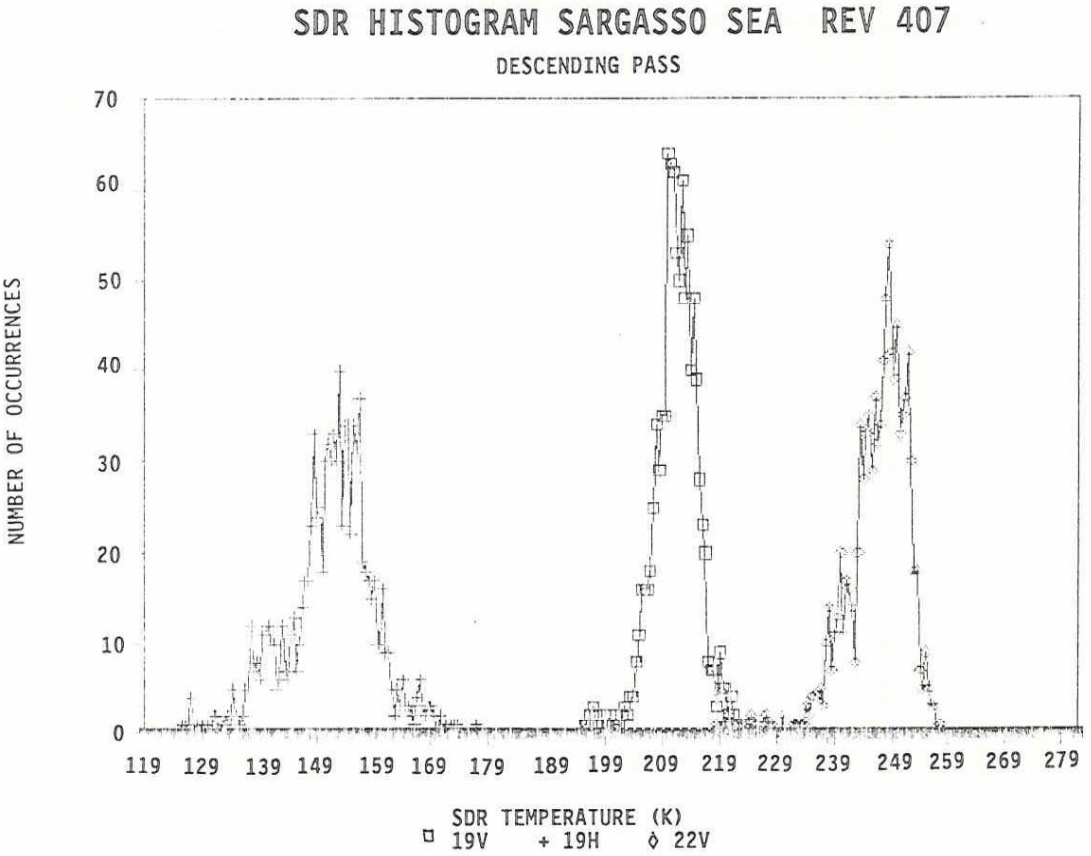

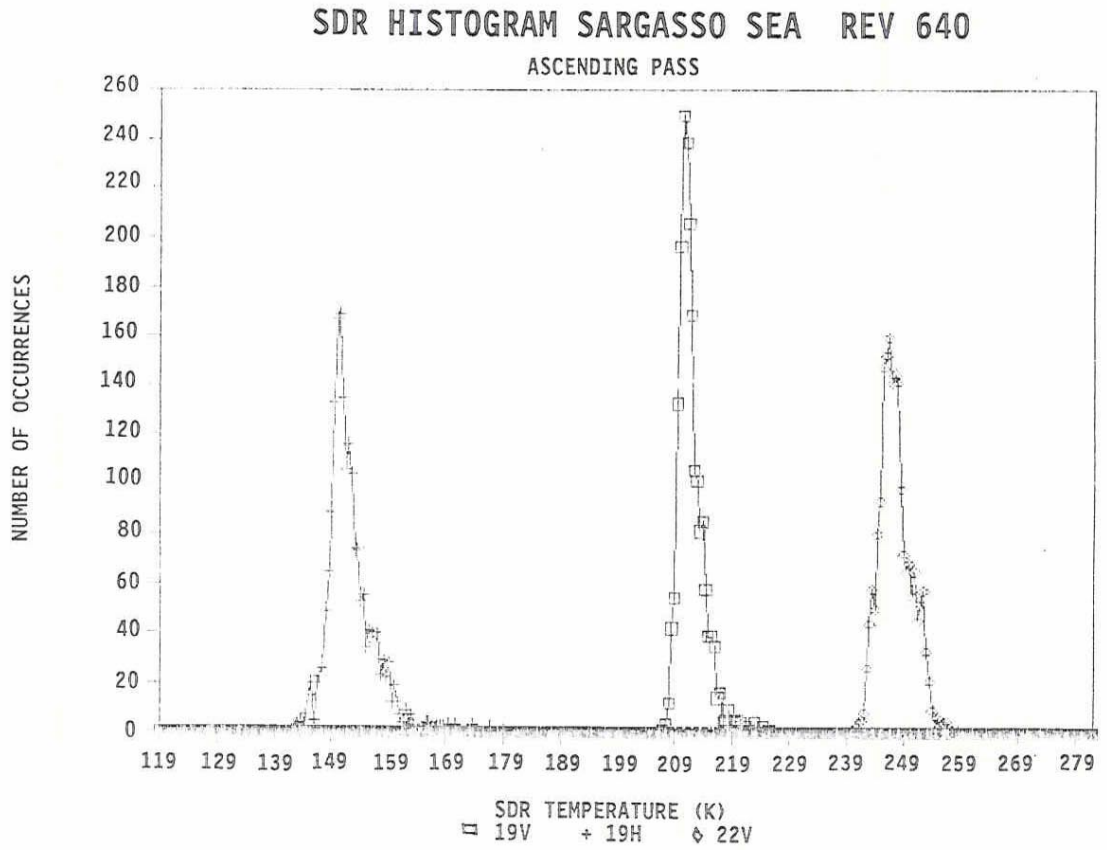

FIGURE 4.21 19 AND 22 GHZ HISTOGRAMS OF THE SARGASSO SEA
REVS 407 (7/18/87) AND 640 (8/4/87)

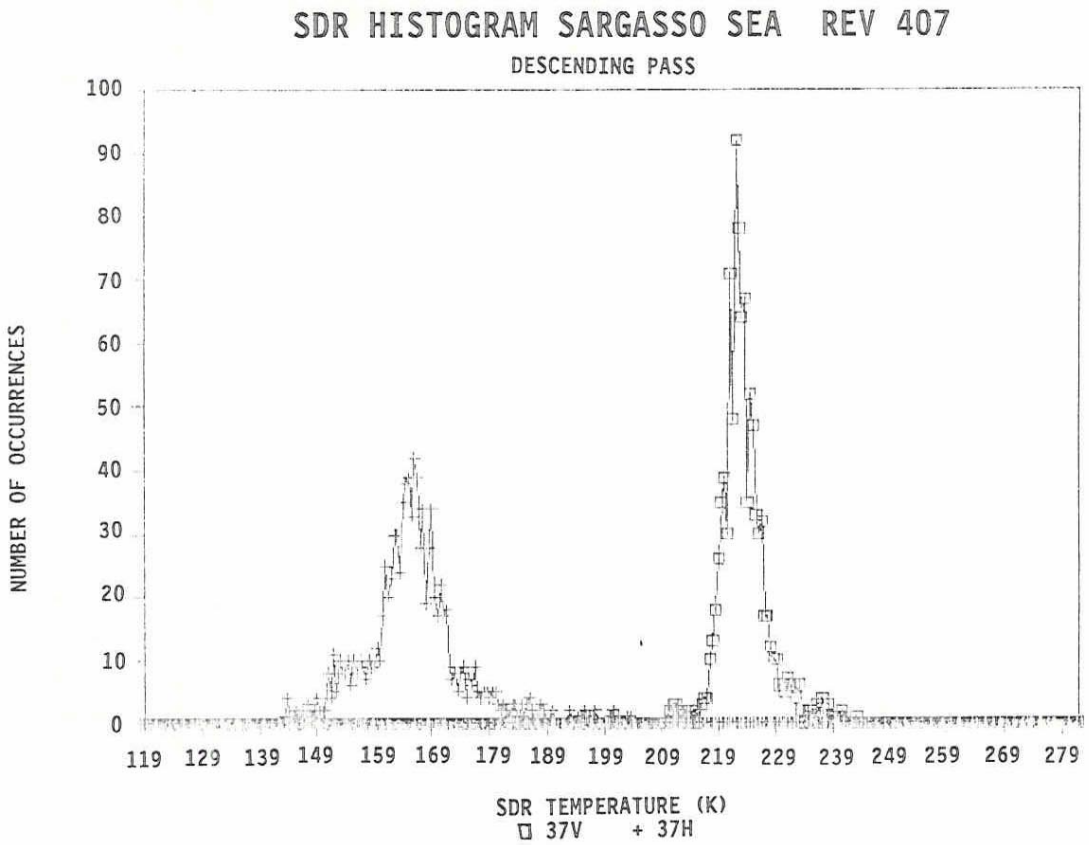

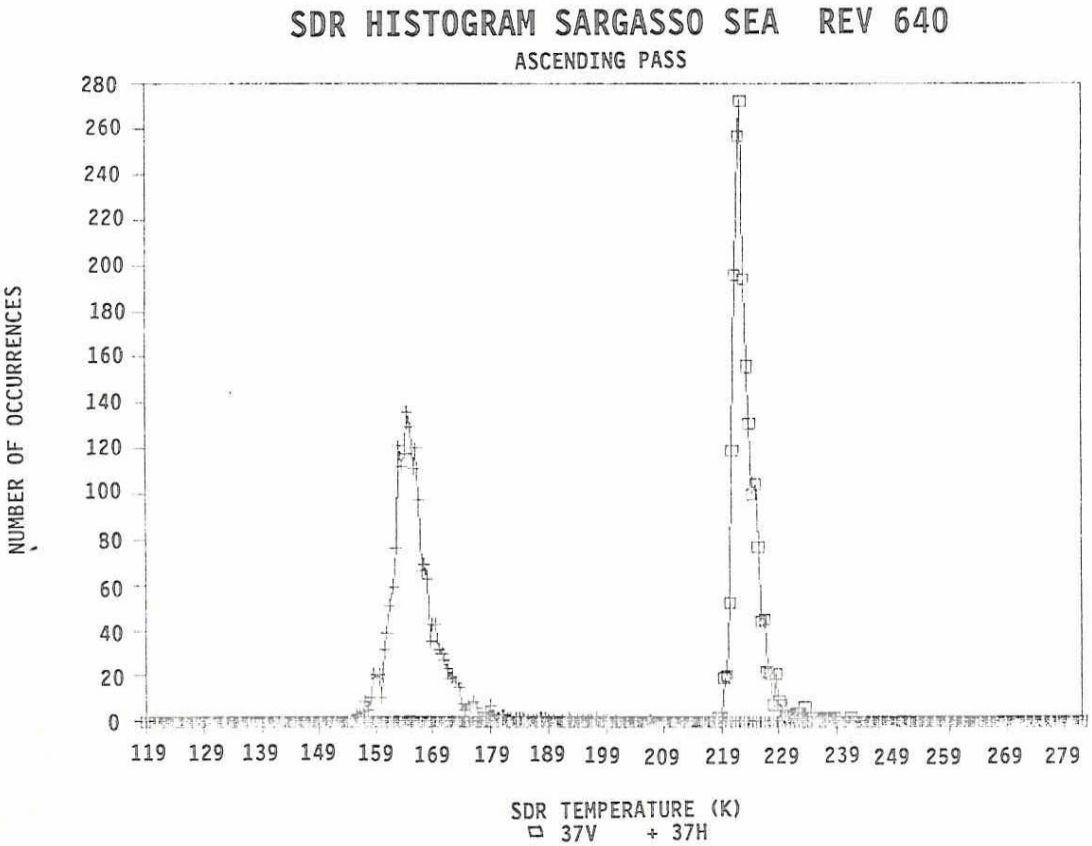

FIGURE 4.22 37 GHZ HISTOGRAMS OF THE SARGASSO SEA REVS 407 (7/18/87) AND 640 (8/4/87)

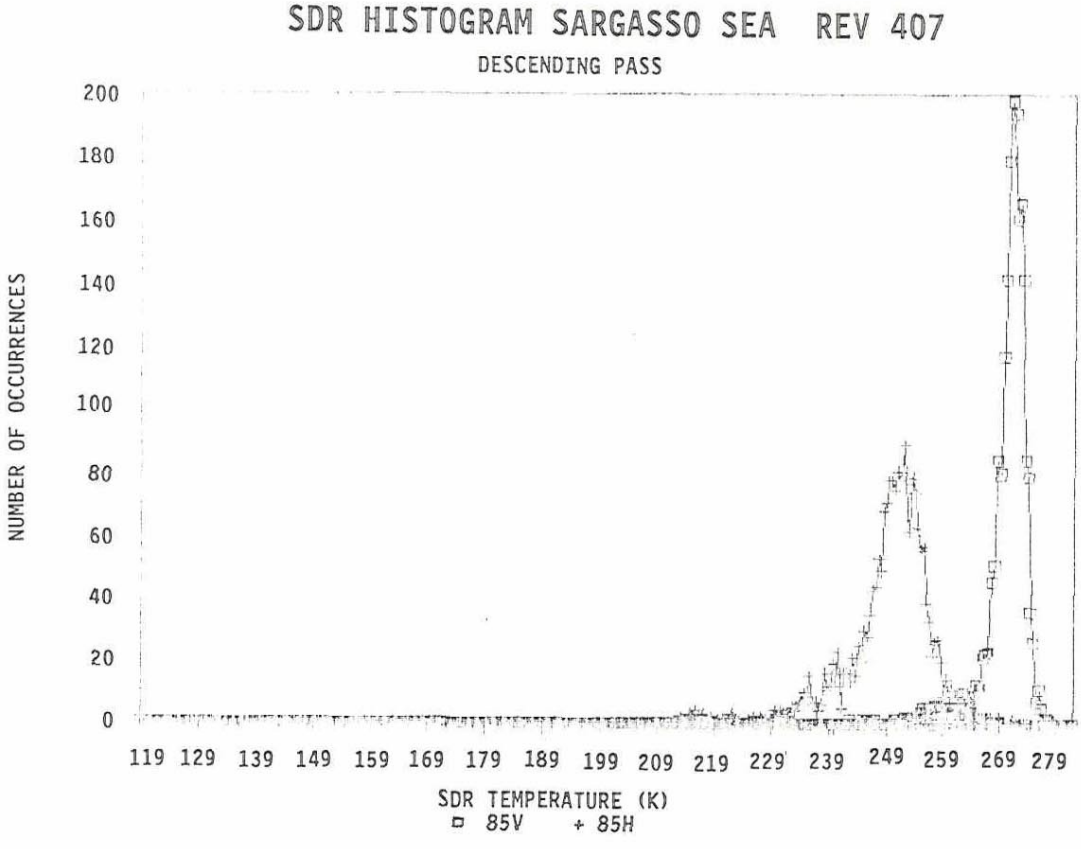

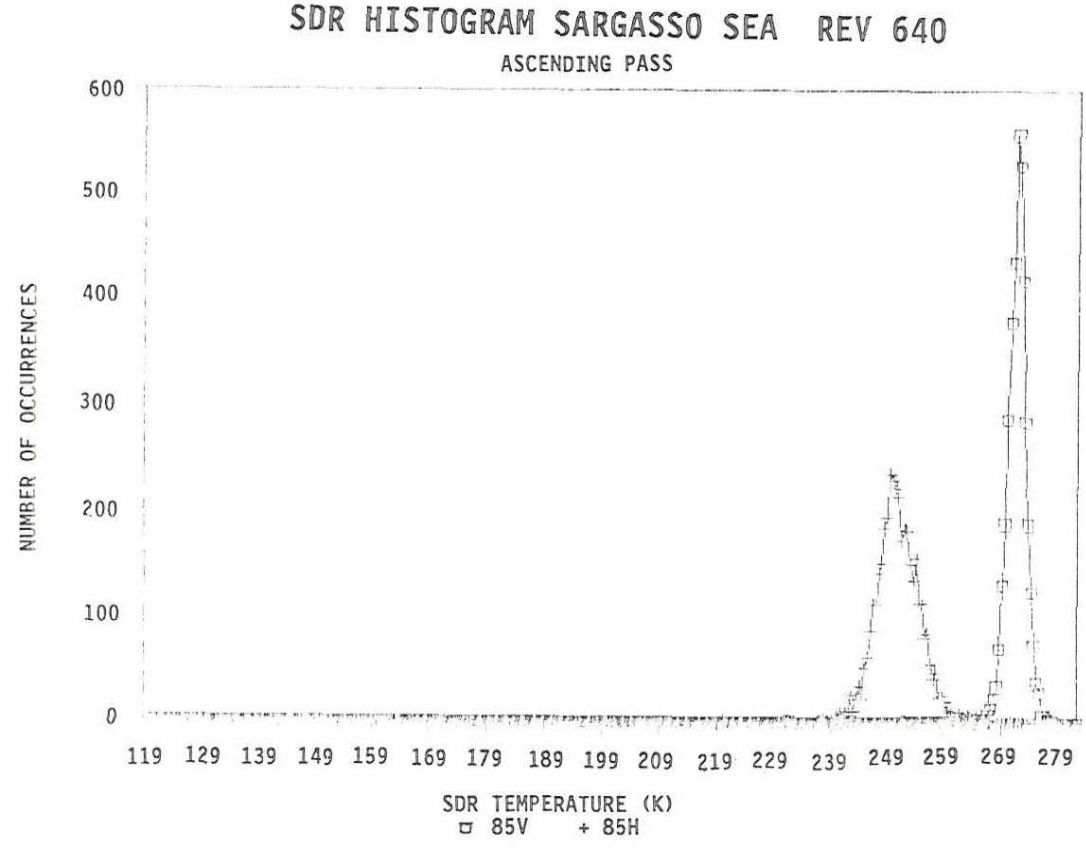

FIGURE 4.23 85 GHZ HISTOGRAMS OF THE SARGASSO SEA
REVS 407 (7/18/87) AND 640 (8/4/87)

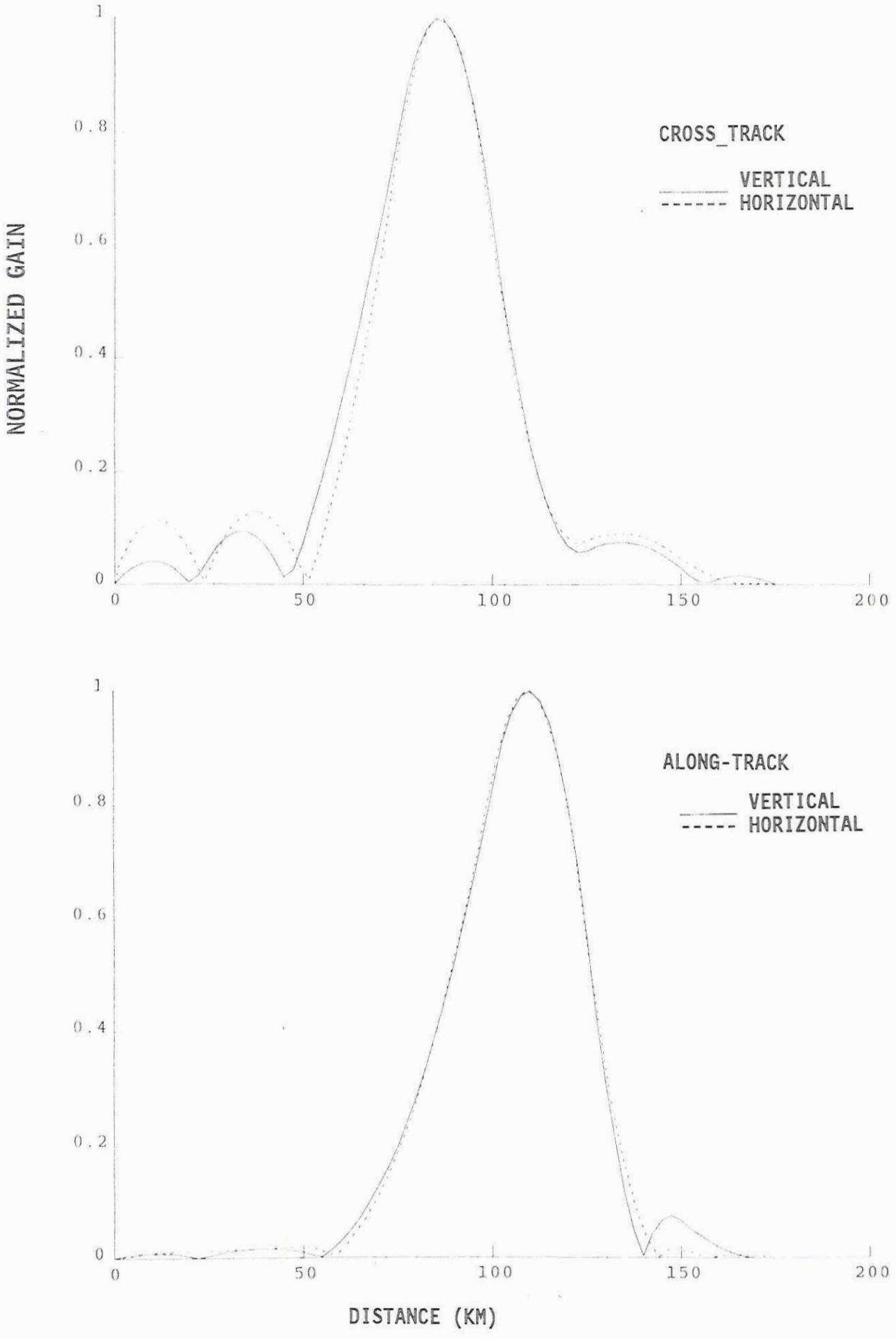

FIGURE 4.24 37 GHZ DERIVED ANTENNA GAIN FUNCTION

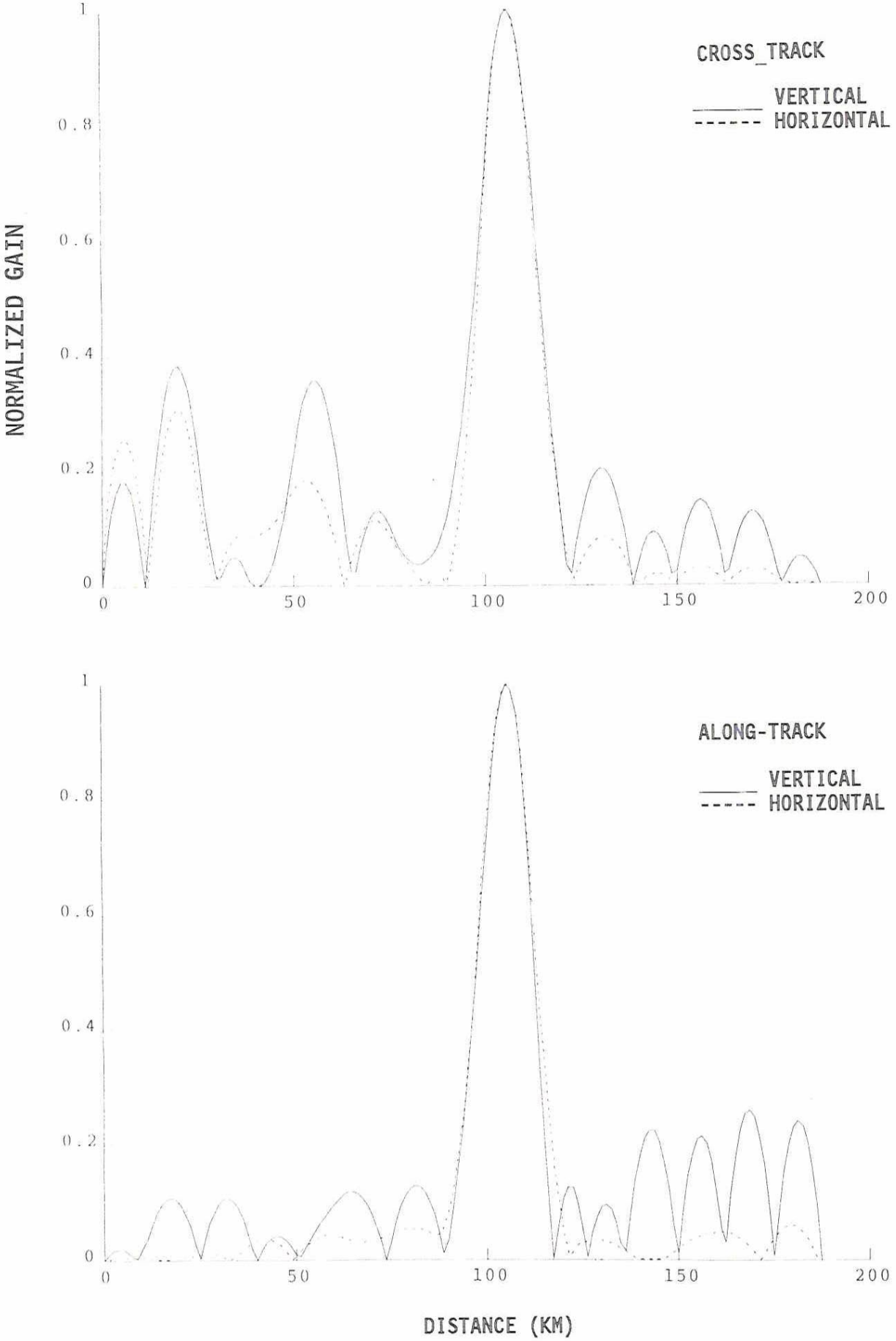

FIGURE 4.25 85 GHZ DERIVED ANTENNA GAIN FUNCTION

5.0 INSTRUMENT ABSOLUTE CALIBRATION

5.1 INTRODUCTION

In general high gain antennas, like the SSM/I's which has a gain of 53 dB at 85.5 GHz, receive radiation primarily over a relatively narrow "main-beam" or solid angle. The half-power beamwidths of the SSM/I are given in Table 2.1. However some radiation is received in antenna sidelobes in directions outside of the mainbeam and from reflections from the spacecraft and direct spillover into the feed horn. The measurement and calibration of the total radiation entering the feed horn from all directions, termed antenna temperature, is described in Section 3.1. The contributions of spurious radiation from outside of the mainbeam to the antenna temperature must be accounted for in order to obtain the mean radiance or brightness temperature from the scene over the mainbeam solid angle which is the quantity to be used in the environmental algorithms. While this involves an antenna pattern correction and a correction for cross polarization, as discussed in Section 3.2, it is the determination of the accuracy of the end-to-end calibration of absolute mainbeam brightness temperature which is discussed in this section. The partial restoration of spatial detail which has been lost due to spatial filtering or smoothing by the antenna, which also involves an antenna pattern correction and is particularly important in regions of strong brightness temperature gradients, such as land-water boundaries, is not considered in this section but is discussed in Section 3.2.3. Only regions which are homogeneous or with nearly linear brightness temperature gradients will be considered here.

The evaluation of the absolute calibration of the SSM/I brightness temperatures is an extremely formidable task due to the difficulty in obtaining an accurate standard with which to compare the SSM/I. Two different methods are used. First is a comparison of the SSM/I brightness temperatures with those derived from aircraft underflight measurements made during satellite overpass using the SSM/I Simulator. The SSM/I Simulator is a set of radiometers, with the same frequencies, polarizations, and incidence angle as the SSM/I, mounted in the NRL RP-3A aircraft. The second method is a comparison of the SSM/I brightness temperatures with those calculated using theoretical models. These two approaches are discussed in turn in Sections 5.1 and 5.2.

5.2 AIRCRAFT RADIOMETRIC UNDERFLIGHTS

A total of 18 underflights of the SSM/I Simulator were made. They are summarized in Table 5.1. Of these one flight had to be aborted due to aircraft mechanical problems before data could be obtained and there is no SSM/I data for five of the flights due to problems either at the data relay sites or at FNOC. One of the flights was made specifically in support of the land parameter validation and one in support of the sea ice validation. Ten flights were over the ocean and are used for the brightness temperature calibration. Eight of these flights were off the Virginia coast over one of the NOAA data buoys and two were southeast of

Iceland. Six of the ocean flights were under clear skies or with only light scattered clouds.

TABLE 5.1

NRL RP-3A AIRCRAFT SIMULATOR FLIGHTS

DATE	LOCATION	STATUS
7/15/87	Gander to Scotland (Transit)	No Simultaneous SSM/I
7/21/87	North Atlantic Ocean	* Total Cloud Cover
7/22/87	Scotland to Iceland (Transit)	No Simultaneous SSM/I
7/23/87	Atlantic Ocean (SE of Iceland)	* Total Cloud Cover
7/30/87	Iceland to Gander (Transit)	No Simultaneous SSM/I
8/13/87	Saskatchewan	* Land Validation
8/18/87	Atlantic Ocean (off Virginia)	Aircraft Failure
10/13/87	Atlantic Ocean (off Virginia)	* Scattered Clouds, RFI
10/22/87	Atlantic Ocean (off Virginia)	* Clear, 37 GHz Noisy
10/26/87	Atlantic Ocean (off Virginia)	* Clear
10/28/87	Atlantic Ocean (off Virginia)	No SSM/I Data
10/29/87	Atlantic Ocean (off Virginia)	* Scattered Clouds
1/23/88	Gulf of St. Lawrence	* Sea Ice Validation
1/25/88	Atlantic Ocean (off Newfoundland)	* Scattered Clouds
1/27/88	Atlantic Ocean (off Newfoundland)	No SSM/I Data
5/26/88	Atlantic Ocean (off Virginia)	* Very Heavy Clouds
10/25/88	Atlantic Ocean (off Virginia)	* Clear
10/26/88	Atlantic Ocean (off Virginia)	* Clouds

* Data Used in Cal/Val

The absolute calibration of the SSM/I Simulator was established using laboratory liquid nitrogen and room temperature black body enclosures. This determination was tested by making roof top zenith sky measurements in February, when the sky radiation is low and most accurately modeled and by making measurements of a small fresh water test tank at selected incidence angles. A further test of the absolute calibration was made by flights over a fresh water lake and a heavily vegetated area near the lake under clear, calm conditions. This test site was also overflown whenever possible on the way to the ocean test site. The NRL ocean environmental model [1] was used to calculate theoretical brightness temperatures for comparison with these measurements. The absolute brightness temperature calibration of the SSM/I aircraft simulator is believed to be ±3 to 4 K.

The ocean underflights were made in the form of a cross with one arm aligned as much as possible along an SSM/I scan line. The flight lines of the July 23, 1987 flight are shown in Figure 5.1 as an example. The legs were each about 200 km long, flown at an altitude of 8 km and required approximately one and a half hours, centered on the satellite overpass time, to fly. This flight path was repeated at an altitude of 0.5 km when weather and fuel permitted. The ideal flight conditions are clear skies with calm seas well away from land to provide a large homogeneous region with no antenna sidelobe effects. As indicated by the

SSM/I CALIBRATION UNDERFLIGHT

REV 476 JULY 23, 1987

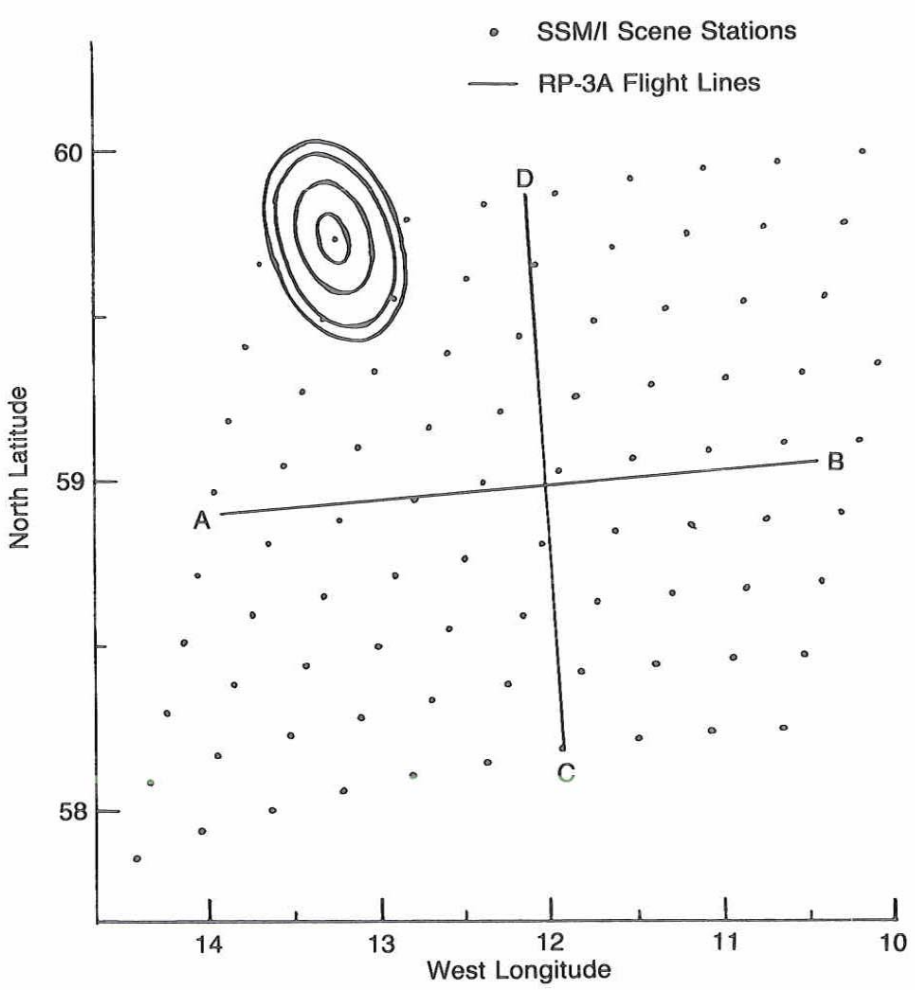

TEST AREA

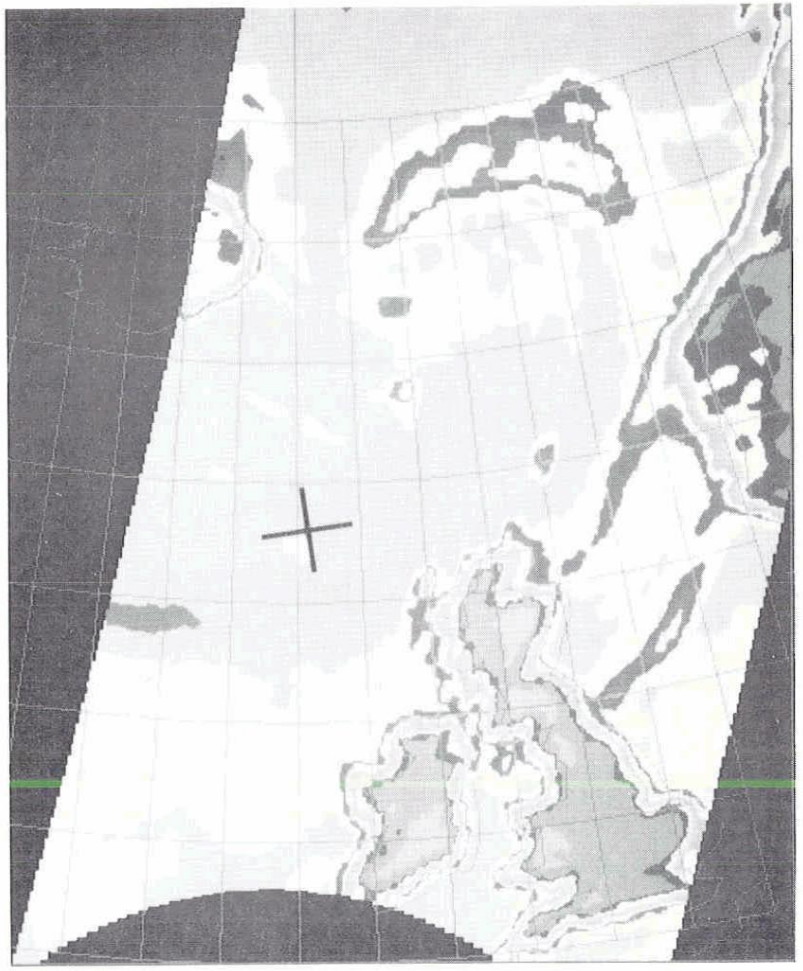

37 GHz Horizontal Polarization

Figure 5.1

SSM/I 37 GHz horizontal channel shown in Figure 5.1 conditions were not homogeneous during the underflight of July 23 as there were clouds present with heavier conditions in the southwest region of the test area.

An additional problem is the time-space mismatch between the SSM/I and the aircraft simulator. The satellite passes over the test area in about a half minute while, as mentioned above, the aircraft measurements required an hour and a half. The half-power beam contour on the surface for the four SSM/I frequencies is shown in the upper left hand corner of Figure 5.1 The half-power contour of the aircraft SSM/I simulator radiometers is 1.5 km, about the size of the dot indicating the scene station location in the figure. Thus the SSM/I integrates radiation over a much larger spatial region for a much shorter time than does the aircraft simulator. Therefore any significant changes in the brightness distribution over the test region during the aircraft measurements will degrade the accuracy of the simulator calibration. In order to minimize the spatial mismatch, the aircraft data were averaged over segments along the flight line equal to the SSM/I footprints and then compared with a weighted average of the SSM/I measurements at the nearest two scene stations. This is only a partial solution since it is an integration in one dimension only and not a weighted average over the two dimensional SSM/I antenna pattern.

The aircraft data were corrected for small incidence angle changes due to pitch and roll of the aircraft and for the effect of the atmosphere above the aircraft using the NRL environmental model [1]. All aircraft measurements are referred to an incidence angle of 53.1 degrees. This corresponds to measurement of the deployed boresight of the SSM/I on the DMSP satellite of 44.8 degrees and a mean satellite altitude of 859 km. These corrections were usually less than 4 K. It should be noted that, even though the DMSP orbit is circular to within 7 meters, the incidence angle of the SSM/I at the earth's surface varies by ±1/2 degree due to altitude variations resulting from the oblateness of the earth and the offset of the orbital center from the earth's geometric center. In addition, as discussed in Section 6, there are geolocation errors which may be due to effective SSM/I pointing errors which result in incidence angle errors of as much as ± 1/2 degree. Depending upon the environmental conditions and frequency, this will result in SSM/I brightness temperature variations of more than a degree K. An example of the possible magnitude of these variations calculated using the NRL environmental model is given in Table 5.2.

TABLE 5.2
BRIGHTNESS TEMPERATURE CHANGES WITH INCIDENCE ANGLE
dTb/dAng (Deg K/Angular degree)

	19V	19H	22V	37V	37H	85V	85H
Polar Winter	2.02	-0.36	1.95	1.53	0.34	0.34	0.40
Tropics Summer	2.13	0.89	1.23	1.71	1.03	-0.04	0.03

Due to these uncertainties no corrections for incidence angle variations were made to the SSM/I measurements.

The results from the SSM/I simulator flights are compared with the SSM/I brightness temperatures in Figure 5.2. The simulator and SSM/I measurements along both legs have been averaged together for each flight to provide a single measurement pair for each SSM/I channel. The error bars shown are the scatter of the measurements about the mean. The average measurements from all of the flights are given in Table 5.3.

TABLE 5.3

SSM/I SATELLITE AND AIRCRAFT
BRIGHTNESS TEMPERATURE MEASUREMENTS OVER OCEAN (K)

	SSM/I	SIMULATOR	DIFFERENCE
19V	191.6±0.9	195.8±1.0	-4.2±1.1
19H	122.5±1.5	124.6±1.6	-2.1±1.7
22V	210.7±1.3	214.8±1.2	-4.1±1.2
37V	211.8±1.3	217.3±2.0	-5.5±2.2
37H	150.7±2.6	157.1±3.6	-6.4±3.8
85V	250.3±1.6	247.3±2.6	3.0±2.6
85H	213.6±4.0	215.6±3.7	-2.0±4.6

Except for the 85V channel the SSM/I brightness temperatures are lower than the aircraft simulator. However only at 37 GHz do the differences exceed 4 K. Both the SSM/I and aircraft simulator measurements have an rms scatter of 1 to 4 K. It is reasonable to apportion the SSM/I-simulator difference errors equally between the SSM/I and simulator. Thus these measurements show the standard error on the determination of the SSM/I absolute calibration to be ± 3 K and are consistent with little or no error in the SSM/I absolute brightness temperatures.

5.3 MODEL COMPARISONS

Three different regions were chosen for comparison of theoretically generated brightness temperatures with those measured by the SSM/I: (1) clear, calm ocean areas selected by having the coldest 85 GHz brightness temperatures observed over the ocean, (2) the Amazon rain forest, and (3) the Arabian desert. These regions were selected because they are homogeneous over large areas, relatively unchanging, and work has been done to develop models for them. The SSM/I revolutions used are given in Table 5.4.

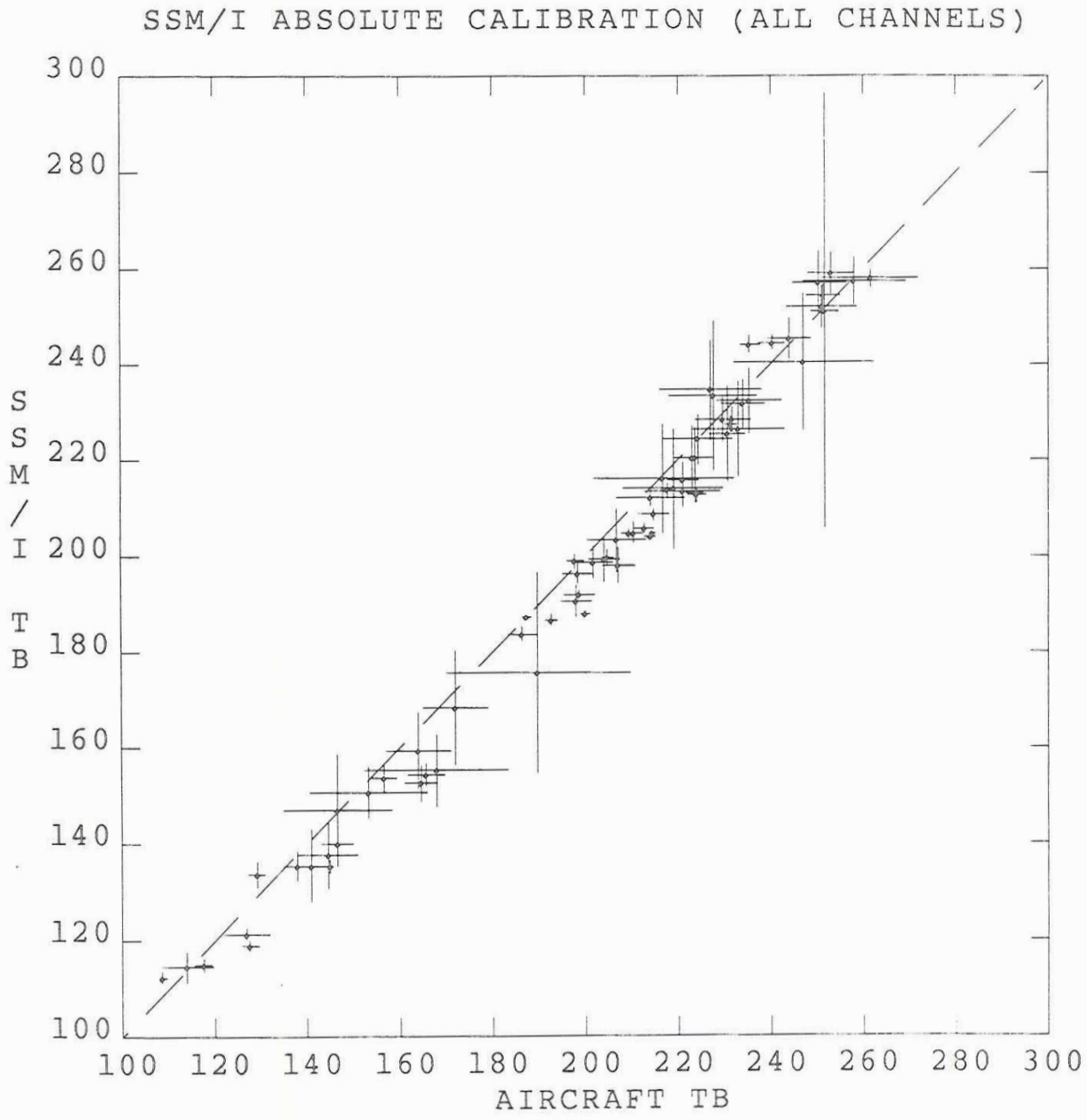
SSM/I ABSOLUTE CALIBRATION (ALL CHANNELS)
SSM/I TB
AIRCRAFT TB
300
280
260
240
220
200
180
160
140
120
100
100 120 140 160 180 200 220 240 260 280 300

Figure 5.2

TABLE 5.4
SSM/I CLEAR CALM OCEAN DATA

JULIAN DAY	191, 198, 206, 208, 214, 217, 223, 232, 286, 290, 292, 293, 302, 312
REVS	292, 386, 499, 532, 612, 659, 736, 866 1626, 1682, 1684, 1718, 1732, 1851, 1993, 2000

SSM/I ARABIAN DESERT DATA

JULIAN DAY	260, 268, 318, 326, 27
REVS	1257, 1370, 2076, 2189, 3120

SSM/I AMAZON DATA

JULIAN DAY	264, 273, 324, 23, 25
REVS	1318, 1445, 2165, 3069, 3096

The ocean areas are the most accurately modeled of the regions selected. The NRL ocean model [1] was used to calculate brightness temperatures for the selected ocean regions. Under the calm sea conditions assumed to prevail for the selected SSM/I data, the ocean departs very little from a smooth dielectric interface whose radiative properties are well known. The radiative transfer of a dry cloudless atmosphere are also very well understood and widely available. The greatest uncertainty is the uniformity and degree to which the selected areas satisfy the assumption of calm, clear ocean and the uncertainty in the physical temperature of the sea.

The Amazon rain forest is expected to be a diffuse scatterer, unpolarized, and approximately a black body. The differential scattering coefficients developed by Peake [2] for a predominantly diffuse scattering surface with no specular reflection except at grazing incidence were used. These have the form

$$\gamma(\mathrm{Cos}\theta_o + \mathrm{Cos}\theta_s)/(2\mathrm{Cos}\theta_o)$$

where atmospheric radiation incident on the surface at an angle θ_s, integrated over the upper hemisphere, is scattered into the viewing angle θ_o. The emissivity of the surface is found by subtracting the integral of the scattering coefficient over the upper hemisphere from unity. The constant γ was taken to be 0.2 and a humid tropical model atmosphere with 5.5 cm of precipital water vapor and surface temperature of 29 C was used.

Modeling the Arabian desert is the least certain. There is very little data on the dielectric constant of sandy soils and the effects of scattering and roughness especially above 19 GHz are not well known. Therefore the model brightness temperature calculations for the Arabian desert are most questionable especially at the higher frequencies. Perhaps the best model available for the desert is to use the Fresnel reflection coefficients for a smooth dielectric interface modified by an empirical roughness factor [3, 4, 5]. This factor, which multiplies the

Fresnel reflection coefficient, is given by exp-(h*Cos$^2\theta$) where θ is the incidence angle. The quantity h depends upon frequency and the scale of surface roughness but this dependency is not known [5]. Measurements at 19.4 GHz indicate a value of 0.6 [3]. Unfortunately no measurements above 19.4 GHz are available. The model brightness temperature calculations presented here used a value of 0.6 for h and 3.0 and 0.3 for the real and imaginary parts of the dielectric constant. A dry model atmosphere with 0.25 cm of precipital water vapor and surface temperature of 29 C was used.

The SSM/I and model brightness temperature calculations are compared in Table 5.5. The scatter of the SSM/I is a measure of the uniformity of the samples but the measurements may contain unknown systematic errors. As expected the ocean and Amazon rain forest modeled brightness temperatures show the best agreement with the SSM/I measurements. The Arabian desert results show poorest agreement for the 37 and 85.5 GHz channels where the effects of roughness and scattering are most uncertain in the model. With the exception of the 37V, 85V and 85H for the Arabian desert all of the model comparisons are consistent with a standard error on the determination of the absolute calibration of the SSM/I of ± 3 K. Again, there is an apparent trend for the SSM/I brightness temperatures to be lower then the modeled values, especially for the higher frequency channels. However the uncertainty of modeling does not allow a more definite determination to be made.

5.4 CONCLUSIONS

In summary, all of the SSM/I Simulator measurements and model calculations, with the exception of the 37 channel simulator measurements and the 37V and 85 GHz channel Arabian desert calculations, are in good agreement with the SSM/I data. The accuracy of the determination of the calibration of the SSM/I appears somewhat better at 19 and 22 GHz becoming less certain at 37 GHz and then 85 GHz. Although there is an apparent trend for the absolute calibration of the SSM/I to be low, especially at 37 GHz, both the aircraft simulator and model differences are consistent with little or no errors in the SSM/I absolute brightness temperatures. The present assessment of the standard error of the determination of the absolute calibration of SSM/I is that it is ± 3 K. It should be noted that the excellent instrument stability and overall calibration scheme permits the effect of biases to be removed. Thus, even if a systematic error or bias is present in the absolute brightness temperature calibration, the validation and adjustment of the retrieval algorithms has removed its effect from the environmental products.

TABLE 5.5

SSM/I SATELLITE AND MODELED
BRIGHTNESS TEMPERATURE MEASUREMENTS (K)

CLEAR CALM OCEAN

	SSM/I	MODEL	DIFFERENCE
19V	178.8±1.0	177.7	1.1
19H	100.6±1.8	99.7	0.9
22V	187.6±2.7	187.1	0.5
37V	202.4±0.8	205.2	-2.8
37H	129.6±2.0	129.3	0.3
85V	234.7±2.2	239.0	-4.3
85H	172.6±1.6	173.7	-1.1

AMAZON RAIN FOREST

	SSM/I	MODEL	DIFFERENCE
19V	282.1±1.0	281.9	0.2
19H	282.1±1.9	281.9	0.2
22V	282.1±1.3	283.2	-1.1
37V	278.3±1.2	281.7	-3.4
37H	277.8±0.9	281.7	-3.9
85V	283.5±1.4	287.9	-4.4
85H	283.3±1.3	287.9	-4.6

ARABIAN DESERT

	SSM/I	MODEL	DIFFERENCE
19V	299.3±1.0	300.0	- 0.7
19H	256.6±2.1	257.1	- 0.5
22V	296.1±0.9	299.6	- 3.5
37V	292.9±1.2	299.1	- 6.2
37H	257.3±2.0	259.2	- 1.9
85V	287.5±1.4	298.5	-11.0
85H	268.8±2.8	261.6	7.2

5.5 REFERENCES

1. Wisler, M.M. and J. P. Hollinger, " Estimation of Marine Environmental Parameters Using Microwave Radiometric Remote Sensing Systems," NRL Memo Report 3661, Naval Research Laboratory, Washingron, D.C. 20375, November 1977.

2. Peake, W. H. " Interaction of Electromagnetic Waves with Some Natural Surfaces," IRE Trans. on Ant. and Prop. Vol. AP-7, pp S324-S329, December 1959.

3. Choudhury, B. J., T. J. Schmugge, A. Chang, and R. W. Newton, "Effect of Roughness on the Microwave Emission from Soils," JGR, Vol. 84, No. C9, pp 5699-5706, Sept 1979.

4. Burke, W. J., T. J. Schmugge, and J. F. Paris, "Comparison of 2.8 and 21 Cm Microwave Radimeter Observations Over Soils with Emission Model Calculations," JGR, Vol 84, No. C1, pp 287-294, Jan 1979.

5. Schmugge, T. J., Private Communication, Nov 1988.

6.0 GEOLOCATION

6.1 INTRODUCTION

The current process of geolocating SSM/I pixels is illustrated in Figure 6.1. The spacecraft downlinks SSM/I data to receiving ground stations which in turn forward the data to both Air Force Global Weather Center (AFGWC), Omaha, Nebraska and Fleet Numerical Oceanography Center (FNOC), Monterey, California. Since only the data processed at FNOC is archived, the SSM/I geolocation calibration/validation effort is focused primarily on the data processed at FNOC.

FNOC receives a set of orbital elements from the U.S. Space Command (North American Defense Command (NORAD)) once a week and generates a ten-day prediction of the spacecraft ephemeris based on these orbital elements using the ephemeris computer program TRACE 66. The ephemeris prediction consists of a tabulation of the subsatellite geodetic latitude, longitude, and spacecraft altitude as a function of time in one minute increments over the ten-day period. This prediction ephemeris is then input to the SSM/I pixel registration algorithm, developed by Hughes Aircraft Company (HAC) to geolocate the SSM/I data. The HAC algorithm uses the down-linked SSM/I scan start times and fixed sample period to interpolate between the nearest predicted ephemeris data and determine the spacecraft position and altitude at the pixel sample times. With this information and knowledge of the SSM/I scan geometry (i.e., azimuthal and elevation angular positions of the antenna boresight for each pixel), the HAC algorithm then registers the SSM/I pixels to geodetic latitudes and longitudes.

A number of assumptions and approximations enter into the HAC geolocation algorithm which are described in [1]. Suffice it to say, the algorithm assumes that (1) the spacecraft nadir vector is always pointed in a direction normal to the geoid, (2) the surface of the earth is adequately modeled by an oblate spheroid, and (3) no corrections are necessary for possible spacecraft attitude variations or for possible misalignment of the SSM/I to the spacecraft. In addition, the algorithm takes into account (4) orbital variations of spacecraft altitude, (5) effects of earth rotation as it influences spacecraft heading, and (6) azimuthal and elevation angular offsets of the antenna boresight directions. The offsets (6) are defined within the SSM/I coordinate system and do not include possible misalignments of the SSM/I to the spacecraft. To minimize computer processing, a number of mathematical approximations are used in the algorithm (e.g., small angle approximation to transcendental functions). The errors arising from these approximations are discussed below.

The reported spacecraft and SSM/I pointing errors are presented in Figure 6.1. The maximum misalignment of the SSM/I to the spacecraft coordinate system is reported to be not greater than 0.1° while the SSM/I deployment errors are reported to be less than 0.03° and the spin-axis misalignment is reported to be less than 0.01°. The azimuthal scan position error is reported to be less than 0.03°. Projecting these errors on the earth's surface results in geolocation errors of the order of 2-4

SSM/I PIXEL GEOLOCATION PROCESS

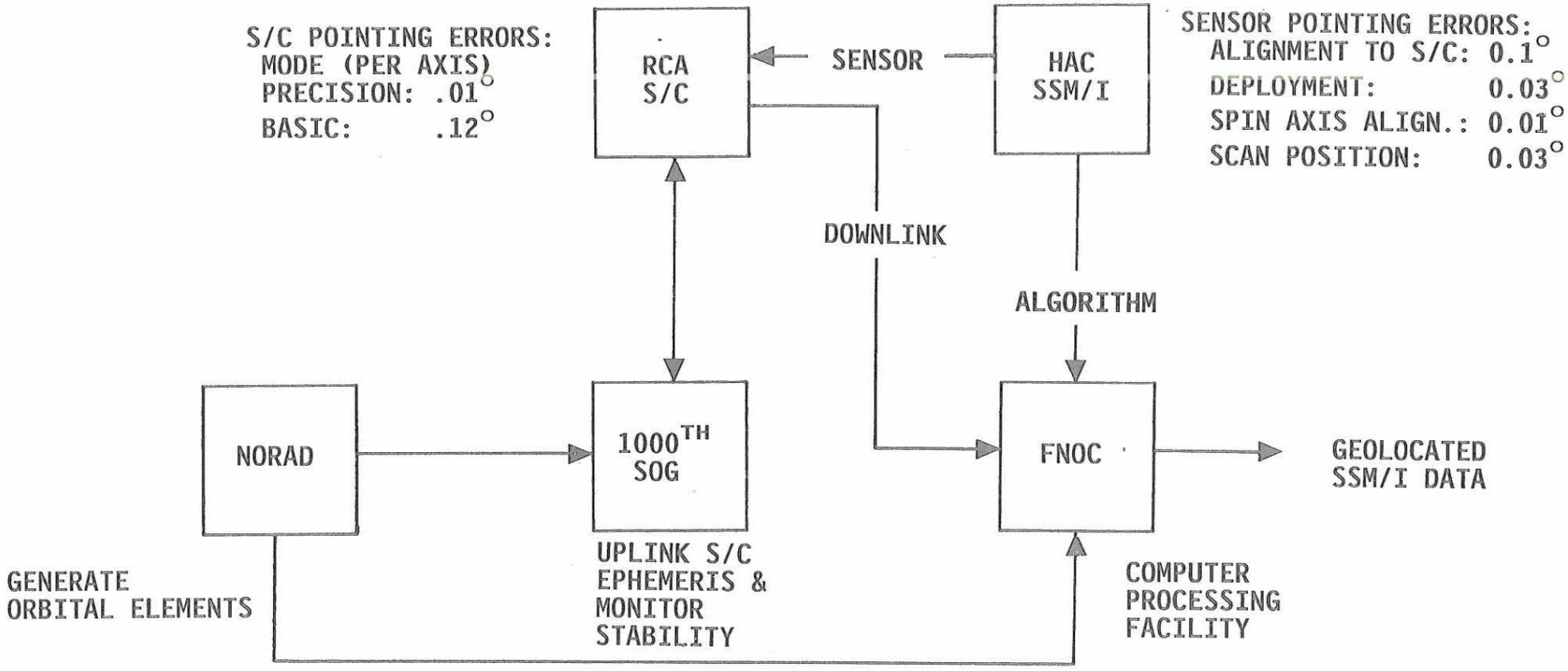

Figure 6.1. SSM/I Pixel Geolocation Process at FNOC

km, well below, as will be shown, the 20-30 km error observed in the SSM/I data.

The spacecraft receives its pointing and ephemeris information from the 1000th Satellite Operations Group (SOG), Space Command), Offutt Air Force Base, Nebraska. The 1000th SOG receives daily orbital element information from NORAD and generates ephemeris data in 12-minute increments that are up-linked to the spacecraft three times each week. The attitude of the spacecraft is continuously monitored to determine the attitude stability of the spacecraft. Table 6.1 presents typical spacecraft attitude information analyzed by the 1000th SOG for DMSP F8 for orbital revolution numbers 3106 through 3111 (January 26, 1988). These stabilities indicate that the spacecraft is operating in its basic mode of attitude control which keeps the pitch, roll, and yaw variations within ±0.1° per axis. The basic mode is a back-up mode of operation that occurs when the precision mode, which keeps the pitch, roll, and yaw variations within ±0.01°per axis, is not maintained. Projecting these variations in spacecraft attitude onto the surface of the earth results in geolocation errors less than 2 km. It should be noted that spacecraft F8 celestial sensors had an unexpected problem with false stars reflections off the SSM/I antenna, causing the spacecraft to operate in the basic mode. This glint problem was resolved January 19, 1988 by a software package implemented at the 1000th SOG, allowing the spacecraft to operate in the precision attitude mode.

TABLE 6.1

Variation of Spacecraft F8 Attitude (Degrees)
(January 26, 1988)

	Pitch		Roll		Yaw		No. Samples
REV	Max	Min	Max	Min	Max	Min	
3106	---	-.035	.028	-.028	.063	-.021	5910
3107	.049	-.042	.021	-.028	.014	-.014	6081
3108	.042	-.042	.021	-.028	.007	-.021	5659
3109	.042	-.042	.021	-.028	.000	-.070	5806
3110	.049	-.042	.021	-.035	-.049	-.049	6112
3111	.049	-.049	.021	-.028	.035	-.021	6043

(Data Courtesy of CAPT Rust of the 1000th SOG, Offutt AFB)

In view of the reported sensor alignment accuracies and stabilities of the spacecraft F8, it is difficult to see how a 20-30 km geolocation error can occur in the data. In an effort to ascertain the origin of these large geolocation errors, a list of candidate errors sources may be identified:

(1) spacecraft orbital elements
(2) predict ephemeris data
(3) sensor pixel location algorithm
(4) sensor deployment/alignment of spin axis
(5) sensor alignment to spacecraft
(6) spacecraft attitude

To these we must include errors in the geographical maps used to compare with the SSM/I data as well as errors due to interpolation and remapping of the SSM/I during image processing.

In the following sections, estimates are provided of the geolocation errors or uncertainties due to sources (1), (2), and (3). A number of cases are considered covering ascending and descending orbits and spanning January through June of 1988. Possible latitude, longitude, and along- and cross-track scan variations are also considered. A number of SSM/I 85H GHz images are presented along with an accurate digitized world data base of shorelines, island, and lakes to visually demonstrate the improvements in geolocation accuracy of the SSM/I when a more accurate spacecraft ephemeris is used and when a fixed set of attitude corrections are made to the spacecraft coordinate system. In addition, several results are presented concerning the geolocation errors of the SSM/I and the Operational Linescan System (OLS). Due to the difficulties in obtaining sufficiently clear atmosphere to identify shorelines, lakes and island, only a very limited number of OLS images were available for analysis. Finally, conclusions are presented at the end of the section.

6.2 ORBITAL ELEMENTS

The orbital elements of a satellite are a set of parameters which define the size, shape, and orientation of the orbit and the position of the satellite at a prescribed time. The classical orbital elements include as a minimum the semi-major axis, eccentricity, inclination, longitude of the ascending node, the argument of perigee and, of course, the time of reference. Two military sources of orbital element information are (1) the North American Defense Command, Cheyenne Mountain, Colorado Spring, Colorado and (2) Naval Space Surveillance System, NAVSPASUR, Dahlgren, Virginia. Both facilities track satellites, NORAD with a world-wide network to provide a fast definition of orbital parameters whenever desired and NAVSPASUR with a network across the continental United States.

To determine the geolocation errors arising from differences between the NORAD and NAVSPASUR orbital elements, a modified form of the NORAD and NAVSPASUR elements for spacecraft F8 were input to the NAVSPASUR ephemeris program, PPT7, to compute the geodetic latitude, longitude, and latitude

of the spacecraft for an entire day, January 26, 1988. The differences between the ephemeris sets when translated into distances are presented in Figure 6.2 as a function of time. To emphasize prediction errors within the 24 hour period, the last revolution associated with January 26, 1988 was used. The results show that the maximum error in the sub-satellite position or satellite altitude due to different orbital elements is less than 1.5 km, with the major difference occurring between subsatellite latitudes. (TOT refers to the rss of the latitude and longitude differences.) These results, typical of many revolutions examined, indicate that possible errors in the orbital elements are a negligible contributor to the SSM/I geolocation error.

6.3 SPACECRAFT EPHEMERIS

The ephemeris of a satellite refers to a tabulation of a satellite's position, i.e., sub-satellite latitude, longitude, and altitude, as a function of a prescribed time interval. The latitude is usually specified in terms of the geodetic latitude as opposed to the geocentric latitude and the altitude usually refers to the distance above the subsatellite point along a vector normal to the earth's surface at the subsatellite point. (See Section 6.4 for relationships between these quantities.) As noted earlier, the satellite ephemeris may be predicted on the basis of a set of orbital elements and an ephemeris model. A number of ephemeris models are available to make the prediction with accuracies that vary depending on the sophistication of the model and available computer resources. Since the accuracy of the prediction degrades with time, for high accuracy it is not advisable to extend the prediction 24-hours beyond the time of the orbital elements. Normally, a compromise must be made between the desired accuracy of the predicted ephemeris and the expense and effort required to achieve this accuracy. (It should be noted that to meet operational needs, predicted ephemeris is required.) To determine the effects of ephemeris prediction errors on the SSM/I geolocation error, the ephemeris model predictions of FNOC were compared with predictions based on ephemeris models currently used at NORAD, NAVSPASUR, and at the 1000^{th} SOG. For reference convenience, we shall henceforth refer to the ephemeris prediction generated by the 1000^{th} SOG as the spacecraft ephemeris. As noted earlier, the TRACE 66 model as employed at FNOC bases its ephemeris predictions with a once a week update of orbital elements from NORAD.

NORAD and NAVSPASUR kindly consented to generate ephemeris data for F8 using their ephemeris models and orbital elements for 24-hour periods on January 29, 1988. Taking the difference between the NORAD and the NAVSPASUR ephemeris and then translating the differences to distances on the Earth's surface, Figure 6.3 presents these differences as a function of time for a revolution near the end of the 24-hour period on January 29, 1988. As shown, the maximum differences are less than 3 km with a mean difference approaching 1 km. Difference in spacecraft altitude predictions are less than 2 km. The rapid fluctuations in the data is believed due to the precision of the ephemeris data supplied, ±0.01°.

Figure 6.4 compares differences in ephemeris data appearing on the archived SSM/I data tapes and NORAD for the same time period of Figure 6.3. Although differences in spacecraft altitude predictions are relatively small, <1.5 km, significant differences occur in both subsatellite latitude and longitude. Again, TOT refers to the rss of the latitude and longitude differences. The behavior of the latitude and longitude differences with time suggest that the source of the ephemeris differences arise from a time offset of the ephemeris. Following this clue, Figure 6.5 presents the differences in ephemeris of NORAD and FNOC when the FNOC data are generated with at time shift of -1.2 seconds. Note that the ephemeris differences are now less than 1 km. (The process of regenerating the ephemeris is discussed in Section 6.4.)

Figure 6.6 presents a comparison of NORAD and FNOC ephemeris data for orbit revolutions 3106 and 3107 on January 26, 1988. Note that the differences in predicted subsatellite positions are similar to those presented in Figure 6.3 except for the sudden jump near 200 minutes where the difference approaches 13 km. The sudden increase was found to occur at the same time FNOC updates its weekly ephemeris set. Thus, for this case, the ephemeris updating process resulted in a degradation of the accuracy of the ephemeris.

Additional comparisons of NORAD and FNOC ephemeris data were made for January 26, 1988 with results similar to those presented in Figure 6.4. Regenerating the FNOC ephemeris with the backward time shifts shown in Figure 6.7 brought the NORAD and FNOC ephemeris to with ~ 1 km. For this data set, the magnitude of the shift lies between 1 and 2 seconds and, for a subsatellite velocity of 6.6 km/sec, translates to a 6 to 13 km shift of the subsatellite point backward along the ground track. This is also the direction required to bring the SSM/I data in better agreement with maps of shorelines, island, and lakes as shown in the SSM/I imagery presented in Section 6.5.

Figures 6.8, 6.9, and 6.10 present comparisons of the FNOC ephemeris and the spacecraft ephemeris predicted by the 1000th SOG on January 14, March 13, and June 16, 1988. The spacecraft ephemeris were obtained from the smoothed OLS data kindly supplied by Captain Jill Schmidt and Sergeant Leahman of Air Force Global Weather Central, Offutt Air Force Base, Nebraska. Dr. Gerry Felde of the Air Force Geophysics Laboratory sent us an unpublished version of the Hughes Aircraft SMIROD computer program which we modified to extract the spacecraft ephemeris from the OLS data. Several conclusions may be drawn from these figures:

1. Differences between the spacecraft and FNOC ephemeris can be as large as 15 km (Figure 6.7, time ~0).

2. Occasions arise when this difference is less than 1 km (Figure 6.8, times near 800 seconds).

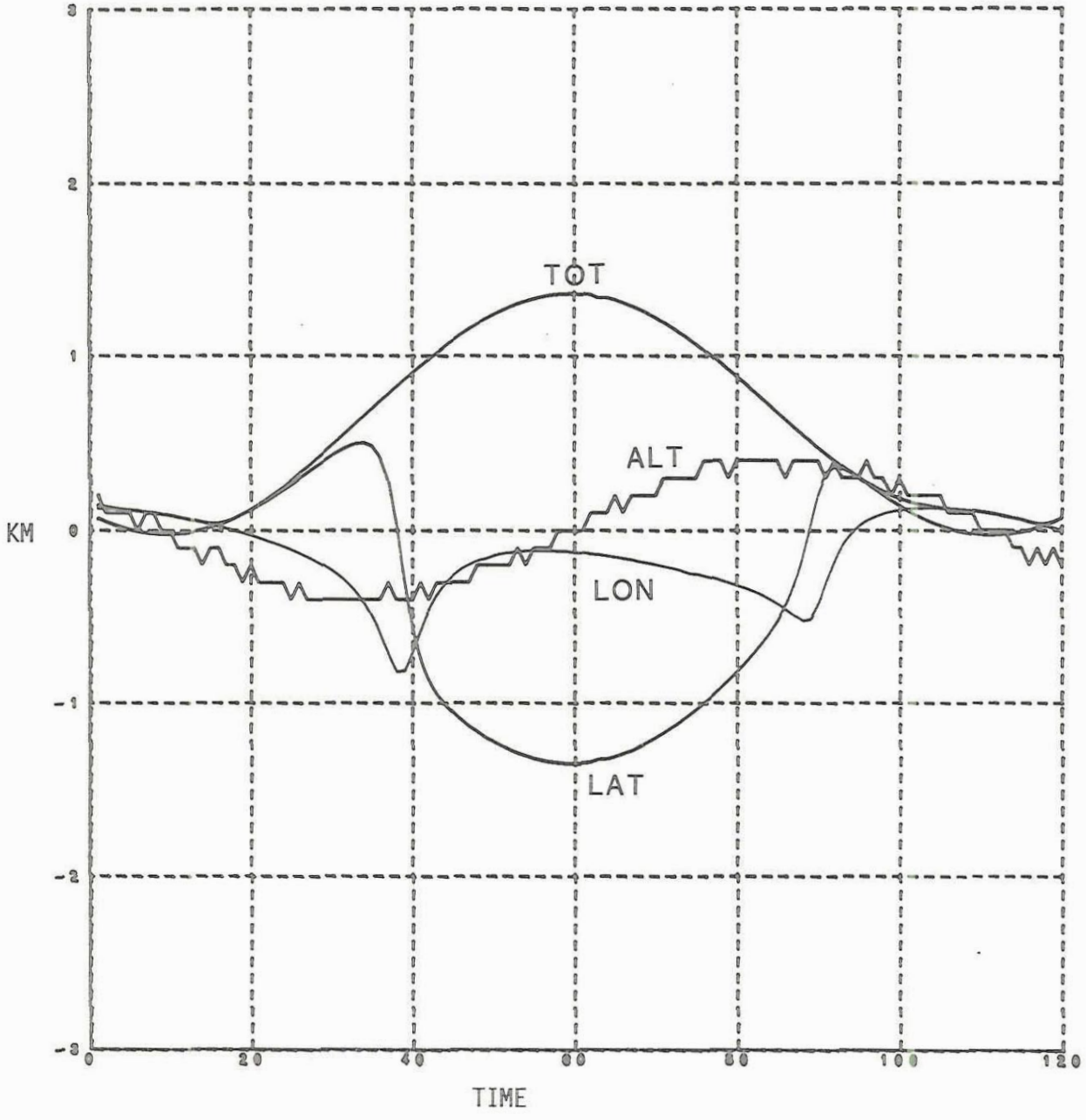

Figure 6.2 NORAD - NAVSPASUR Ephemeris Due to Differences in Orbital Elements (January 26, 1988)

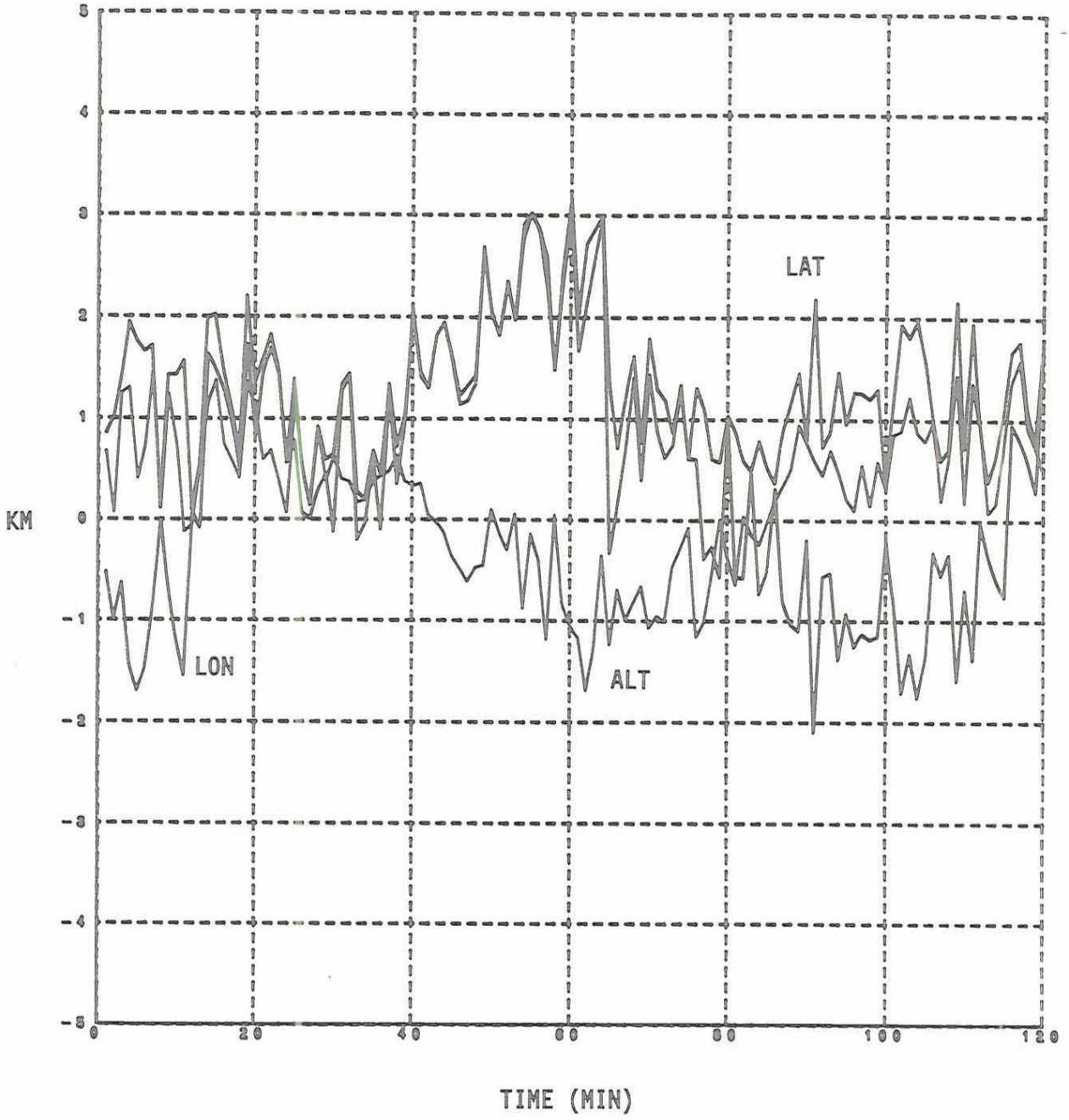

Figure 6.3. NORAD-NAVSPASUR Ephemeris (January 29, 1988)

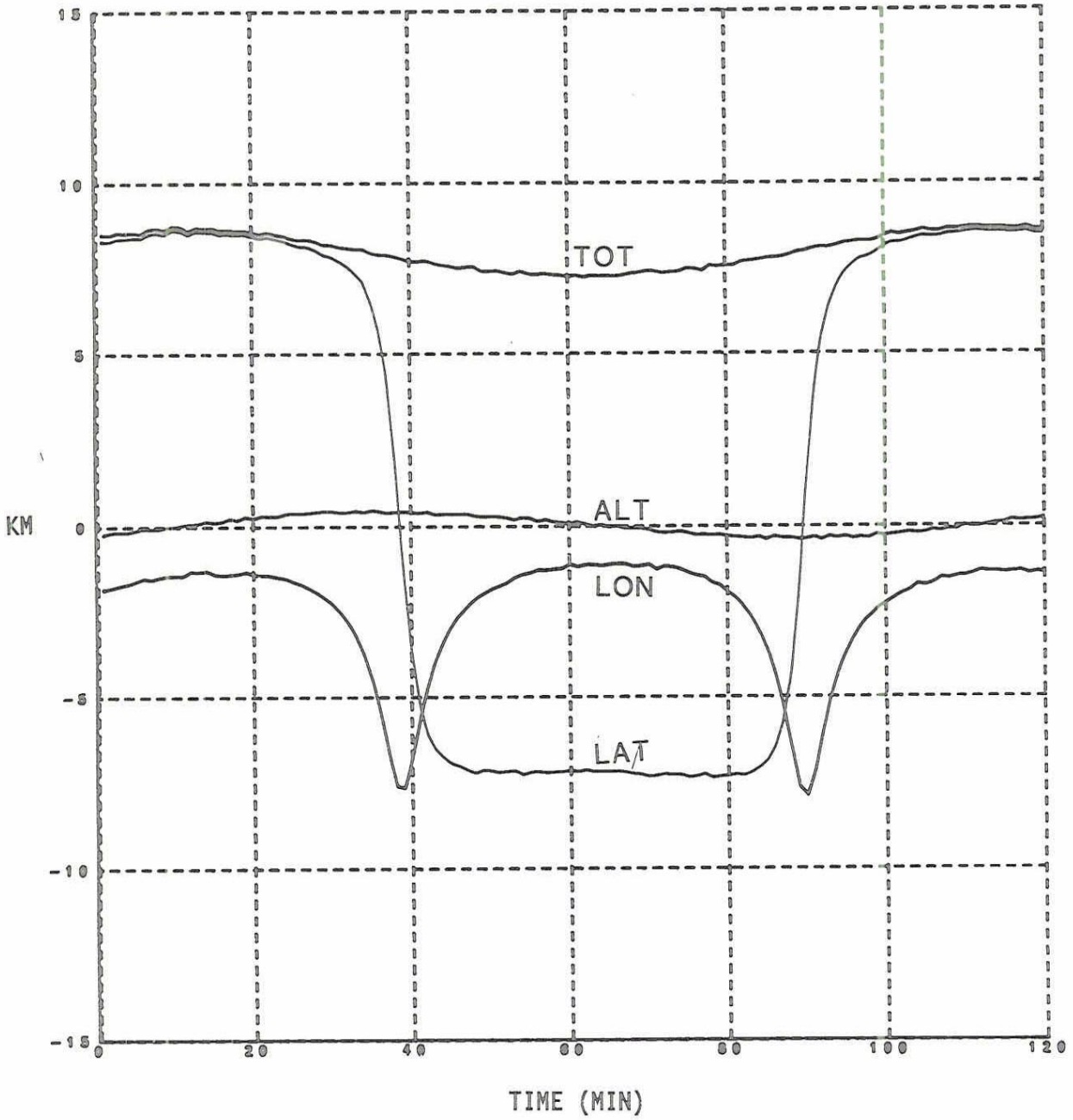

Figure 6.4. NORAD-FNOC Ephemeris (January 29, 1988)

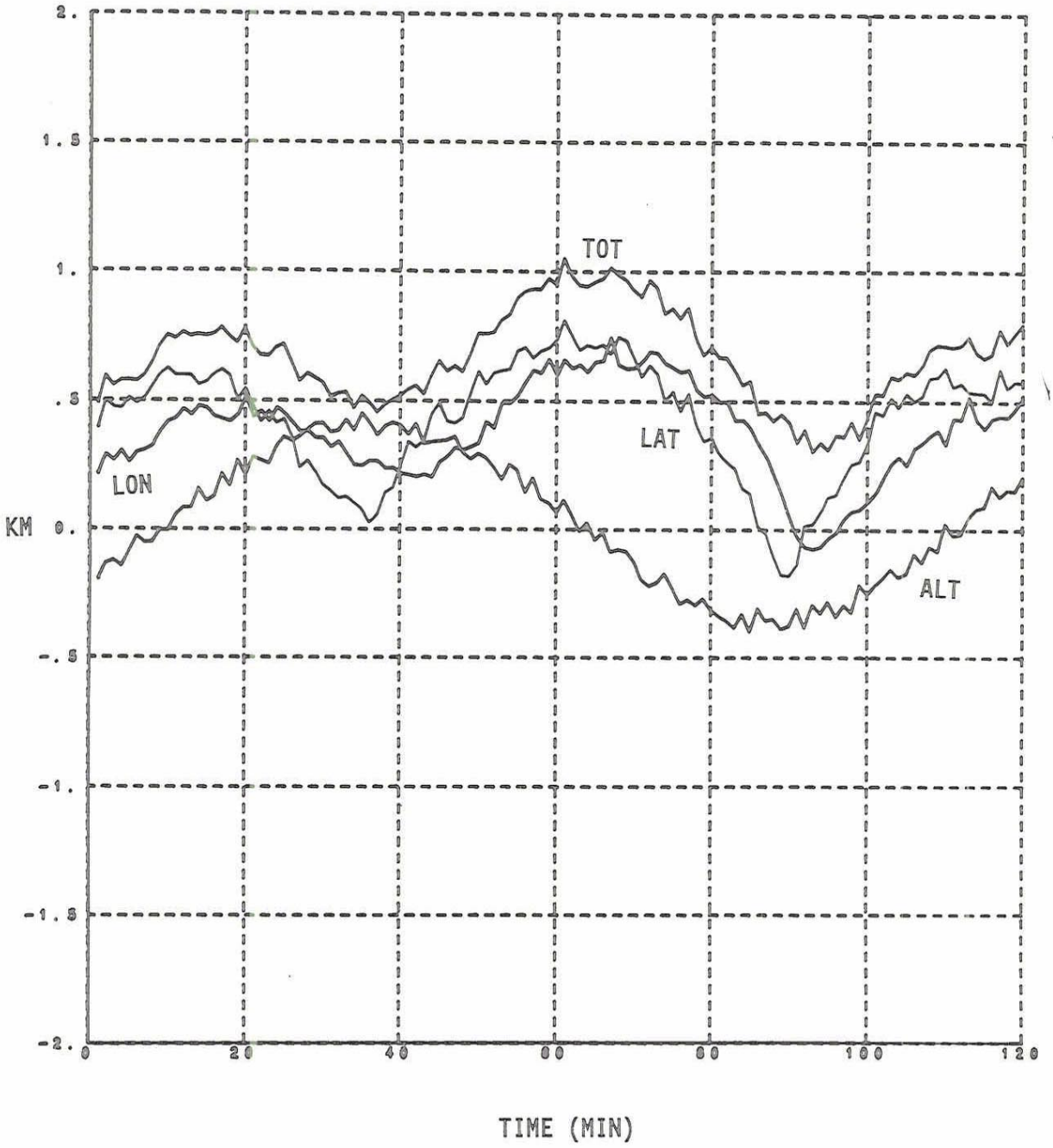

Figure 6.5. NORAD-FNOC Ephemeris (FNOC Regenerated with 1.2 Sec Time Offset) (January 29, 1988)

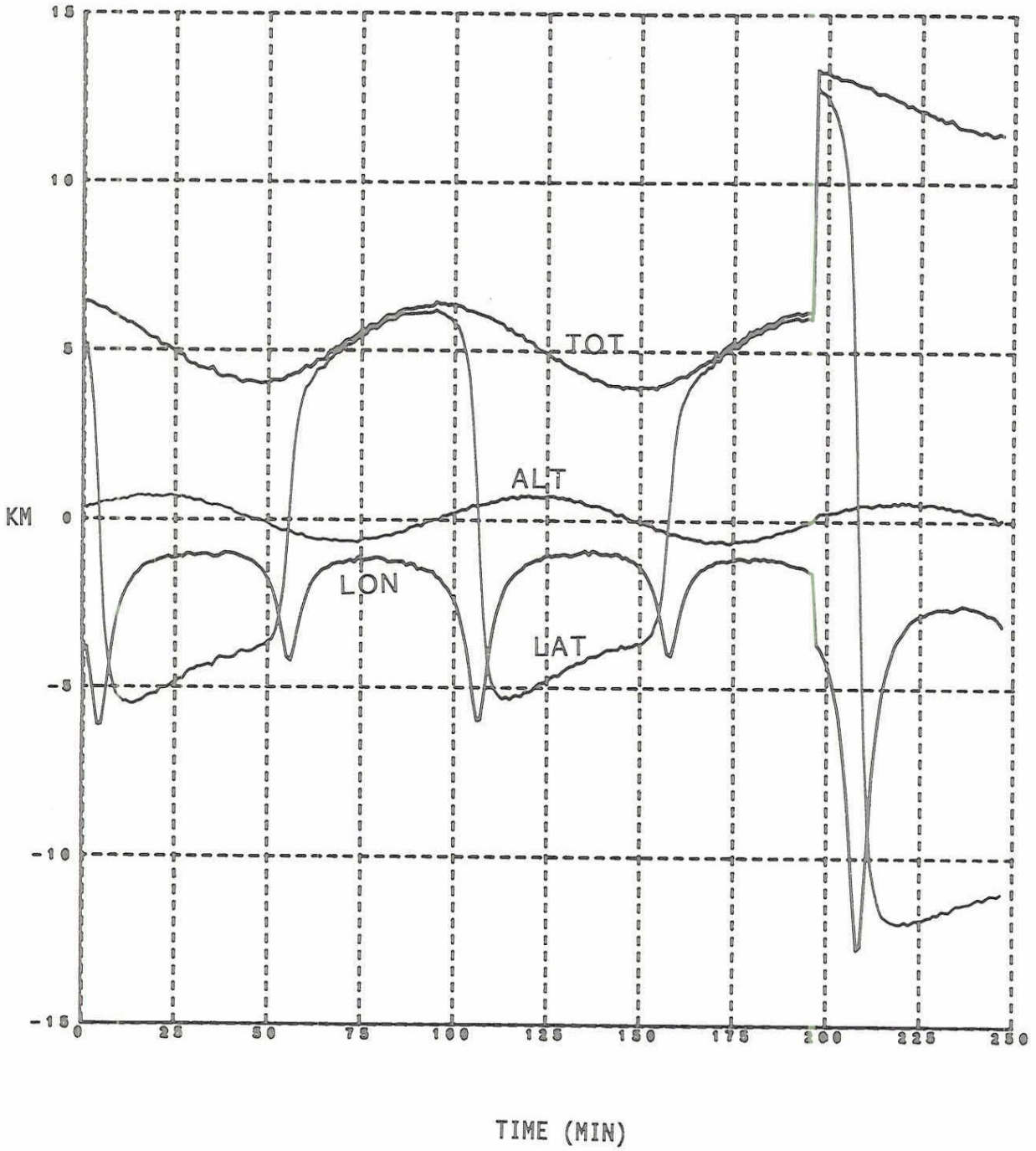

Figure 6.6 NORAD - FNOC Ephemeris (January 26, 1988)

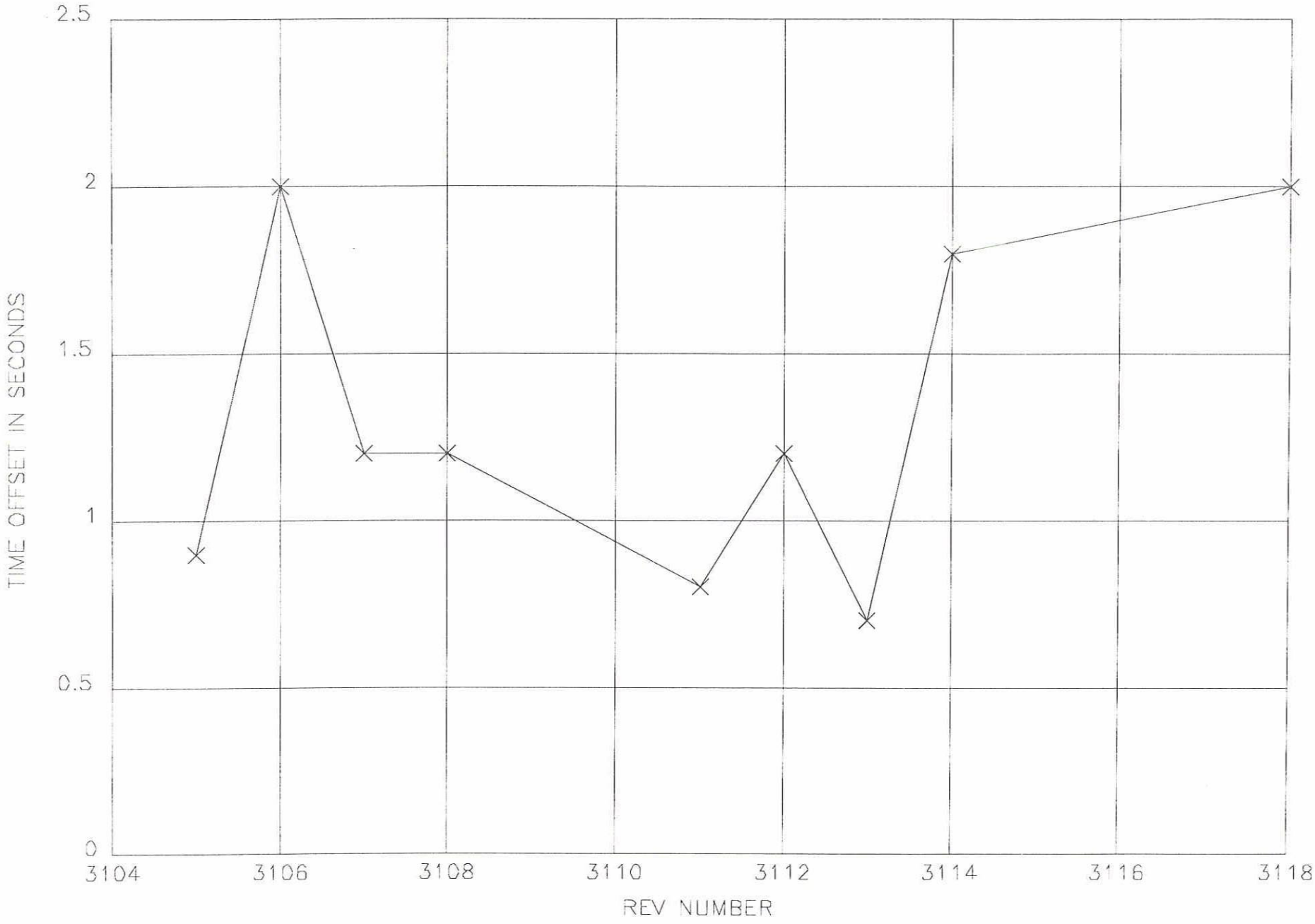

Figure 6.7. Time Offsets Needed to Make FNOC Ephemeris Agree with NORAD

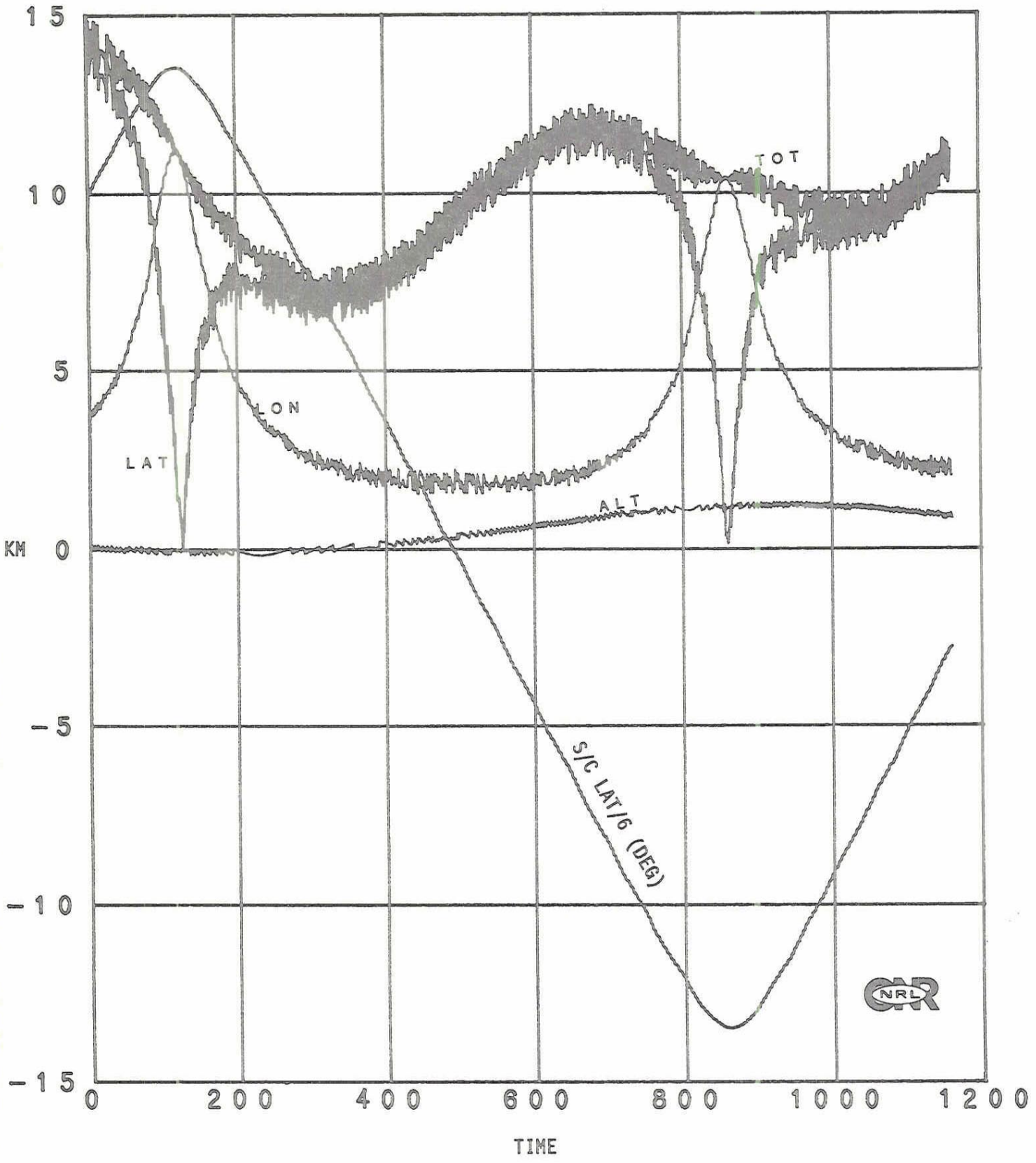

Figure 6.8. Spacecraft-FNOC Ephemeris REV 2945 (January 14, 1988)

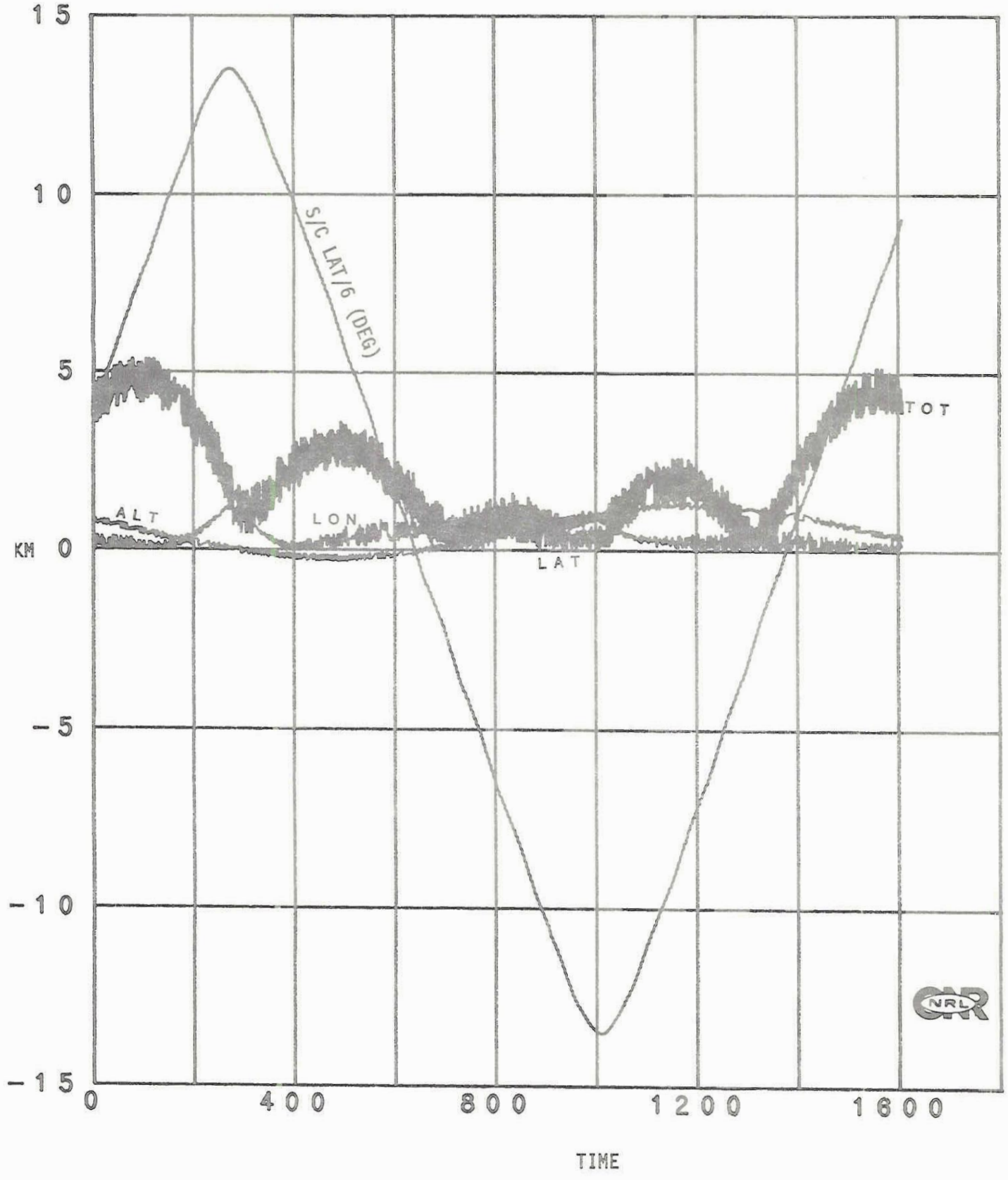

Figure 6.9. Spacecraft-FNOC Ephemeris REV 3776 (March 13, 1988)

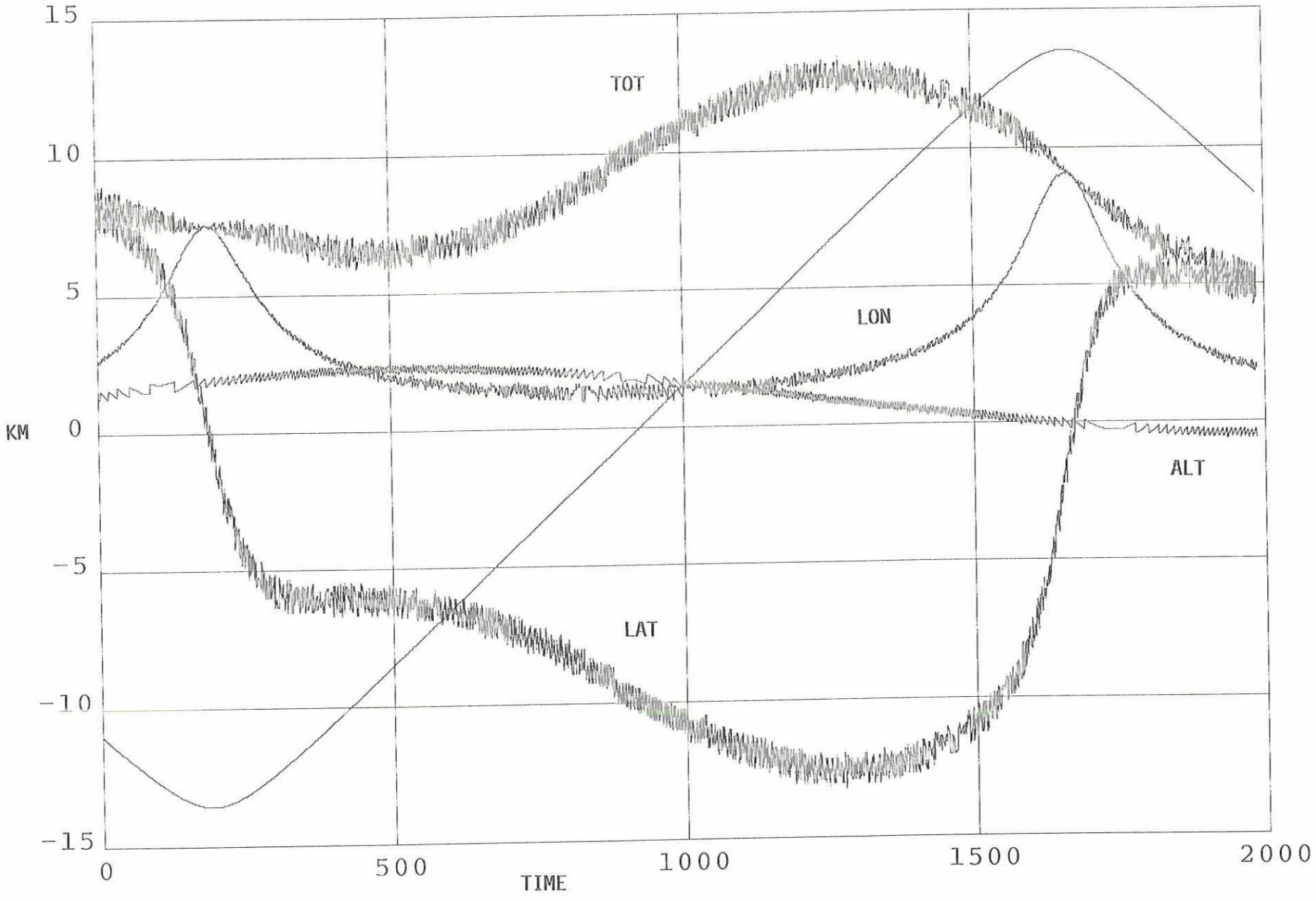

Figure 6.10. Spacecraft-FNOC Ephemeris REV 5100 (June 15, 1988)

3. In most cases, the differences may be reduced to less than 1 km by regenerating the FNOC ephemeris with a backward shift in time on the order of 1 to 2 seconds.

Additional comparisons of the spacecraft and FNOC ephemeris were examined during the effort reported herein. In all cases, the results exhibited the same range of differences as those presented in Figures 6.8 through 6.10. In addition, no consistent behavior of these differences could be determined from the data sets analyzed.

6.4 GEOLOCATION ALGORITHM

The current SSM/I geolocation algorithm registers the data by associating a latitude and longitude to each pixel and is described on pages 2-105 through 2-143 in the HAC SSM/I Program Maintenance Manual (Rev. A), Volume II dated February 1986 [1]. In addition, the manual contains a listing of the current computer code within an appendix. As noted previously, the HAC geolocation algorithm employs a number of numerical approximations to minimize the computer processing load associated with registering over 400,000 pixels each satellite orbit (128 pixels/scan x 3125 scans/rev). At the same time, these approximations can not introduce significant errors since the total system error budget for geolocating SSM/I pixels was set at half the resolution of the highest resolution channel, 6 km for the 85 GHz pixels. As stated in [1], the primary numerical approximations center on (1) making series expansions of transcendental functions where possible and (2) interpolating between a small number of so-called "base points" latitudes and longitudes associated with each scan. The "base points" are defined as those pixels having geolocation accuracy determined only by approximation (1) with no interpolation error. Comparisons are made below of the current SSM/I geolocation algorithm employed at FNOC with a model that does not use approximations (1) or (2). Before presenting the results, it appears appropriate to discuss briefly the model used herein to compute the pixel positions.

Earth Model

The Earth's surface is approximated by an oblate spheroid with a flattening factor $f = 0.00335281$ and translates to an eccentricity of $e = 0.0818191830$. See Wertz [2]. The mean equatorial radius is taken to be 6378.14 km. The earth rotation rate, needed below to determine the orbit plane of the spacecraft, is 15°/hr. The time for the predict ephemeris data is expressed in solar time. Also needed below is the unit vector, $\hat{n}$, normal to the surface of the oblate spheroid. In terms of the geocentric latitude θ'_s and longitudes ϕ_s at point (θ'_s, ϕ_s) $\hat{n}$ may be expressed as

$$\hat{n} = \frac{\cos\theta'_s \cos\phi_s \hat{x} + \cos\theta'_s \sin\phi_s \hat{y} + (1-e^2)^{-1} \sin\theta'_s \hat{z}}{\sqrt{\cos^2\theta'_s + (1-e^2)^{-2} \sin^2\theta'_s}}$$

where e is the earth's eccentricity and $\hat{x}$, $\hat{y}$, $\hat{v}$ are unit vectors along the inertial cartesian coordinate system shown in Figure 6.11. The geocentric latitude θ'_s is related to the geodetic latitude by

$$\tan\theta'_s = (1-e^2)\tan\theta_s$$

Note that $\theta'_s = \theta_s$ at the equator and the poles but differs by nearly 0.2° at $\theta_s = 45°$.

Spacecraft Position and Attitude

As noted previously the spacecraft ephemeris is a tabulation of the spacecraft position as a function of time. This usually takes the form of subsatellite geodetic latitude, longitude, and altitude at a sequence of times which usually do not coincide with SSM/I pixel sample times. Thus, an interpolation of the spacecraft ephemeris is necessary to locate the spacecraft at the pixel times. In addition, the attitude of the spacecraft must be determined at these pixel times.

Based on an analysis of the spacecraft ephemeris for spacecraft F8, it was found that the unit vector normal to the plane of the spacecraft is extremely stable over large portions of a revolution. Typically, the maximum angle or variation of the orbit normal vector from a mean vector was found to be less than 0.02° over half an orbit. The analysis also revealed that the orbit normal, $\hat{v}$, may be accurately determined from the ephemeris by

$$\hat{v} = \frac{\hat{r}_{s1} \times \hat{r}_{s2}}{|\hat{r}_{s1} \times \hat{r}_{s2}|}$$

where $\hat{r}_{s1}$ and $\hat{r}_{s2}$ are subsatellite position unit vectors of the spacecraft emanating from the center of the oblate spheroidal Earth model. The times associated with $\vec{r}_{s1}$ and $\vec{r}_{s2}$ span the pixel time of interest and are separated by sufficient time to avoid errors in v due to noise or resolution of the ephemeris data. Vectors r_{s1} and r_{s2} may be expressed as

$$\hat{r}_{s1} = \cos\theta'_{s1} \cos\phi_{s1} \hat{x} + \cos\theta'_{s1} \sin\phi_{s1} \hat{y} + \sin\theta'_{s1} \hat{z}$$

$$\hat{r}_{s2} = \cos\theta'_{s2} \cos(\phi_{s2}+\Delta\phi) \hat{x} + \cos\theta'_{s2} \sin(\phi_{s2}+\Delta\phi) \hat{y} + \sin\phi'_{s2} \hat{z}$$

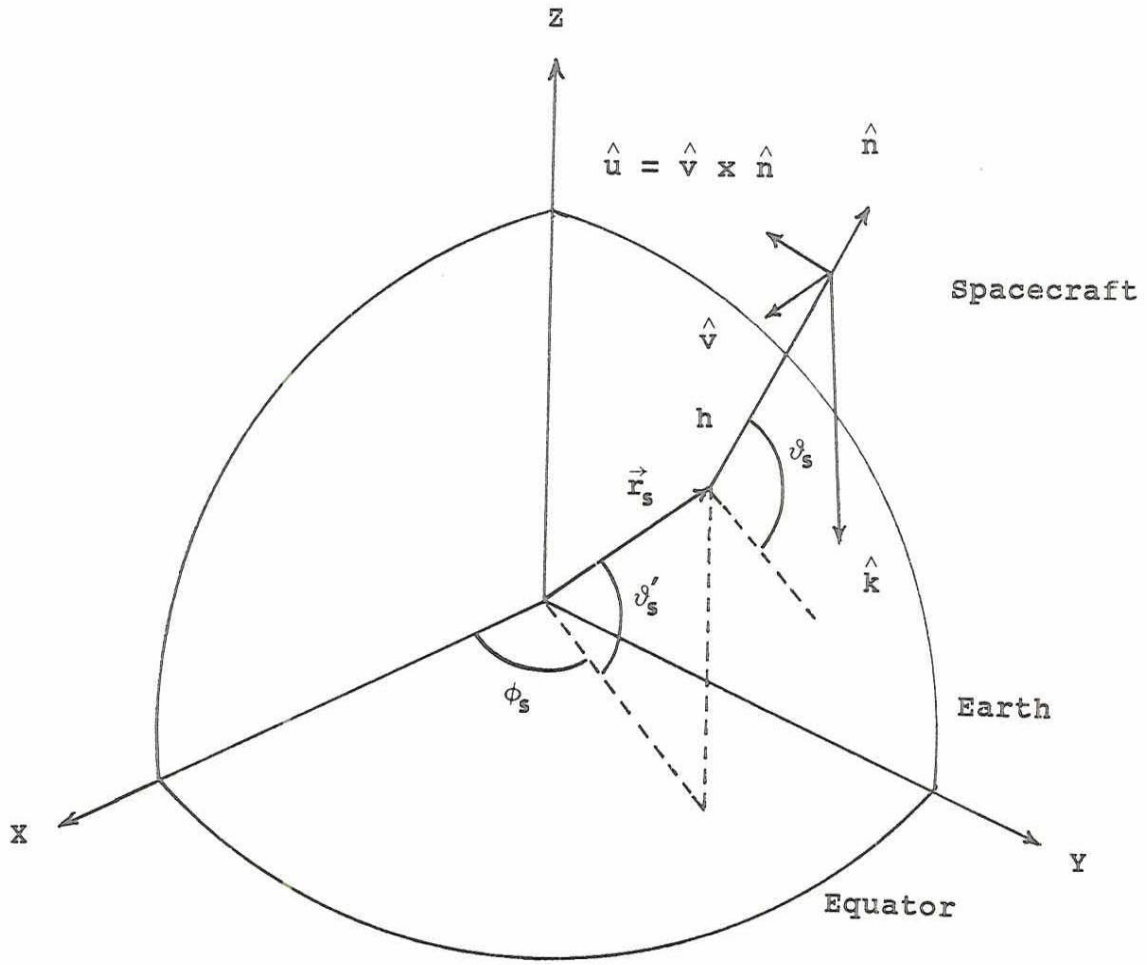

Geocentric Latitude	ϑ_s'
Geodetic Latitude	ϑ_s
S/C Altitude	h
Sub-satellite Position	$\vec{r}_s$
Unit Normal to Geoid	$\hat{n}$
Unit Normal to Orbit Plane	$\hat{v}$
Antenna Boresight for one of 128 pixels	$\hat{k}$

Figure 6.11 Spacecraft Geometry with Oblate Spheroidal Earth Model

where

$\Delta\phi$ = $\dot{\phi}_e$ (t_2-t_1)
$\dot{\phi}_e$ = Earth rotation rate (0.25068 deg/min)
t_2-t_1 = Time separation between $\hat{r}_{s1}$ and $\hat{r}_{s2}$

and θ'_s is the subsatellite geocentric latitude and ϕ_s is the subsatellite longitude. Typically, the time separation t_2-t_1 should be not less than one-two minutes to avoid numerical errors in computing a stable orbit normal. Note that a correction for Earth rotation on the longitude ϕ_{s2} is needed to determine the orbit normal. Once the SSM/I pixels have been geolocated this longitudinal correction is removed.

Once the orbit normal vector is known, the position of the spacecraft at the pixel time may be determined by interpolation within the orbit plane. Since the angular velocity of the spacecraft is extremely stable over the time period of interest, a linear interpolation of the angular position in the orbit plane at the pixel time appears adequate. Following this procedure, the subsatellite geocentric latitude θ'_{sp} at pixel time t lying between t_1 and t_2 is given by

$$\sin\theta'_{sp} = \frac{\sin\psi_0-\psi}{\sin\psi_0}\sin\theta'_{s1} + \frac{\sin\psi}{\sin\psi_0}\sin\theta'_{s2}$$

where

$$\psi = \psi_0 \frac{t-t_1}{t_2-t_1}$$

$$\psi_0 = \cos^{-1}(\hat{r}_{s1} \circ \hat{r}_{s2})$$

The subsatellite longitude ϕ_{sp} at pixel time t is found from

$$\tan(\phi_{sp}-\phi_{s1}+\Delta\phi_{sp}) = \frac{\sin\psi \sin(\phi_{s2}-\phi_{s1}+\Delta\phi) \cos\theta'_{s2}}{\sin(\psi_0-\psi) \cos\theta'_{s1} + \sin\psi \cos(\phi_{s2}-\phi_{s1}+\Delta\phi) \cos\theta'_{s2}}$$

where

$$\Delta\phi_{sp} = \dot{\phi}_e(t-t_1).$$

This process of interpolation of θ'_{sp} and ϕ_{sp} in conjunction with a linear interpolation of spacecraft altitude was found to be extremely accurate over the time period of interest. Indeed, for a given set of ephemeris data having a 60 second separation between spacecraft positions, this interpolation process was used on several occasions to regenerate an entirely new set of ephemeris spaced at 60 second intervals midway between the old data. When the new ephemeris was, in turn, interpolated at the times of the old ephemeris, the ephemeris set generated was the same as the old ephemeris to within ±0.1 km.

The attitude of the spacecraft is maintained by on board computers to keep the spacecraft nadir vector pointing normal to the geoid at the subsatellite point. The attitude stability in the precision mode is, as noted earlier, ±0.01° per axis. This implies that the orbit normal and spacecraft nadir, over the time period of interest, are known and maintained in the precision mode to within ±0.01°. A third unit vector may be identified $\hat{u}$

$$\hat{u} = \hat{v} \times \hat{n}$$

to complete a right-handed spacecraft coordinate system. It should be noted that unit vectors n and u are changing rather rapidly with time. For the model presented herein both n and u are recomputed for each pixel sample time, t, whereas the orbit normal v is computed only once each scan.

SSM/I Scan Geometry

The conical scan geometry of the SSM/I is illustrated in Section 2.0. Since all SSM/I channels share a common beam boresight, the geolocation of the 85 GHz channel also geolocates the remaining channels. Assuming for the moment that the SSM/I is perfectly aligned to the spacecraft coordinates v, n, u, the antenna boresight unit vector, k, associated with the Nth pixel sample on a given scan, may be expressed as

$$\hat{k} = -\cos(\theta_0+\Delta\theta)\,\hat{n} - \sin(\theta_0+\Delta\theta)\cos\psi_N\,\hat{u} + \sin(\theta_0+\Delta\theta)\sin\psi_N\,\hat{v}$$

where the azimuthal scan angle ψ_N (in degrees)

$\psi_N = -51.0 + (N-1)\ 0.8 + \Delta\psi \qquad N= 1,2, \ldots\ldots,128$
$\Delta\psi$ = Offset in azimuthal angle (0.1° for S/N 002)
θ_0 = Nominal elevation angle (45°)
$\Delta\theta$ = Offset in elevation (0.25° for S/N 002).

The effects of possible misalignment of the SSM/I to the spacecraft is covered in Section 6.5. Note that a time increment of 4.22 msec is associated with each azimuthal pixel sample increment of 0.8°. The scan start time, t_{sc}, identifies the time of the first sample N=1. Thus, the pixel sample time, t_N, for the Nth sample is

$$t_N = t_{sc} + (N-1)\ 4.22.10^{-3}\ (\text{sec})$$

Pixel Location

In view of the above results, the position vector of a pixel at time, t, may be expressed as

$$\vec{r}_p = \vec{r}_{sp} + h\,\hat{n} + s\,\hat{k}$$

where

$\vec{r}_{sp}$ = Subsatellite position vector of spacecraft at time t
h = Spacecraft altitude at time t
$\hat{n}$ = Unit vector normal to the surface of the oblate spheroid Earth model at subsatellite point $\vec{r}_{sp}$
$\hat{k}$ = Antenna boresight of the pixel at time t

The quantity, s, is the slant range from the spacecraft along vector, $\hat{k}$, to the surface of the oblate spheroid. Once s is known, the pixel geocentric latitude and longitude may be determined from $\vec{r}_p$.

The geodetic latitude may then be computed and the corrections of earth rotation removed from the pixel longitudes. The solution for the range, s, follows by solving for the intersection of a line, i.e., the antenna boresight vector, k, and the surface of the oblate spheroid. A quadratic equation arises in s during this process with the desired solution corresponding to the minimum range.

Comparison of Models

Using the geolocation model described above in conjunction with the FNOC ephemeris data, computations were made of geodetic latitude and longitude of the SSM/I pixels for a number of orbit revolutions. These were then compared with the pixel latitude and longitudes appearing in the archived SSM/I data. Figure 6.12 presents the differences in latitude and longitude of these data translated into distance on the earth's surface for the first pixel sample on the SSM/I scan over an entire orbit. The latitude of this pixel is shown for reference. Note that the differences vary over the orbit with maximum changes of ±4 km near the poles. Figure 6.13 presents the positional differences for pixel number 64, located near the center of the SSM/I swath. The differences exhibit a behavior similar to those presented for the first pixel sample with nearly the same magnitude. Figure 6.14 presents the positional differences for the 127th sampled pixel and Figure 6.15 presents the differences for the 128th or last sampled pixel. Note the differences for the 128th sample exceeds ~15 km for the higher latitudes. This error is traceable to an interpolation error in the geolocation algorithm software at FNOC. The subroutine LOCINT in SMISDP incorrectly extrapolates for the last pixel on each scan when the subsatellites latitudes lies above 60° or below -60°. Outside of this region, the differences are less than ±4 km. Comparisons made for a number of revolutions show essentially the same behavior.

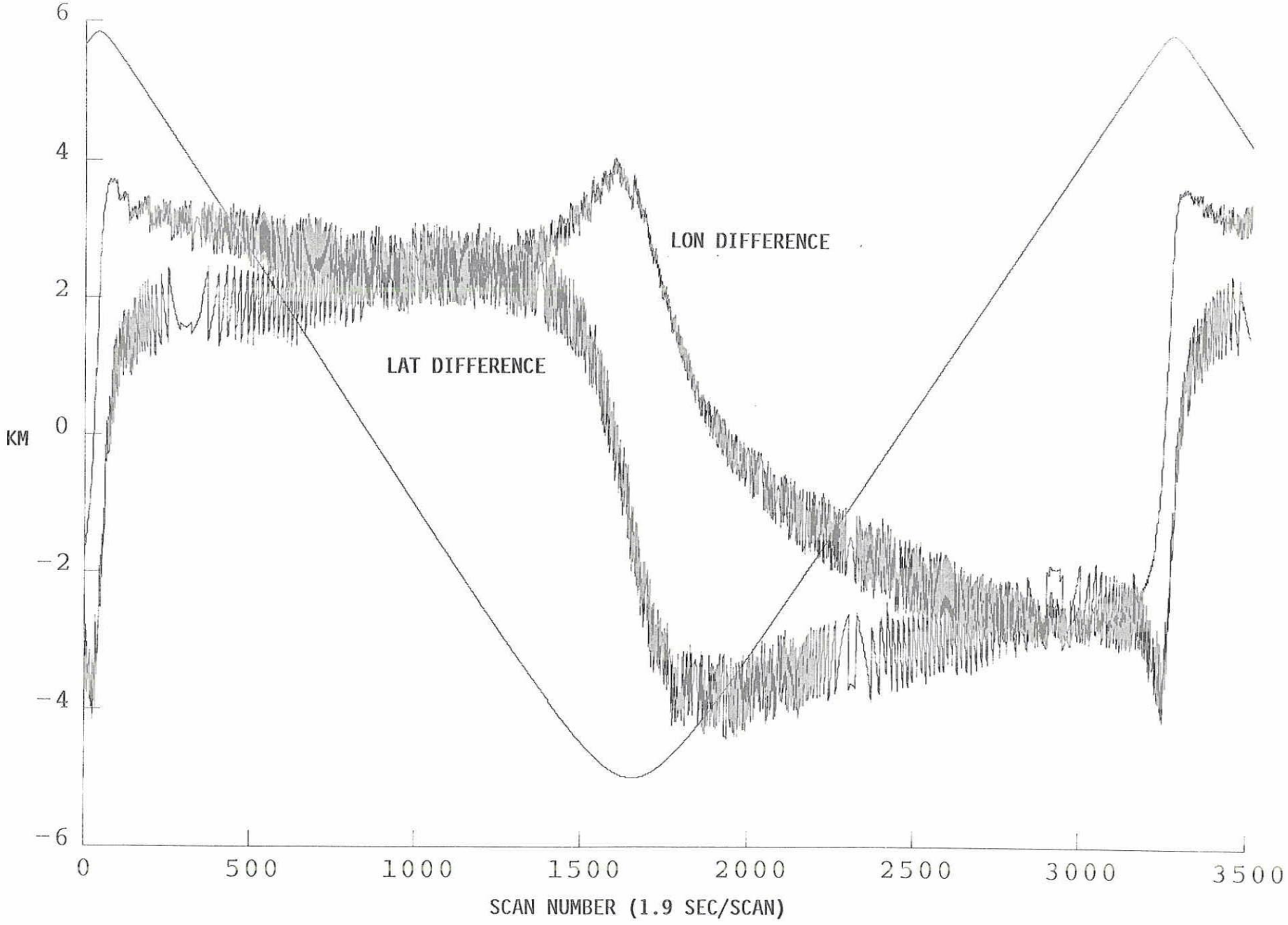

Figure 6.12. Positional Errors of First Sampled Pixel Due to Numerical Approximations in Geolocation Algorithm (REV 5100, June 15, 1988)

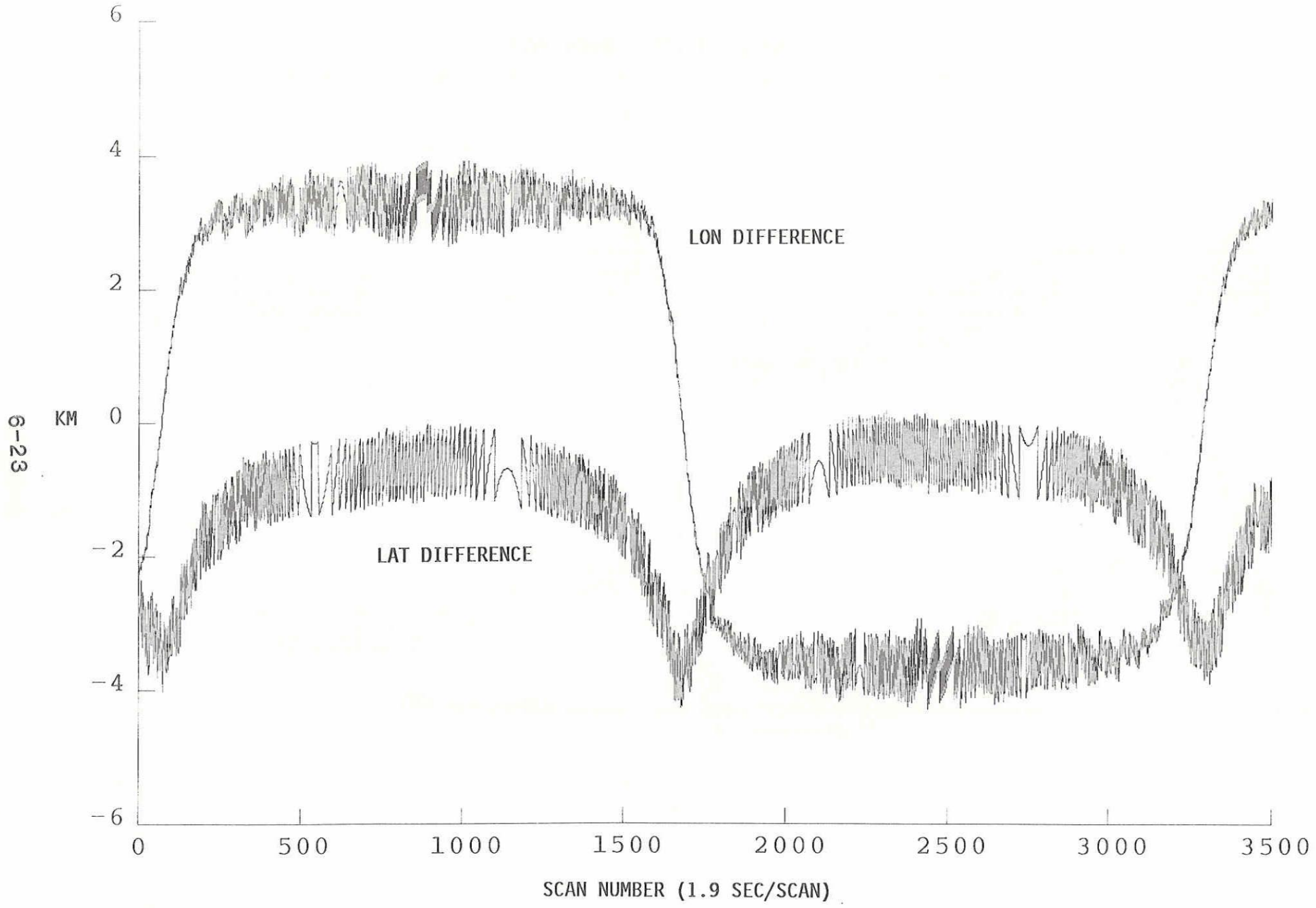

Figure 6.13. Positional Errors of 64th Sampled Pixel (REV 5100, June 15, 1988)

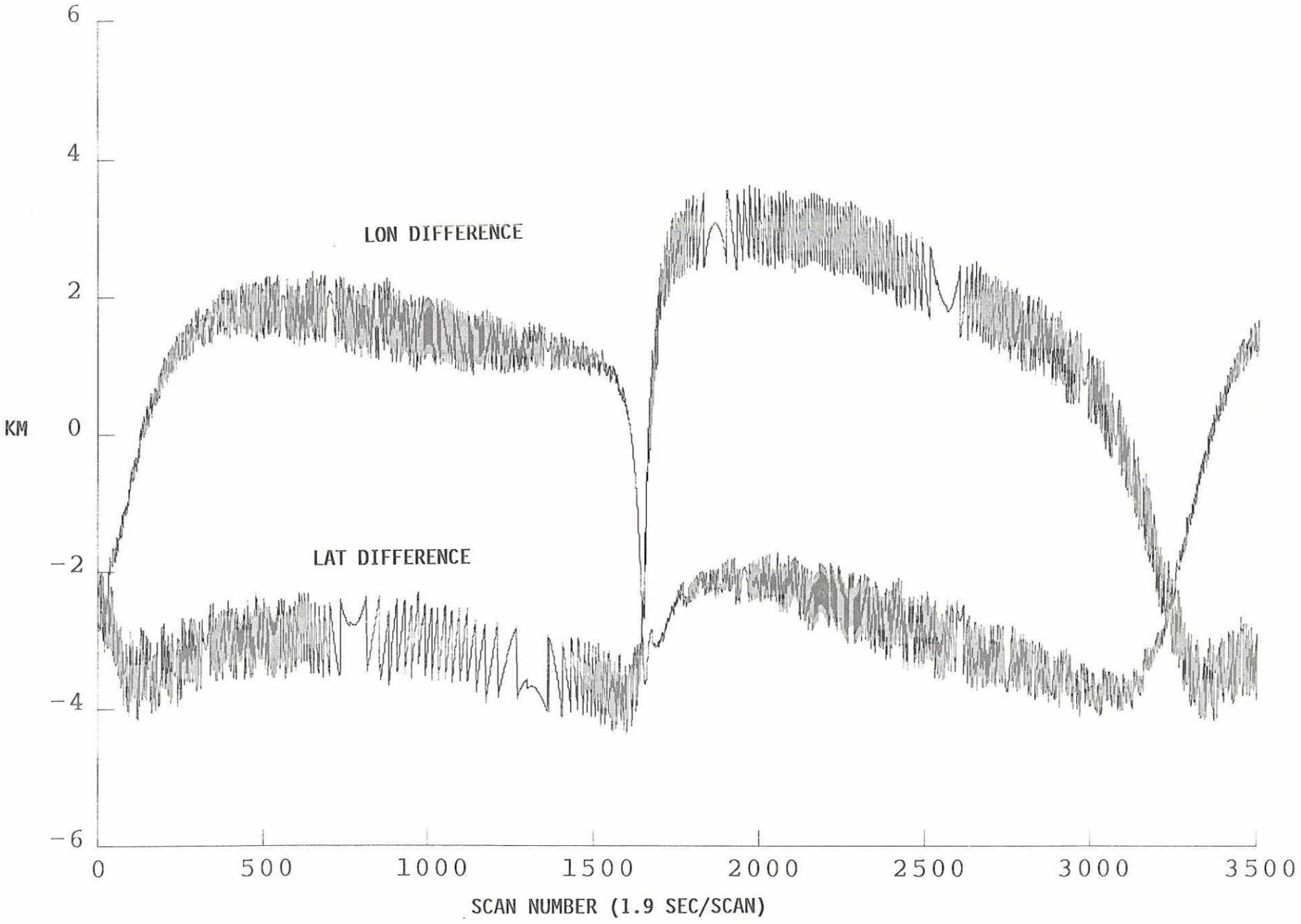

Figure 6.14 Positional Errors of 127th Sampled Pixel (REV 5100, June 15, 1988)

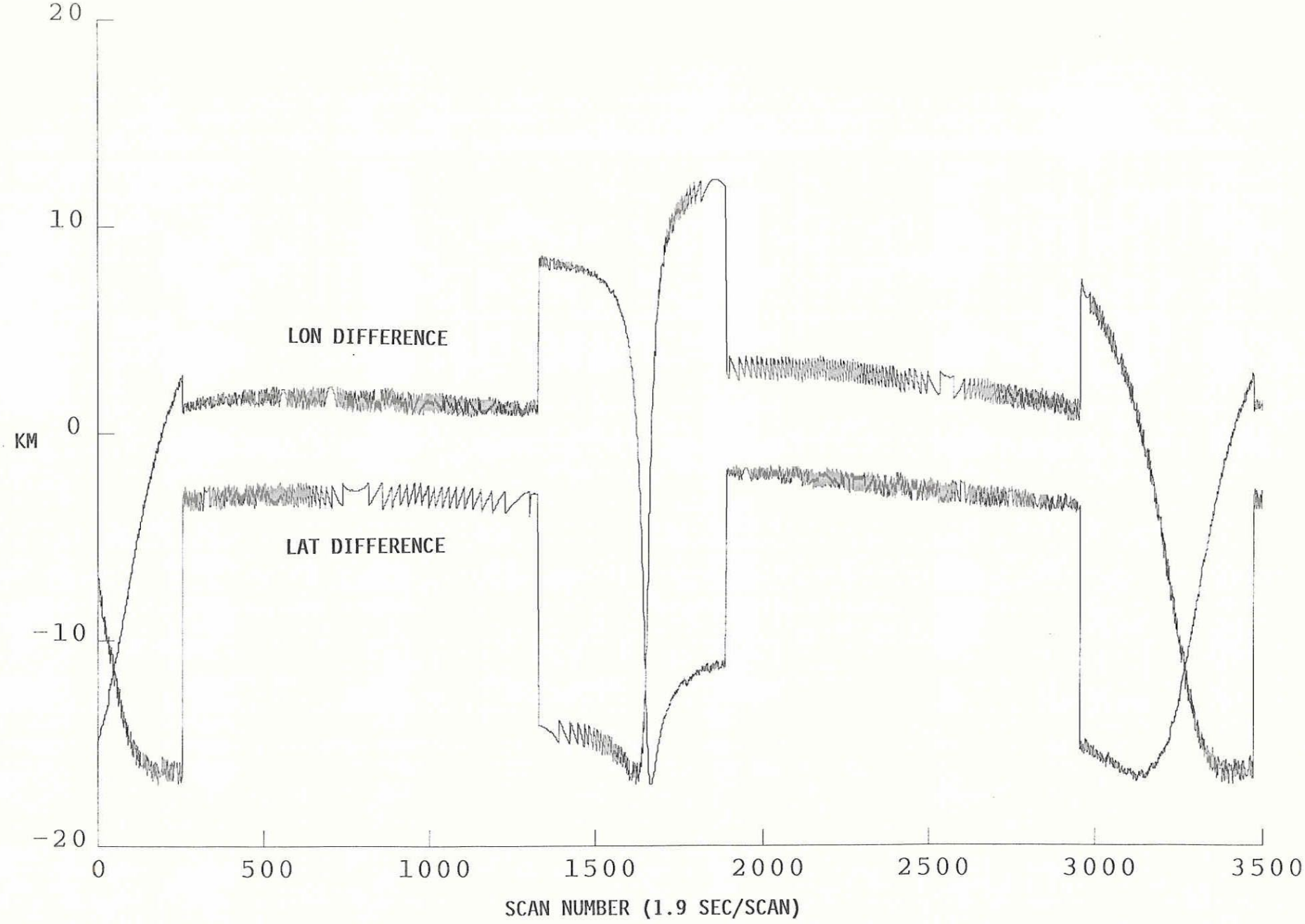

Figure 6.15 Positional Errors of 128th (last) Sampled Pixel
(REV 5100, June 15, 1988)

6.5 IMAGING RESULTS

To provide a visual presentation of SSM/I geolocation errors and their dependence on the ephemeris data, spacecraft attitude changes and sensor boresight corrections a number of SSM/I images were produced. The horizontally polarized 85 GHz channel (85H) was selected for most of the images since it has (with the 85 vertical channel) the highest spatial resolution as well as a large dynamic response to land/water boundaries. In some instances, the horizontally polarized 19 and 37 GHz channels were used to make inter-channel comparisons. For all cases considered, the geolocation errors of the 19 and 37 GHz channels were in agreement with those observed at 85 GHz, confirming the fact that the channels share a common antenna boresight.

A novel interpolation scheme was used to increase the number of samples in the along and cross-track directions before mapping the SSM/I data into a standard Mercator projection. The technique uses the actual antenna patterns and the SSM/I scan geometry to estimate the brightness temperature between along and cross-track pixels and is discussed briefly in Section 3. The number of samples were increased by a factor of 4 in both the along and cross-track directions. Since the resulting spacing between samples is ~3 km, mapping errors are kept well below the resolution of the data.

The geolocation of the 85H imagery was determined by superimposing world coastlines and large islands and lakes. Several world digital data base maps were investigated: World Data Banks (WDB) I and II and the Defense Mapping (DMA) World Vector Shoreline Data Base. Comparisons of WDB I and II revealed significant differences for the coastline of Florida, up to 10-12 km in some instances. A comparison of the WDB II with DMA maps revealed excellent shoreline agreement over all regions considered, which included Eastern and Western USA coastlines, Cuba, Central America, Great Britain, Spain, and the Mediterranean. The reported accuracy of DMA shoreline is better than 1 km over 90% of all identifiable shoreline features. Thus, the accuracy of the coastline maps are expected to be negligible compared with the magnitude of the SSM/I geolocation errors. No terrain height features are included in the data bases.

To account for possible spacecraft attitude errors, sensor misalignment to the spacecraft or sensor deployment misalignment, pitch, roll, and yaw corrections to the spacecraft coordinate system were implemented in the model discussed above. For this purpose, the xyz convention shown in Figure 6.16 was used. With this convention, the euler parameters are related to the pitch θ, roll ψ, and yaw by

$$
\begin{aligned}
e_0 &= \cos(\phi/2)\cos(\psi/2)\cos(\theta/2) + \sin(\phi/2)\sin(\psi/2)\sin(\theta/2) \\
e_1 &= \sin(\phi/2)\cos(\psi/2)\sin(\theta/2) - \cos(\phi/2)\sin(\psi/2)\cos(\theta/2) \\
e_2 &= -\cos(\phi/2)\cos(\psi/2)\sin(\theta/2) - \sin(\phi/2)\sin(\psi/2)\cos(\theta/2) \\
e_3 &= -\sin(\phi/2)\cos(\psi/2)\cos(\theta/2) + \cos(\phi/2)\sin(\psi/2)\sin(\theta/2)
\end{aligned}
$$

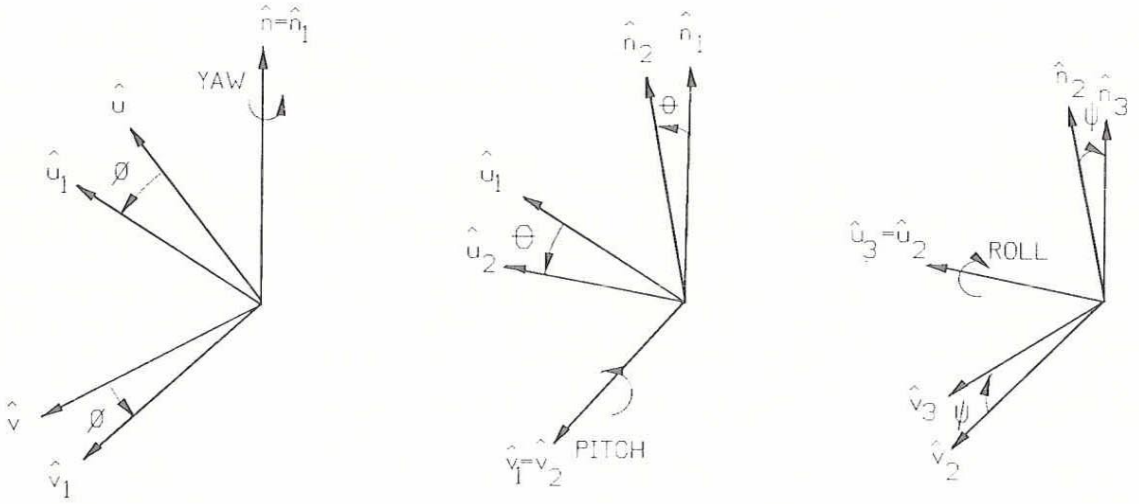

Figure 6.16 XYZ Conventions for Pitch/Roll/Yaw Corrections

where e_i satisfy

$$\sum_{i=o}^{3} e_i^2 = 1$$

The euler parameters form a transformation matrix which relates vectors in the rotated coordinate system, v_3, n_3, u_3 to the coordinate system v, n, u See Goldstein [3]. In particular, the antenna boresight vector, k, of each pixel is subject to this coordinate transformation prior to solving for the slant range along the boresight to the surface of the oblate spheroid Earth model discussed above.

During the course of study of the SSM/I geolocation error, a relatively large number of SSM/I images were produced for detailed analysis. To insure the results derived from the images were not biased significantly, an attempt was made to include a wide range of possible influences. These included, for example,

- o Ascending and descending orbit revolutions
- o Seasonal effects
- o Latitudinal dependence
- o Hemispheric variations
- o Along- and cross-track effects.

Based on the results obtained from the comparisons of FNOC ephemeris data sets with those of NORAD and the F8 spacecraft (See Section 6.3), it was desired to evaluate the relative reduction of the geolocation errors in the images when the spacecraft ephemeris was used. In addition it was desired to determine whether a fixed set of angular coordinate corrections, such as pitch, roll, and yaw discussed above, would bring any residual geolocation errors appearing in the images to within half the spatial resolution of the 85 GHz channels, i.e., within 6 km.

To illustrate the major results derived from the analysis of numerous SSM/I images, Figures 6.17, 6.18, and 6.19 each present a sequence of three 85 H images. At the left the FNOC predict ephemeris is used during the image formation. In the middle, the spacecraft ephemeris is used while at the right, the spacecraft ephemeris is used with fixed pitch, roll and yaw corrections for antenna boresight correction. (As noted previously, this correction could describe spacecraft attitude bias errors, sensor misalignment to the spacecraft or sensor deployment/spin axis misalignment.) The figures span a wide time period, January through June 1988, and are typical of the images studied. In these figures the latitude and longitude grids are 5°.

In the image at the left of Figure 6.17, relatively large geolocation errors ~15-20 km are evident around the Sinai Peninsula and along the coastline of the Red Sea. In addition large errors appear along the

SSM/I GEOLOCATION VALIDATION

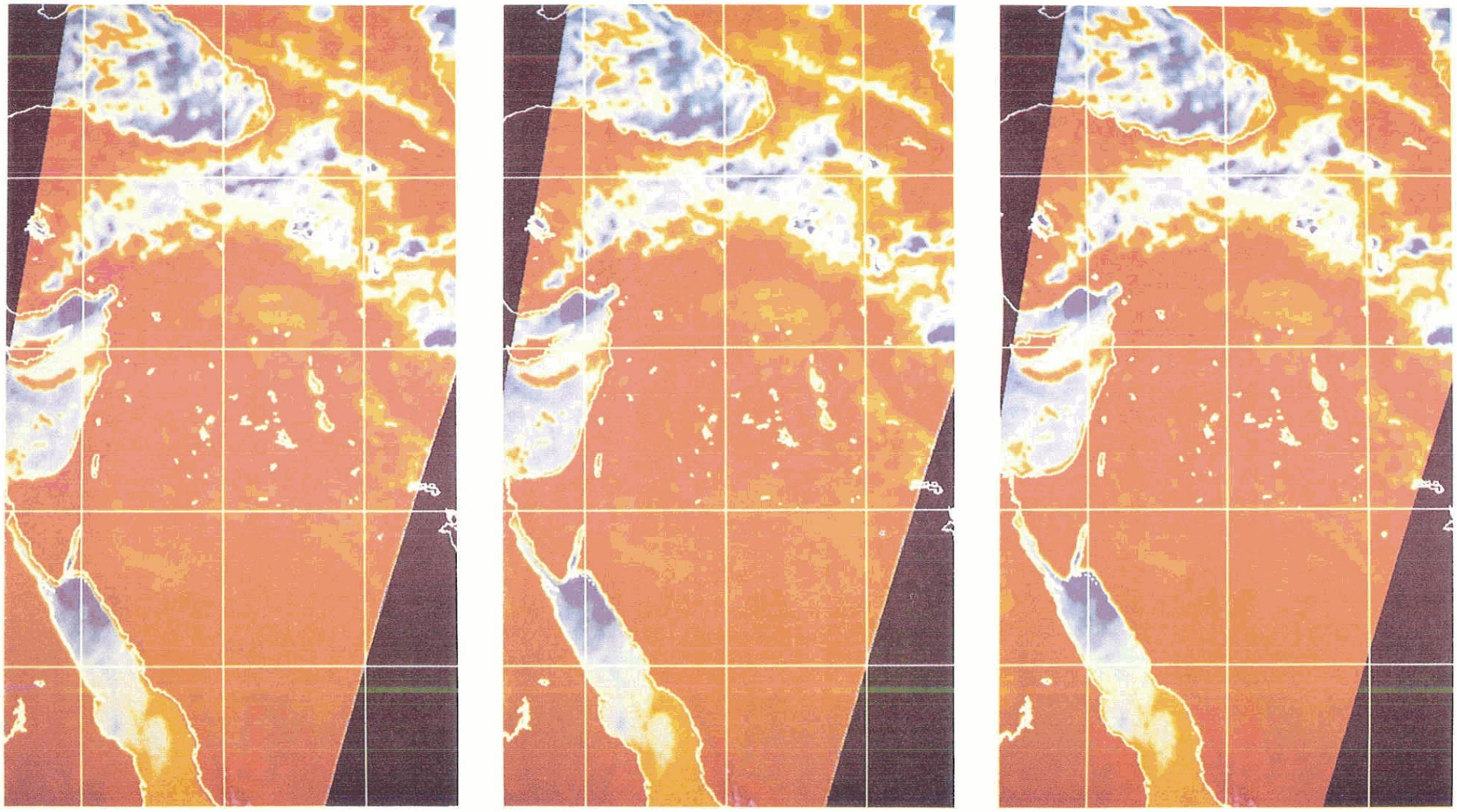

FNOC
PREDICT
EPHEMERIS

SATELLITE
EPHEMERIS

SATELLITE
EPHEMERIS +
BORESIGHT
CORRECTION

Figure 6.17 REV 2945 JANUARY 14, 1988 85 H CHANNEL
(5°GRID)

SSM/I GEOLOCATION VALIDATION

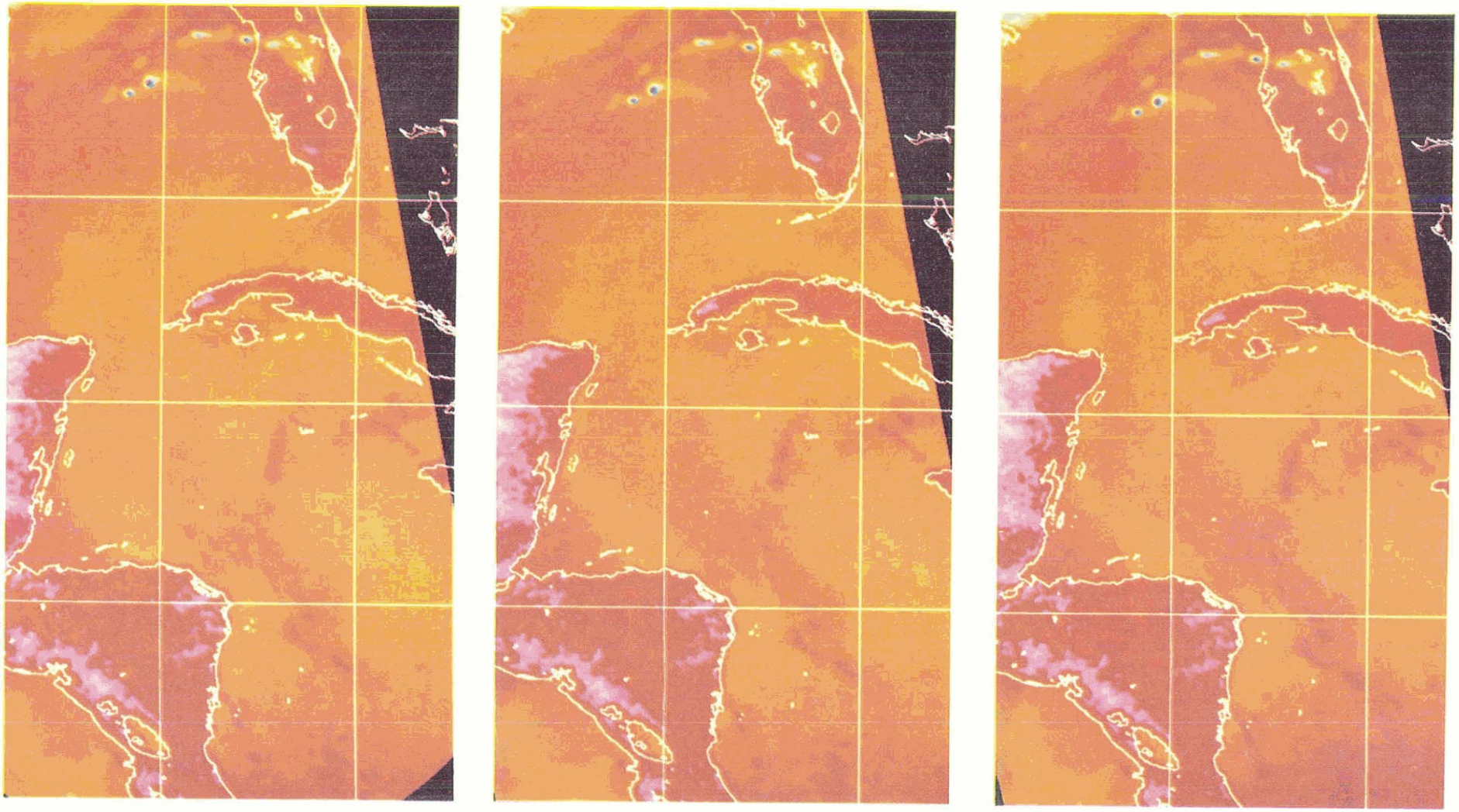

FNOC PREDICT EPHEMERIS

SATELLITE EPHEMERIS

SATELLITE EPHEMERIS + BORESIGHT CORRECTION

Figure 6.18 REV 3776 MARCH 14, 1988 85 H CHANNEL (5°GRID)

SSM/I GEOLOCATION VALIDATION

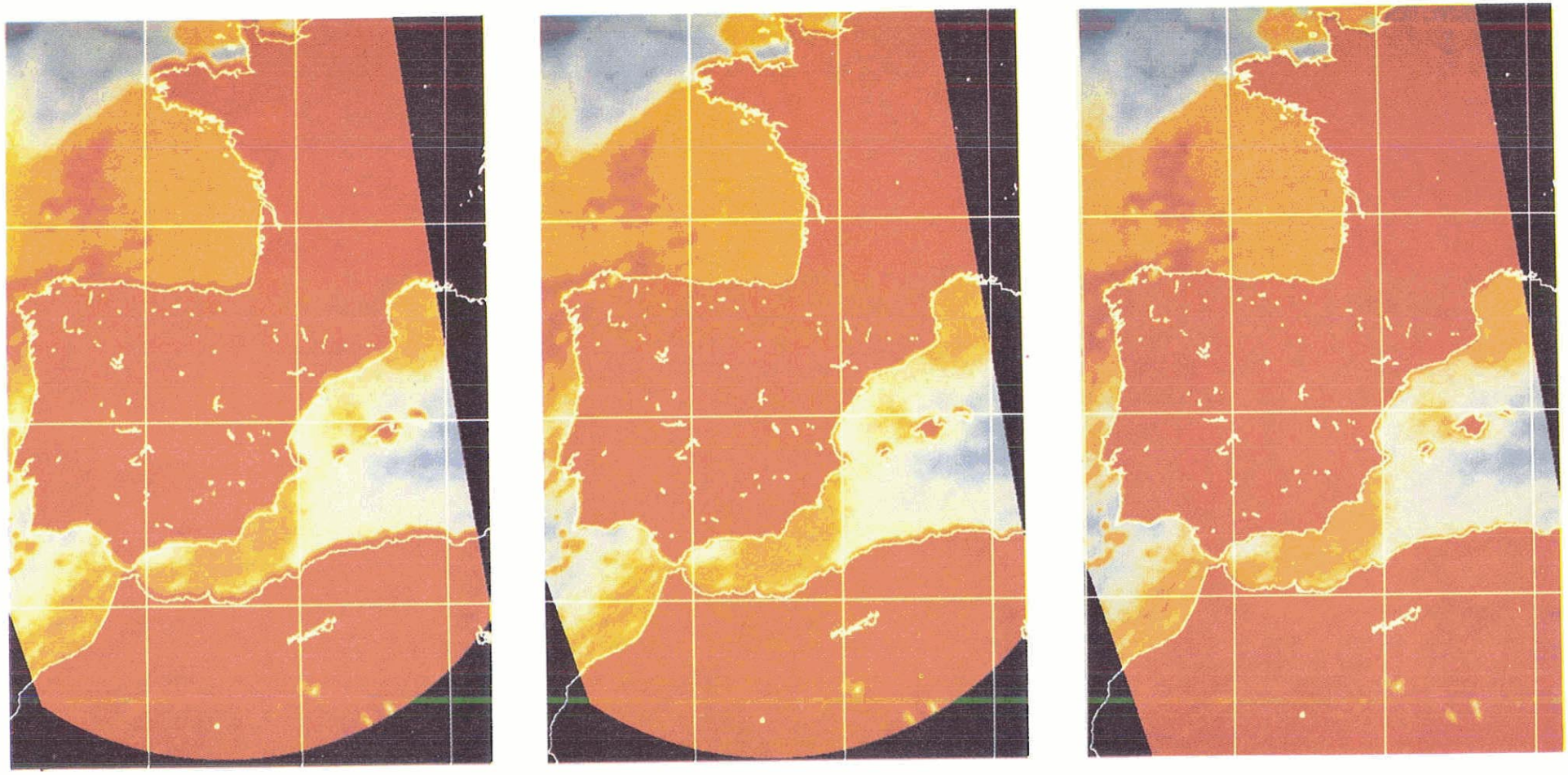

FNOC PREDICT EPHEMERIS 20-30 KM ERROR

SATELLITE EPHEMERIS 10-12 KM ERROR

SATELLITE EPHEMERIS + BORESIGHT CORRECTION < 5 KM ERROR

Figure 6.19 REV 5100 JUNE 15, 1988 85 H CHANNEL
(5°GRID)

Mediterranean coastline of Turkey and with Cyprus. These errors are appreciably reduced in the middle image to a level of 7-8 km. Again using the same pitch, roll, and yaw corrections given above, the image at the right shows the further reduction of geolocation errors. Note especially the Sinai Peninsula and the Red Sea coastlines. A small error < 5 km still persists about Cyprus.

In Figure 6.18 relatively large geolocation errors ~ 15-20 km are visible along the Cuban Jamaican coastlines and the Isle of Juventud. Errors are also evident along the Honduras coastline in the Caribbean Sea. The middle image shows a smaller reduction in geolocation error ~ 5-6 km than obtained in Figure 6.17 when using the spacecraft ephemeris. The image at the right, which uses the same pitch, roll, and yaw correction values given above, reduces the geolocation errors to less than 4-5 km. Note the improvements of the coastlines of Cuba and Jamaica as well as the Isle of Juventud.

In Figure 6.19 relatively large geolocation errors are evident when using the FNOC ephemeris. The Mediterranean coastlines of Morocco and Algeria show ~20-30 km errors while similar errors are visible with the Islands Mallorca, Menorca, and Ibiza. The northern coastline of Spain and the French peninsula in the Bay of Biscay also reveal large geolocation errors. In all cases the image needs to be shifted backward along the spacecraft track to reduce these errors. The middle image of Figure 6.17 shows a dramatic reduction in geolocation error when the spacecraft ephemeris is used, although a residual geolocation error less than 10-12 km remains. A trial and error process was implemented in hopes of obtaining pitch, roll, and yaw values which would remove these residual geolocation errors. After a number of exasperating attempts, it was found that if the values

Pitch θ = -0.1 (degrees)
Roll Ψ = -0.4
Yaw ϕ = -0.6

were employed, the residual error could be reduced to less than ~3 to 5 km.

The results presented in Figures 6.17-6.19 show that once the FNOC ephemeris error has been removed, a fixed set of pitch, roll, and yaw corrections will bring the geolocation errors to within ~5 km. Since geolocation errors have been reported for the OLS, it was decided to determine if the same set of pitch, roll, and yaw corrections would also reduce the geolocation errors appearing in the OLS imagery. To this end, Capt Schmidt and Sergeant Leahman of Air Force Weather Central kindly provided digital tapes of smoothed OLS data for a period of several months covering approximately 2-3 orbital revolutions per week. A computer program was implemented to geolocate the OLS imagery based on scan geometry information obtained from the Westinghouse Corporation. The spacecraft ephemeris (which appears with the OLS sensor data) was used with this program to produce a number of images which could be compared with the SSM/I imagery. Unfortunately, significant cloud cover or large

storms prevented a clear determination of coastlines and islands in many cases. Consequently, relatively few of the OLS images permitted a visual means of evaluating OLS geolocation errors. (It should also be pointed out that due to time constraints not all of the OLS data supplied by AFGWC has been reviewed.) However, based on the OLS images produced, the pitch, roll, and yaw corrections used for the SSM/I do not reduce OLS geolocation error. For example, Figure 6.20 present a typical situation observed without pitch, roll and yaw corrections and should be compared with the SSM/I middle image shown in Figure 6.18. Aside from strong correlations between the cloud structures in the SSM/I and OLS images, the OLS geolocation error visible on the southern coastlines of Cuba and Jamaica as well as Lake Nicaragua, although are of the same magnitude ~ 9-10 km, are not in the same direction as those observable in the SSM/I image. This lack of correlation was noted in all the OLS images produced. Although at first this might be thought to be a result of differences in the scan geometries between the OLS and SSM/I OLS images produced with the pitch, roll, and yaw corrections used for the SSM/I resulted in an increase of the OLS geolocation errors. Figure 6.21 presents a corrected OLS image when using the pitch, roll, and yaw values

Pitch = -0.5 (degrees)
Roll = -0.2
Yaw = -0.2

Note that the error have been reduced below ~3 km. For the OLS images considered a fixed set of pitch, roll, and yaw corrections were found to reduce the geolocation errors to ~ 3 km.

6.6 EARTH INCIDENCE ANGLE

The results presented in Section 6.5 indicate that pitch and roll corrections are needed to remove geolocation error from the SSM/I data. These corrections also influence the pixel earth incidence angle (EIA). Although yaw does not affect the EIA, pitch introduces a fixed offset in EIA and roll introduces a variation across the scan. Of course, the EIA exhibits orbital variations due to variations of the spacecraft altitude and the oblateness of the earth. In terms of the quantities identified earlier, the EIA is given by

$$EIA = \cos^{-1}[-\hat{k} \cdot \hat{r}_p]$$

where $\hat{k}$ is the unit vector along the antenna boresight of a prescribed pixel and $\hat{r}_p$ is the unit vector from the earth's center to the prescribed pixel. Figure 6.22 presents the EIA for REV 5100 as a function of SSM/I scan number without pitch and roll corrections for the first and 64th pixels sampled on each scan. The remaining pixels lie between those extremes. Note that the EIA orbital variations approach ~ 0.5°, peak to peak, and are much larger than the variations across the scan. Of course, the particular phase and amplitude variation depends on the revolution since the spacecraft argument of perigee rotates ~ 2.5° per day.

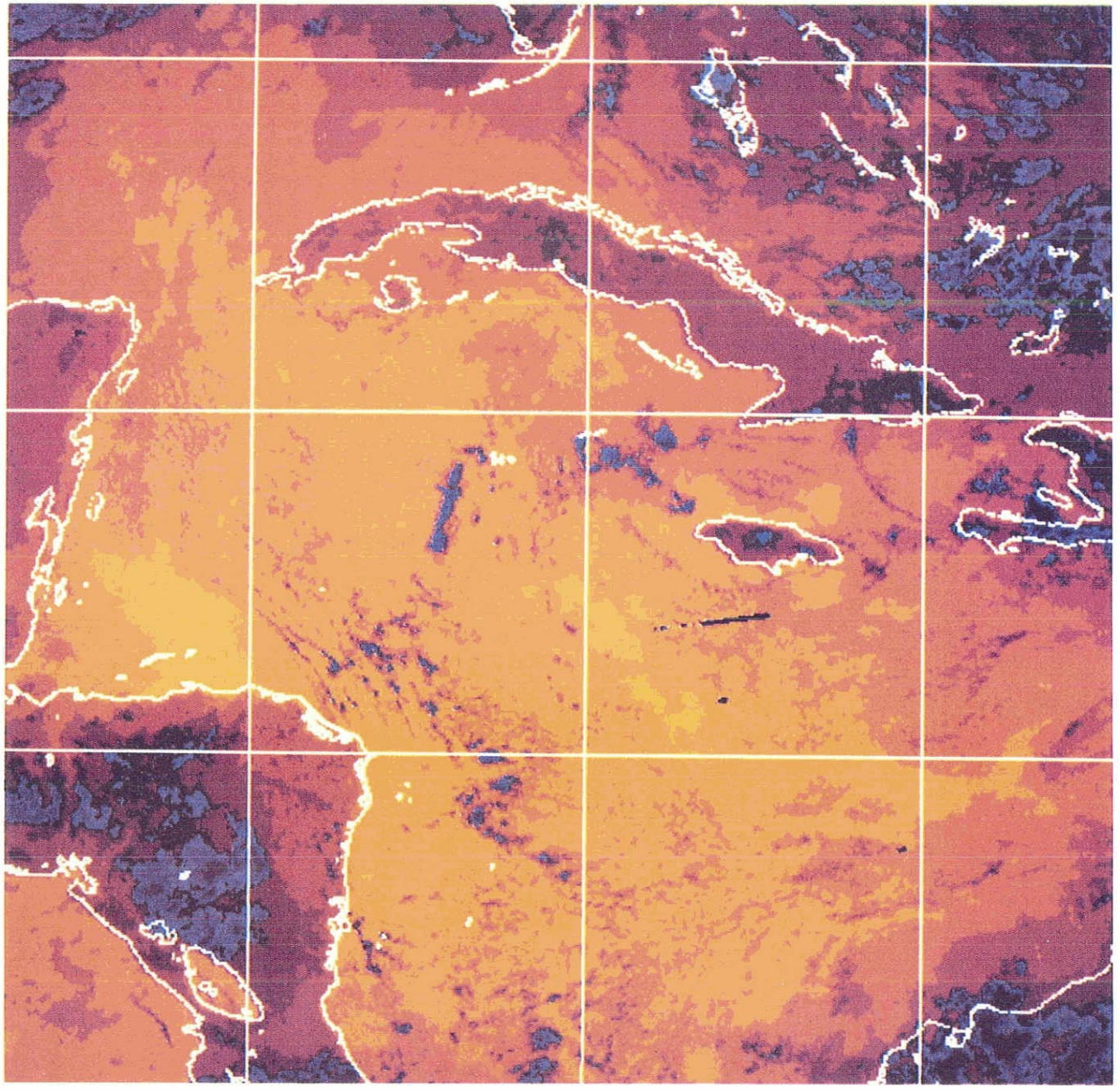

Figure 6.20 Infrared OLS Image REV 3776 (March 14, 1988) (5° Grid)

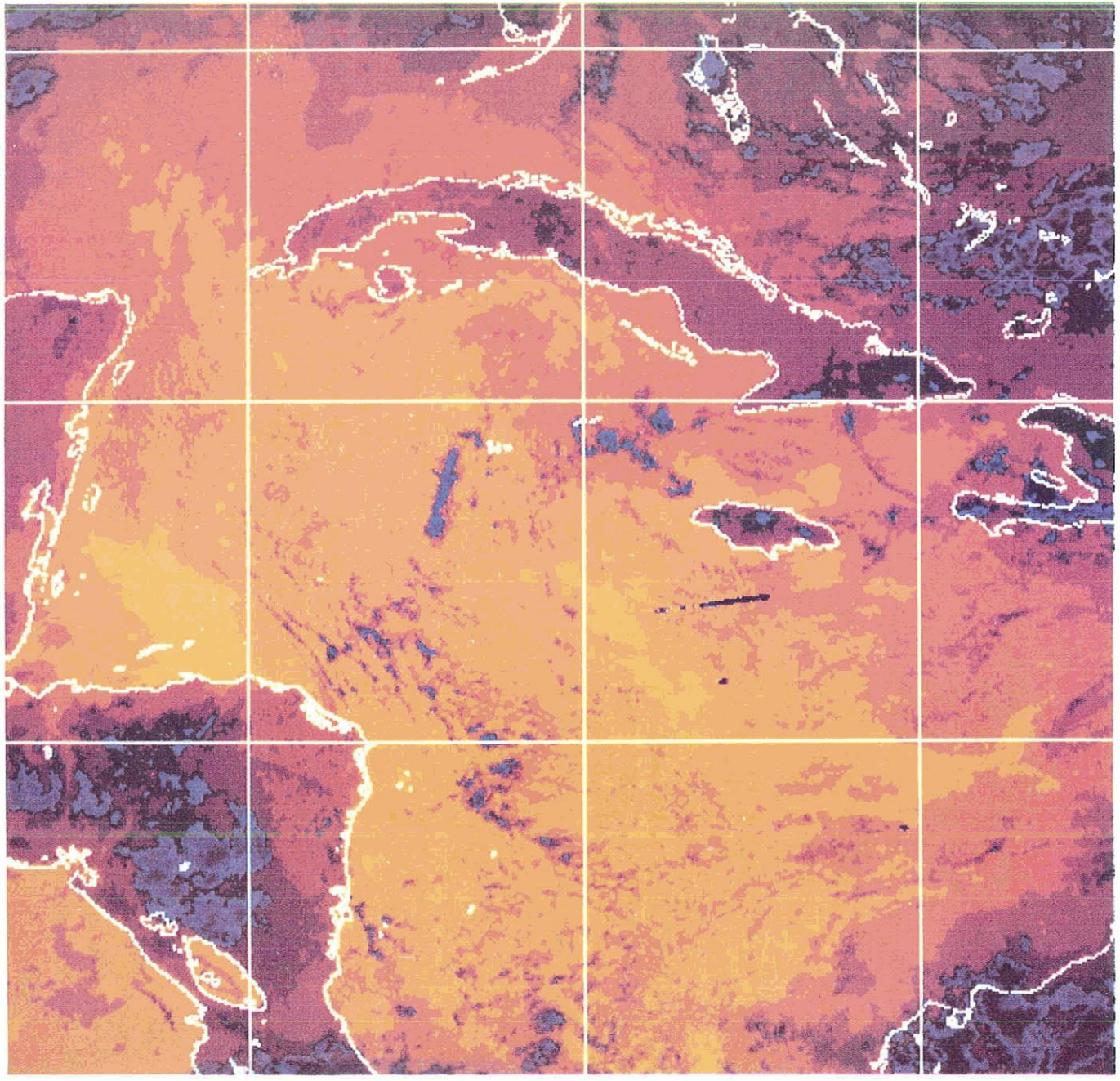

Figure 6.21 Infrared OLS Image with Pitch, Roll, Yaw Corrections REV 3776 (March 14, 1988)

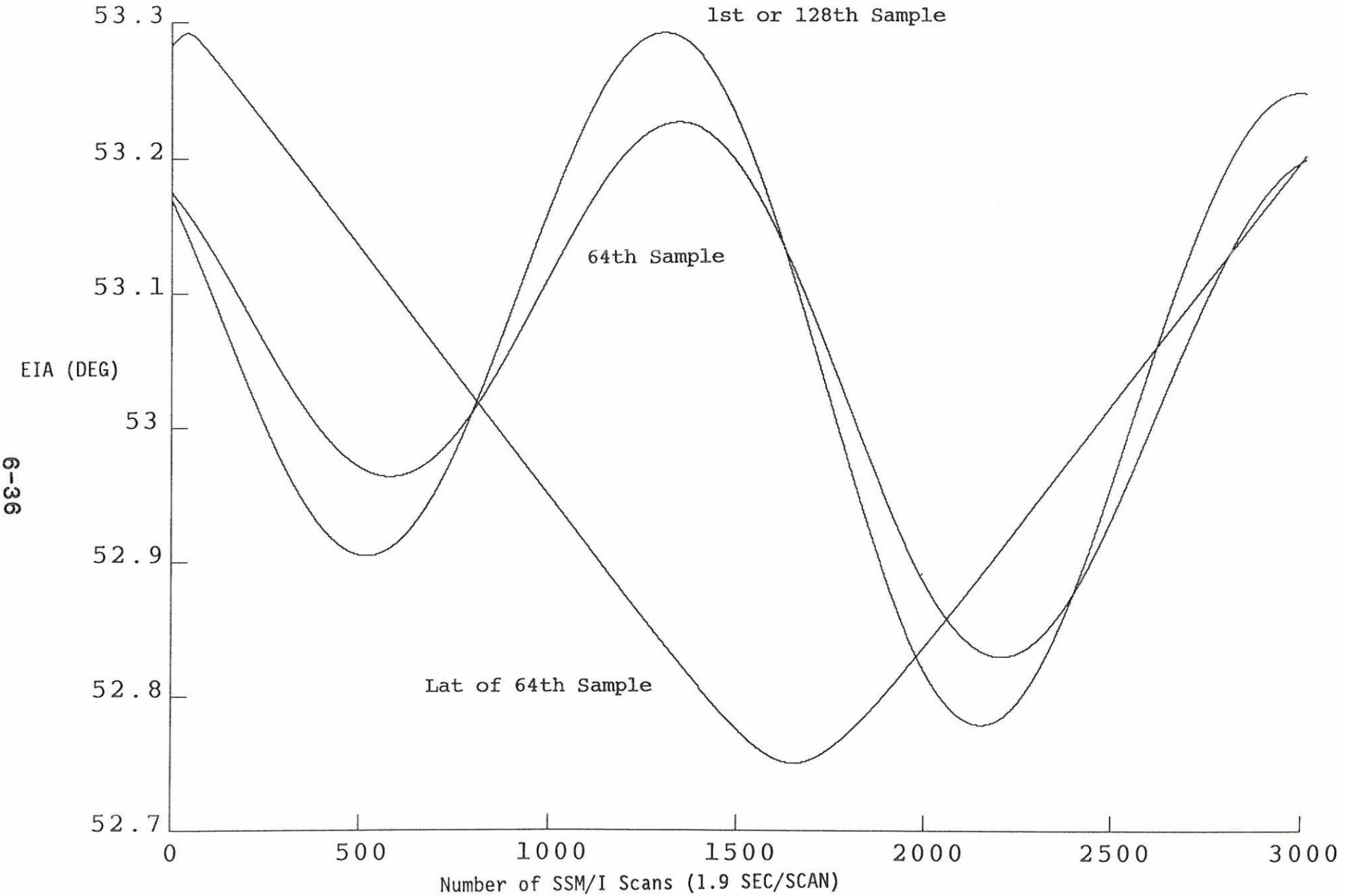

Figure 6.22. Orbital Variation of Earth Incidence Angle EIA (REV 5100)

Figure 6.23 presents the variation of the EIA for the first, 64th and 128th sampled pixels for REV 5100 when using the pitch and roll values of Section 6.5. Note that now the cross-track EIA variation ~0.9° peak to peak is much larger than the orbital variation. For reference, the latitude of the 64th sample is shown. Similar results apply to other revolution although the phase of the variations changes due to rotation of the spacecraft argument of perigee.

6.7 CONCLUSIONS

In view of the above results the following conclusions may be made:

(1) The orbital elements generated by NORAD are a small contributor to the SSM/I geolocation error, typically less than 1 km.

(2) The spacecraft ephemeris used at FNOC contributes a significant and variable error to SSM/I geolocation error. The error appears to arise from a variable time delay in spacecraft motion and in some instances introduces ~ 15 km spacecraft position error.

(3) Numerical approximations appearing in the geolocation algorithm used at FNOC can contribute up to ~ 4 km geolocation error. In addition, the last pixel sampled on each scan has a large geolocation error, ~ 15 km, for subsatellite latitudes greater than 60° or less than -60°. The cause of this error was traced to an interpolation error in the computer module LOCINT in SMISDP.

(4) A fixed set of pitch, roll, and yaw corrections may be found to reduce the SSM/I geolocation error to as low as 3 - 5 km once the ephemeris error had been removed. Although a reasonable confidence can be placed in these corrections, further validation seems appropriate before including the final corrections in the software at FNOC.

(5) Due to the magnitude of the pitch and roll corrections found in (4), the pixel earth incidence angle was found to vary considerably, ~ 0.9°, across the scan.

(6) For the relatively few cases analyzed, a fixed set of pitch, roll, and yaw corrections was found to reduce the OLS geolocation error below ~3-5 km. These corrections were not the same as found for the SSM/I.

Finally, it should be noted that the source(s) of the geolocation errors not due to the ephemeris errors could not be determined conclusively. Although the error could be due to (a) sensor deployment or spin axis misalignment, (b) sensor misalignment with the spacecraft, or (c) spacecraft attitude biases, in view of the results presented it appears that (c) is probably not the main contributor.

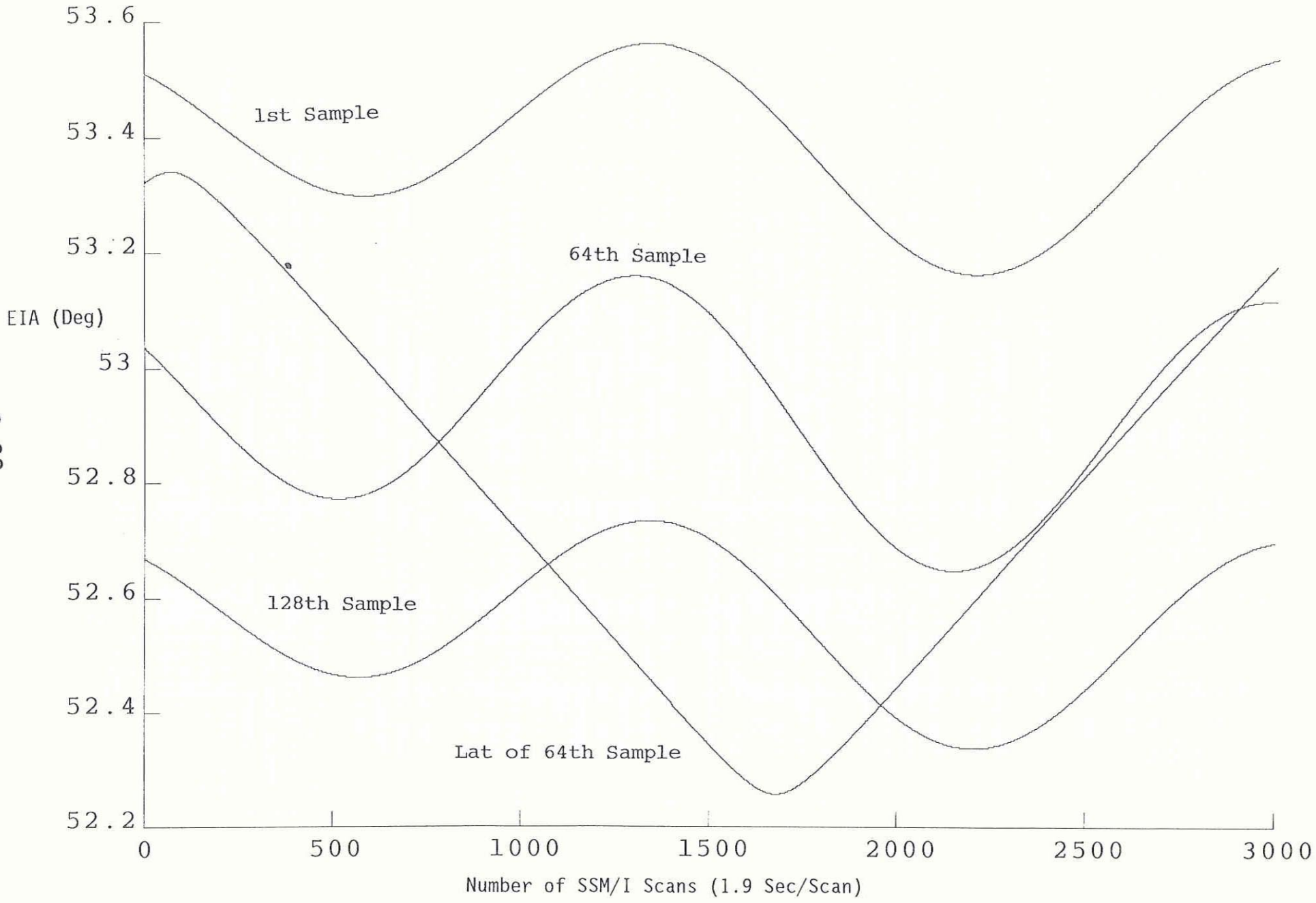

Figure 6.23. Orbital Variation of the EIA Pitch (-.1) and Roll (-.4) Corrections (Rev 5100)

6.8 REFERENCES

[1] SSM/I Program Maintenance Manual for FNOC (REV. A), Vol. II SMISDP, Hughes Aircraft Co Report HS256-0807-0101, Contract No. FO4701-84-C-0036, Feb. 1986.

[2] Wertz, J. R. (Editor) Spacecraft Attitude Determination and Control, Appendix L, D. Reidel Publishing Co., 1985.

[3] Goldstein, H., Classical Mechanics, Addison-Wesley Publishing Co., 1985.